VIBRATION ANALYSIS AND ACTIVE VIBRATION CONTROL OF THE MAGNETICALLY SUSPENDED FLYWHEEL ROTOR

XIANG BIAO

PhD

The Hong Kong Polytechnic University

2021

The Hong Kong Polytechnic University

Department of Mechanical Engineering

Vibration Analysis and Active Vibration Control of The Magnetically Suspended Flywheel Rotor

XIANG BIAO

A thesis submitted in partial fulfilment of the requirements for the degree of Doctor of Philosophy

July 2020

Certificate of Originality

I hereby declare that this thesis is my own work and that, to the best of my knowledge and belief, it reproduces no material previously published or written, nor material that has been accepted for the award of any other degree or diploma, except where due acknowledgement has been made in the text.

(Signed)

XIANG Biao (Name of student)

Acknowledgements

I wish to express my sincere appreciation to all those who have offered me invaluable help during the four years of my study here at The Hong Kong Polytechnic University.

Firstly, I would like to express my heartfelt gratitude to my supervisor, Dr. Waion Wong, for his constant encouragement and guidance. He has walked me through all the stages of the writing of this thesis. Without his consistent and illuminating instruction, this thesis could not have reached its present form.

Secondly, I should give my hearty thanks to all the other faculty members of the Department of Mechanical Engineering of PolyU for their patient instructions in various courses and their precious suggestions for my study here.

Lastly, my thanks would go to my beloved family for their loving considerations and great confidence in me all through these years. I also owe my sincere gratitude to my friends and my fellow classmates who gave me their help and time in listening to me and helping me work out my problems during the difficult course of the thesis.

Abstract

This thesis is focused on the vibration analysis and the active vibration control of the magnetically suspended flywheel (MSFW) rotor system, which has five degrees-of-freedom (DOF) with the control of the axial and radial active magnetic bearing (AMB). The main contents of this thesis contain five parts as following,

Firstly, the vibration characteristics of the MSFW rotor are modeled and analyzed, and the stiffness characteristics and the damping characteristics are studied. The vibration transmissibility of MSFW rotor is affected by the damping coefficient of control system. The natural frequency of MSFW rotor is determined by the stiffness coefficient of control system. So, the vibration characteristics of MSFW rotor are controllable through tuning damping parameters and stiffness parameters of magnetic suspension system. Research contents in this part provide the theoretical foundation to the active vibration control of the MSFW rotor in the following parts.

Moreover, the relationships amongst the vibration characteristics of MSFW rotor, the suspension span ratio and the moment of inertia ratio are studied. Based on the phase margin and the response magnitude, the vibration response of translational motion is regulated by tuning the control parameters. The frequency response of radial rotation is analyzed based on the open-loop poles of the rotational control loop. The critical whirling frequency of MSFW rotor is decided by the moment of inertia ratio, and the BW motion and the FW motion of MSFW rotor are affected by the suspension span ratio. This result provides a new method of analyzing the vibration response of MSFW rotor and the design guideline for MSFW rotor.

In addition, the vibration absorbing ability of axial AMB in MSFW rotor is testified, and the axial AMB mounted at the suspension end of MSFW rotor is regard as a dynamic vibration absorber (DVA) model. Furthermore, the frequency responses of MSFW rotor considering the DVA model are researched. The vibration magnitude of MSFW rotor is suppressed by tuning damping parameter and stiffness parameter of axial AMB. Experiments are conducted to testify the

effectiveness of axial DVA on tuning the dynamic characteristics of MSFW rotor, and the stiffness coefficient is regulated to suppress the dynamic displacement deflections of load rotor and MSFW rotor. The damping coefficient of axial DVA could then be controlled to enhance the stability of MSFW rotor. This part of research expands the application range of MSFW rotor on the active vibration control.

Furthermore, for the MSFW system with great equatorial moment of inertia and great self-weight, the uncertainties about displacement stiffness and current stiffness cause disturbances on the stable control of the MSFW rotor. Therefore, robust control is applied to attenuate the influence on the MSFW rotor introduced by the uncertainties of current stiffness and displacement stiffness. Simulations about axial suspension of MSFW rotor is developed when a transient impulse disturbance, a harmonic disturbance and a random disturbance are respectively added on the MSFW rotor, and maximum displacement deflection from the balanced position is mitigated by the robust control function. Based on experimental results, the maximum displacement deflection from the balanced position using the robust control function is smaller than that with the proportional integral derivative control. These results indicate that the stability of MSFW system with great equatorial moment of inertia and great self-weight could be improved by using the robust control function.

Finally, for the MSFW rotor great equatorial moment of inertia and great self-weight, the coupling effect in radial tilting becomes serious with increasing the rotating speed. So, an internal model control (IMC) method is designed to enhance the robust performance of MSFW rotor. Then, a decoupling control model based on the IMC model is applied to control the translation of the MSFW rotor on four DOFs. Simulations and experiments are performed to validate the IMC model for enhancing the anti-disturbance ability of MSFW rotor. The decoupling IMC model could effectively realize decoupling control in four radial DOFs of MSFW rotor.

Keywords: magnetically suspended flywheel rotor; vibration analysis; active vibration control; dynamic vibration absorber; robust control; rotation and translation; internal mode control.

Table of Contents

List of Tables

List of Figures

List of Acronyms

3-D	Three-Dimensional
A/D	Analog to Digital
AMB	Active Magnetic Bearing
BW	Backward Whirling
CAN	Controller Area Network
CF	Crossover Frequency
CMG	Control Moment Gyro
DAQ	Data Acquisition
DC	Direct Current
DOB	Disturbance Observer
DOF	Degree of Freedom
DSP	Digital Signal Processor
DVA	Dynamic Vibration Absorber
FESS	Flywheel Energy Storage System
FPGA	Field Programmable Gate Array
FW	Forward Whirling
GM	Gain Margin
IPC	Industrial Personal Computer
ISP	Inertial Stabilized Platform
MIMO	Multi-Input Multi-Output
MOSFET	Metal Oxide Silicon Field Effect Transistor
MPU	Main Processing Unit
MSCMG	Magnetically Suspended Control Moment Gyro
MSFW	Magnetically Suspended Flywheel
NI	National Instrument
PD	Proportional-Derivative
PI	Proportional-Integral
PID	Proportional-Integral-Derivative
PM	Phase Margin
PMB	Passive Magnetic Bearing

PMSM	Permanent Magnet Synchronous Motor
PSD	Power Spectrum Density
PWM	Pulse Width Modulation
RMS	Root Mean Square
SISO	Single-Input Single-Output
SMC	Sliding Mode Control
T-S	Takagi-Sugeno

Glossary

A	Cross-sectional area of axial AMB in DVA
A_l , A_l' , A_l'' , A_l'''	Response magnitude of load rotor
A_m , A_m' , A_m'' , A_m'''	Response magnitude of MSFW rotor
$A_{n=x+,\ x-,\ y+,\ y-}$	Cross-sectional area of radial AMB
A_{z+}	Cross sectional area of magnetic pole at upper axial AMB
A_{z-}	Cross-sectional area of magnetic pole at lower axial AMB
$\boldsymbol{A}$	The state matrix
$\boldsymbol{B}$	The input matrix
C	Coupling damping between MSFW rotor and load rotor
$\boldsymbol{C}$	The output matrix
c_{at}, c_y, c_z	Tilting damping of axial AMB in DVA
c_{va}	Damping coefficient of axial AMB in DVA
d	Controllable airgap of axial AMB in DVA
d_0	Bias airgap of axial AMB in DVA
d_{x0}	Bias airgap of radial AMB in x axis
d_x	Controllable airgap of radial AMB in x axis
d_{y0}	Bias airgap of radial AMB in y axis
d_y	Controllable airgap of radial AMB in y axis
d_z	Controllable airgap of axial AMB in z axis
d_{z0}	Bias airgap of axial AMB in z axis
d_{z+}	Length of airgap in upper axial AMB
d_{z-}	Length of airgap in lower axial AMB
$e(s)$	Error function
f_{x+}	Magnetic force of radial AMB in x+ direction
f_{x-}	Magnetic force of radial AMB in x- direction
f_{y+}	Magnetic force of radial AMB in y+ direction
f_{y-}	Magnetic force of radial AMB in y- direction
f_{z+}	Magnetic force of axial AMB in z+ direction
f_{z-}	Magnetic force of axial AMB in z- direction
$f_x(i_x, d_x)$	Magnetic force of radial AMB in x axis

$f_y(i_y, d_y)$	Magnetic force of the radial AMB in y axis
$f_z(i_z, d_z)$	Magnetic force of the axial AMB in z axis
F	Magnet motive force of the axial AMB in DVA
$G_D(s)$	Model transfer function of the MSFW rotor
$G_{DIMC}(s)$	DIMC model of the MSFW rotor
$G_{IMC}(s)$	IMC model of the MSFW rotor
$G_f(s)$	Low pass filter
$G_R(s)$, $G_r(s)$	Transfer function of rotational control loop
$G_T(s)$, $G_t(s)$, $G_{ry}(s)$	Transfer function of translational control loop
$G_{dy}^{DIMC}(s)$	Disturbance transfer function of the DIMC model
$G_{dy}^{IMC}(s)$	Disturbance transfer function of the IMC model
$G_m(s), G'_m(s),$	Transfer function of the MSFW rotor
$G_l(s), G'_l(s),$	Transfer function of the load rotor
H	The angular momentum of the MSFW rotor
$\boldsymbol{I}$	The unit matrix
I_0	Bias current of the axial AMB in DVA
i	Real current of the axial AMB in DVA
$I_{n=1\text{-}8}$	Control current of the radial AMB
I_{x0}	Bias current of the radial AMB in x axis
i_x	Control current of radial AMB in x axis
I_{y0}	Bias current of the radial AMB in y axis
i_y	Control current of the radial AMB in y axis
I_{z0}	Bias current of the axial AMB in z axis
i_z	Control current of the axial AMB in z axis
I_{z+}	Control current of the axial AMB in z+ direction
I_{z-}	Control current of the axial AMB in z- direction
J_m	Equatorial moment of inertia of the MSFW rotor
J_l	Equatorial moment of inertia of the load rotor
J_x, J_y	Equatorial moment of inertia of the MSFW rotor
J_z	Polar moment of inertia of the MSFW rotor
k_{amb}	Electromagnetic force coefficient of the radial AMB
k_{at}, k_y, k_z	Tilting stiffness of the MSFW rotor

k_{av}	Electromagnetic force coefficient of axial AMB in DVA
k_d	Displacement stiffness of axial AMB in DVA
k_{dx}	Displacement stiffness of radial AMB in x axis
k_{dy}	Displacement stiffness of radial AMB in y axis
k_{dz}	Displacement stiffness of axial AMB in z axis
k_i	Current stiffness of axial AMB in DVA
k_{ix}	Current stiffness of radial AMB in x axis
k_{iy}	Current stiffness of radial AMB in y axis
k_{iz}	Current stiffness of axial AMB in y axis
k_w	The amplification coefficient
K	Stiffness between MSFW rotor and load rotor
K_D	The derivative coefficient
K_P	The proportional coefficient
$K(s)$	Equivalent control function of IMC model
k_s	The sensitivity of displacement sensor
$K_r(s)$	Synthesis controller of rotational motion
$K_t(s)$	Synthesis controller of translational motion
k_{va}	Comprehensive stiffness of axial AMB in DVA
l	Span from mass of center to radial AMB
l_{lm}	Span from mass of center to radial AMB at lower end
l_{ls}	Span from mass of center to sensor at lower end
l_{um}	Span from mass of center to radial AMB at upper end
l_{us}	Span from mass of center to sensor at upper end
L^{-1}	The inverse Laplace transformation operator
m	Mass of MSFW rotor
N	Turn number of radial AMB's winding
N_{va}	Turn number of AMB's winding in DVA
N_{z+}, N_{z-}	Turn number of axial AMB's winding
$\boldsymbol{u}$	The input vector
$W_d(s)$	Transfer function of disturbance
$W_e(s)$	Performance weighting function
$W_n(s)$	Transfer function of sensor noise

$W_p(s)$	Output weighting function
$W_u(s)$	Input weighting function
r	Frequency ratio of translational motion
r_l	Suspension span ratio of radial AMB
r_j	Moment of inertia ratio of MSFW rotor
R	Equivalent reluctance of axial AMB in DVA
$R_{n=1\text{-}8}$	Equivalent reluctance of radial AMB
R_{x+}	Reluctance in positive direction of x axis
R_{x-}	Reluctance in negative direction of x axis
R_{y+}	Reluctance in positive direction of y axis
R_{y-}	Reluctance in negative direction of y axis
R_{z+}	Reluctance in positive direction of z axis
R_{z-}	Reluctance in negative direction of z axis
$R(s)$	Penalty sensitivity function
$S(s)$	Sensitivity function
$S_{DIMC}(s)$	Sensitivity function of DIMC model
$S_{IMC}(s)$	Sensitivity function of IMC model
T_m	Driving torque of MSFW rotor
T_x	Tilting torque of MSFW rotor about x axis
T_y	Tilting torque of MSFW rotor about y axis
T_z	Tilting torque of MSFW rotor about z axis
TR, A_{tr}	Vibration transmissibility of translational motion
$T(s)$	Complementary sensitivity function
$\boldsymbol{x}$	The state vector
$\boldsymbol{y}$	The output vector
α	Tilting angle of MSFW rotor about x axis
β	Tilting angle of MSFW rotor about y axis
θ_l	Radial tilting angle of the load rotor
θ_m	Radial tilting angle of the MSFW rotor
Φ_{x+}	Magnet flux in positive direction of x axis
Φ_{x-}	Magnet flux in negative direction of x axis
Φ_{y+}	Magnet flux in positive direction of y axis

Φ_{y-}	Magnet flux in negative direction of y axis
Φ_{z+}	Magnet flux in positive direction of z axis
Φ_{z-}	Magnet flux in negative direction of z axis
$\delta(t)$	The Dirac delta function
μ_0	The vacuum permeability
ξ	Damping coefficient of translational motion
ξ_l	Coupling damping between MSFW rotor and load rotor
$\xi_m, \xi_m', \xi_m'', \xi_m'''$	Damping coefficient between axial AMB and MSFW
γ	The optimization factor
λ_l	Ratio between frequency and natural frequency of load
$\lambda_m, \lambda_m'', \lambda_m'''$	Ratio between frequency and natural frequency of MSFW
v	Ratio between moment of inertia of load and MSFW
ω_l	Natural frequency of shaft connecting MSFW and load
$\omega_m, \omega_m'', \omega_m'''$	Natural frequency of shaft connecting axial AMB and MSFW
ω_n	The natural frequency of translational motion
$\omega_{n\varphi}$	The critical rotational frequency of MSFW rotor
ω_{rn}	Natural rotational frequency
ω_t	Vibration frequency of translational motion
Ω	Rotational frequency of MSFW rotor about z axis
σ_i	Singular values of frequency function matrix

Chapter 1. Introduction

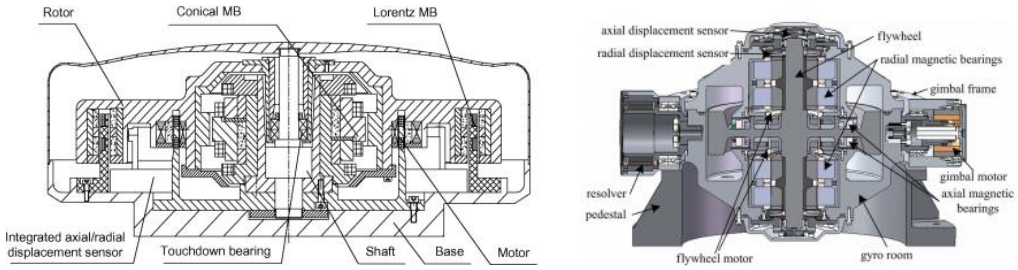

(a) (b)

Fig. 1.1. (a) The MSFW for the attitude control of satellite, (b) the control moment gyro for the attitude control of satellite.

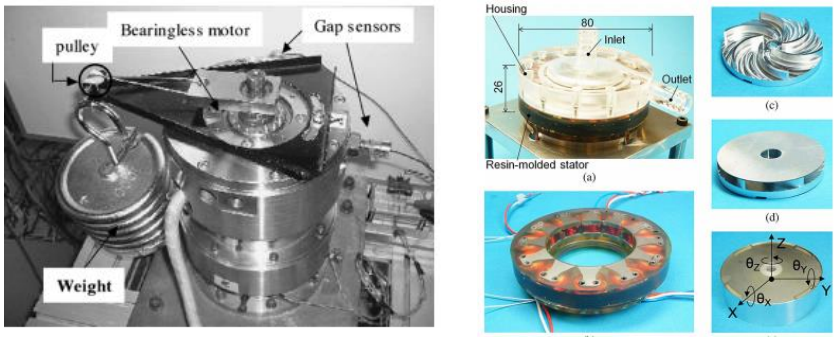

(a) (b)

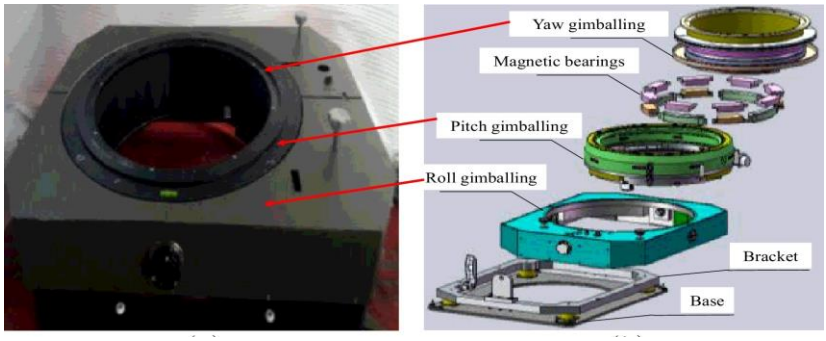

(c)

Fig. 1.2. (a) The high energy density motor, (b) the magnetically suspended molecular pump, (c) the magnetically suspended ISP.

The rotor is supported by the mechanical bearing in the general rotating machinery. The friction between the rotor and the stator is unavoidable, so the lubrication system is needed to improve the system lifetime of the general rotating machinery. Moreover, the vibration of the rotor in the general rotating machinery is uncontrollable because of the passive support method of mechanical bearing.

Therefore, the magnetic suspension technology is developed to suspend the rotor. Because it have advantages on longevity, high-efficiency [1, 2], zero friction [3, 4] and lubrication-free [5], the magnetic bearing technology had been widely applied to rotating machines. Some common examples are the energy storage and attitude control flywheel system in Fig. 1.1(a) for realizing the power conversion and the acritude control of satellite [6, 7], the control moment gyro (CMG) in Fig. 1.1(b) [8-11] for controlling attitude of satellite, the high energy density motor in Fig. 1.2(a) [12-14], the magnetically suspended molecular pump in Fig. 1.2(b) [15-20], and the inertial stabilized platform (ISP) in Fig. 1.2(c) [21-23]. In detail, the magnetically suspended flywheel (MSFW) is used to stabilize the attitude of satellite because of its benefits of micro-vibration and lubrication-free during a very long work cycle [24-27]. The friction between the stator and the rotor in rotational machines such as the turbo-molecular pumps [28-30], the compressors [31-33] and the high-speed motors [34-37] could be eliminated by integrating a magnetic suspension system and a high-speed motor, so the working efficiency and control precision of the rotational machine could be improved. For the MSFW system, the suspension method between the static stator and the rotating rotor is contactless, so the friction between the static stator and the rotating rotor could be avoided, and the disturbance forces and torques acting on the rotor could be effectively isolated [30, 38, 39]. Moreover, through tuning the control current based on the feedback displacement of MSFW rotor at static suspension and dynamic rotation states, the active controllability of the magnetic suspension system could maintain the position precision of the MSFW rotor when it runs at a high rotational speed [40-42].

A thorough study about vibration characteristics of the MSFW rotor is very important to realize its position control and to improve the suspension precision of the rotor. A five controllable degrees of freedom (DOFs) bearingless motor with a magnetic suspension system was designed by Asama et al. [43], and it had the benefits on zero wearing, high rotational speed and low maintenance cost. Tang et al. [44] studied the dynamic performances of a MSFW rotor in the magnetically suspended control moment gyro (MSCMG) whose rotor is suspended by the passive magnetic bearing (PMB) and the active magnetic bearing (AMB), and then the

modal shape of the magnetically suspended rotor was affected by the current stiffness and the displacement stiffness of the AMB. Ji et al. [45] studied the vibration characteristics of a magnetically suspended rigid rotor, and the axial and radial vibration characteristics of the magnetically suspended rigid rotor were disturbed by the rotor mass. Ji and Hansen [46] researched the vibration characteristics of MSFW rotor at the resonant frequency, and the influence of the proportional coefficient and the derivative coefficient on the nonlinear vibration were tested. Yang [47] found that the radial vibration of a miniature magnetically levitated rotating machine became obviously great when the rotational frequency of the rotating machine approaches to the resonant frequency, and then a control model for the electromagnetic actuator was proposed to mitigate the resonance oscillation. The mechanical characteristics of a high-speed MSFW rotor in a MSCMG was investigated in [48], the analysis results indicated that the control stability of the high-speed MSFW rotor was affected highly by the mass, the stiffness and the shape coefficient of the rotor. Yan et al. [49] applied a magnetic suspension system to bearing−less switched reluctance motor, and researched the vibration characteristics, and the vibration magnitude of the bearing−less switched reluctance motor with a magnetic suspension system was smaller comparing to the ordinary switched reluctance motor.

Although some research publications about the vibration characteristics of MSFW rotor could be found in literature, the relationship between the vibration characteristic and the system parameter of MSFW rotor has not been established. Therefore, in this research, the vibration characteristics of the MSFW rotor used for a flywheel energy storage system (FESS) are analyzed theoretically and tested experimentally. The relationships amongst the control coefficients, the system parameters and the vibration characteristics of the MSFW rotor are developed theoretically and analyzed experimentally, and the tilting vibration of MSFW rotor with different disturbances are also researched.

In this research, the basic dynamic models of MSFW rotor in translational motion and the radial rotation are developed. The dynamic vibration characteristics of the MSFW rotor with

different types of disturbances are analyzed. The stiffness characteristics and the damping characteristics of the MSFW rotor are researched.

Many problems of the MSFW rotor system are still needed to be solved when it is running at high rotational speed. Especially, more research about the stability analysis method of the MSFW rotor are required. Sugimoto and Chiba [50] analyzed the stability of the MSFW rotor in a two-axis actively positioned bearing−less motor. They found that the tilting motion of the MSFW rotor could cause serious interference to its stability, and the stable suspension of the MSFW rotor could be achieved by regulating the integral gain of the control system. Fang et al. [50] developed the stability testing method of the nutation and the precession of the MSFW rotor using the gain margin and the phase margin of the rotational control loop. They proposed a stability criterion which was independent to the rotational frequency of the MSFW rotor. The relationship between the stability margins of different whirling motions and the parameters of the control system was also investigated. Ren et al. [51] analyzed the influences of the time-delay on the stable control of the rotational motion for the MSFW rotor with coupling effect. A multi-input multi-output (MIMO) system was converted into several single-input single-output (SISO) control systems through the variable reconstruction in complex field. The relationship between the control stability of the cross-feedback system and the time-delay effect was also studied. Tang et al. [19] studied the relationship between the precession frequency of the MSFW rotor and the moment of inertia ratio in a MSCMG. They found that the moment of inertia ratio of the MSFW rotor was related to the mass and the generalized stiffness. Zheng et al. [52] proposed an optimization method of damping compensation for a flexible rotor. They designed a phase-shift filter to compensate the phase difference about the bending frequency of the flexible rotor suspended by the AMB. Zhang et al. [53] studied the relationship between the stiffness and the parameters of MSFW rotor. They found that their modelling method could be used to achieve a high stiffness of the MSFW rotor in a compact FESS. Dimond et al. [54] quantified the influence of the gyroscopic coupling effect on a magnetically suspended rigid rotor, and they used the dimensionless proportional-derivative (PD) control gain, the moment

of inertia ratio and a dimensionless speed ratio to evaluate the stability of the rigid flywheel rotor with the gyroscopic coupling effect.

However, the relationship between the structural parameters of magnetic suspension system and vibration characteristics of translation and rotation was not studied. The research on the vibration analysis method of the MSFW rotor using the distribution of open-loop pole and the dynamic response of the rotational loop was not found in literatures. Therefore, the relationship between the structural parameters of the MSFW rotor and vibration characteristics of translation and rotation is worthy of being researched. The vibration analysis method based on the distribution of the open-loop pole and the frequency response of the MSFW rotor are developed. It is a new way to analyze the vibration characteristics of the MSFW rotor and provides some guidelines to the suspension span of the radial AMB system in the MSFW rotor. Moreover, the analysis results validate that the whirling vibrations of the MSFW rotor could be avoidable by regulating moment of inertia ratio and suspension span ratio of radial AMB. The frequency bandwidth between the backward whirling (BW) and the forward whirling (FW) of the MSFW rotor could be regulated by adjusting the moment of inertia ratio and the suspension span ratio of the radial AMB, so the different control methods would be utilized to control the different whirling vibrations of the MSFW rotor.

For the rotating machinery of driving other rotational components and loads, the vibration disturbance imposing on the load rotor and the motor affects the stability of the motor and load rotor system. Therefore, the researches about vibration characteristic and active vibration control of the motor and the load is significant to attenuate the disturbance and improve the control precision of the rotating machines such as the FESS with great equatorial moment of inertia [55, 56] and the high energy density motors [57-61].

A dynamic vibration absorber (DVA) with the positive stiffness coefficient and the negative stiffness coefficient was proposed to mitigate vibration response of the driving motor and driven load rotor system in literature [62], and the experimental results indicated that the

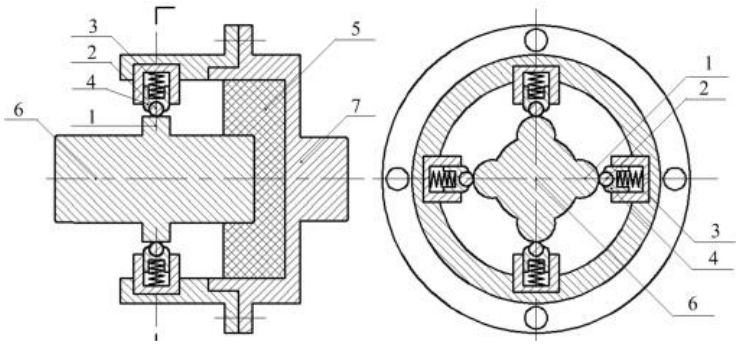

(a)

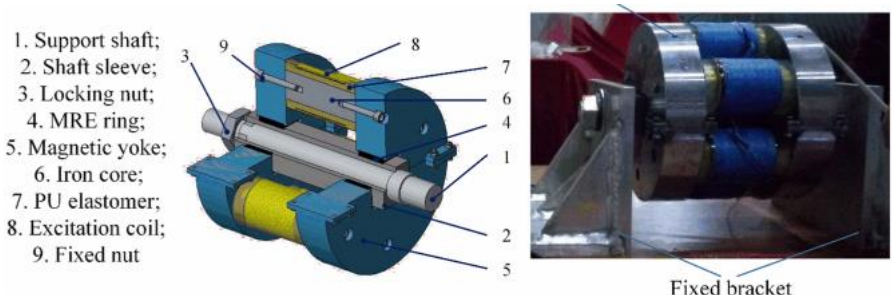

(b)

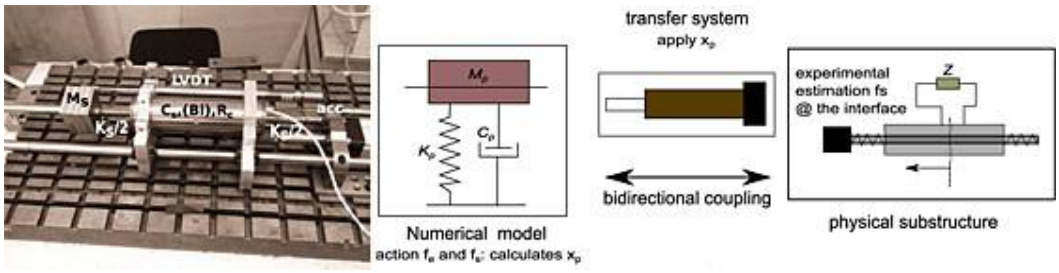

(c)

Fig. 1.3. (a) The quasi-zero stiffness vibration isolator, (b) the semi-active DVA model, (c) the electromagnetic vibration absorber.

negative stiffness coefficient of the DVA system could broaden the control frequency of the driving motor. The torsional vibration system with the different stiffness excitations were investigated, and the vibration performances of the driving motor was evaluated in [63]. The results showed that this driving motor is beneficial for enhancing the dynamic performances of the motor and load rotor system. An actively controllable DVA using the coil springs and the magnetic springs [64] was used to attenuate the vibration displacement response caused by the rotor's unbalance terms. The experiments were conducted to prove that this DVA could effectively mitigate the vibration displacement response of the unbalanced rotor model in Fig. 1.3(a). The high-static low-dynamic stiffness DVA system was used to suppress vibration

responses of the rotor model with unbalance mass terms in [65-68], the designed DVA could be equivalent to a linear stiffness-damping system. By using two inertia rings, a dual DVA could connect the driving end and the driven end of a motor, and then the torsional vibration of the motor was suppressed [69]. The results indicated the response magnitude of the transient vibration disturbance imposing on the rotating motor was greatly mitigated. The quasi-zero stiffness vibration isolator was proposed to suppress the torsional angles of the rotating motor shaft, the experimental result showed that this DVA for torsional vibration could effectively surpass the linear counterpart of the rotor shaft [70]. Using the viscoelastic material and structure, a viscoelastic DVA was designed to suppress the vibration acting on a rotating machine [71]. As shown in Fig. 1.3(b), Liu et al. used the magnetorheological elastomer to design a semi-active DVA for a propulsion system [72], and the simulation results including electromagnetics and thermodynamics presented that the vibration absorbing ability was acceptable although this DVA had frequency shift. In Fig. 1.3(c), an electromagnetic transducer combing with an electrical circuit system was embedded in an electromagnetic DVA [73, 74], the results presented that the proposed electromagnetic DVA could reduce the displacement variations of the host mass. An electrorheological DVA was proposed to suppress torsional angles caused by the torsional vibration in a rotor system [75]. A magnetic actuator was used to measure dynamic characteristics, the optimal control method was further applied to actively control the synchronous vibration phenomenon of rotor, and then the magnetic actuator was used to a multi-mass rotating machine system to verify the effectiveness [76]. By using a smart spring structure with an indirect piezoelectric stack, a semi-active vibration control system with tunable stiffness was designed for a rotating machine to mitigate the great amplitude vibration, and the experimental results validated that it could reduce the vibration magnitudes of the rotor at different operation situations [77]. The damping characteristics of the PMB was researched, and then controllable characteristics of the restoring torques were studied in [78]. The experimental results displayed that the translational displacement in radial directions could increase the restoring torque to control the vibration displacements of the flywheel rotor.

In references [79, 80], the frequency characteristics of a motor and load rotor resonant system were investigated, the proportional-integral-derivative (PID) control model using the feedback compensation was designed to regulate the rotational speed of the motor, and the analysis results showed that the proposed PID control model could actively control the vibration response of the motor and load rotor resonant system. For the elastic rotor model with limited shaft torque, a proportional integral (PI) control model based on the model predictive control (MPC) was proposed to control the torsional angles and displacements. The results indicated that the designed PI control model combining the MPC was more useful on mitigating the torsional angles and displacements than the PI control model based on the pole-placement method. To eliminate the torsional vibration imposing on the permanent magnet synchronous motor (PMSM), Lee et al. [81] applied the adaptive notch filter to realize the active vibration control of rotating machine, and then the displacement variation was greatly reduced. The neural network estimator [82, 83] was used to observe the state variations of the rotor system with an elastic joint, so the torsional torques and the rotational speed could be estimated to reduce the torsional vibration imposing on the rotor system.

In the above-mentioned research, most of the vibration absorbing methods applied to rotational machines were passive methods. The DVAs only suppressed vibration of the machine at a fixed frequency, and then the frequency bandwidth for active vibration control is quite narrow. So, those vibration absorbers become useless when the vibration frequency adding on the rotating machine surpasses the efficient frequency range. On the other hand, many methods of active vibration control for the rotating machines are concentrated on rotational speed governing methods about the driving motor. Those methods are difficult to be implemented in practice. Therefore, it will be very useful if an active vibration control method with wide range and easy implementation is created to enhance the stability and the operational accuracy of the MSFW rotor.

Therefore, a controllable and tunable AMB system, used as a DVA system, is tried to control the vibration responses of the driving MSFW rotor and the driven load rotor. The stiffness coefficient of the DVA is tuned to output corresponding forces and torques, and the

damping coefficient is regulated to control the vibration response of the driving MSFW rotor and the driven load rotor. The dynamic vibration responses of load rotor and MSFW rotor could be effectively mitigated, so this DVA based on a controllable and tunable AMB system could provide an active vibration suppression method for the high-speed rotating machine with load prat.

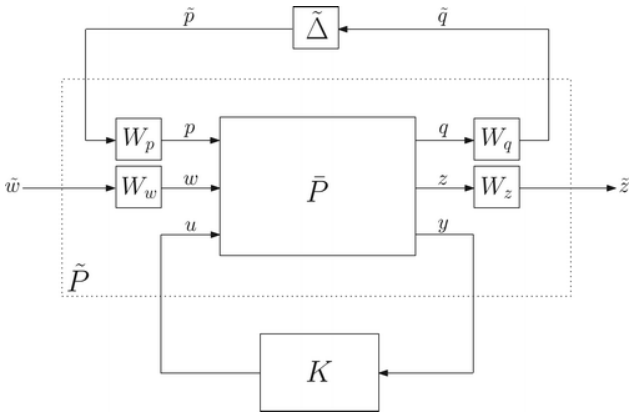

(a)

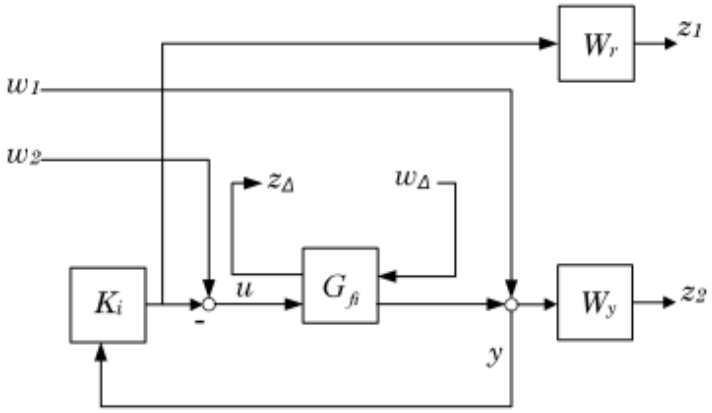

(b)

Fig. 1.4. (a) The control system with uncertainty, (b) the H-infinity synthesis.

For realizing the stable suspension and the position control of the MSFW rotor system, the active control of the AMB is the research focus of the MSFW rotor system. In general, based on the timely feedback of the rotor displacement, the PID control [84-86] was applied to realize the closed-loop control of the AMB, and other control methods such as the sliding-mode control (SMC) [87-89], the Kalman filter [90], the adaptive control [91, 92] and the fuzzy control [93-95] also were proposed for the AMB system in the MSFW rotor. To reduce the influences of

any disturbance torque acting on the MSFW rotor, a series of control methods of the AMB were proposed and tested. A compound control model combining a feedback H_∞ control model in external loop and a disturbance observer (DOB) in inner loop was proposed to mitigate the constant disturbance and the harmonic disturbance adding on the MSFW rotor at different rotating speeds, and it significantly improved the control performance of the MSFW rotor [96, 97]. In a AMB-rotor system working at high rotating speed, the μ-synthesis control model [98] was applied to reduce the position difference between the reference input displacement and the estimated output displacement. The controller could address the tracking problem, and it could measure the real-time position of the rotor with the disturbances. A robust stabilization control model with two SMC stages was proposed to solve the problem of mismatch errors in a three-pole AMB-rotor system [99]. Gosiewski and A. Mystkowski [100] proposed a robust control model of an radial homopolar AMB for controlling the vibration responses of a rigid rotor. Their research consequents verified that the designed control model could improve the robustness by controlling the initial/transient responses of right rotor. Lee et al. [101] applied the Takagi-Sugeno (T-S) fuzzy model to derive the H_∞ control of a nonlinear AMB system, and their method was more tractable and accessible than the previous methods by eliminating the truncation error and the non-convex bilinear matrix inequality. As illustrated in Fig. 1.4(b), Balini et al. [102] synthesized a H_∞ controller to attenuate the disturbance in a AMB spindle rotor. They increased the disturbance attenuation by suppressing the displacement deflection of the spindle rotor. Sun et al. [103] designed two H_∞ controllers for a horizontal AMB-rotor system, and the uncertainties of model parameters ware mitigated. They also tested the limits for the allowable range of parameters with μ-synthesis.

However, the uncertainties about the current stiffness and the displacement stiffness of the AMB in the MSFW rotor system had not been analyzed. Especially for the MSFW rotor with great equatorial momentum of inertia and great self-weight, the great self-weight MSFW rotor would deflect from the nominal initial position, and then the displacement stiffness and the current stiffness of the AMB possibly vary from their nominal values. A transient displacement deflection of the MSFW rotor would cause the displacement stiffness and the current stiffness

departure from the nominal values at the balanced status when the external disturbance is imposed on the MSFW rotor. More importantly, the gyroscopic coupling effect of the MSFW rotor becomes strong at the high rotating speed, so it possibly generates a disturbance toque about the radial axes. Therefore, considering the gyroscopic effect as a kind of external disturbance to the rotor's motion, a robust control model is important to improve the stability and the position precision of MSFW rotor regarding the great self-weight, the great equatorial moment of inertia and the variation of rotational speed.

For the coupling effect among different DOFs of the MSFW rotor affecting its control precision, an inter model control (IMC) model was proposed for the active control of MSFW rotor with great equatorial moment of inertia and great self-weight at different rotational speeds. The IMC model has characteristics on affecting the response performance and the robustness virtually through the parameter design of filter, so the control stability of the closed-loop system is ensured. Moreover, because the model identification is not necessary for the control plant, so the robustness of MSFW rotor could be regulated by varying the low-pass filter coefficient of the IMC model [104-106]. A control model of regulating rotational speed based on the fuzzy adaptive law and an IMC model was proposed to improve the performances on speed-tracking and anti-disturbance and to suppress the sensitivity to the input saturation [107]. It could automatically tune the control parameters of the rotational speed according to the identified inertia. A control strategy using an IMC model and an inverse system method was designed to suppress the influence of gyroscopic coupling effect and the gimbal motion in a single-gimbal MSCMG [108]. Based on the neural network inverse system model and an IMC model, a decoupling control model in four radial DOFs was used to an AMB system to attenuate the influence of unmodeled dynamics [109]. The control scheme could be used to adjust the tracking performance and disturbance rejection.

Most of the MSFW rotors in above-mentioned literatures are small or 'normal' size. Since the system parameters such as the displacement stiffness and the current stiffness of MSFW rotor with great self-weight could often deflect from the nominal values, such kind of MSFW rotor would be more easily affected by the external disturbances and the parameter uncertainties

comparing to the “small” MSFW rotors [23]. There are strong coupling terms in the rotation motions of the MSFW rotor around radial axes, and the coupling terms become obvious when the rotational speed increases to the rate value.

Therefore, the IMC and DIMC models about the MSFW rotor with great equatorial moment of inertia and great self-weight require more in-depth research for decoupling control and improving robustness. Compared to those above-mentioned IMC models used in the MSFW rotor, the DIMC model could realize the decoupling control in four radial control DOFs of MSFW rotor, and then the robust stability of MSFW rotor with great self-weight and great equatorial moment of inertial could be improved when it works at high rotational speed.

In summary, the analysis about the vibration characteristics of the MSFW rotor is the foundation of the whole research. The research on the dynamic characteristics of the MSFW rotor due to the variations of the suspension span ratio and the moment of inertia ratio is critical to the control of the structural vibration of the MSFW rotor. Moreover, the axial AMB is designed as a kind of DVA for realizing the vibration suppression of the MSFW rotor. Furthermore, to enhance the control precision of MSFW rotor with great equatorial moment of inertia and great self-weight, the robust control function is applied to attenuate the effect of disturbance torques acting on the MSFW rotor. Finally, the DIMC model is proposed for the MSFW rotor with great equatorial moment of inertia and great self-weight to realize the decoupling control on four radial DOFs.

Chapter 2. The Vibration Characteristics of MSFW Rotor

In this chapter, the vibration characteristics of MSFW rotor are analyzed, and the detailed relationship between the vibration characteristic and system parameter is established theoretically and analyzed experimentally. The analysis result shows that the comprehensive damping of MSFW rotor could be regulatable by tuning derivative coefficient. The comprehensive stiffness of MSFW rotor could also be controllable by changing proportional coefficient such that MSFW rotor could approach to desirable natural frequency. So, the vibration transmissibility of MSFW rotor could be suppressed by controlling the damping coefficient, and the natural frequency could be controlled to avoid the resonance frequency of MSFW rotor. Moreover, the tilting vibrations of MSFW rotor are analyzed when different disturbance forces and torques are imposed on it. The titling angle and radial displacement of MSFW rotor would increase with the rotating frequency when the harmonic disturbance is added on it, but the tilting angle would decrease with the rotating frequency. Therefore, the titling torque generated by the radial AMBs could be applied to mitigate the tilting vibration of MSFW rotor.

2.1 The Working Principle of MSFW

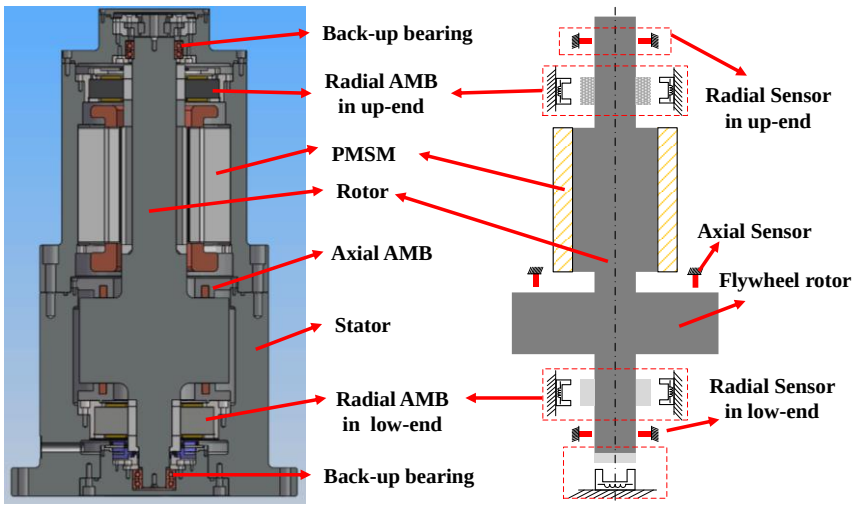

Fig. 2.1. The structure of the MSFW system.

The mechanical structure and simplified model of the MSFW system are illustrated in Fig. 2.1. It consists of a magnetic suspension system of MSFW rotor to suspend the rotor, a PMSM system to drive the MSFW rotor and a measurement system to detect the dynamic displacements of the MSFW rotor.

Firstly, the suspension system of the MSFW rotor has two parts: a magnetic suspension system based on AMB system and a mechanical supporting system based on backup ball bearing. The radial AMB could control the motions and positions of MSFW rotor in radial direction (along x and y axes). The force difference between the magnetic forces generated by the radial AMB at the upper end and the magnetic forces generated by the radial AMB at the lower end could be formed into the torque to control the tilting motion of the MSFW rotor about the radial axes. The two axial AMBs located at the upper end and the lower end of flywheel rotor stably suspend the MSFW rotor at the equilibrium position in axial direction. The mechanical supporting system is the back-up bearing at the bottom-end and the top-end of the MSFW rotor. Its function is to ensure the stability of the MSFW rotor when the magnetic suspension system fails to work or off.

The PMSM mounted at the upper end of MSFW system is the driving unit of whole MSFW system. It could realize the switches among different working modes by accelerating and deaccelerating the rotating speed of MSFW rotor about the axial principal axis, and then drives the load rotor connecting with the MSFW rotor. So, the acceleration process and the deacceleration process of the MSFW rotor are realized by controlling the PMSM.

The measurement system of MSFW system based on the eddy current displacement sensors in radial and axial directions is mounted on the stator of the MSFW system. In detail, the radial eddy current displacement sensors at the lower end and the upper end of the stator could timely measure the dynamic displacement variations of MSFW rotor deflecting from the equilibrium position in radial direction. Furthermore, the displacement difference between the radial displacements at the lower end and the upper end is used to calculate the tilting angle of the MSFW rotor about the radial axes. Moreover, the axial eddy current displacement sensor at

the upper end of the flywheel rotor could detect the displacement variations of the MSFW rotor in the axial direction.

2.2 The Magnetic Force Analysis of MSFW Rotor

2.2.1 The Magnetic Force of Radial AMB

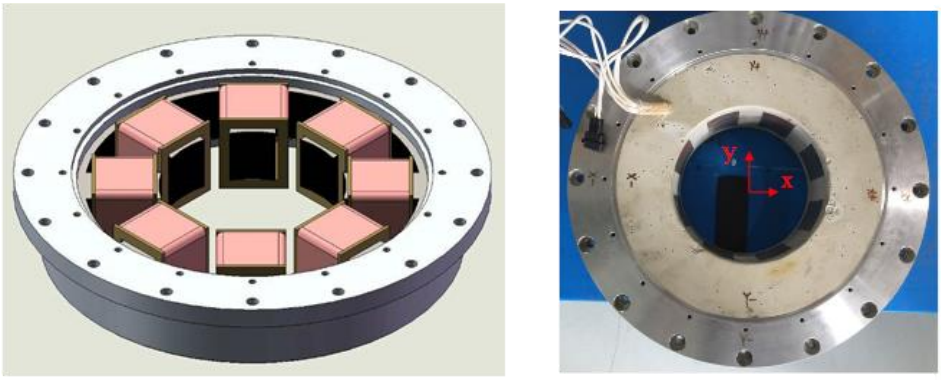

(a) (b)

Fig. 2.2. The mechanical structure and prototype of radial AMB, (a) the three-dimensional structure of radial AMB, (b) the prototype of radial AMB.

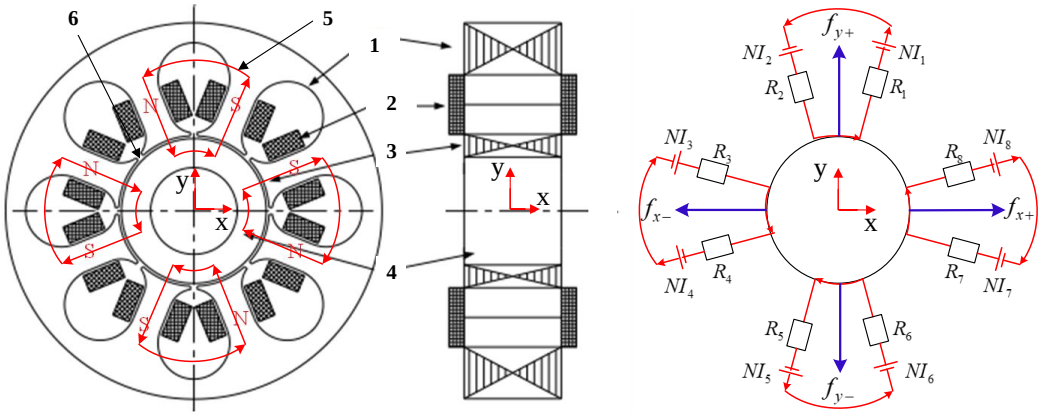

(a) (b)

Fig. 2.3. The magnetic path of the radial AMB, (a) the cross-section drawing of the radial AMB (1--the stator, 2--the windings on stator, 3--the magnet rings on stator, 4--the rotor, 5--the magnetic flux of winding, 6--the airgap between the stator and the rotor), (b) the equivalent magnetic circuits in four radial airgaps of the radial AMB.

In the MSFW system, the magnetic forces generated by the magnetic suspension system control the position and motion of MSFW rotor with five DOFs except the rotational motion about the principal axial axis. The radial AMB could control the translation and the rotation of MSFW rotor along and about radial axes, respectively. The detailed mechanical structure and

prototype of the radial AMB is shown in Fig. 2.2. The winding is fixed on the magnetic pole of the stator, and eight independent magnetic poles are paired up into four independent single-pole AMBs to control the radial translations of the MSFW rotor along x and y axes. As shown in Fig. 2.3, in the radial direction, the magnetic fluxes generated by windings of radial AMBs passes through the stator, the magnet ring on stator, the airgap between the stator and the rotor. For the single magnetic pole in one direction, the equivalent magnet reluctances $R_{n=1\text{-}8}$ of the stator, the airgap and rotor are in series connection. N is the number of turns of winding of the radial AMB. $I_{n=1\text{-}8}$ are the control currents in the eight windings of the radial AMB, respectively.

Assuming that there is no coupling effect among the magnet circuits of four radial AMBs, the equivalent reluctances of the airgaps in the radial direction are written respectively as

$$\begin{cases} R_{y+} = R_1 + R_2 = \dfrac{2d_{y+}}{\mu_0 A_{y+}} \\ R_{y-} = R_5 + R_6 = \dfrac{2d_{y-}}{\mu_0 A_{y-}} \\ R_{x+} = R_7 + R_8 = \dfrac{2d_{x+}}{\mu_0 A_{x+}} \\ R_{x-} = R_3 + R_4 = \dfrac{2d_{x-}}{\mu_0 A_{x-}} \end{cases} \tag{2.1}$$

where $d_{n=x+,x-,y+,y-}$ are the airgap lengths between the rotor and the stator in radial direction, and $A_{n=x+,x-,y+,y-}$ is the effective cross-sectional area of the magnetic pole in radial direction. μ_0 is the vacuum permeability. The magnet flux of four control channels in radial direction could be expressed as

$$\begin{cases} \Phi_{y+} = \dfrac{NI_1 + NI_2}{R_1 + R_2} \\ \Phi_{y-} = \dfrac{NI_5 + NI_6}{R_5 + R_6} \\ \Phi_{x+} = \dfrac{NI_7 + NI_8}{R_7 + R_8} \\ \Phi_{x-} = \dfrac{NI_3 + NI_4}{R_3 + R_4} \end{cases} \tag{2.2}$$

Based on the Bio-savart law[110], the magnetic forces in radial direction could be derived and written as

$$\begin{cases} f_{y+} = \dfrac{\Phi_{y+}^2}{\mu_0 A_{y+}} \\ f_{y-} = \dfrac{\Phi_{y-}^2}{\mu_0 A_{y-}} \\ f_{x+} = \dfrac{\Phi_{x+}^2}{\mu_0 A_{x+}} \\ f_{x-} = \dfrac{\Phi_{x-}^2}{\mu_0 A_{x-}} \end{cases} \tag{2.3}$$

In general, the airgap and the current of the radial AMB are both divided into the control term and the bias term, so the current of the radial AMB could be defined as the resultant of the control current and bias current as following

$$\begin{cases} I_1 = I_2 = I_{y0} + i_y \\ I_5 = I_6 = I_{y0} - i_y \\ I_3 = I_4 = I_{x0} + i_x \\ I_7 = I_8 = I_{x0} - i_x \end{cases} \tag{2.4}$$

where I_{y0} and I_{x0} are the bias currents of the radial AMB. i_y and i_x are control currents along y and x axis of the radial AMB, respectively.

Similarly, the displacement along radial direction could be defined as the sum of the bias displacement and the control displacement, and there are

$$\begin{cases} d_{y+} = d_{y0} - d_y \\ d_{y-} = d_{y0} + d_y \\ d_{x+} = d_{x0} - d_x \\ d_{y-} = d_{x0} + d_x \end{cases} \tag{2.5}$$

where d_{y0} and d_{x0} are the bias displacements in radial direction, d_y and d_x are the control displacements of the radial AMB om radial direction.

Finally, the resultant magnetic force of the radial AMB in x and y axes could be written respectively as

$$\begin{cases} f_y(i_y, d_y) = f_{y+} - f_{y-} = \dfrac{\mu_0 A_y N^2}{4}\left[\dfrac{(I_{y0}+i_y)^2}{(d_{y0}-d_y)^2} - \dfrac{(I_{y0}-i_y)^2}{(d_{y0}+d_y)^2}\right] \\ f_x(i_x, d_x) = f_{x+} - f_{x-} = \dfrac{\mu_0 A_x N^2}{4}\left[\dfrac{(I_{x0}+i_x)^2}{(d_{x0}-d_x)^2} - \dfrac{(I_{x0}-i_x)^2}{(d_{x0}+d_x)^2}\right] \end{cases} \tag{2.6}$$

The electromagnetic force coefficient of the radial AMB is defined as

$$k_{amb} = \frac{\mu_0 A_x N^2}{4} = \frac{\mu_0 A_y N^2}{4} \tag{2.7}$$

Given that the MSFW rotor is located at the balanced position in radial direction with the conditions $i_x = i_y = 0$ and $d_x = d_y = 0$, so the current stiffness equation and the displacement stiffness equation of the radial AMB along x and y axes are written respectively as

$$\begin{cases} k_{ix} = \dfrac{\partial f_x}{\partial i_x} = 4k_{amb} \cdot \dfrac{I_{x0}+i_x}{(d_{x0}+d_x)^2} \approx 4k_{amb} \cdot \dfrac{I_{x0}}{d_{x0}^2}\Bigg| \begin{matrix} i_x = 0 \\ d_x = 0 \end{matrix} \\ k_{dx} = \dfrac{\partial f_x}{\partial d_x} = -4k_{amb} \cdot \dfrac{(I_{x0}+i_x)^2}{(d_{x0}+d_x)^3} \approx -4k_{amb} \cdot \dfrac{I_{x0}^2}{d_{x0}^3}\Bigg| \begin{matrix} i_x = 0 \\ d_x = 0 \end{matrix} \\ k_{iy} = \dfrac{\partial f_y}{\partial i_y} = 4k_{amb} \cdot \dfrac{I_{y0}+i_y}{(d_{y0}+d_y)^2} \approx 4k_{amb} \cdot \dfrac{I_{y0}}{d_{y0}^2}\Bigg| \begin{matrix} i_y = 0 \\ d_y = 0 \end{matrix} \\ k_{dy} = \dfrac{\partial f_y}{\partial d_y} = -4k_{amb} \cdot \dfrac{(I_{y0}+i_y)^2}{(d_{y0}+d_y)^3} \approx -4k_{amb} \cdot \dfrac{I_{y0}^2}{d_{y0}^3}\Bigg| \begin{matrix} i_y = 0 \\ d_y = 0 \end{matrix} \end{cases} \tag{2.8}$$

So, the magnetic forces of the radial AMB along x and y axes could be expressed into

$$\begin{cases} f_x = k_{ix} i_x + k_{dx} d_x \\ f_y = k_{iy} i_y + k_{dy} d_y \end{cases} \tag{2.9}$$

According to Eq.(2.6) and parameters in TABLE. 2.I, the relationship between the radial magnetic force and the control current of the radial AMB is illustrated in Fig. 2.4(a). So, the radial magnetic force is proportionally linear to the control current of the radial AMB in the small vicinity of radial equilibrium position, and the nominal current stiffness k_{ix} in radial direction is about 620N/A. Fig. 2.4(b) shows that the radial magnetic force is also proportionally linear to the control displacement in radial direction in the small vicinity of radial equilibrium position, and the nominal displacement stiffness k_{dx} of radial AMB is about -2800N/mm. Therefore, the displacement stiffness is the negative value, and the control current could be

regulated to counteract the magnetic forces of displacement stiffness to realize the stable suspension of the MSFW rotor.

TABLE. 2.I. The parameter of the radial AMB.

Parameter	Value	Unit
number of turns of winding of radial AMB	N=400	
cross-sectional area of the magnetic pole	A_x=4292	mm^2
cross-sectional area of the magnetic pole	A_y=4292	mm^2
bias current of the radial AMB	I_{x0}=1.8	A
bias current of the radial AMB	I_{y0}=1.8	A
bias displacement of the radial AMB	d_{x0}=1	mm
bias displacement of the radial AMB	d_{y0}=1	mm

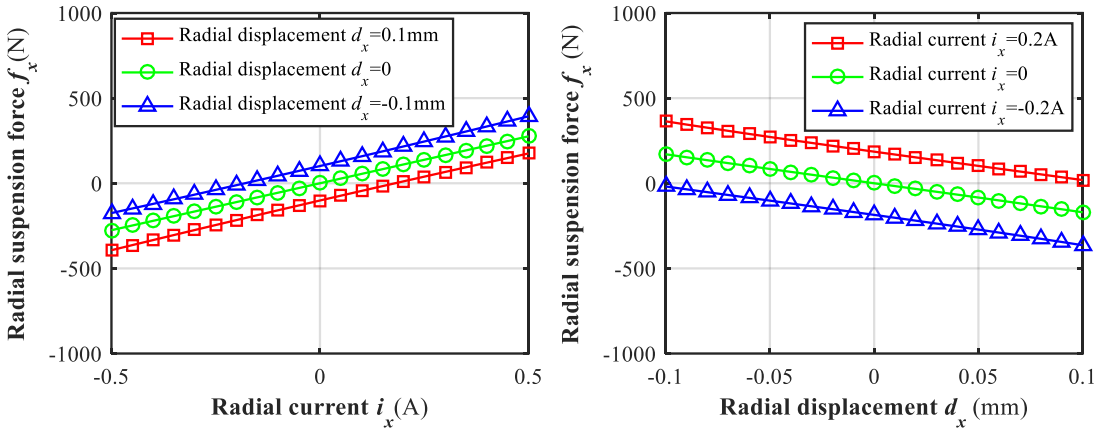

(a) (b)

Fig. 2.4. The magnetic force of the radial AMB, (a) the relationship between the radial magnetic force and the control current of radial AMB, (b) the relationship between the radial magnetic force and the control displacement of MSFW rotor.

2.2.2 The Magnetic Force of Axial AMB

The axial suspension system located at the upper end and the lower end of the flywheel rotor generates the suspension forces to control the stable suspension of MSFW rotor at the equilibrium position in axial direction. As shown in Fig. 2.5, the axial AMB consists of the stator and the axial winding on the magnetic pole, and the windings of the axial AMB are in series connection because it controls the translation of the MSFW rotor on one DOF. The equivalent magnet circuit of the axial AMB at the upper end of the flywheel rotor is plotted in Fig. 2.6. The equivalent magnet flux in axial direction of axial AMB passes through the stator

of the axial AMB, the magnet ring, the airgap, and the flywheel rotor, and then it finally returns to another magnetic pole. Let $R_{n=a1,\ a2,\ a3,\ a4}$ be the equivalent reluctance of the airgap and the magnet ring in the axial direction. N_a is turn of windings of the axial AMB, and I_{z+} is the control current in the windings of the axial AMB at the upper end of the flywheel rotor.

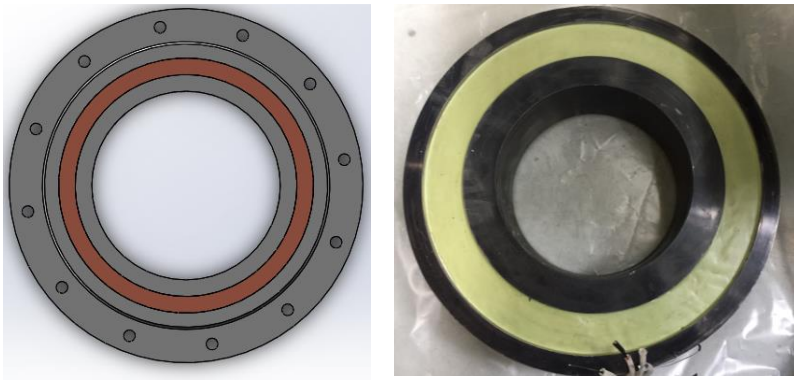

(a) (b)

Fig. 2.5. The axial AMB, (a) the three-dimensional model of the axial AMB, (b) the prototype of the axial AMB.

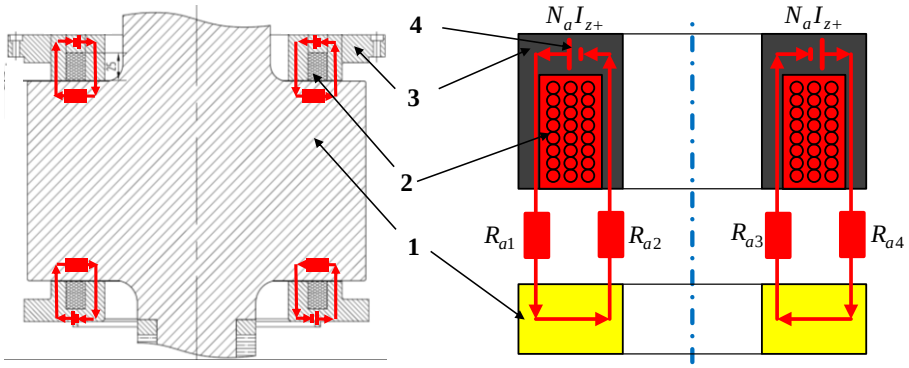

Fig. 2.6. The equivalent magnetic circuit at upper end of the axial AMB (1--the flywheel rotor, 2--the winding, 3--the stator, 4--the magnet flux).

Using the equivalent magnet circuit[110], the equivalent reluctance of the airgap in axial direction is written as

$$\begin{cases} R_{al} = R_{a1} + R_{a2} = \dfrac{2d_{z+}}{\mu_0 A_{z+}} \\ R_{ar} = R_{a3} + R_{a4} = \dfrac{2d_{z+}}{\mu_0 A_{z+}} \end{cases} \tag{2.10}$$

where d_{z+} is length of the airgap in the upper end of the flywheel rotor, and A_{z+} is the cross-sectional area in the upper end of the flywheel rotor. The magnet flux in the airgap of the h upper end and the lower end of the flywheel rotor could be expressed as

$$\begin{cases} \Phi_{al} = \dfrac{N_a I_{z+}}{R_{al}} \\ \Phi_{ar} = \dfrac{N_a I_{z+}}{R_{ar}} \end{cases} \tag{2.11}$$

The total magnet flux of the axial AMB at the upper end of the flywheel rotor is

$$\Phi_{z+} = \Phi_{al} + \Phi_{ar} \tag{2.12}$$

Similarly, the total magnet flux of the axial AMB at the lower end of the flywheel rotor could be achieved, so the magnetic forces of the axial AMB in the axial direction could be derived and written as following

$$\begin{cases} f_{z+} = \dfrac{\Phi_{z+}^2}{\mu_0 A_{z+}} \\ f_{z-} = \dfrac{\Phi_{z-}^2}{\mu_0 A_{z-}} \end{cases} \tag{2.13}$$

In general, the control current and the control displacement of axial AMB could be divided into the control term and the bias term. We could define the control current of the axial AMB as

$$\begin{cases} I_{z+} = I_{z0} + i_z \\ I_{z-} = I_{z0} - i_z \end{cases} \tag{2.14}$$

where I_{z0} is the bias term of the control current in the axial AMB, and i_z is the control term of the control current in the axial AMB.

The control displacement in the axial direction could be defined as the sum of the bias displacement and the control displacement, and there are

$$\begin{cases} d_{z+} = d_{z0} + d_z \\ d_{z-} = d_{z0} - d_z \end{cases} \tag{2.15}$$

where d_{z0} is the bias displacement in the axial AMB, and d_z is the control displacement in the axial AMB.

Finally, the resultant magnetic force of the axial AMB in axial direction could be expressed as

$$f_z(i_z,d_z)=f_{z+}-f_{z-}=\mu_0 A_z N_a^2[\frac{(I_{z0}+i_z)^2}{(d_{z0}-d_z)^2}-\frac{(I_{z0}-i_z)^2}{(d_{z0}+d_z)^2}] \tag{2.16}$$

The electromagnetic coefficient of the axial AMB is

$$k_{zamb}=\mu_0 A_z N_a^2 \tag{2.17}$$

When the MSFW rotor is stably suspended at the equilibrium position in axial direction with the conditions i_z=0 and d_z=0, so the current stiffness and the displacement stiffness of the axial AMB in axial direction are written respectively as

$$\begin{cases} k_{iz}=\dfrac{\partial f_z}{\partial i_z}=4k_{zamb}\cdot\dfrac{I_{z0}+i_z}{(d_{z0}+d_z)^2}\approx 4k_{zamb}\cdot\dfrac{I_{z0}}{d_{z0}^2}\Big|\begin{matrix} i_z=0 \\ d_z=0 \end{matrix} \\ k_{dz}=\dfrac{\partial f_z}{\partial d_z}=-4k_{zamb}\cdot\dfrac{(I_{z0}+i_z)^2}{(d_{z0}+d_z)^3}\approx -4k_{zamb}\cdot\dfrac{I_{z0}^2}{d_{z0}^3}\Big|\begin{matrix} i_z=0 \\ d_z=0 \end{matrix} \end{cases} \tag{2.18}$$

The magnetic force in axial direction could be expressed as

$$f_z=k_{iz}i_z+k_{dz}d_z \tag{2.19}$$

According to Eq.(2.18) and the parameters in TABLE. 2.II, the relationship between the axial magnetic force and the control current of axial AMB is illustrated in Fig. 2.7(a). It presents that the axial magnetic force is proportionally linear to the control current of axial AMB. The axial current stiffness k_{iz} is about 500N/A. Fig. 2.7(b) shows that the axial magnetic force is proportionally linear to the axial displacement of MSFW rotor in the small vicinity of axial equilibrium position. The nominal displacement stiffness of axial AMB in axial direction k_{dz} is about -1700N/mm. Consequently, to accomplish the stable suspension of MSFW rotor in axial direction, the control current is also tuned to compensate the negative magnetic forces introduced by the negative displacement stiffness.

TABLE. 2.II. The parameter of the axial AMB.

Parameter	**Value**	**Unit**
number of turns of winding of radial AMB	N_a=356	
cross-sectional area of the magnetic pole	A_z=1272	mm^2
bias current of the axial AMB	I_{y0}=1.5	A
bias displacement of the axial AMB	d_{y0}=1	mm

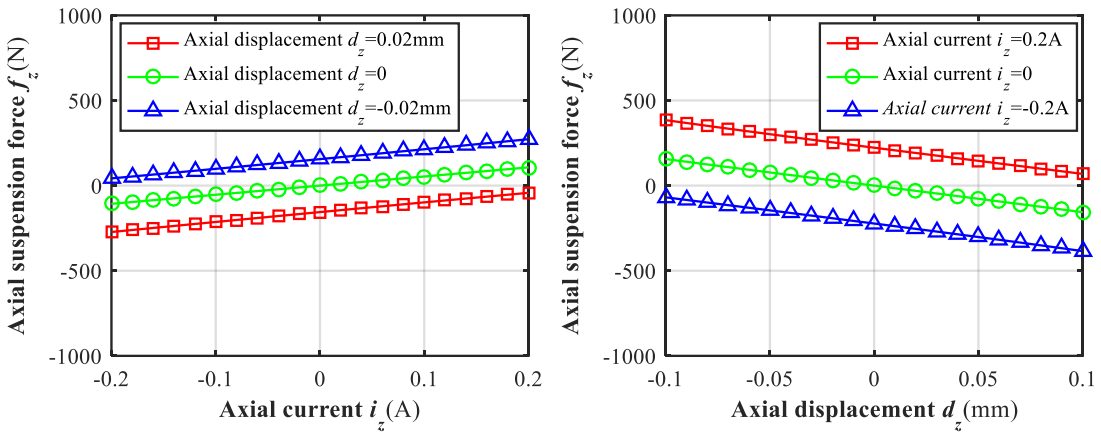

(a) (b)

Fig. 2.7. The magnetic force of the axial AMB, (a) the relationship between the axial magnetic force and the axial control current, (b) the relationship between the axial magnetic force and the axial control displacement.

2.3 The Dynamics Modeling of MSFW Rotor

2.3.1 The Force Analysis of MSFW Rotor

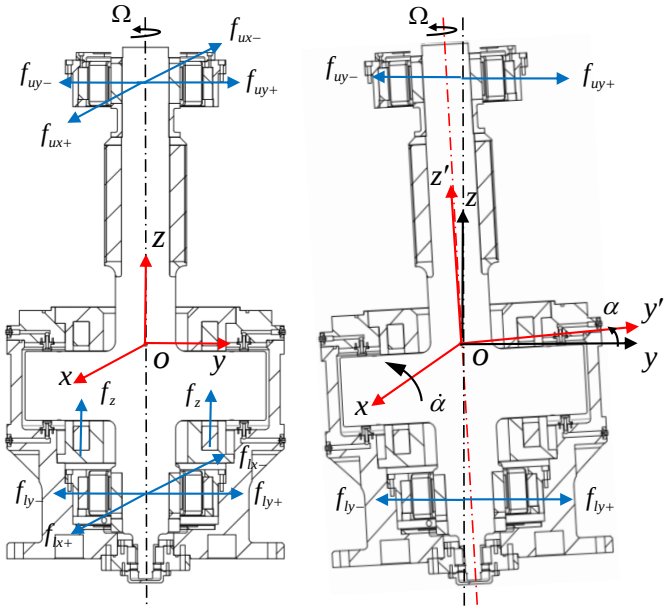

(a) (b)

Fig. 2.8. The force analysis acting on the MSFW rotor, (a) the balanced status of MSFW rotor, (b) the tilting status of MSFW rotor.

As shown in Fig. 2.8(a), the pair of radial AMBs at the lower suspension end of the MSFW rotor generate magnetic forces, f_{lx+}, f_{lx-}, f_{ly+} and f_{ly-}, to control the radial motions of the MSFW rotor at the lower end in radial direction. Another pair of radial AMBs at the upper suspension

end of the MSFW rotor generate magnetic forces, f_{ux+}, f_{ux-}, f_{uy+} and f_{uy-}, for the radial motions control of the MSFW rotor at the upper end in radial direction. Moreover, the resultant magnetic force f_{ux}-f_{lx} of the radial AMBs between the upper end and the lower end controls the tilting of the MSFW rotor about y axis. Similarly, the resultant magnetic force, f_{uy}-f_{ly}, controls the tilting of the MSFW rotor about x axis. The axial magnetic force f_z is used to control the axial motion and position of the MSFW rotor, the stable suspension at the axial equilibrium position could be realized by overcoming gravity.

When the resultant force of radial magnetic force at the lower end and upper end of the MSFW rotor both equal to zero, the equations of motion of the MSFW rotor in radial direction are

$$\begin{cases} f_{ux+} - f_{ux-} = 0 \\ f_{lx+} - f_{lx-} = 0 \\ f_{uy+} - f_{uy-} = 0 \\ f_{ly+} - f_{ly-} = 0 \end{cases} \tag{2.20}$$

It represents the stable suspension of MSFW rotor at the radial balanced position. Moreover, in the axial direction, when the axial magnetic force equals to the gravity of the MSFW rotor, there is

$$f_z - mg = 0 \tag{2.21}$$

It represents that the MSFW rotor could be stably suspended at the axial equilibrium position. Consequently, the MSFW rotor works at the balanced status when there is no external force acting on the MSFW rotor. However, the tilting of the MSFW rotor is easily occurred because of the existence of the external disturbance, the self-excited vibration, and the gyroscopic coupling effect at a high rotational speed. Therefore, based on rotor's feedback displacement in radial direction, the radial AMBs at upper end and lower end of the MSFW rotor would regulate the resultant magnetic force, f_{uy}-f_{ly}, to force the MSFW rotor back to the balanced suspension status.

2.3.2 The Dynamic Equations of MSFW Rotor

During the developing dynamic equation of MSFW rotor, there are two assumption as following,

(1) There is no mismatch between the geometric center and the center of mass for MSFW rotor system in Fig. 2.8,

(2) The force distance and the sensor distance from are equivalent, so the location transformation could be neglected.

Based on the force analysis of the MSFW rotor as illustrated in Fig. 2.8, the equations of translational motion could be written as

$$\begin{cases} m\ddot{d}_x = f_{x+} - f_{x-} \\ m\ddot{d}_y = f_{y+} - f_{y-} \\ m\ddot{d}_z = f_z - mg \end{cases} \tag{2.22}$$

The equations of rotational motion of the MSFW rotor could be written as

$$\begin{cases} J_y\ddot{\beta} - J_z\Omega\dot{\alpha} = T_x \\ J_x\ddot{\alpha} + J_z\Omega\dot{\beta} = T_y \end{cases} \tag{2.23}$$

where f_{x+} and f_{x-} are the respective magnetic forces in the positive direction of x axis and negative directions of x axis. f_{y+} and f_{y-} are the respective magnetic forces in the positive direction of x axis and negative directions of y axis. J_x and J_y are the equatorial moment of inertia of MSFW rotor. J_z is the polar moment of inertia of MSFW rotor. Ω is the rotational speed of the MSFW rotor. α and β are the respective tilting angles of MSFW rotor about x axis and y axis, and they had similar dynamic characteristics. According to the mechanical structure of MSFW rotor as shown in Fig. 2.1, the relationship between the radial displacement in radial direction and the titling angle around radial axis could be expressed into

$$\begin{cases} \alpha = \dfrac{\left(d_{ly} - d_{uy}\right)}{2l} \\ \beta = \dfrac{\left(d_{ux} - d_{lx}\right)}{2l} \end{cases} \tag{2.24}$$

where d_{ly} is the radial displacement of the MSFW rotor at the lower end along y axis. d_{uy} is the radial displacement of the MSFW rotor at the upper end along y axis. d_{lx} is the radial displacement of the MSFW rotor at lower end along x axis. d_{ux} is the radial displacement of the

MSFW rotor at upper end along x axis, and l is the span from the mid-point of the radial AMB to the mass of center.

2.4 The Dynamic Characteristics of MSFW Rotor

2.4.1 The Translational Characteristics of MSFW Rotor

By designing the negative feedback loop of the dynamic displacement in radial direction, the relationship between the dynamic displacement and the control current of MSFW rotor in radial direction could be written as

$$i_x = -\left(K_{Px}d_x + K_{Dx}\dot{d}_x\right)\cdot k_{sx}k_{wx} \tag{2.25}$$

where K_P is the proportional coefficient for regulating the stiffness of the MSFW rotor, and K_D is the derivative coefficient for tuning the damping of the MSFW rotor. k_s is the sensitivity coefficient of eddy current displacement sensor. k_w is the amplification parameter of the power amplifier.

Combining Eq.(2.22) and Eq.(2.25), the equations of translational motions in three directions could be written as

$$\begin{cases} m\ddot{d}_x + k_{ix}k_{wx}k_{sx}K_{Dx}\dot{d}_x + (k_{ix}k_{wx}k_{sx}K_{Px} - k_{dx})d_x = 0 \\ m\ddot{d}_y + k_{iy}k_{wy}k_{sy}K_{Dy}\dot{d}_y + (k_{iy}k_{wy}k_{sy}K_{Py} - k_{dy})d_y = 0 \\ m\ddot{d}_z + k_{iz}k_{wz}k_{sz}K_{Dz}\dot{d}_z + (k_{iz}k_{wz}k_{sz}K_{Pz} - k_{dz})d_z = 0 \end{cases} \tag{2.26}$$

Since similar the closed loop control mode based on the negative displacement feedback is applied to three DOFs translational motions in of MSFW rotor, the motion control of MSFW rotor in x axis is selected as the analysis case in this chapter. To ensure the stability of the translational control loop of the MSFW rotor, the equation of the translational motion should satisfy

$$\begin{cases} K_P > \dfrac{k_d}{k_i k_w k_s} \\ K_D > 0 \end{cases} \tag{2.27}$$

The natural translational frequency of MSFW rotor could then be written into

$$\omega_n = \sqrt{\frac{k_i k_w k_s K_P - k_d}{m}} \tag{2.28}$$

The damping coefficient of the translational motion is

$$\xi = \frac{k_i k_w k_s K_D}{2\sqrt{m(k_i k_w k_s K_P - k_d)}} \tag{2.29}$$

The translational vibration transmissibility of MSFW rotor could be expressed into

$$TR = \sqrt{\frac{1+(2\xi r)^2}{(1-r^2)^2+(2\xi r)^2}} \tag{2.30}$$

where $r=\omega_t/\omega_n$ is defined as the frequency ratio between the translational frequency and the natural frequency, and ω_t is the vibration frequency of the translational motion.

2.4.2 The Rotational Characteristics of MSFW Rotor

From Eq. (2.28), the natural frequency of the MSFW rotor's translation would increase with the proportional coefficient of the control loop. The vibration transmissibility of MSFW rotor's translation could be reduced with the derivative coefficient of the control loop, and the vibration transmissibility of MSFW rotor's translation could be increased by increasing the proportional coefficient of the control loop. Moreover, the tilting torque outputted by the radial AMBs at upper end and lower end for controlling tilting motion of MSFW rotor could be written as

$$\begin{cases} T_x = \left(f_{ux} - f_{lx}\right) \cdot l = -2k_i k_w k_s K_D l^2 \dot{\beta} - 2(k_i k_w k_s K_P - k_d) l^2 \beta \\ T_y = \left(f_{ly} - f_{uy}\right) \cdot l = 2k_i k_w k_s K_D l^2 \dot{\alpha} + 2(k_i k_w k_s K_P - k_d) l^2 \alpha \end{cases} \tag{2.31}$$

An analysis about the tilting vibration of the MSFW rotor like the translational vibration above can be carried out. It is possible that the tilting torque formed by the AMBs at upper end and lower end in radial direction could be applied to control the tilting vibration of MSFW rotor. In detail, the response amplitude of the tilting vibration could be suppressed by increasing the derivative coefficient of the control system, and it could be improved by the proportional coefficient of the control system. Using Eq. (2.23) and Eq. (2.31), the equations of the rotational motion of the MSFW rotor could be written as

$$\begin{cases} J_y\ddot{\beta} - 2k_i k_w k_s K_D l^2 \dot{\beta} - 2(k_i k_w k_s K_P - k_d) l^2 \beta - J_z \Omega \dot{\alpha} = 0 \\ J_x\ddot{\alpha} + 2k_i k_w k_s K_D l^2 \dot{\alpha} + 2(k_i k_w k_s K_P - k_d) l^2 \alpha + J_z \Omega \dot{\beta} = 0 \end{cases} \tag{2.32}$$

Comparing Eq. (2.32) to Eq. (2.26), the equations of the translational motion are uncoupled but the rotational motion equations are coupled. The coupling terms appear in the rotational motion equations of the MSFW rotor are the gyroscopic moments, and these gyroscopic moments change with the rotating speed of MSFW rotor.

For the tilting motion of MSFW rotor, the tilting angle of the MSFW rotor $\boldsymbol{x}=[\alpha\ \alpha'\ \beta\ \beta']^{\mathrm{T}}$ is defined as the state vector. The torque of the MSFW rotor $\boldsymbol{u}=[T_x\ T_y]^{\mathrm{T}}$ is defined as The input vector, and the tilting angle of the MSFW rotor $\boldsymbol{y}=[\alpha\ \beta]^{\mathrm{T}}$ is chosen as the output vector. The state space equations of rotational motion around two radial axes could be expressed into

$$\begin{cases} \dot{\boldsymbol{x}} = \boldsymbol{A}\boldsymbol{x} + \boldsymbol{B}\boldsymbol{u} \\ \boldsymbol{y} = \boldsymbol{C}\boldsymbol{x} \end{cases} \tag{2.33}$$

where the state matrix is

$$\boldsymbol{A} = \begin{bmatrix} 0 & 1 & 0 & 0 \\ 0 & 0 & 0 & \dfrac{-J_z\Omega}{J_x} \\ 0 & 0 & 0 & 1 \\ 0 & \dfrac{J_z\Omega}{J_y} & 0 & 0 \end{bmatrix},$$

the input matrix is

$$\boldsymbol{B} = \begin{bmatrix} 0 & 0 \\ 0 & \dfrac{1}{J_x} \\ 0 & 0 \\ \dfrac{1}{J_y} & 0 \end{bmatrix},$$

and the output matrix is

$$\boldsymbol{C} = \begin{bmatrix} 1 & 0 & 0 & 0 \\ 0 & 0 & 1 & 0 \end{bmatrix}.$$

The transformation matrix of the state space equations could be derived and written into

$$e^{\boldsymbol{A}t} = L^{-1}(s\boldsymbol{I} - \boldsymbol{A})^{-1} \tag{2.34}$$

where $\boldsymbol{I}$ is chosen as the unit matrix, and L^{-1} is defined as the inverse Laplace transformation operator.

Let the angular momentum is defined as $H=J_z\Omega$, and the natural rotational frequency of the MSFW rotor is defined as

$$\omega_{rn} = \frac{H}{\sqrt{J_x J_y}}.$$

The transformation matrix transformation matrix of the state space equations could be written as

$$e^{\boldsymbol{A}t} = \begin{bmatrix} 1 & \dfrac{\sin\omega_{rn}t}{\omega_{rn}} & 0 & \dfrac{J_x(1-\cos\omega_{rn}t)}{H} \\ 0 & \cos\omega_{rn}t & 0 & \dfrac{H\sin\omega_{rn}t}{J_y\omega_{rn}} \\ 0 & \dfrac{-J_y(1-\cos\omega_{rn}t)}{H} & 1 & \dfrac{\sin\omega_{rn}t}{\omega_{rn}} \\ 0 & \dfrac{-H\sin\omega_{rn}t}{J_x\omega_{rn}} & 0 & \cos\omega_{rn}t \end{bmatrix} \tag{2.35}$$

The angle solution of the state space equations could be solved as following

$$x(t) = e^{\boldsymbol{A}t}x(0) + \int_0^t e^{\boldsymbol{A}(t-\tau)}\boldsymbol{B}u(\tau)d\tau \tag{2.36}$$

Given the titling angle has the zero initial conditions with $x(0)=0$, and the transient impulse torque $u(t)=\delta(t)\cdot[1\ 1]^{\mathrm{T}}$ is chosen the input vector, and $\delta(t)$ is the Dirac delta function. So, the angle solution of the state space equations in Eq.(2.36) is

$$x(t) = \int_0^t e^{\boldsymbol{A}(t-\tau)}\boldsymbol{B}\delta(\tau)[1 \quad 1]^T d\tau \tag{2.37}$$

The tilting angles of MSFW rotor about radial axes could be obtained as following

$$\begin{cases} \alpha(t) = \dfrac{1}{H}\sqrt{\dfrac{J_x}{J_y}}\sin\omega_{rn}t - \dfrac{1}{H}\cos\omega_{rn}t + \dfrac{1}{H} \\ \beta(t) = \dfrac{1}{H}\sqrt{\dfrac{J_x}{J_y}}\sin\omega_{rn}t + \dfrac{1}{H}\cos\omega_{rn}t - \dfrac{1}{H} \end{cases} \tag{2.38}$$

The above equation implies that tilting angles α and β of MSFW rotor about radial axes would change with the natural rotational frequency ω_{rn} of MSFW rotor.

When a harmonic torque input, $u(t)=[M_{x0}\sin\omega_x t \; M_{y0}\sin\omega_y t]^{\mathrm{T}}$ is chosen as the input vector, the angle solution of state space equations are solved as

$$x(t)=\int_0^t e^{\mathbf{A}(t-\tau)}\boldsymbol{B}[M_{x0}\sin\omega_x t \quad M_{y0}\sin\omega_y t]^T d\tau \tag{2.39}$$

The tilting angles of MSFW rotor about radial axes are achieved as following

$$\begin{cases} \alpha(t)=\dfrac{M_{x0}}{H\omega_x}-\dfrac{\omega_{rn}^2 M_{x0}}{H\omega_x(\omega_{rn}^2-\omega_x^2)}\cos\omega_x t+\dfrac{M_{y0}}{J_y(\omega_{rn}^2-\omega_y^2)}\cos\omega_y t \\ \qquad +\dfrac{\omega_x M_{x0}}{H(\omega_{rn}^2-\omega_x^2)}\cos\omega_{rn} t+\dfrac{\omega_y M_{y0}}{J_y\omega_{rn}(\omega_{rn}^2-\omega_y^2)}\sin\omega_{rn} t \\ \beta(t)=\dfrac{M_{y0}}{H\omega_y}-\dfrac{\omega_{rn}^2 M_{y0}}{H\omega_y(\omega_{rn}^2-\omega_y^2)}\cos\omega_y t+\dfrac{M_{x0}}{J_x(\omega_{rn}^2-\omega_x^2)}\cos\omega_x t \\ \qquad -\dfrac{\omega_y M_{y0}}{H(\omega_{rn}^2-\omega_y^2)}\cos\omega_{rn} t-\dfrac{\omega_x M_{x0}}{J_x\omega_{rn}(\omega_{rn}^2-\omega_x^2)}\sin\omega_{rn} t \end{cases} \tag{2.40}$$

These angle solutions of state space equations indicate that the tilting angles α and β of MSFW rotor would change with the natural rotational frequency ω_{rn} of MSFW rotor and the vibration frequencies ω_x and ω_y of harmonic input torque.

When a constant torque input, $u(t)=[1 \; 1]^{\mathrm{T}}$, is used as the input vector to the MSFW rotor, the angle solution of the state space equation could be solved as following

$$x(t)=\int_0^t e^{\mathbf{A}(t-\tau)}\mathbf{B}[1 \quad 1]^T d\tau \tag{2.41}$$

The tilting angles of MSFW rotor could be achieved as following

$$\begin{cases} \alpha(t)=\dfrac{J_x}{H^2}+\dfrac{1}{H}t-\dfrac{\sqrt{J_x J_y}}{H^2}\sin\omega_{rn} t-\dfrac{J_x}{H^2}\cos\omega_{rn} t \\ \beta(t)=\dfrac{J_y}{H^2}+\dfrac{1}{H}t-\dfrac{\sqrt{J_x J_y}}{H^2}\sin\omega_{rn} t-\dfrac{J_y}{H^2}\cos\omega_{rn} t \end{cases} \tag{2.42}$$

It shows that the tilting angles of the MSFW rotor also change with the natural rotational frequency ω_{rn} of MSFW rotor.

2.5 Numerical Simulation

2.5.1 The Control Scheme of MSFW Rotor

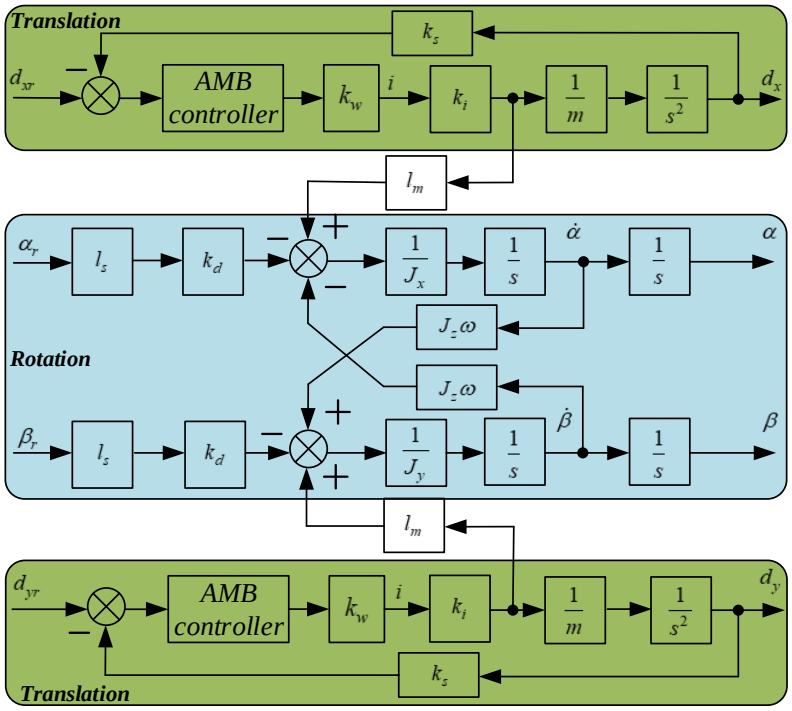

Fig. 2.9. The control scheme of the MSFW rotor.

The whole control diagram of MSFW rotor is shown in Fig. 2.9, and it contains the control loop of translational motion and the control loop of rotational motion. The reference displacement $[d_{xr}\ d_{yr}]^T$ in radial direction and the reference angle $[\alpha_r\ \beta_r]^T$ of MSFW rotor are used as input signals of the closed loop control system, $[d_x\ d_y]^T$ and $[\alpha\ \beta]^T$ are output signals of the closed loop control system. In the control loop of translational motion, the radial displacements $[d_x\ d_y]^T$ measured by the eddy current displacement sensors are used as feedback signals. The control system then generates the control current for the differential control of the MSFW rotor in radial and axial directions. In the control loop of the rotational motion around the radial axes, the tilting angles of MSFW rotor are the system inputs based on the feedback of the radial displacement. The cross-compensation terms using the speed feedback are used to mitigate the gyroscopic coupling effect of MSFW rotor. Finally, the simulation and experiment are designed, and the simulation has two parts—the translational vibration in radial direction and the tilting vibration around radial axes.

2.5.2 The Translational Vibration Analysis of MSFW Rotor

TABLE. 2.III. The simulation parameters of MSFW rotor system.

Parameter	Value	Unit
Polar moment of inertia	J_m=0.67	kg·m^2
Equatorial moment of inertia	J_l=1.24	kg·m^2
Mass of MSFW rotor	m=150	kg
Current stiffness of radial AMB	k_{ix}=520	N/A
Displacement stiffness of radial AMB	k_{dx}=-2800	N/mm
Current stiffness of axial AMB	k_{iz}=500	N/A
Displacement stiffness of axial AMB	k_{dz}=-1700	N/mm
Span from radial sensor to center of mass	l=476	mm
Amplification coefficient	k_w=0.2	A/V
Sensitivity of displacement sensor	k_s=3.3	V/mm

By using the simulation parameters listed TABLE. 2.III and choosing different control parameters, the relationship between the vibration characteristics of the MSFW rotor and the proportional coefficient K_P is illustrated in Fig. 2.10(a). Given that the derivative coefficient is defined as 0.1, the natural frequency of MSFW rotor is 3Hz when the proportional coefficient is K_P=10. The natural frequency increases to 20Hz when the proportional coefficient is K_P=150 as shown in Fig. 2.10(b), so the natural frequency of MSFW rotor could increase with the proportional coefficient of control system. In addition, the relationship between the proportional coefficient of control system and the vibration transmissibility of the MSFW rotor is shown in Fig. 2.10(c). The vibration transmissibility of MSFW rotor could be increased by the proportional coefficient. Therefore, these results show that the natural frequency and the vibration transmissibility of MSFW rotor could be controlled by adjusting the proportional coefficient of control system.

Moreover, the relationship between and the derivative coefficient K_D of control system and the vibration characteristics of MSFW rotor is illustrated in Fig. 2.11(a). The proportional coefficient is chosen as 50, when the derivative coefficient K_D=0.005, the vibration transmissibility of the MSFW rotor is about 22 but it decreases to 1.2 when the derivative coefficient K_D of control system is increased to 5. The relationship between the derivative

coefficient K_D of the control system and the natural frequency ω_n of MSFW rotor is illustrated in Fig. 2.11(b). The natural frequency of MSFW rotor does not change with the derivative coefficient of the control system. Consequently, the vibration transmissibility of MSFW rotor could be suppressed by tuning the derivative coefficient with no effect to the natural frequency of the MSFW rotor.

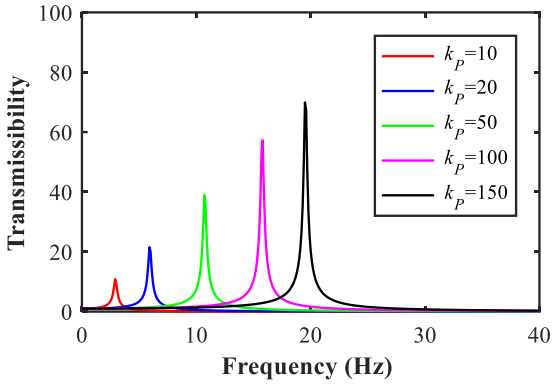

(a)

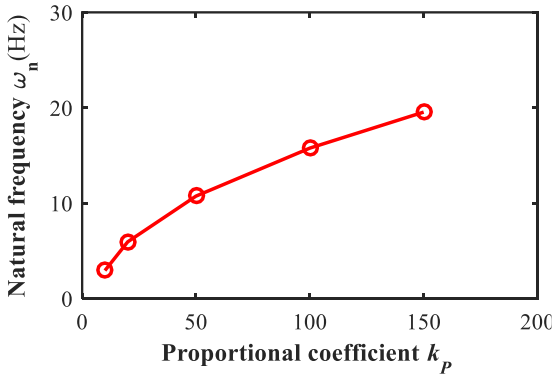

(b)

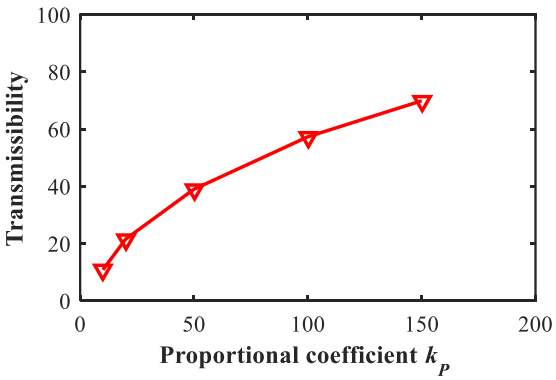

(c)

Fig. 2.10. (a) The vibration responses of the MSFW rotor with different proportional coefficients, (b) the relationship between the proportional coefficient and the natural frequency of MSFW rotor, (c) the relationship between the proportional coefficient and the vibration transmissibility of MSFW rotor.

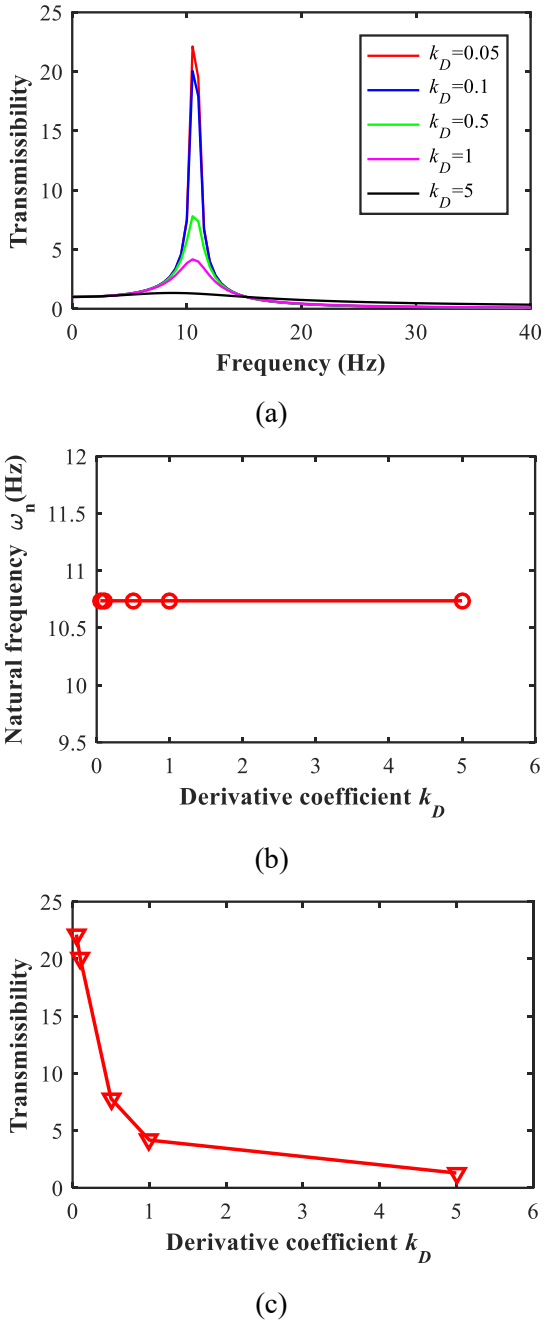

Fig. 2.11. (a) The vibration responses of the MSFW rotor with different derivative coefficients, (b) the relationship between the derivative coefficient and the natural frequency of MSFW rotor, (c) the relationship between the derivative coefficient and the vibration transmissibility of MSFW rotor.

Above all, the natural frequency of MSFW rotor could increase with the proportional coefficient of the control system, and the vibration transmissibility of MSFW rotor also increases with the proportional coefficient of the control system. Moreover, the vibration transmissibility of MSFW rotor is suppressed by increasing the derivative coefficient, and the natural frequency of MSFW rotor does not vary with variation of the derivative coefficient. Therefore, a great proportional coefficient would make the stability of the MSFW rotor declines.

Therefore, a design guideline for the vibration control of the MSFW rotor is proposed in the following based on these analysis results. Firstly, the wide ranges of the derivative coefficient and the proportional coefficient should be defined to ensure stability of MSFW rotor. Furthermore, the vibration transmissibility of the MSFW rotor is reduced by increasing the derivative coefficient, and the natural frequency of the MSFW rotor is controlled by tuning the proportional coefficient to avoid the resonance vibration. Moreover, when the real-time operational frequency is far away the natural frequency of MSFW rotor, the vibration transmissibility could be suppressed by increasing the derivative coefficient of control system.

2.5.3 The Tilting Vibration Analysis of MSFW Rotor

The tilting vibrations of MSFW rotor at different rotational frequencies with the transient impulse disturbance are plotted in Fig. 2.12, and the vibration frequency of the titling angle is the natural rotational frequency of MSFW rotor. The response magnitude of the tilting angle is decreased from $3.1°\times10^{-3}$ to $0.7°\times10^{-3}$ when the rotating speed of the MSFW rotor is increased from 100Hz to 400Hz. According to the power spectrums of the MSFW rotor's displacements at different rotating speeds as shown in Fig. 2.12(b), the response magnitude of MSFW rotor caused by the transient impulse torque decreases with rotational speed of MSFW rotor.

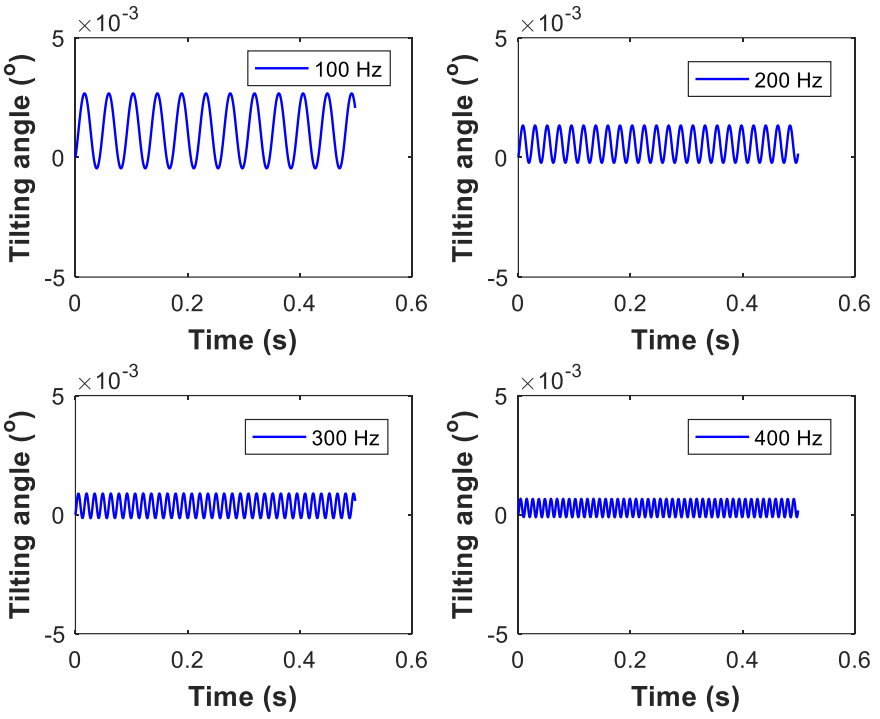

(a)

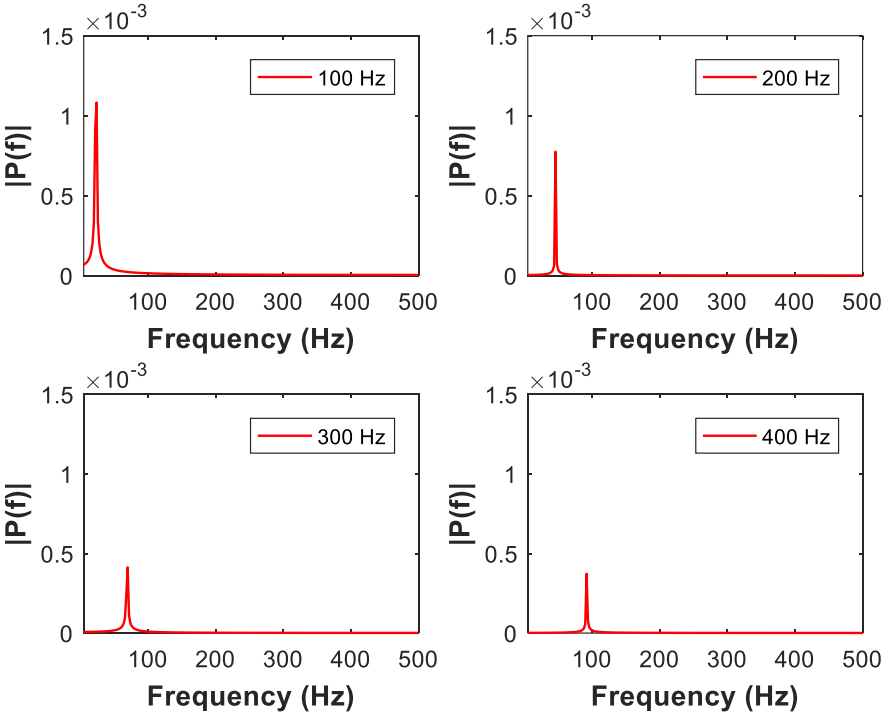

(b)

Fig. 2.12. The tilting response curves of MSFW rotor when the transient impulse disturbance is added on it, (a) the angle response of the MSFW rotor, (b) the power spectrum of the corresponding angle response.

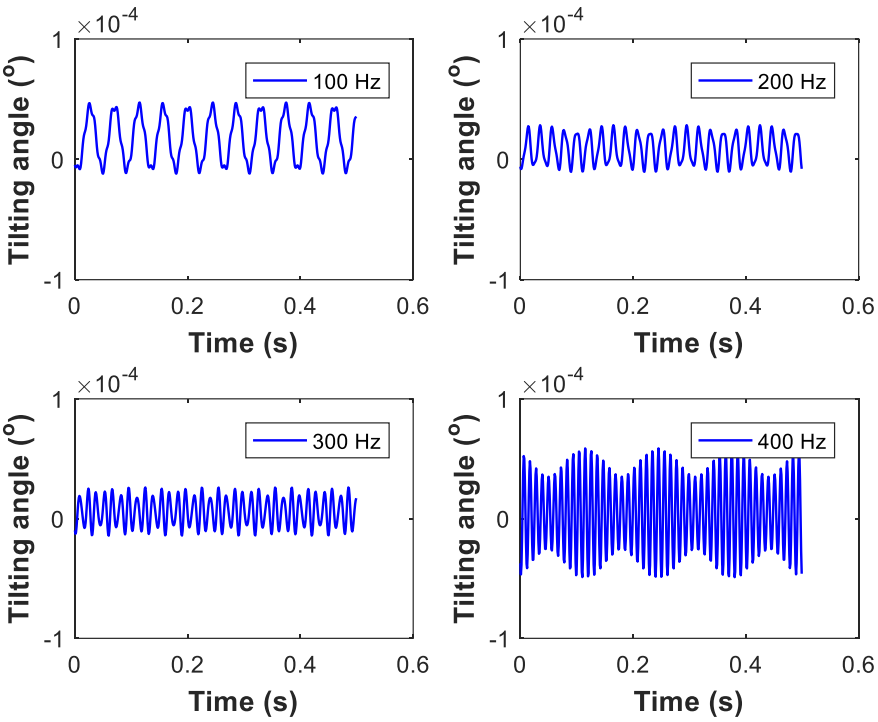

(a)

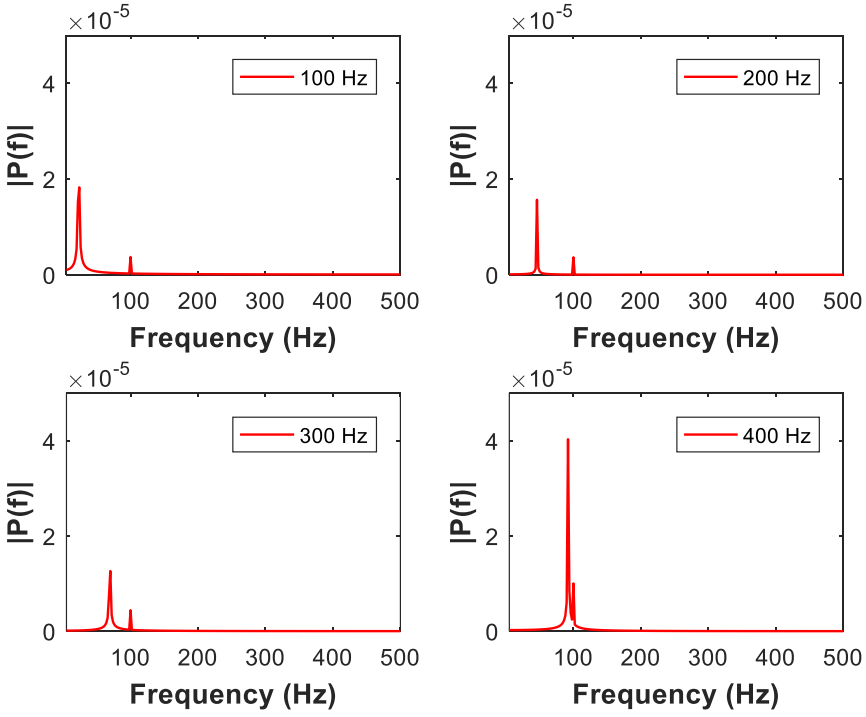

(b)

Fig. 2.13. The tilting response curves of MSFW rotor when the harmonic disturbance is imposed on it, (a) the angle response of the MSFW rotor, (b) the power spectrum of the angle response curve.

The tilting response of the MSFW rotor with a harmonic disturbance (the frequency is 100Hz) is plotted in Fig. 2.13, and there are two rotational vibrations with two frequencies including and the vibration frequency of harmonic disturbance and the natural rotational

frequency of MSFW rotor. According to displacement deflection of MSFW rotor, the response magnitude of tilting angle is increased from $5.45°\times10^{-6}$ in the first figure to $3.45°\times10^{-5}$ in the fourth figure when the rotational frequency of MSFW rotor increases to 400 Hz. As shown in the power spectra of tilting vibration in Fig. 2.13 (b), the tilting angles of MSFW rotor has great variations at the respective vibration frequency of harmonic disturbance and natural frequency of MSFW rotor's rotational motion. In detail, the resonance vibration happens when the natural rotational frequency of MSFW rotor is equal to vibration frequency of harmonic disturbance.

The tilting response of MSFW rotor with a constant disturbance is plotted in Fig. 2.14. The disturbance caused by the constant disturbance always increases with the time, but its final amplitude decreases with the rotational speed of the MSFW rotor. When the rotation frequency of the MSFW rotor is 100Hz, the final value of titling angel is about $6°\times10^{-5}$, but it is decreased to $1.8°\times10^{-5}$ when the rotational speed increases to 400Hz. In addition, as shown in the power spectra of the MSFW rotor's displacements at different rotational speeds in Fig. 2.14 (b), the tilting angle response of the MSFW rotor has obvious vibration when the rotational frequency of MSFW rotor is equal to the natural rotational frequency.

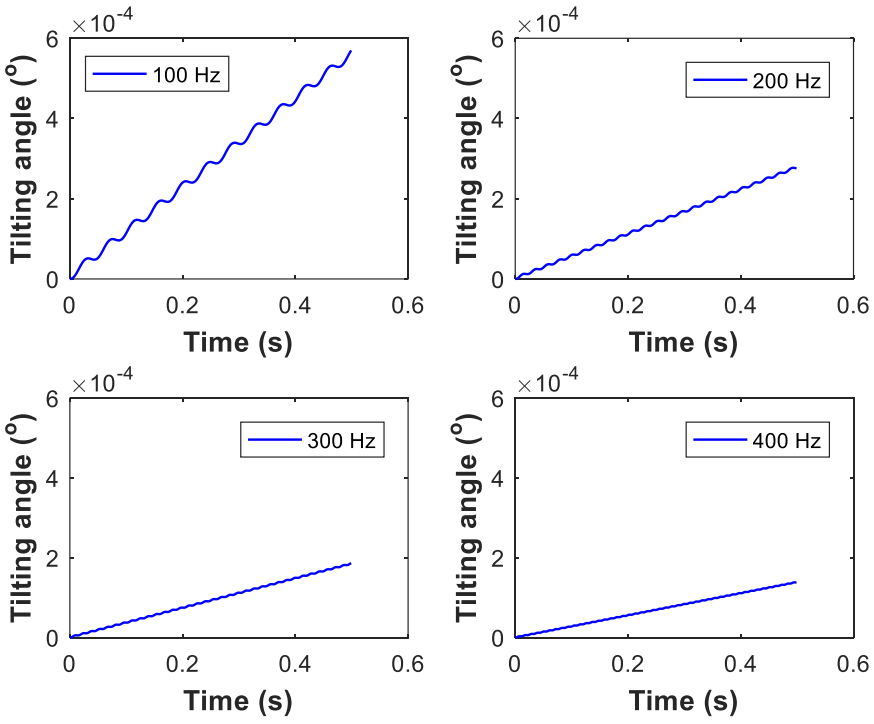

(a)

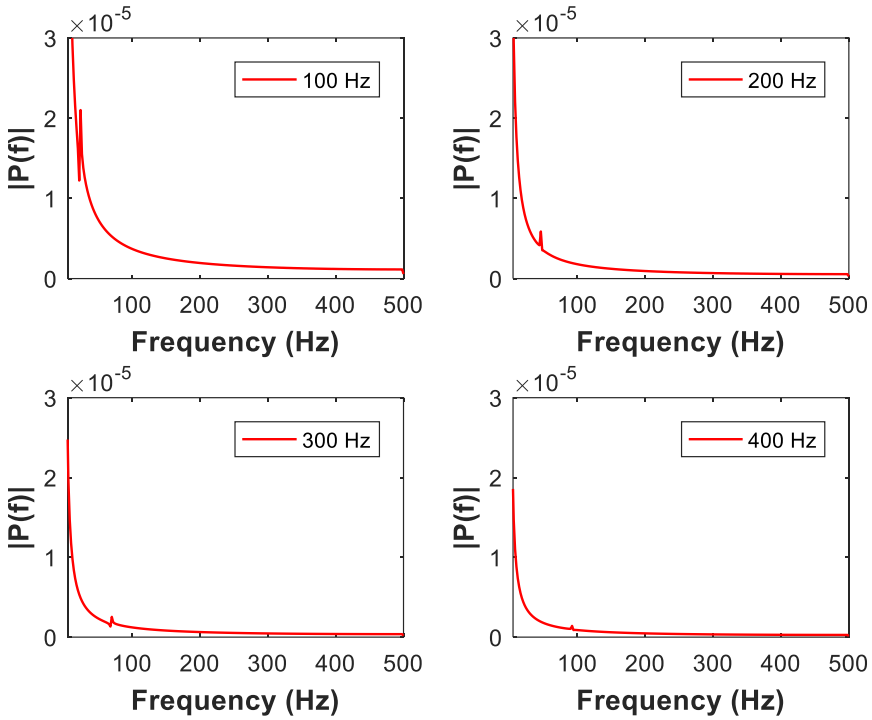

(b)

Fig. 2.14. The tilting response curves of MSFW rotor when the constant disturbance is imposed on it, (a) the angle response of the MSFW rotor, (b) the power spectrum of the angle response curve.

2.5.4 The Tilting Response of MSFW Rotor with Stiffness and Damping

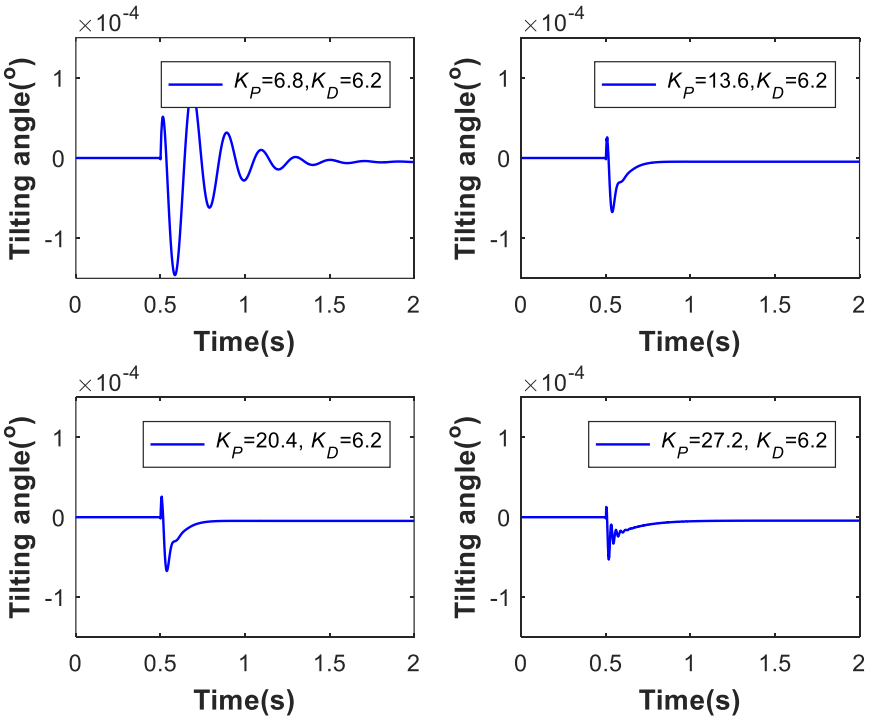

(a)

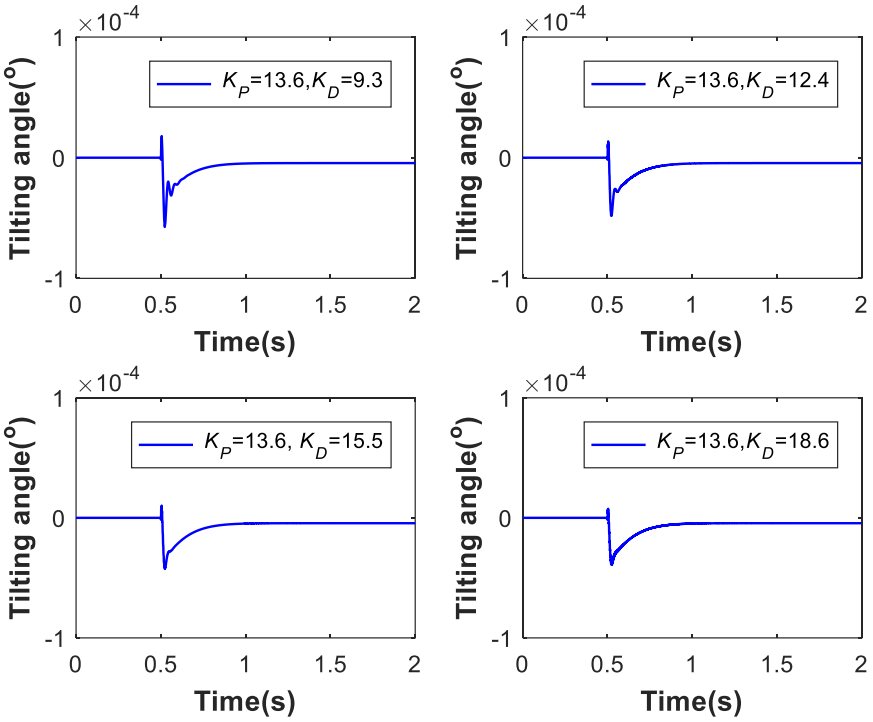

(b)

Fig. 2.15. The tilting response curves of MSFW rotor when the transient impulse disturbance is added on it, (a) the relationship between the proportional coefficient and the angle response, (b) the relationship between the derivative coefficient and the angle response.

The response curve of tilting angle of the MSFW rotor with a transient impulse disturbance is plotted in Fig. 2.15(a) shows that the response magnitude and the settling time of tilting angle decreases with increasing proportional coefficient. When proportional coefficient is K_P=6.8, the tilting angle of the MSFW rotor is about 2.2°×10^{-4}, and the settling time is about 1s. The tilting angle of the MSFW rotor decreases to 0.7°×10^{-4} when the proportional coefficient K_P increases from 6.8 to 27.2, also the settling time is shortened to 0.1s. The vibration amplitude of the tilting angle could be declined by increasing the derivative coefficient as shown in Fig. 2.15(b). When the derivative coefficient is K_D=9.3, the tilting angle of the MSFW rotor is about 0.7°×10^{-4}, and the settling time is about 0.5s. When the derivative coefficient is K_D increases to 18.6, the tilting angle of the MSFW rotor decreases to 0.4°×10^{-4}, and the settling time is reduced to 0.2s.

The vibration response curves of tilting angle with adding the harmonic torque disturbance are shown in Fig. 2.16. The response magnitude of the tilting angle is suppressed by increasing the derivative coefficient and the proportional coefficient of control system. In Fig. 2.16(a), when the proportional coefficient K_P=6.8, the response magnitude of the tilting angle is about

$1°\times10^{-4}$. The tilting angle of the MSFW rotor decreases to $0.3°\times10^{-4}$ when the proportional coefficient K_P increases to 27.2. In Fig. 2.16(b), when the derivative coefficient K_D=9.3, the tilting angle of the MSFW rotor is about $0.8°\times10^{-4}$. When the proportional coefficient K_D is increased to 18.6, the tilting angle of the MSFW rotor decreases to $0.3°\times10^{-4}$. The relationship between derivative coefficient and response magnitudes of tilting angle is illustrated in Fig. 2.17(b).

Therefore, for the cases of system input with either a transient impulse disturbance or a sinusoidal disturbance to the MSFW rotor, the curve of the response magnitude shows that the tilting vibration of MSFW rotor could be mitigated through improving the proportional coefficient or the derivative coefficient. In the meanwhile, the great proportional coefficient could generate the great magnetic torque to suppress the disturbance torque by improve the corresponding stiffness of MSFW rotor. The derivative coefficient could reduce the disturbance torque by enhancing the damping characteristics of MSFW rotor.

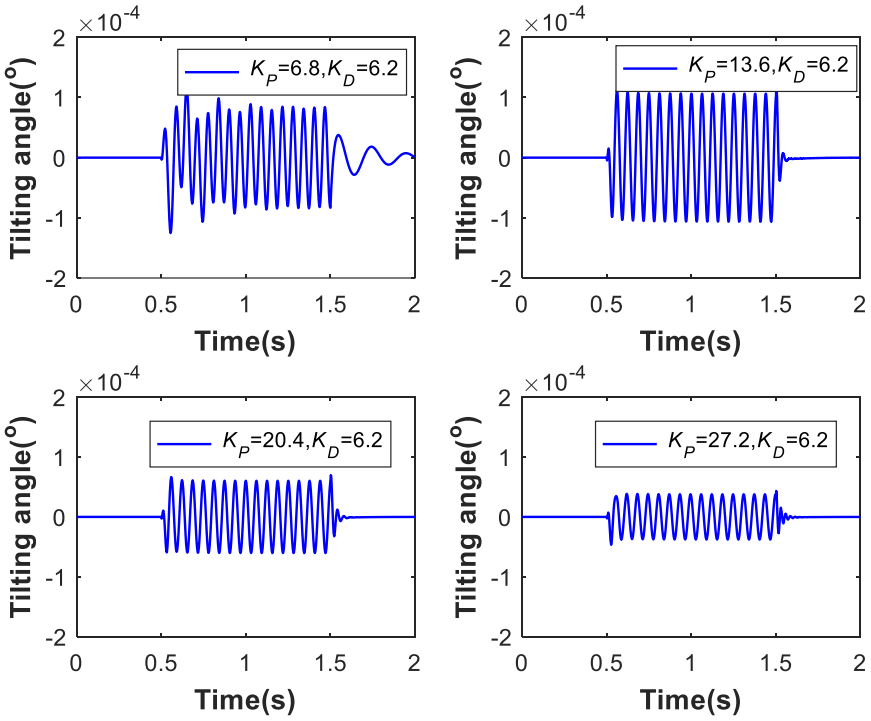

(a)

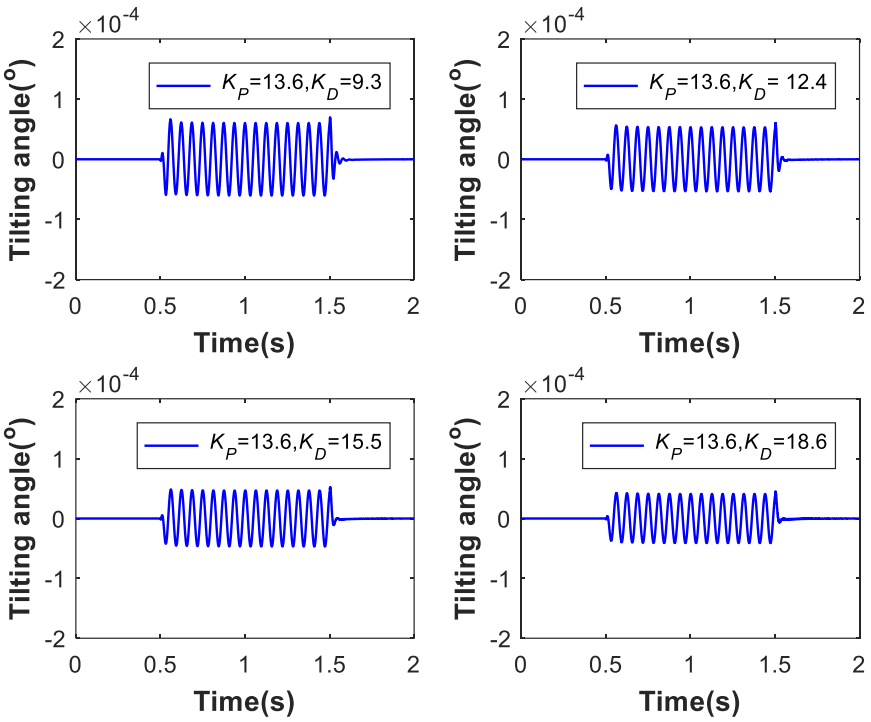

(b)

Fig. 2.16. The tilting response curves of MSFW rotor when the harmonic disturbance is imposed on it, (a) the angle response versus the proportional coefficient, (b) the angle response versus the derivative coefficient.

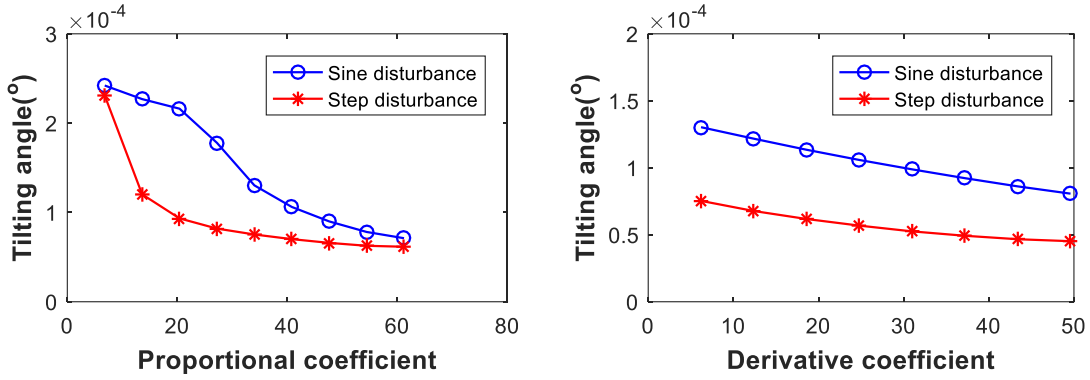

(a) (b)

Fig. 2.17. The vibration amplitudes of the MSFW rotor's tilting angle with different disturbances, (a) the angle response versus the proportional coefficient, (b) the angle response versus the derivative coefficient.

2.6 Experiment

2.6.1 The Experimental Setups

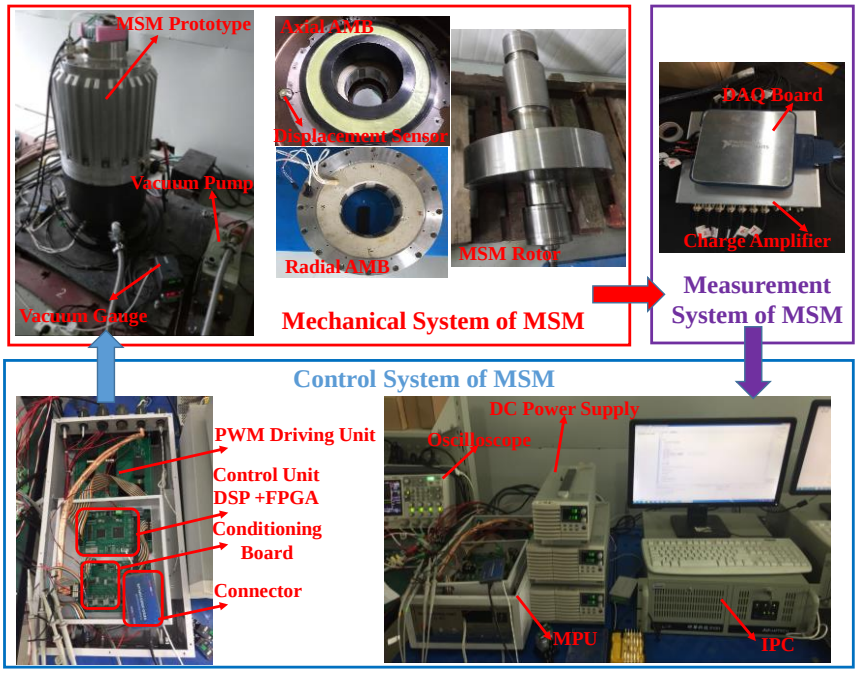

Fig. 2.18. The experimental setup of the MSFW rotor.

TABLE. 2.IV. The instrument used in the experiment.

Setup	Model
DAQ board	NI PCI-9655
DSP	TMS320F28335
FPGA	Altera EPF10K30RC208
Oscilloscope	Keysight 2000 X-Series
DC power supply	Tektronix Keithley T2231A-30-3
IPC	Advantech IPC 610H
Magnetic suspension system	Self-designed
Signal conditioning module	Self-designed
PWM driving unit	Self-designed

The whole MSFW system is shown in Fig. 2.18. It has three sub-systems including a mechanical structure system, a real-time measurement system and a high-performance control system. The mechanical structure system of MSFW rotor is composed of the axial AMB system, the radial AMB system and the flywheel rotor. The vacuum pump could mitigate the wind drag when MSFW system rotates at high rotational speed, and the working pressure is less than 3Pa.

TABLE. 2.V. The parameters of MSFW rotor system.

Parameter	Value	Unit
Polar moment of inertia	J_m=0.67	kg·m^2
Equatorial moment of inertia	J_l=1.24	kg·m^2
Mass of MSFW rotor	m=150	kg
Current stiffness of radial AMB	k_{ix}=520	N/A
Displacement stiffness of radial AMB	k_{dx}=-2800	N/mm
Current stiffness of axial AMB	k_{iz}=500	N/A
Displacement stiffness of axial AMB	k_{dz}=-1700	N/mm
Span from radial sensor to center of mass	l=476	mm
DC power supply of AMB	2	A
Bias current of radial AMB	1.5	A
Bias current of axial AMB	1.8	A
Power supply of control system	28	V
Amplification coefficient	k_a=0.2	A/V
Sensitivity of displacement sensor	k_s=3.3	V/mm

The vacuum gauge system could timely detect the vacuum situation of MSFW system. For MSFW rotor, the 35CrMnSiA is used as the rotor material with 0.3 Poisson ratio, and the elastic modulus is 195GPa. The PMSM with four pole pairs is used as the drive unit of MSFW rotor. The eddy current displacement sensors installed on the stator of MSFW system could measure the displacement variations of MSFW rotor about the equilibrium positions. The displacement signals measured by the eddy current displacement sensors are collected by the charge amplifiers, and then the National Instrument (NI) data acquisition (DAQ) PCI9655 board could collect the displacement signals through the charge amplifier and feed them back into the control system. In the meanwhile, the oscilloscope would timely display the dynamic displacements of the MSFW rotor. The control system of the MSFW rotor contains the main processing unit (MPU), the direct current (DC) power supply system, the oscilloscope, and the industrial personal computer (IPC). The MPU has a digital signal processor (DSP) chip and a field programmable gate array (FPGA) chip. It processes the control algorithm and outputs the control signal based on the feedback displacement of the MSFW rotor. The pulse width modulation (PWM) unit could generate the driving currents for the axial and radial AMBs. The IPC could timely monitor the operational situations of whole MSFW system such as the radial

and axial displacement variations, the vacuum degree, the rotational speed of MSFW rotor and the control currents of AMB's windings. Those series number of instruments used in the experiment are listed in TABLE. 2.IV, and the relative parameters of the experiment are listed in TABLE. 2.V.

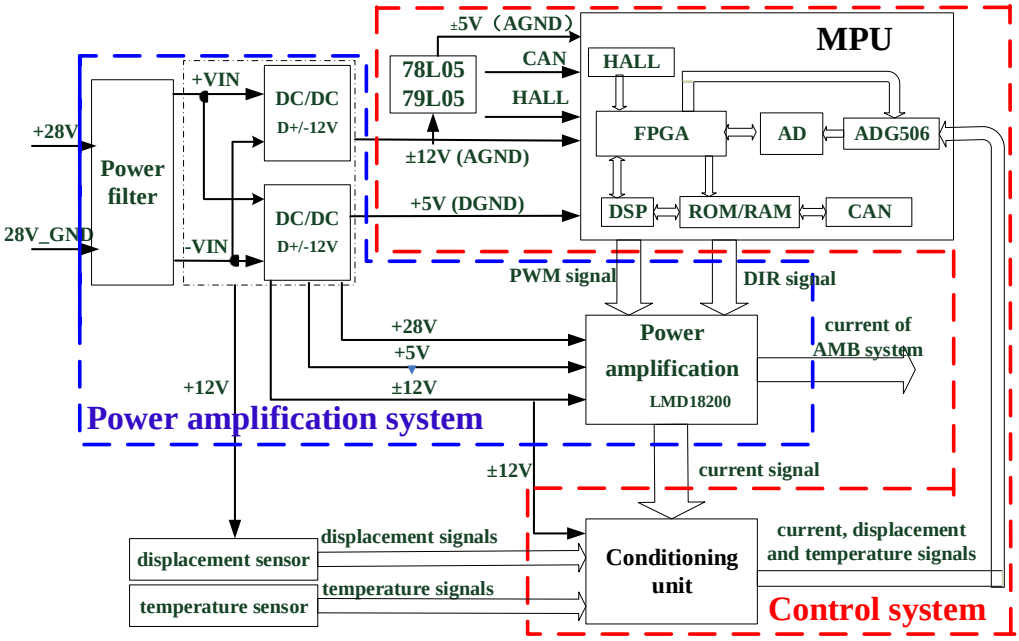

Fig. 2.19. The topology of the control system.

The topology of the control system of the MSFW rotor is plotted in Fig. 2.19, there are two main parts including a power supply system and a MPU system. For the power system in the blue box, its functions are to transfer the input voltage into the supply voltages of the MPU (FPGA chip and DSP chip), the real-time measurement system and the power amplification unit. The power amplification unit could continually output the control current up to 3A, the peak current could reach to 6A, and the maximum working voltage is 55V. For the MPU system in the red box, it would process the displacement signals through the conditioning unit and the rotational speed signal captured by the HALL sensor, and then the programming of the control model would be finished. The duty cycles of PWM signal for driving the AMB system would be outputted finally.

2.6.2 The Control Process of Experimental Setup

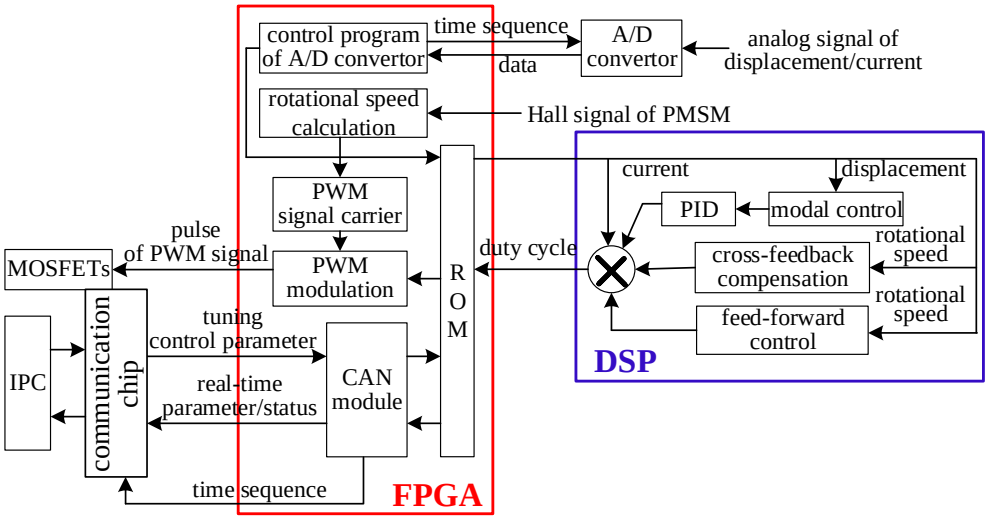

Fig. 2.20. The whole control process of the MPU.

Based on the control system of the MSFW rotor in Fig. 2.19, the control process of the MPU system is shown in Fig. 2.20, there are two control chips including the FPGA and the DSP. As illustrated in red box, the FPGA could finish some procedures about logic operation such as communication with the IPC, capturing the Hall signal and control of the analog to digital (A/D) convertor. Furthermore, the FPGA could generate the PWM control signal to drive the metal oxide silicon field effect transistor (MOSFET). For the DSP chip as shown in blue box, the DSP chip could complete the programming of the MSFW rotor including the PID control, the cross-feedback compensation, and the feed-forward control.

The control process of the DSP is shown in Fig. 2.21, the control program would be at the waiting state to capture the external interrupt after the initialization. The interruption service programming has these sub-programs including the reading sampling value of the A/D convertor, the PID control, cross-feedback compensation, the negative current feedback control and the PWM modulation. Those sub-programs are executed by the way of series operation.

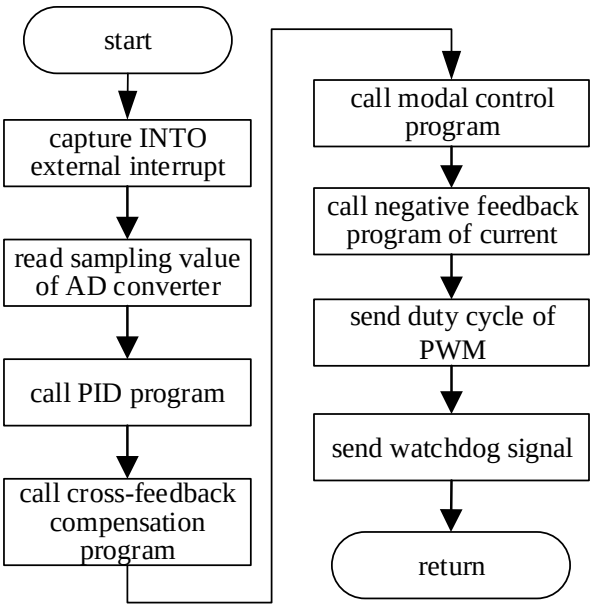

Fig. 2.21. The control process of the DSP.

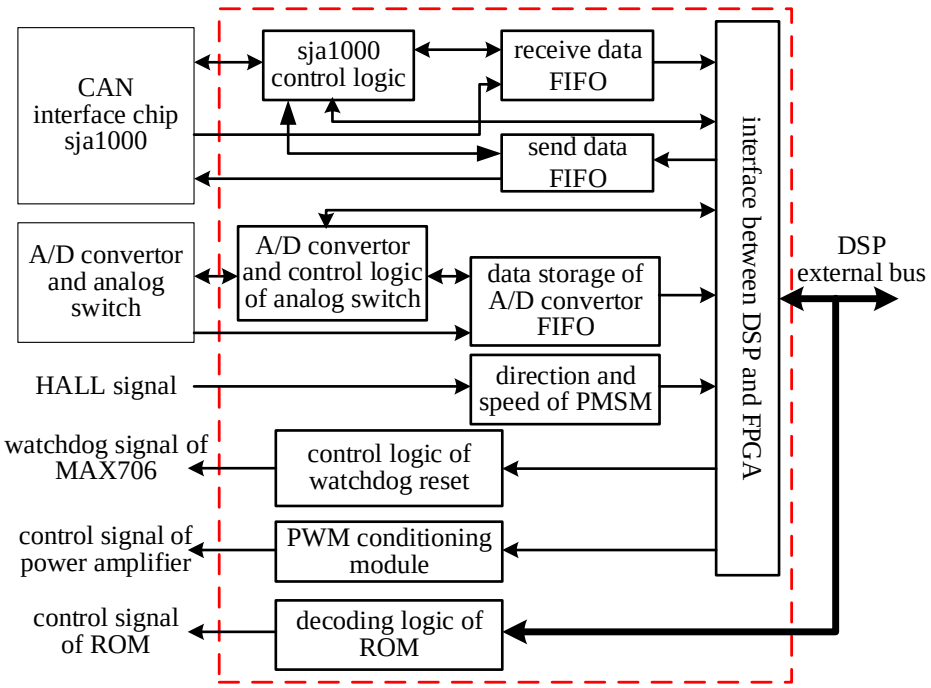

Fig. 2.22. The control logic of the FPGA.

For the control process of the FPGA chip as illuminated in Fig. 2.22, it works at the way of parallel operation, so the control process is consisted of different logic modules. The logic module of the controller area network (CAN) communication is to receive/send data, and the logic module of the A/D convertor could implement the communication between the FPGA and the A/D convertor. Especially, the logic module of the PWM condition could generate the

control signal for the power amplifier to drive the MOSFETs, and then the magnetic forces of the AMB system are achieved to suspend the MSFW rotor.

2.6.3 The Suspension Characteristics of MSFW Rotor

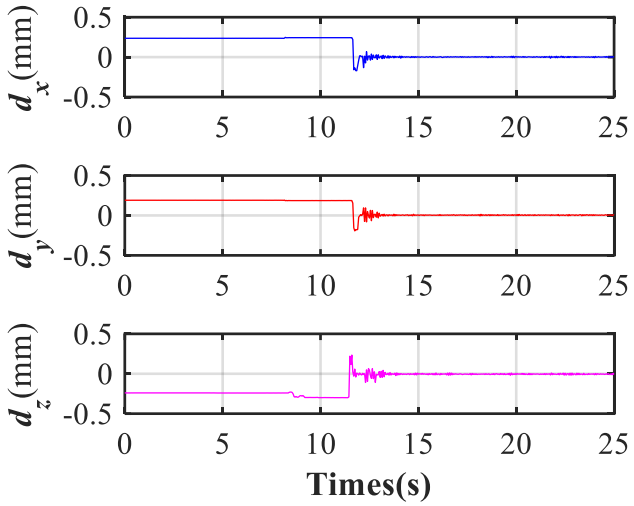

Fig. 2.23. The dynamic displacements of the MSFW rotor during suspension process in radial and axial directions

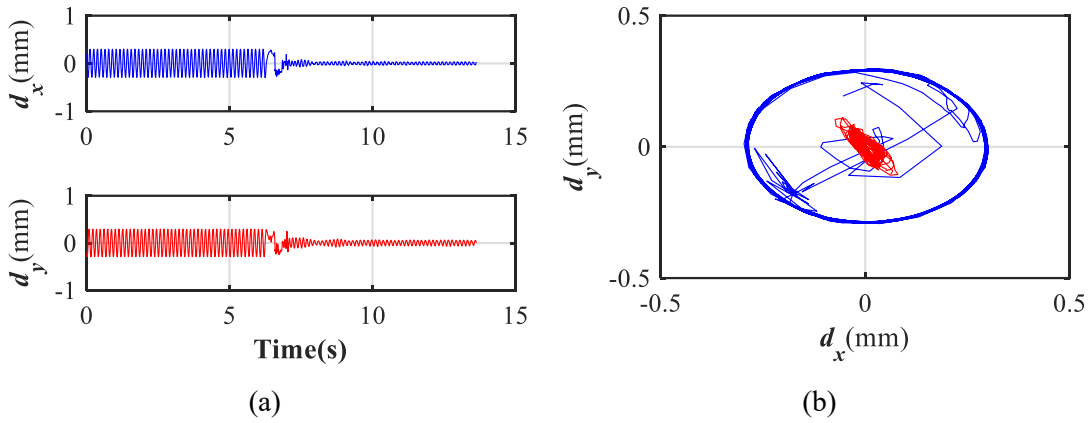

Fig. 2.24. The radial suspension curves of MSFW rotor, (a) the radial displacement curves of MSFW rotor, (b) the axis orbit of MSFW rotor.

The control parameters of radial translational suspension are chosen as K_{Px}=6.8 and K_{Dx}=6.2, and that of axial radial translational suspension are chosen as K_{Pz}=12 and K_{Dz}=8.3, the translational suspensions of the MSFW rotor along three axes are shown in Fig. 2.23. When the radial and axial AMBs are switched on, the translational displacements of the MSFW rotor in axial and radial directions are zeroes representing that the MSFW rotor is stably suspended at the radial and axial equilibrium points. The stable suspension in radial direction of the MSFW

rotor could be also verified by the axis orbit around radial axes as shown in Fig. 2.24. The MSFW rotor rotates around the back-up ball bearing when the MSFW rotor is not forced to suspend at the equilibrium position in radial direction, its axis orbit of MSFW rotor is the blue cycle with radius 0.3mm. The red cycle represents the axis orbit with radius 0.05mm when the MSFW rotor is stably suspended at the radial equilibrium point. These experimental results indicate that the axial and radial AMBs could force the MSFW rotor to stably suspend at the equilibrium position in radial and axial directions, and the active controllability of the MSFW rotor is verified.

The translational response curves of MSFW rotor choosing different derivative coefficients and proportional coefficients are shown in Fig. 2.25. The dynamic displacement deflecting from the radial equilibrium position is applied to evaluate the dynamic characteristics of MSFW rotor. When the proportional coefficient K_P=6.8 and the derivative coefficient K_D=6.2, the displacement deflection of the MSFW rotor from the radial equilibrium position is about 0.1648mm. When the proportional coefficient of the MSFW rotor increases to 20.4, the displacement variation of the MSFW rotor from the radial equilibrium position increases to 0.31mm. In addition, the displacement deflection from the radial balanced position of MSFW rotor increases from 0.2849mm to 0.2365mm when the derivative coefficient of control system is increased from 9.3 to 15.5.

Therefore, the response magnitude of the translational motion of the MSFW rotor increases with an increase of the proportional coefficient which represents the system stiffness, and it decreases with an increase of the derivative coefficient which represents the system damping. The proportional coefficient could increase the vibration response of translational motion, and the derivative coefficient could suppress the vibration response of translational motion.

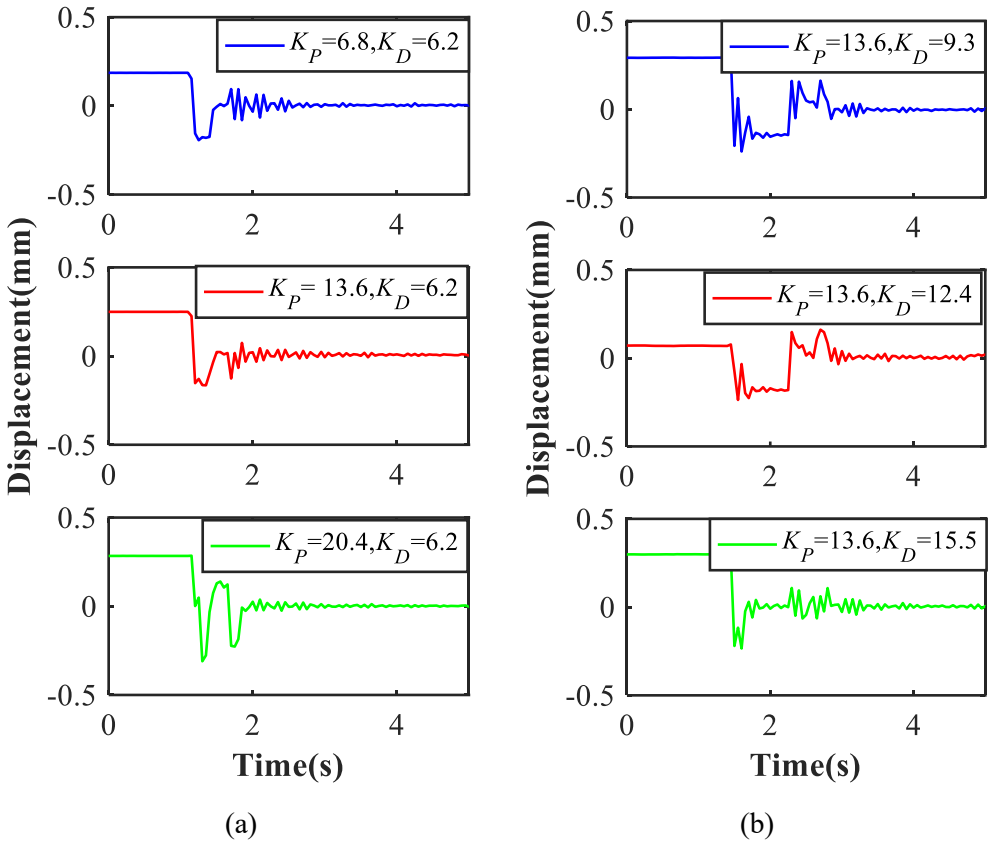

Fig. 2.25. The translational responses of MSFW rotor with different derivative coefficients and proportional coefficients, (a) the relationship between the proportional coefficient and the translational displacement, (b) the relationship between the derivative coefficients and the translational displacement.

2.6.4 The Tilting Characteristics of MSFW Rotor

In the experiments about tilting vibration around radial axes of the MSFW rotor, the dynamic displacement deflection of the MSFW rotor from the radial equilibrium position is applied to judge the response magnitude of tilting vibration. A transient impulse disturbance and a harmonic disturbance are added on MSFW rotor respectively when rotating speed of MSFW rotor is 10000rpm. When a transient impulse disturbance is imposing on MSFW rotor, the dynamic displacement deflection of MSFW rotor is shown in Fig. 2.26. The displacement deflection of the MSFW rotor from the radial equilibrium point decreases from 0.2338mm to 0.137mm when the proportional coefficient increases from 6.8 to 20.4. As illuminated in Fig. 2.26(b), the displacement of the MSFW rotor deflecting from the equilibrium position in radial direction is reduced from 0.1809mm to 0.0921mm when the derivative coefficient increases from 9.3 to 15.5.

As illustrated in Fig. 2.27, when a harmonic disturbance is acting on the MSFW rotor, the displacement deflections of the MSFW rotor from the radial equilibrium point resonant at two frequencies (the vibration frequency of the imposed harmonic disturbance and the rotational frequency of MSFW rotor). The tilting torque formed by the radial AMBs at upper end and lower end is used to mitigate the tilting vibration of the MSFW rotor. The dynamic displacement variation of the MSFW rotor deflecting from the radial equilibrium position is about 0.1015mm when the proportional coefficient K_P=6.8. It decreases to 0.0798mm when the proportional coefficient is increased to 20.4. Similarly, the displacement variation of the MSFW rotor deflecting from the radial equilibrium position is reduced from 0.0898mm to 0.0534mm when the derivative coefficient increases from 9.3 to 15.5 as shown in Fig. 2.27(b). Therefore, the experimental results of titling response are consistent with the simulation results. The tilting torque generated by the radial AMB could effectively suppress the disturbance acting on the rotational motion of the MSFW rotor.

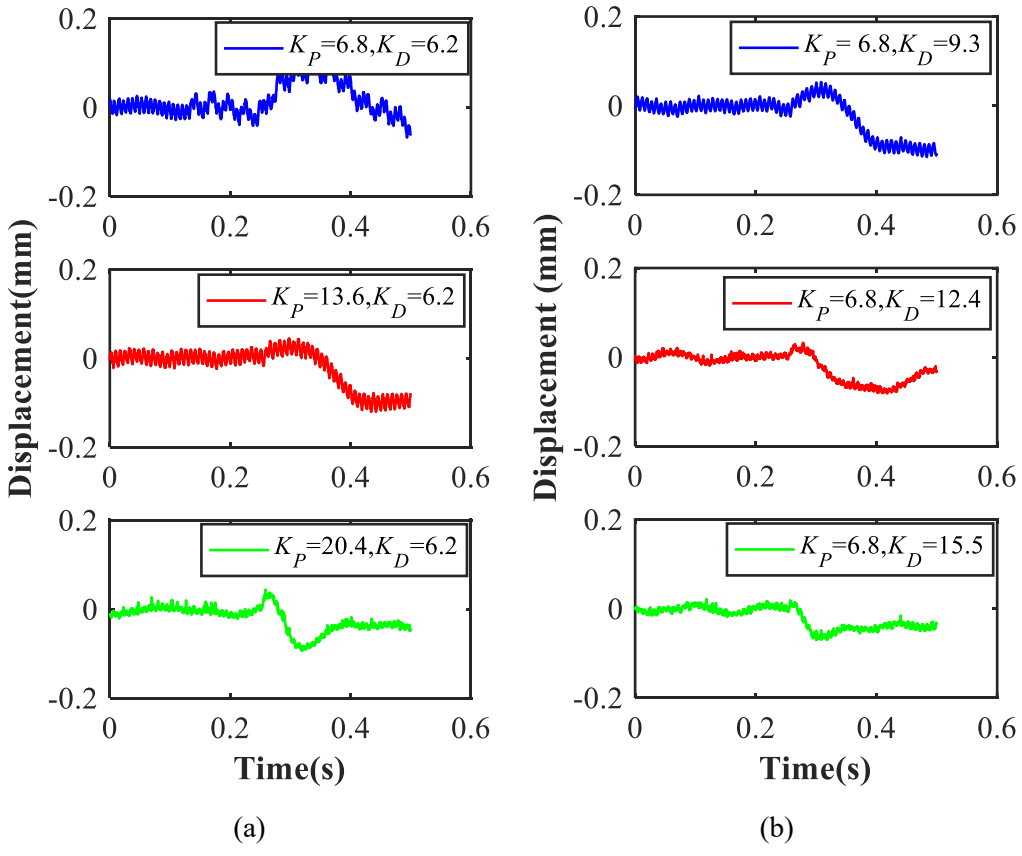

Fig. 2.26. The response curves of MSFW rotor for the transient impulse with different derivative coefficients and proportional coefficients, (a) the relationship between the displacement and the proportional coefficient, (b) the relationship between the displacement and the derivative coefficients.

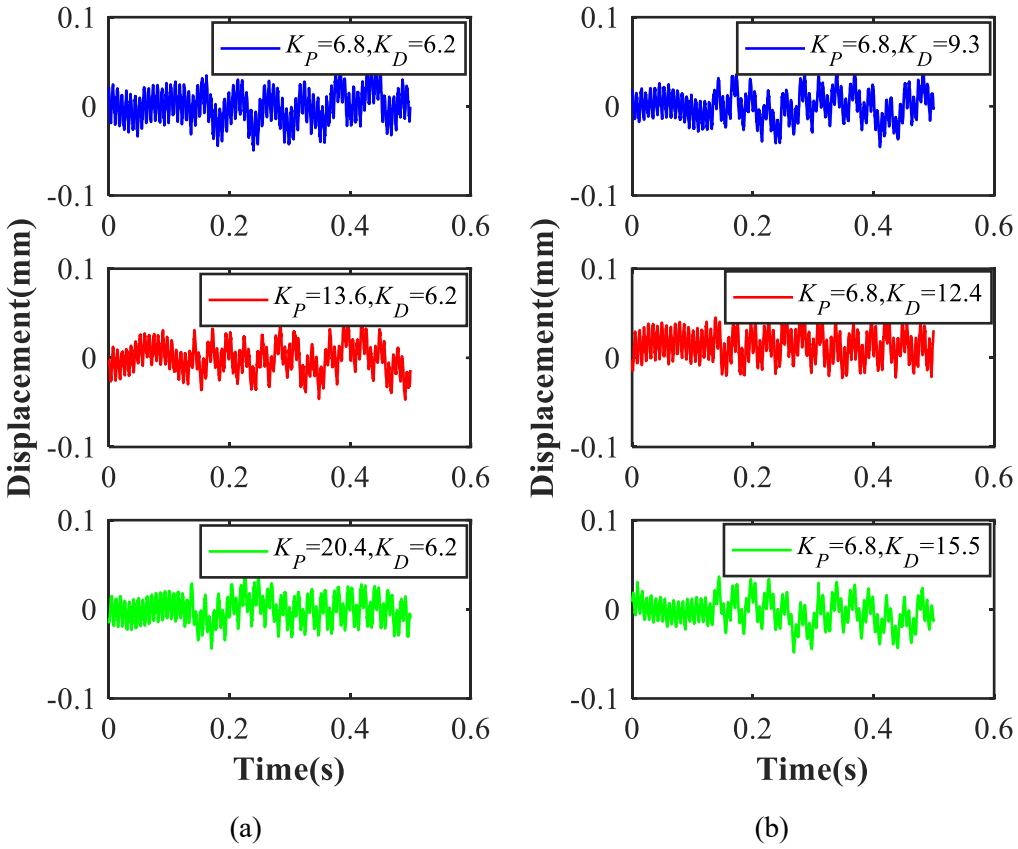

Fig. 2.27. The dynamic response curves of MSFW rotor for harmonic disturbance with different proportional coefficients and derivative coefficients, (a) the relationship between the displacement and the proportional coefficient, (b) the relationship between the displacement and the derivative coefficients.

2.7 Summary

The vibration characteristics of an MSFW rotor are investigated in this chapter. For the vibration characteristics of MSFW rotor's translational motion, the vibration transmissibility of MSFW rotor could be suppressed by the derivative coefficient of control system, but it would become more serious by increasing the proportional coefficient of control system. In the meanwhile, the natural frequency of MSFW rotor is linear to the proportional coefficient of control system, so the natural frequency should be set greater than the real-time frequency of MSFW rotor by controlling proportional coefficient to avoid the resonance vibration of MSFW rotor. If the real-time frequency does not approach to the natural frequency of MSFW rotor, the vibration magnitude could be suppressed by the derivative coefficient, but a great value of proportional coefficient could cause negative influence to the stability of MSFW rotor.

For the tilting vibration of MSFW rotor with imposing different disturbances are investigated. In the case of a transient impulse disturbance acting on the MSFW rotor, the titling angle of MSFW rotor would decrease with its rotational frequency. On the other hand, in the case of a harmonic disturbance, the titling angle of MSFW rotor would increase with the rotational frequency. When the natural rotational frequency is equal to the vibration frequency of harmonic disturbance acting on the MSFW rotor, the resonant vibration of the MSFW rotor occurs. The simulation results and experimental results prove that the tilting torque formed by the radial AMBs at lower end and upper end could mitigate vibration responses of MSFW rotor. The tilting angle could be suppressed by proper tuning of the derivative coefficient and the proportional coefficient.

Chapter 3. The Stability Analysis Method of MSFW Rotor

The vibration characteristics of the MSFW rotor had been analyzed using the state space function and its solution is presented in Chapter 2. The research focus is about the translational vibration of the MSFW rotor with symmetrical suspension span. The rotational vibration of the MSFW rotor with the asymmetrical structure is more worthy of being investigated.

In Chapter 2, the vibration characteristics of the MSFW rotor are analyzed assuming the radial AMBs are located symmetrically to the mass center of the MSFW rotor. However, in the real structural design of the radial AMBs and the MSFW rotor, this kind of symmetry about the locations of the radial AMBs is not guaranteed. Therefore, the vibration characteristics of the MSFW rotor with considerations of the suspension span ratio between the upper and lower radial AMBs and the moment of inertia ratio between the equatorial and polar moment of inertia are analyzed. In the case of the translational vibration of the MSFW rotor, the gain margin and the phase margin of the frequency response spectrum of the translational control loop are used as evaluation indices of the stability of the MSFW rotor. The rotational vibration of the MSFW rotor is analyzed based on the distribution of the open-loop pole and the frequency response of the rotational control loop. The relationships amongst the critical rotational frequency of the MSFW rotor, the moment of inertia ratio and the suspension span ratio are investigated, the frequency of the back whirling (BW) increases with the moment of inertia ratio and the suspension span ratio, but the frequency of the forward whirling (FW) decreases with the moment of inertia ratio and the suspension span ratio. Furthermore, based on the response curve of the negative frequency and the positive frequency, the stability criterion of the radial rotation control based on the dual frequency bode diagram is developed, and the influence of the suspension span ratio and the moment of inertia ratio are analyzed. The proposed vibration analysis method of the MSFW rotor by considering the suspension span ratio and the moment of inertia ratio is a potential method for the analysis of the vibration characteristics of the MSFW rotor.

3.1 The Unsymmetrical Structure of MSFW Rotor

3.1.1 The MSFW Rotor with Unsymmetrical Suspension Span

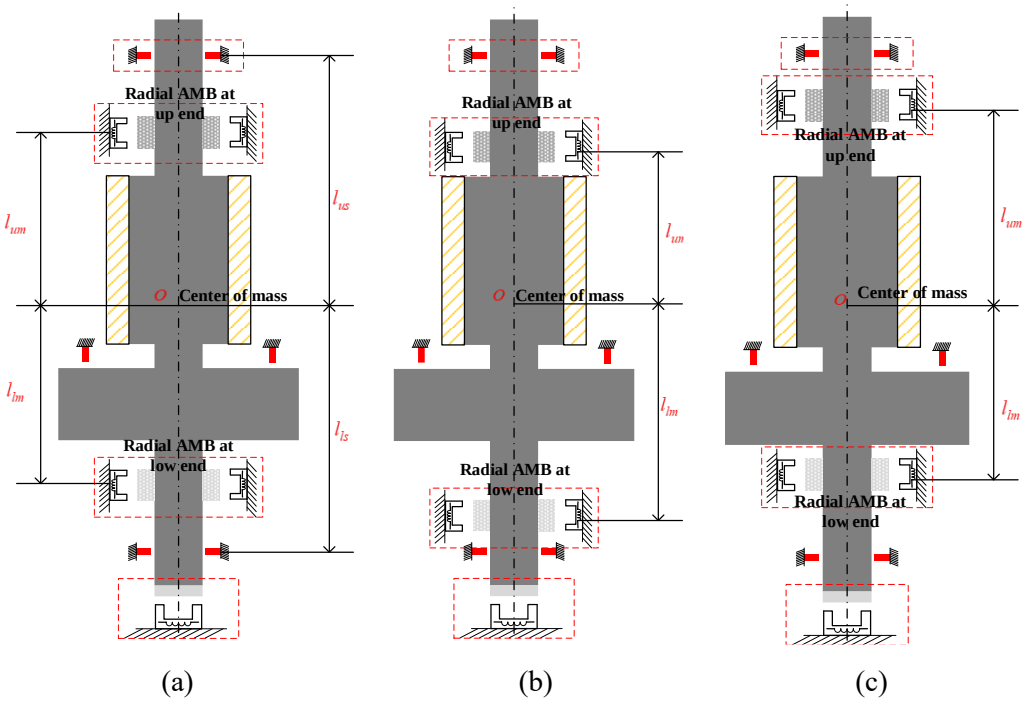

Fig. 3.1. The different structures of the MSFW rotor with different suspension span ratios, (a) the symmetrical structure of the MSFW rotor with l_{lm}/l_{um}=1, (b) the unsymmetrical structure of the MSFW rotor with l_{lm}/l_{um}>1, (c) the unsymmetrical structure of the MSFW rotor with l_{lm}/l_{um}<1.

As illustrated in Fig. 3.1, there are three different structures of the MSFW rotor with different suspension ratios of the radial AMB. Fig. 3.1(a) illustrates the symmetrical structure of an MSFW rotor. The suspension span from the radial AMB at the lower end to the mass center of the MSFW rotor equals to the suspension span from the radial AMB at the upper end to the mass center of the MSFW rotor. So, in this kind of structure, the suspension span ratio of the radial AMB is l_{lm}/l_{um}=1. This kind of MSFW rotor is defined as the symmetrical MSFW rotor. However, this kind of the symmetry about the locations of the radial AMB is not guaranteed in the practical design, an unsymmetrical MSFW rotor is illustrated in Fig. 3.1(b). The suspension span from the radial AMB at lower end to the mass center of the MSFW rotor is longer than the suspension span from the radial AMB at the upper end to the mass center of the MSFW rotor. In this kind of unsymmetrical MSFW rotor, the suspension span ratio of the radial AMB is defined as l_{lm}/l_{um}>1. Similarly, there is another situation about the suspension

span ratio of the radial AMB $l_{lm}/l_{um}<1$ as shown in Fig. 3.1(c). The suspension span from the radial AMB at the lower end to the mass center of the MSFW rotor is smaller than the suspension span from the radial AMB at the upper end to the mass center of the MSFW rotor.

3.1.2 The MSFW Rotor with Unsymmetrical Moment of Inertia

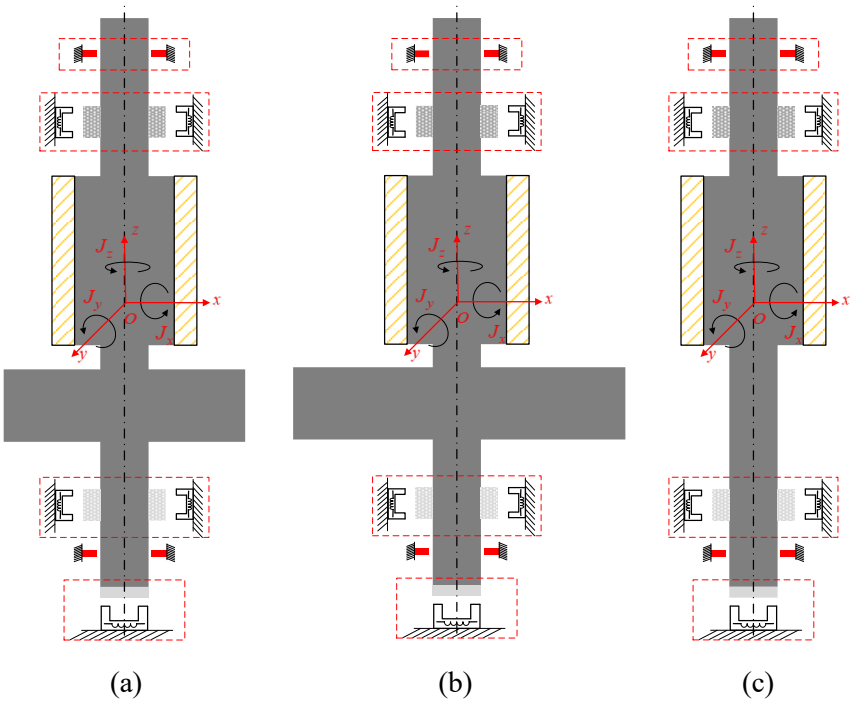

Fig. 3.2. The structures of the MSFW rotor with different moment of inertia ratios, (a) the nominal structure of the MSFW rotor, (b) the structure of the MSFW rotor with $J_x/J_y<1$, (c) the structure of the MSFW rotor with $J_x/J_y>1$.

The structures of the MSFW rotor with different ratios between the equatorial moment of inertia and the polar moment of inertia are illustrated in Fig. 3.2. The nominal model of the MSFW rotor is shown Fig. 3.2(a). When the MSFW rotor is designed as a disc with a great moment of inertia in Fig. 3.2(b), and the equatorial moment of inertia is smaller than the polar moment of inertia, so the ratio between the equatorial moment of inertia and the polar moment of inertia is $J_x/J_y<1$. Moreover, the MSFW rotor is designed as a spindly rotor in Fig. 3.2(c), and the equatorial moment of inertia is greater than the polar moment of inertia, so the ratio between the equatorial moment of inertia and the polar moment of inertia is $J_x/J_y>1$.

3.2 The Translational Response Analysis of MSFW Rotor

As illustrated in Fig. 2.9, the whole control scheme of the MSFW rotor consists of a translational control loop and a rotational control loop. In the closed loop control system of translational motion, the dynamic displacement variations of MSFW rotor detected by the displacement sensors are used as feedback signals. The AMBs generate magnetic forces for the translational control of the MSFW rotor in three directions. In the rotational control loop, the tilting angles of the MSFW rotor are used as the feedback signals for the closed-loop control. A cross-feedback compensation with the rotational speed is applied to suppress the gyroscopic coupling effect when MSFW rotor works at a high rotational speed.

3.2.1 The Modeling of Translational Control Loop

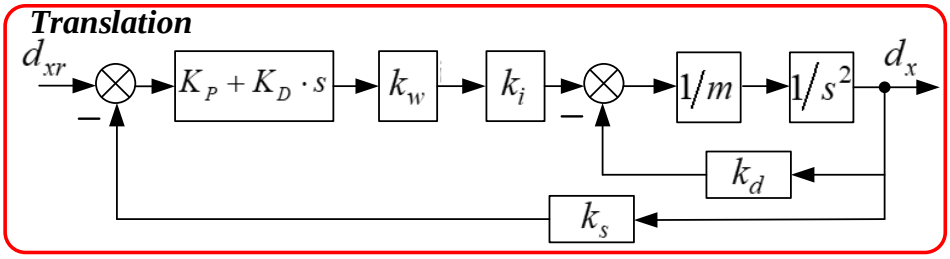

Fig. 3.3. The translational control loop of MSFW rotor based on the negative displacement feedback.

The closed loop control system of translational motion as illustrated in Fig. 3.3. The translational displacement of the MSFW rotor is fed back to the control input. Through tuning the damping coefficient and the stiffness coefficient of the AMB system, the control system could generate the control currents through synthesizing control input between the reference input and the feedback displacement. The closed loop transfer function of translational motion could be expressed into

$$G_T(s) = \frac{k_e K_D s + k_e K_P - k_d}{ms^2 + k_e K_D s + k_e K_P - k_d} \tag{3.1}$$

where K_P is proportional coefficient for regulating the system stiffness. K_D is the derivative coefficient for tuning the system damping. k_e is the electromagnetic constant of the radial AMB as following

$$k_e = k_i k_w k_s \tag{3.2}$$

where k_a is the amplification coefficient of the current amplifier, and k_s is the sensitivity of the eddy current displacement sensor.

3.2.2 The Response of Translational Control Loop

TABLE. 3.I. Parameters of MSFW rotor system for the analysis of critical rotational frequency.

Parameter	Value	Unit
Radial current stiffness	k_{ix}=520	N/A
Radial displacement stiffness	k_{dx}=-2800	N/mm
Axial current stiffness	k_{iz}=500	N/A
Axial displacement stiffness	k_{dz}=-1700	N/mm
Nominal moment of inertia about z axis	J_z=1.43	kg·m^2
Nominal moment of inertial about x axis	J_x=6.21	kg·m^2
Nominal moment of inertial about y axis	J_y=6.21	kg·m^2
Nominal distance from center of mass to upper end	l_{um}=0.42622	m
Nominal distance from center of mass to lower end	l_{lm}=0.28378	m
Distance from center of mass to radial sensor at upper end	l_{us}=0.49222	m
Distance from center of mass to radial sensor at lower end	l_{ls}=0.30578	m
Sensitivity of displacement sensor	k_s=3.3	V/mm
Amplification coefficient	k_w=0.2	A/V
Rotor mass	m=150	kg

The frequency responses of the translational control loop with different values of the proportional coefficient K_P are plotted in Fig. 3.4(a) using the parameters of the MSFW rotor as listed in TABLE. 3.I. The response magnitude of the translational control loop increases with the proportional coefficient of translational control loop. On the other hand, the frequency responses of the translational control loop with different values of the derivative coefficient K_D are plotted in Fig. 3.4(b). The response magnitude of translational control loop is reduced with the derivative coefficient, so the translational vibration of MSFW rotor could be suppressed by tuning the derivative coefficient of translational control loop.

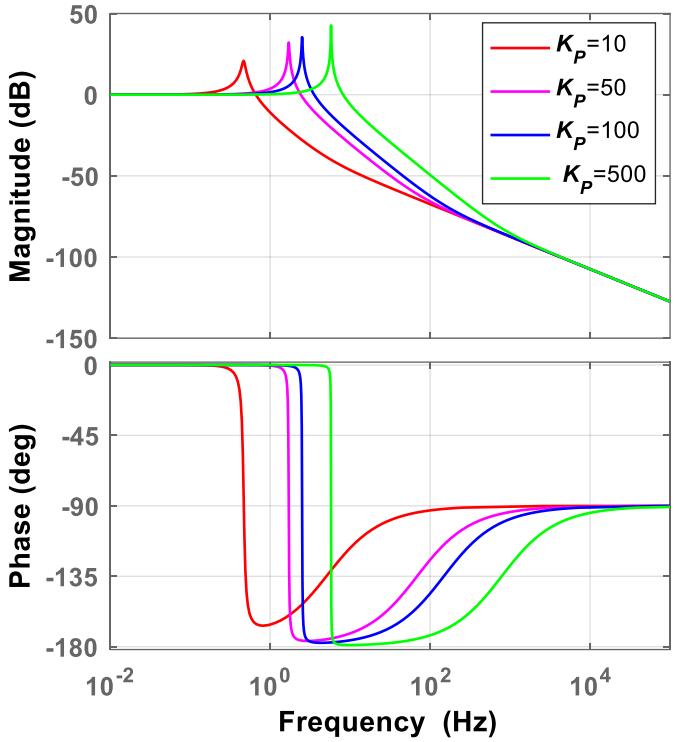

(a)

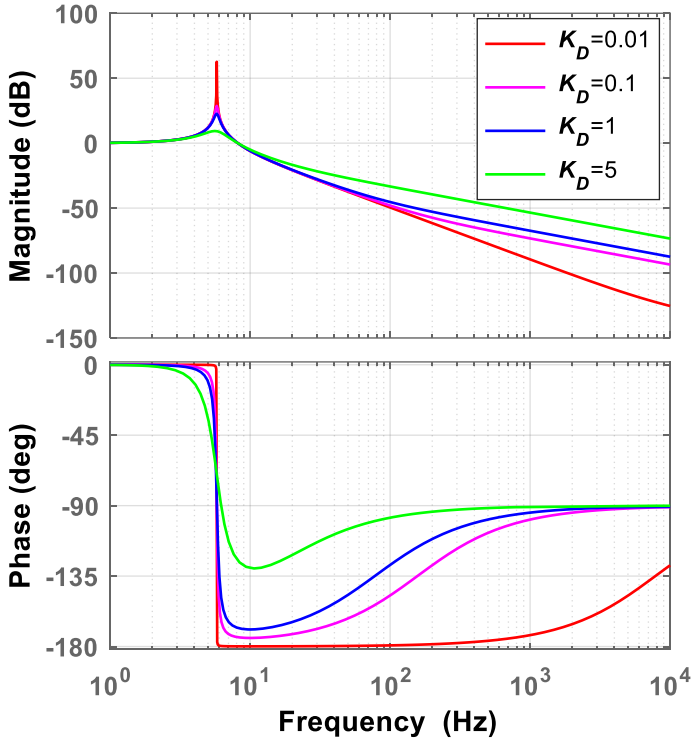

(b)

Fig. 3.4. The frequency responses of the translational control loop, (a) influence of the proportional coefficient of translational control loop, (b) influence of the derivative coefficient of translational control loop.

The relationship between the phase margin of translational control loop and the proportional coefficient K_P is plotted in Fig. 3.5(a). The phase margin of the translational control loop decreases with the proportional coefficient. It indicates that the stability of the translational control loop is weakened by improving the proportional coefficient of translational control loop. The relationship between the phase margin of translational control loop and the derivative coefficient K_D is plotted in Fig. 3.5(b). The phase margin is positively proportional to the derivative coefficient, so the stability of the translational control loop could be improved by increasing the derivative coefficient of the translational control loop.

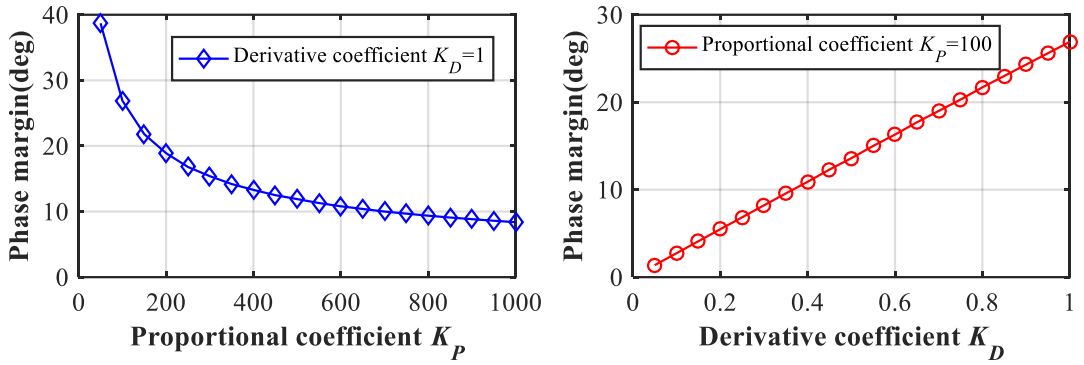

(a) (b)

Fig. 3.5. The phase margin of the translational control loop, (a) influence of the proportional coefficient, (b) influence of the derivative coefficient.

3.3 The Rotational Response Analysis of MSFW Rotor

3.3.1 The Modelling of Rotational Control Loop

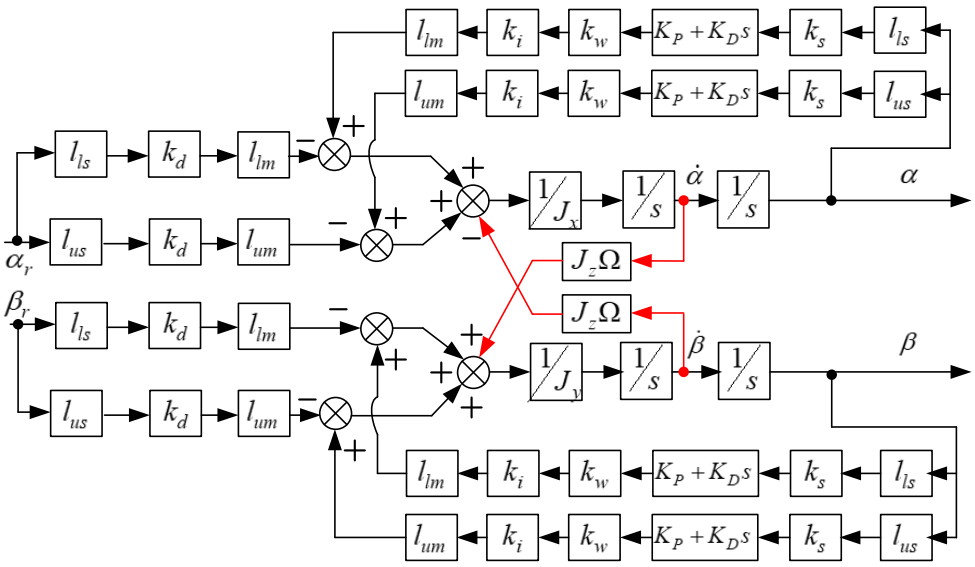

Fig. 3.6. The control scheme of the tilting motion of the MSFW rotor.

The control block diagram of the tilting motion of the MSFW rotor is shown in Fig. 3.6. The tilting angle of the MSFW rotor is fed back to the control input, and the tilting torques generated by the upper end and lower end radial AMBs control the tilting response of the MSFW rotor. The tilting angles about two radial axes are cross fed into the tilting control loop to suppress the influence caused by the gyroscopic coupling effect of the MSFW rotor at high speed.

The dynamic equations of the radial tilting about radial axes could be rewritten as

$$\begin{cases} J_y\ddot{\beta} - J_z\Omega\dot{\alpha} + k_d\left(l_{um}^2 + l_{lm}^2\right)\beta = -k_e\left(K_P\beta + K_D\dot{\beta}\right)\left(l_{um}l_{us} + l_{lm}l_{ls}\right) \\ J_x\ddot{\alpha} + J_z\Omega\dot{\beta} + k_d\left(l_{um}^2 + l_{lm}^2\right)\alpha = -k_e\left(K_P\alpha + K_D\dot{\alpha}\right)\left(l_{um}l_{us} + l_{lm}l_{ls}\right) \end{cases} \tag{3.3}$$

where l_{um} is the distance between the radial AMB at upper end and the mass center of the MSFW rotor, and l_{lm} is the distance between the radial AMB at lower end and the mass center of MSFW rotor. The damping coefficient and the stiffness coefficient of radial rotation could be written as the form of

$$\begin{cases} D_\alpha = D_\beta = k_e \left(l_{um} l_{us} + l_{lm} l_{ls} \right) K_D \\ K_c = k_e \left(l_{um} l_{us} + l_{lm} l_{ls} \right) K_P \\ K_\alpha = K_\beta = k_d \left(l_{um}^2 + l_{lm}^2 \right) \end{cases} \tag{3.4}$$

The tilting angle of the MSFW rotor in the complex form is defined as

$$\varphi(s) = \alpha(s) + \beta(s)\, j \tag{3.5}$$

The first equation of Eq.(3.3) is multiplied with the imaginary unit *j*, the dynamic function in complex field could be obtained by adding the result to second equation in Eq.(3.3). Given that the moment of inertia J_x=J_y and the rotational moment H=$J_z\Omega$, we could write

$$J_x \varphi(s) s^2 - jH\varphi(s) s + K_\alpha \varphi(s) = -\left[D_\alpha \varphi(s) s + K_c \varphi(s) \right] \tag{3.6}$$

Therefore, the equations of the radial rotations in Eq.(3.3) including the gyroscopic coupling terms and two rotational angles about radial axis could be simplified into a complex equation with single variable. Therefore, the stability analysis about radial rotation of MSFW rotor is equivalent to analyze a single complex equation with single variable. The characteristic function of the radial rotation of the MSFW rotor could be written as

$$J_x \lambda^2 + \left(D_\alpha - jH \right) \lambda + K_\alpha + K_c = 0 \tag{3.7}$$

The equivalent open-loop transfer function of the radial rotational control loop is

$$G_{ol}(s) = \frac{D_\alpha s + K_c}{J_x s^2 - jHs + K_\alpha} \tag{3.8}$$

When stiffness coefficient and damping coefficient of the radial AMB are used to regulate control the radial rotations of MSFW rotor, the open-loop transfer function of the radial rotation could be expressed as

$$G'_{ol}(s) = \frac{D_\alpha s + K_c}{J_x s^2 + \left(D_\alpha - jH \right) s + K_\alpha + K_c} \tag{3.9}$$

Furthermore, the frequency response functions for the positive frequency and the negative frequency could be derived and written as

$$\begin{cases} G_{ol}(j\omega)=\dfrac{jD_\alpha\omega+K_c}{-J_x\omega^2+H\omega+K_\alpha} \\ G_{ol}(-j\omega)=\dfrac{-jD_\alpha\omega+K_c}{-J_x\omega^2-H\omega+K_\alpha} \\ G'_{ol}(j\omega)=\dfrac{jD_\alpha\omega+K_c}{-J_x\omega^2+H\omega+K_\alpha+K_c+jD_\alpha\omega} \\ G'_{ol}(-j\omega)=\dfrac{-jD_\alpha\omega+K_c}{-J_x\omega^2-H\omega+K_\alpha+K_c-jD_\alpha\omega} \end{cases} \tag{3.10}$$

Moreover, the response magnitudes of the open-loop transfer function with the negative frequency and the positive frequency could be written as

$$\begin{cases} \left|G_{ol}(\omega)\right|=\dfrac{\sqrt{K_c^2+D_\alpha^2\omega^2}}{\left|-J_x\omega^2+H\omega+K_\alpha\right|} \\ \left|G_{ol}(-\omega)\right|=\dfrac{\sqrt{K_c^2+D_\alpha^2\omega^2}}{\left|-J_x\omega^2-H\omega+K_\alpha\right|} \\ \left|G'_{ol}(-\omega)\right|=\dfrac{\sqrt{K_c^2+D_\alpha^2\omega^2}}{\sqrt{\left(-J_x\omega^2+H\omega+K_\alpha+K_c\right)^2+D_\alpha^2\omega^2}} \\ \left|G'_{ol}(-\omega)\right|=\dfrac{\sqrt{K_c^2+D_\alpha^2\omega^2}}{\sqrt{\left(-J_x\omega^2-H\omega+K_\alpha+K_c\right)^2+D_\alpha^2\omega^2}} \end{cases} \tag{3.11}$$

The logarithmic response magnitudes of the open-loop transfer function with the negative frequency and the positive frequency could be written as

$$\begin{cases} L_{ol}(\omega)=20\log\left|G_{ol}(j\omega)\right| \\ L_{ol}(-\omega)=20\log\left|G_{ol}(-j\omega)\right| \\ L'_{ol}(\omega)=20\log\left|G'_{ol}(j\omega)\right| \\ L'_{ol}(-\omega)=20\log\left|G'_{ol}(j\omega)\right| \end{cases} \tag{3.12}$$

Therefore, the response curves of the MSFW rotor with the negative and positive frequencies could plotted, and then the stability criterion of the MSFW rotor could be developed according to the dual-frequency bode diagram [50].

3.3.2 The Stability Criterion of Rotational Control Loop

The classical frequency-based stability criterion for the SISO system only depends on the frequency response of the SISO system with the positive frequency, but the system response of the negative frequency should be considered for the system response of the complex transfer function with an imaginary part. Therefore, an equivalent stability criterion of the SISO system including an imaginary part is required to be established for the stability criterion of the SISO system with the negative frequency. This stability criterion is defined as dual frequency bode diagram analysis method. The stability criterion of the radial rotations of the MSFW rotor is used to verify the stability of the SISO system in Eq.(3.8) for both the negative frequency and the positive frequency. As illustrated in Fig. 3.7, the detailed steps of the stability criterion for the radial rotations are described in the following.

1, define the crossovers of negative-frequency and positive-frequency response curve. For the negative-frequency response curve, the crossover through $(2k+1)\pi$ from up-side to low-side is the positive crossover. For the positive-frequency response curve, the crossover through $(2k+1)\pi$ from low-side to up-side is the positive crossover.

2, get numbers of the open-loop poles located at the positive real part Q and numbers of the closed-loop poles located at the positive real part Z.

3, specify the crossover frequency (CF) when the gain margin (GM) $L(\omega)>0$ and $L(-\omega)>0$, the CF when $L(\omega)>0$ is ω_{pc}, and the CF when $L(-\omega)>0$ is ω_{nc}.

4, determine numbers of the phase margin (PM) $\varphi(-\omega)$ crossover $(2k+1)\pi$ within ω_{nc}, and numbers of positive crossover $(2k+1)\pi$ is n_{n+}, numbers of negative crossover $(2k+1)\pi$ is n_{n-}.

5, determine numbers of the PM $\varphi(\omega)$ crossover $(2k+1)\pi$ within ω_{pc}, and numbers of positive crossover $(2k+1)\pi$ is n_{p+}, numbers of negative crossover $(2k+1)\pi$ is n_{p-}.

6, get total numbers of crossover $(2k+1)\pi$, total number is $n= n_{p+}+n_{n-}-n_p-n_{n-}$.

7, If $Z=Q-n=0$, the response of BW and FW are both stable.

8, if $Z=Q-n\neq 0$, the stability of BW and FW would be judged, respectively. The stability of BW is judged by repeating step 2-7 when the frequency is smaller than the separating frequency,

and the stability of FW could be judged by repeating step 2-7 when the frequency is higher than the separating frequency.

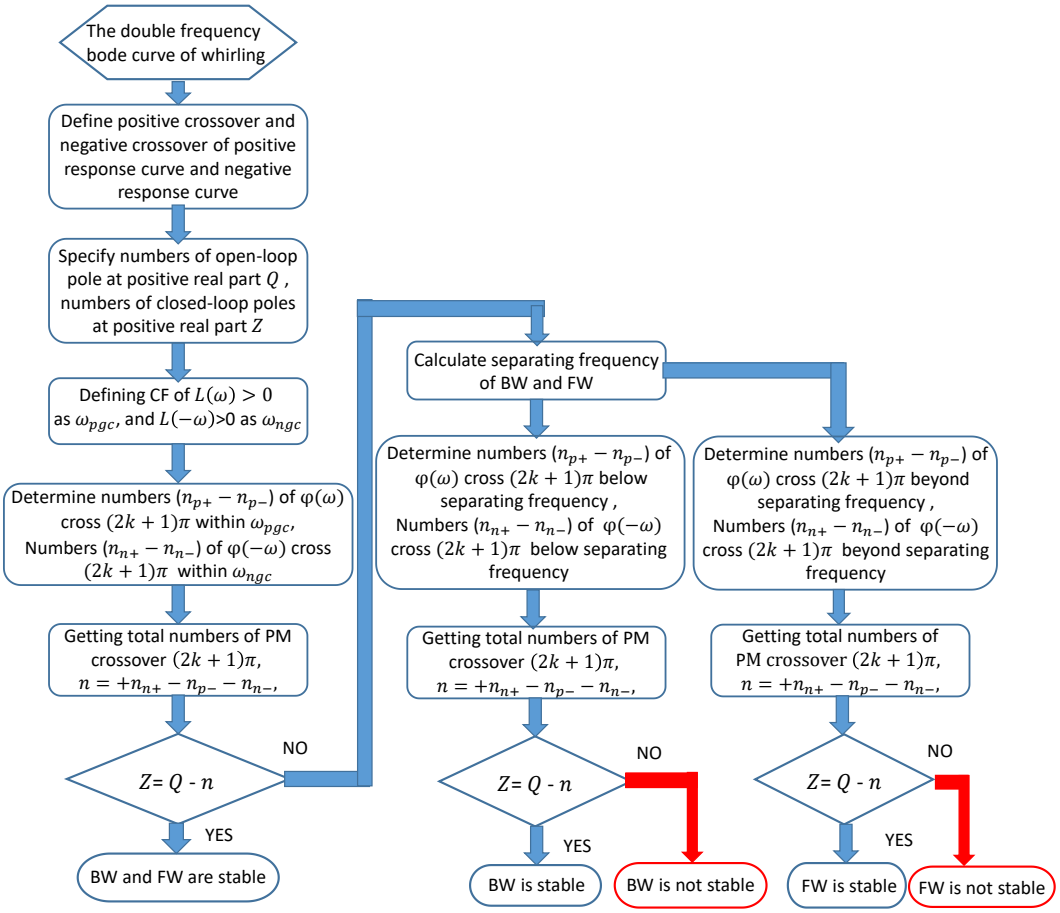

Fig. 3.7. The stability criterion of whirling characteristic of the MSFW rotor.

3.3.3 The Whirling Vibration of Rotational Control Loop

When the stiffness coefficient and the damping coefficient of the MSFW rotor are not introduced into the cross-feedback compensation of radial rotations, the frequency of the BW and the FW in Eq.(3.8) could be derived and written as

$$\begin{cases} \omega_{BW} = \dfrac{H - \sqrt{-4J_x k_d \left(l_{um}^2 + l_{lm}^2\right) - H^2}}{2J_x} \\ \omega_{FW} = \dfrac{H + \sqrt{-4J_x k_d \left(l_{um}^2 + l_{lm}^2\right) - H^2}}{2J_x} \end{cases} \tag{3.13}$$

If the stiffness coefficient and the damping coefficient of the MSFW rotor are applied, the frequency of the BW and the FW in Eq.(3.9) could be derived and written as

$$\begin{cases} \omega'_{BW} = \dfrac{D_\alpha + H - \sqrt{(D_\alpha + H)^2 - 4J_x(K_c + K_\alpha)}}{2J_x} \\ \omega'_{FW} = \dfrac{D_\alpha + H + \sqrt{(D_\alpha + H)^2 - 4J_x(K_c + K_\alpha)}}{2J_x} \end{cases} \tag{3.14}$$

The relationship between the frequencies of the BW and the FW and the moment of inertia ratio is shown in Fig. 3.8. It shows that the frequencies of the FW and the BW increase with the rotational frequency of the MSFW rotor. The frequency of the FW increases slowly with the rotational frequency of the MSFW rotor when the moment of inertia ratio sets at a great value in Fig. 3.8(a), and the frequency of the FW decreases with the moment of inertia ratio. As shown in Fig. 3.8(b), the frequency of the BW approaches to zero with the increase of the rotational frequency of the MSFW rotor, and it increases slowly with the moment of inertia ratio. Therefore, the frequency of the FW decreases with the moment of inertia ratio, and the frequency of the BW increases with the moment of inertia ratio.

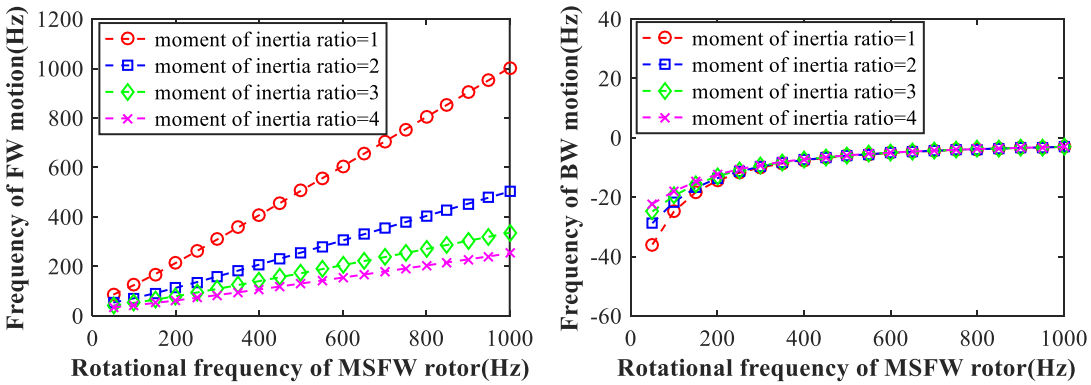

Fig. 3.8. The whirling frequency of the MSFW rotor versus the moment of inertia ratio, (a) the frequency of the FW, (b) the frequency of the BW.

Fig. 3.9 shows the relationship between the whirling frequency of the MSFW rotor and the suspension span ratio of the radial AMB. The initial frequency of the FW increases with the suspension span ratio of the radial AMB as shown in Fig. 3.9(a). The increasing rate of the FW frequency is constant even when the suspension span ratio of the radial AMB is set at different values. The relationship between the frequency of the BW and the suspension span ratio is shown in Fig. 3.9(b). The initial value of the BW frequency decreases with the suspension span

ratio. The frequency of the BW approaches to zero at high rotational frequency of the MSFW rotor.

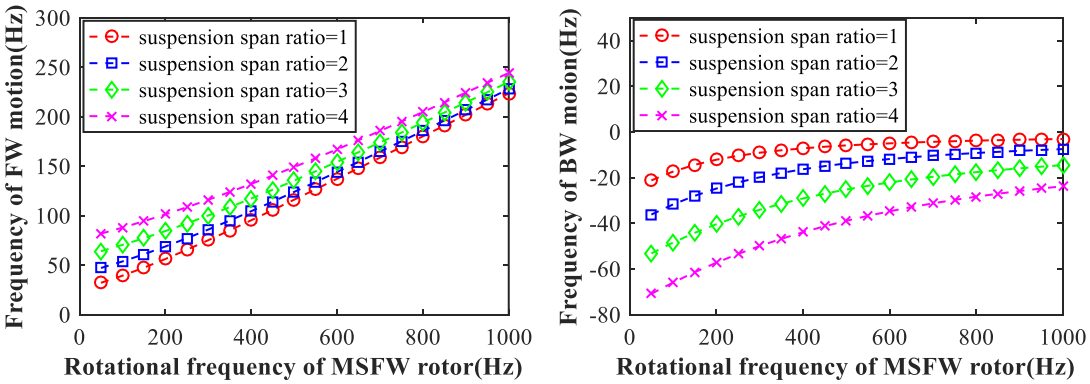

(a) (b)

Fig. 3.9 The whirling frequency of the MSFW rotor versus the suspension span ratio, (a) the frequency of the FW, (b) the frequency of the BW.

When the stiffness coefficient and the damping coefficient of the radial AMB are introduced in the cross-feedback compensation of the control loop, and the rotational frequency of the MSFW rotor is 200Hz, the relationships among the whirling frequency of the radial rotation, the damping coefficient and the stiffness coefficient are analyzed and plotted in Fig. 3.10. As shown in Fig. 3.10(a), the frequency of FW would be decreased by the stiffness coefficient, but it could be increased by the damping coefficient. Furthermore, the frequency of BW increases and approaches to zero with the increase of the damping coefficient and the stiffness coefficient.

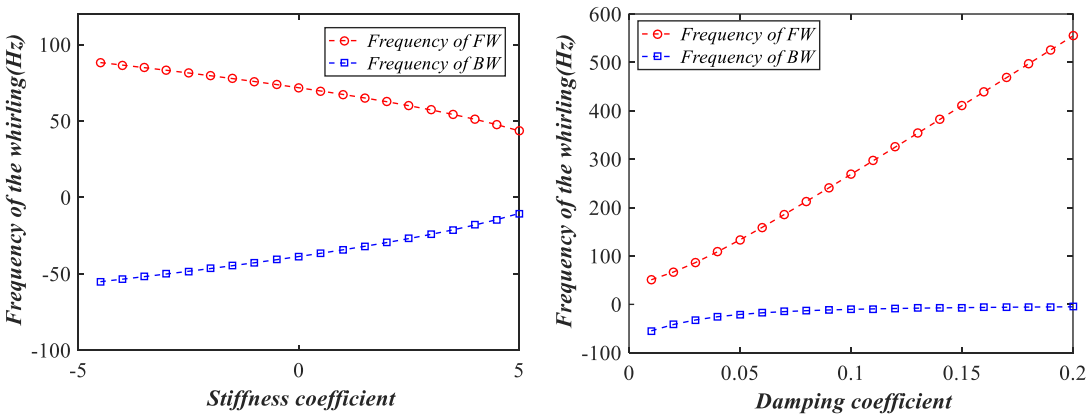

(a) (b)

Fig. 3.10. (a) The frequency of whirling versus the stiffness coefficient, (b) the frequency of whirling versus the damping coefficient.

Above all, the whirling frequencies of the MSFW rotor are affected by the moment of inertia ratio, the suspension span ratio of the radial AMB, the stiffness coefficient and the damping coefficient in the cross-feedback compensation of the radial AMB. The frequency of the FW is positively proportional to the moment of inertia ratio, the suspension span ratio and the damping coefficient in the cross-feedback compensation of the radial AMB. On the other hand, the frequency of the BW motion is positively proportional to the moment of inertia ratio and decreases with the increase of suspension span ratio in the cross-feedback compensation of the radial AMB.

3.3.4 The Critical Rotational Frequency of Rotational Control Loop

Using the denominator of Eq.(3.8), the solutions of the open-loop poles are

$$S_{olp} = \frac{jH \pm \sqrt{-4J_x k_d \left(l_{um}^2 + l_{lm}^2\right) - H^2}}{2J_x} \tag{3.15}$$

If $-4J_x k_d \left(l_{um}^2 + l_{lm}^2\right) - H^2 > 0$, the solutions of the open-loop poles could be written as the form of real number as following

$$S_{olp} = \frac{jH \pm \sqrt{-4J_x k_d \left(l_{um}^2 + l_{lm}^2\right) - H^2}}{2J_x} \tag{3.16}$$

If $-4J_x k_d \left(l_{um}^2 + l_{lm}^2\right) - H^2 < 0$, the solutions of the open-loop poles could be written as the form of imaginary number as following

$$S_{olp} = \frac{jH \pm j\sqrt{-4J_x k_d \left(l_{um}^2 + l_{lm}^2\right) - H^2}}{2J_x} \tag{3.17}$$

If $-4J_x k_d \left(l_{um}^2 + l_{lm}^2\right) - H^2 = 0$, the critical rotational frequency about the open-loop poles could be solved and written as

$$\omega_{n\varphi} = \frac{2\sqrt{-J_x k_d \left(l_{um}^2 + l_{lm}^2\right)}}{J_z} \tag{3.18}$$

The suspension span ratio of the radial AMBs is defined as $r_l = l_{lm}/l_{um}$, and the moment of inertia ratio is $r_j = J_x/J_z$. the critical rotational frequency in Eq.(3.18) could be rewritten as

$$\omega_{n\varphi} = \frac{2l_{um}\sqrt{J_z k_d r_j \left(1 + r_l^2\right)}}{J_z} \tag{3.19}$$

So, the critical rotational frequency of the MSFW rotor depends on the displacement stiffness k_d of the radial AMB, the moment of inertia ratio r_j and the suspension span ratio r_l. In general, the displacement stiffness of the radial AMB is designed and independent from the structural parameters of the MSFW rotor. Therefore, only the moment of inertia ratio r_j and suspension span ratio r_l are considered in the following analysis of the critical rotational frequency $\omega_{n\varphi}$.

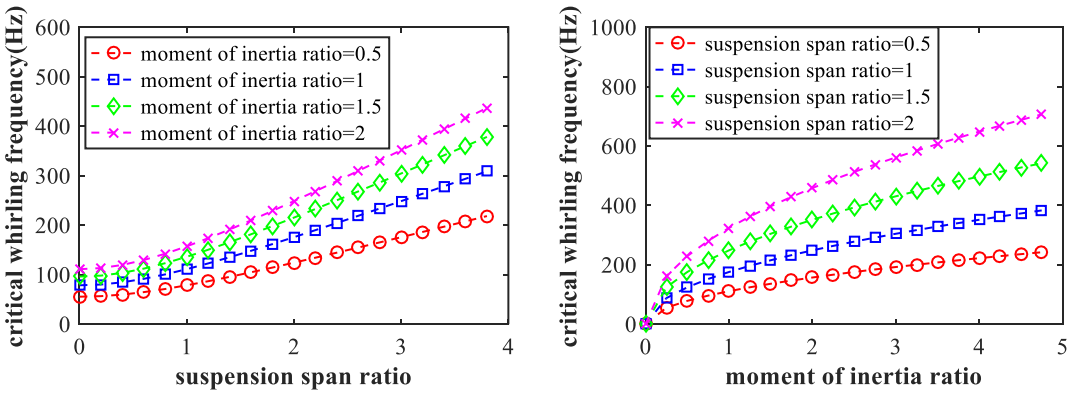

Fig. 3.11. (a) The critical rotational frequency versus the suspension span ratio, (b) the critical rotational frequency versus the moment of inertia ratio.

The relationship between the critical rotational frequency and the suspension span ratio is illustrated in Fig. 3.11(a). The critical rotational frequency of the MSFW rotor is 139Hz when the suspension span ratio is set at 0.5 and the moment of inertia ratio is 1, and it increases to 267Hz when the suspension span ratio increases to 1.9 with the same value of the moment of inertia ratio. It shows that the critical rotational frequency of the MSFW rotor increases with the suspension span ratio. As illustrated in Fig. 3.11(b), the critical rotational frequency of the MSFW rotor is about 176Hz when the suspension span ratio is 1 and the moment of inertia ratio

is 1. The critical rotational frequency increases to 352Hz when the moment of inertia ratio increase to 4 with the same value of the suspension span ratio. Therefore, the critical rotational frequency of the MSFW rotor is affected by the variation of moment of inertia ratio.

3.4 The Open-loop Pole Distribution of Rotational Control Loop

3.4.1 The Open-loop Pole versus Moment of Inertia Ratio

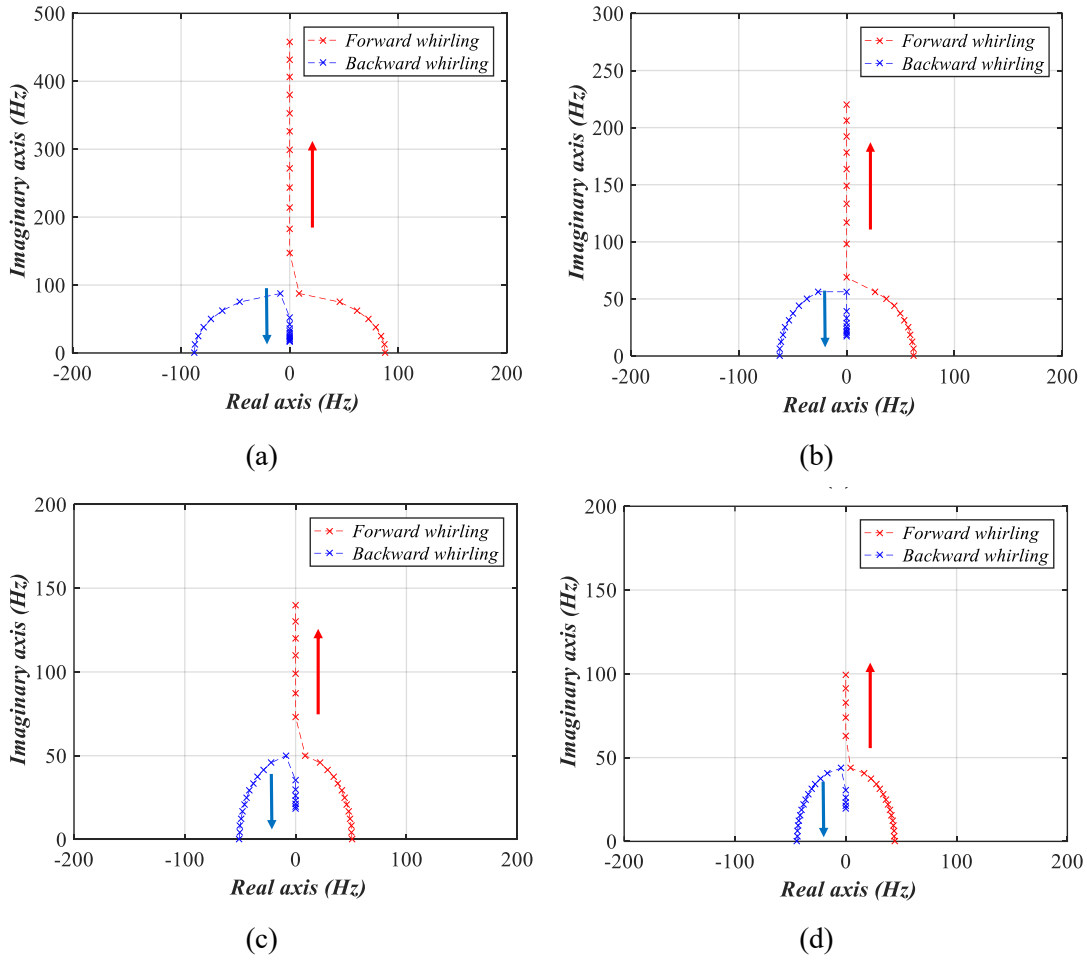

Fig. 3.12. The open-loop pole versus the moment of inertia ratio when the rotational frequency is lower than 500Hz, (a) the moment of inertia ratio is 1, (b) the moment of inertia ratio is 2, (c) the moment of inertia ratio is 3, (d) the moment of inertia ratio is 4.

According to the calculation in Eq.(3.15) and Eq.(3.16), the relationship between the distribution of the open-loop poles and the moment of inertia ratio is plotted in Fig. 3.12. The suspension span of the MSFW rotor is assumed to be a symmetrical structure, so the suspension span ratio of the radial AMB is sets at 1. The direction of the arrow in Fig. 3.12 indicates the

increasing direction of the rotational frequency. When the rotational frequency of the MSFW rotor is greater than the critical rotational frequency, the open-loop poles bifurcate into the increasing part as shown by the red cross and the decreasing part as shown by the blue cross. Moreover, the increasing part shown by the red dash line is the frequency locus of the FW, and the decreasing part marked by the blue dash line is the frequency locus of the BW motion.

In Fig. 3.12(a), when the moment of inertia ratio is 1, the furcation of the whirling motion occurs at 100Hz. The critical rotational frequency of the MSFW rotor is about 175.89Hz which is very close to the furcation frequency. When the moment of inertia ratio increases to 4, the critical rotational frequency of the MSFW rotor is about 351.77Hz, but the furcation of the whirling motion happens at 43.75Hz. Therefore, the critical rotational frequency of the MSFW rotor increases with an increase of moment of inertia ratio but the furcation frequency decreases with an increase of the moment of inertia ratio. Moreover, as listed in TABLE. 3.II, the frequency of the FW declines with an increase of moment of inertia ratio, and the frequency of the BW motion increases with an increase of moment of inertia ratio at a lower rate. Therefore, the frequency bandwidth between the BW and the FW motions could be enlarged by increasing the moment of inertia ratio.

TABLE. 3.II. Frequency of the whirling versus the moment of inertia ratio.

Moment of inertia ratio	1	2	3	4
Critical rotational frequency (Hz)	175.89	248.74	304.65	351.77
Furcation frequency (Hz)	100	62.5	54.16	43.75
Frequency of BW motion (Hz)	16.88	17.88	18.43	19.48
Frequency of FW (Hz)	458.1	219.9	139.9	99.27
Bandwidth (Hz)	441.22	202.02	121.47	79.79

3.4.2 The Open-loop Pole versus Suspension Span Ratio

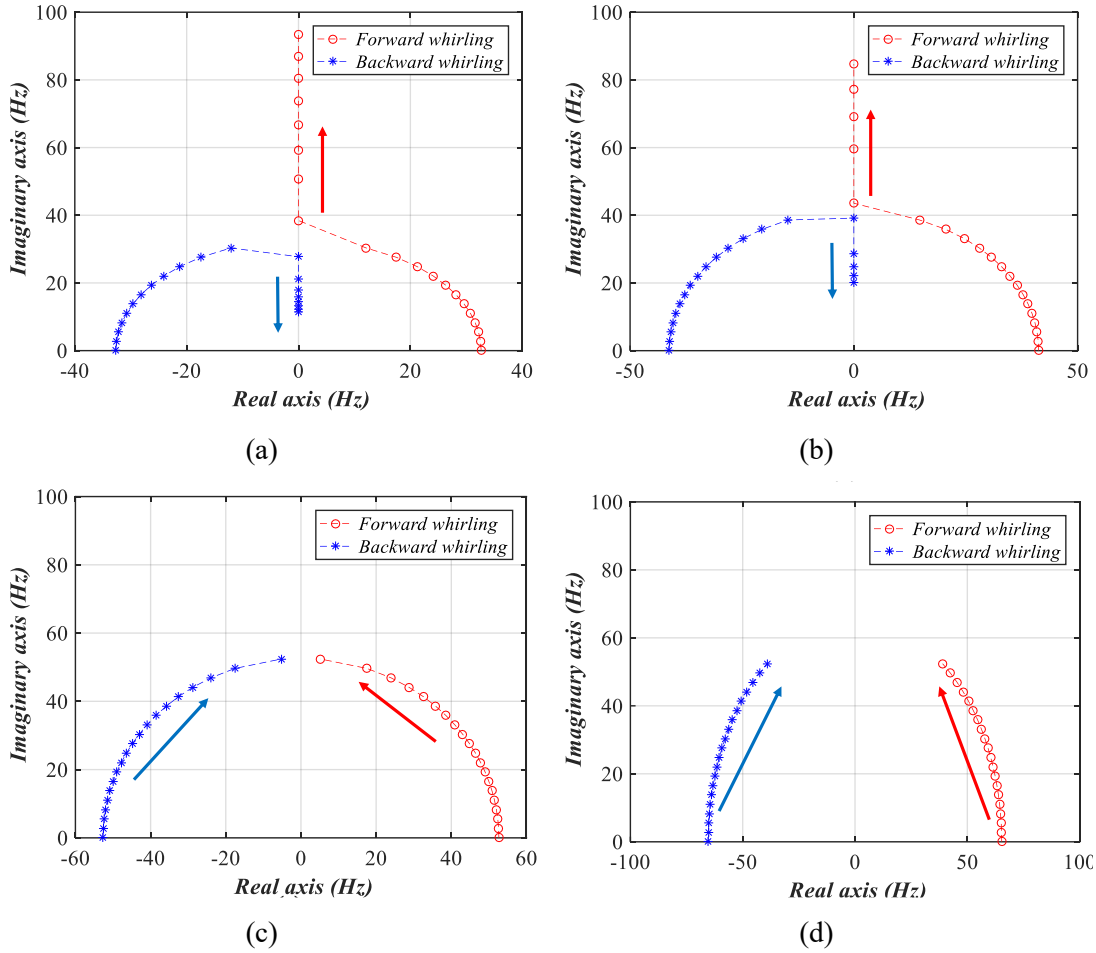

Fig. 3.13. The open-loop pole with the suspension span ratio when the rotational frequency is lower than 500Hz, (a) the suspension span ratio is 0.5, (b) the suspension span ratio is 1, (c) the suspension span ratio is 1.5, (d) the suspension span ratio is 2.

The relationship between the distribution of the open-loop poles and the suspension span ratio of the radial AMBs is plotted in Fig. 3.13. Like Fig. 3.12, the blue star line is the frequency locus of the BW motion, and the red circle line is the frequency locus of the FW. When the rotational frequency of the MSFW exceeds the critical rotational frequency, the whirling motion of the MSFW rotor bifurcates into the FW and the BW motion at the critical rotational frequency. As illustrated in Fig. 3.13(a), the critical rotational frequency of the MSFW rotor is about 296.05Hz when the suspension span ratio is set at 0.5. The furcation of the FW (red line) and the BW motion (blue line) starts at 33.1Hz. Moreover, the critical rotational frequency of the MSFW rotor increases to 592.09Hz when the suspension span ratio increases to 2 as shown in Fig. 3.13(d). The FW and the BW motion do not bifurcate on distribution of the open-loop poles

because the rotational frequency of the MSFW rotor is lower than the critical rotational frequency. Therefore, the suspension span ratio of the radial AMBs affects the critical rotational frequency of the MSFW rotor. Moreover, as listed in TABLE. 3.III, the frequency of the FW decreases with an increase of the suspension span ratio, but the frequency of the BW motion increases with an increase of the suspension span ratio. So, the frequency bandwidth between the BW motion and the FW could be enlarged by increasing the moment of inertia ratio.

TABLE. 3.III. Frequency of the whirling versus the suspension span ratio.

Suspension span ratio	0.5	1	1.5	2
Critical rotational frequency (Hz)	296.05	374.47	477.36	592.09
Furcation frequency (Hz)	33.1	41.36	null	null
Frequency of BW motion (Hz)	11.42	20.16	null	null
Frequency of FW (Hz)	93.34	84.63	null	null
Bandwidth (Hz)	81.92	64.47	null	null

The analysis shows that the whirling vibration of the MSFW rotor could be avoidable by increasing the moment of inertia ratio and the suspension span ratio. Moreover, the frequency of the FW could be reduced by increasing the moment of inertia ratio and the suspension span ratio, and the frequency of the BW motion could be increased by increasing the moment of inertia ratio and the suspension span ratio.

3.5 Frequency Response of Rotational Control Loop

3.5.1 The Frequency Response of Rotation versus Moment of Inertia Ratio

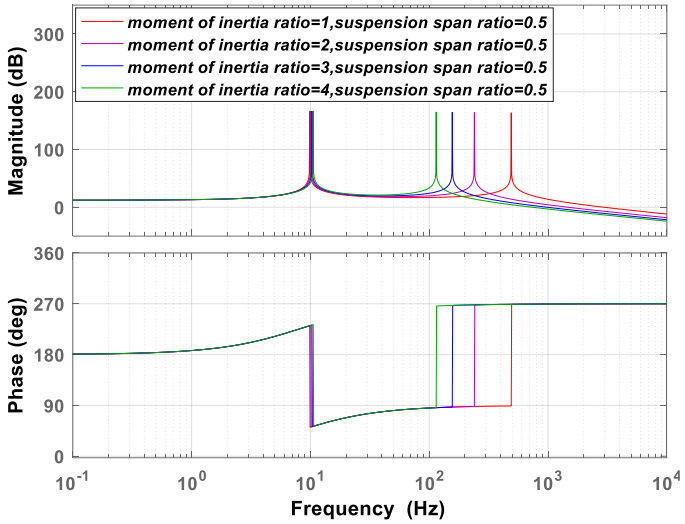

(a)

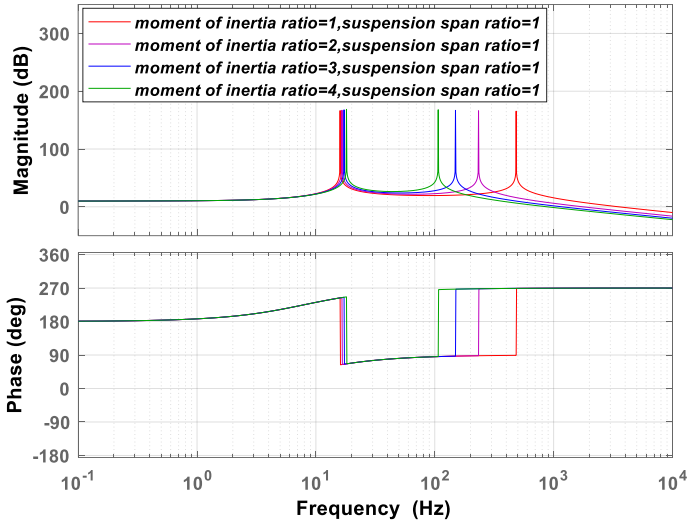

(b)

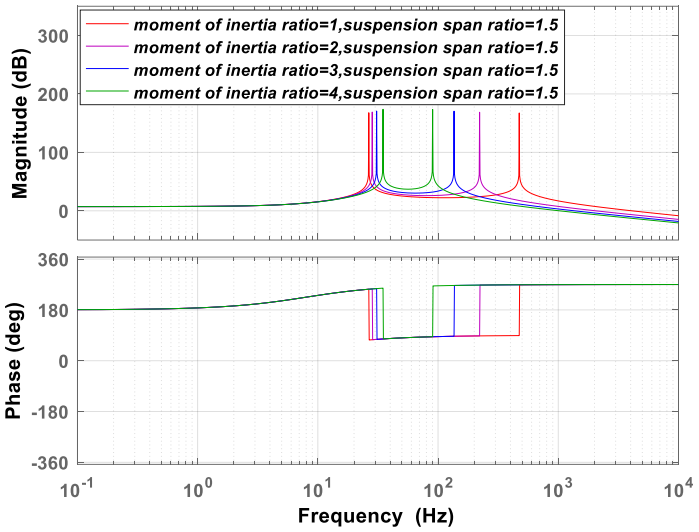

(c)

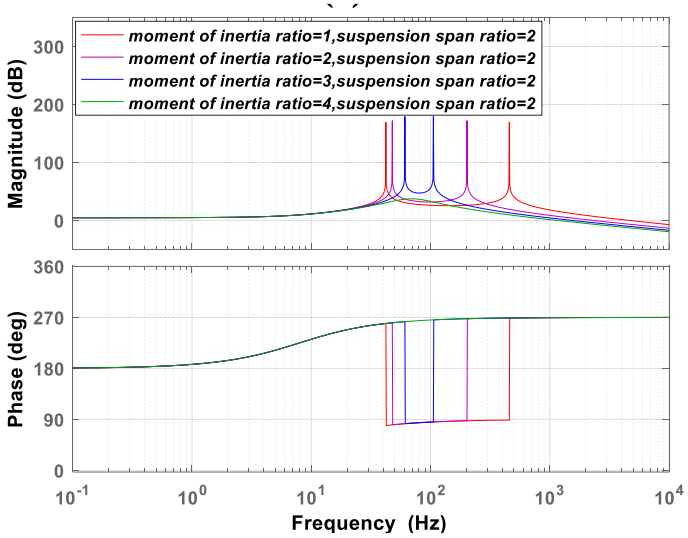

(d)

Fig. 3.14. The frequency response curves of the rotation versus the moment of inertia ratio, (a) the suspension span ratio is 0.5, (b) the suspension span ratio is 1, (c) the suspension span ratio is 1.5, (d) the suspension span ratio is 2.

The relationship between the frequency response of the rotational control loop and the moment of inertia ratio is illustrated in Fig. 3.14 with the rotational frequency of the MSFW rotor at 500Hz. At the beginning, the suspension span ratio is 0.5 and the moment of inertia ratio is 1. The frequency response of the radial rotation in Fig. 3.14(a) shows that there are two response peaks, the peak amplitude at lower frequency is the response amplitude of the BW motion while the peak amplitude at higher frequency is the response amplitude of the FW motion. The response frequency of the BW motion is about 9.86Hz, and the response frequency of the FW is about 491Hz. The frequency bandwidth between the FW and the BW motion is

therefore about 481.14Hz. When the moment of inertia increases to 4 and the suspension span ratio is kept at 0.5, the frequency response of the radial rotation is represented by the green line in Fig. 3.14(a). The response frequency of the BW motion is about 10.6Hz, and the response frequency of the FW is about 114Hz. Hence the frequency bandwidth between the BW motion and the FW is about 103.4Hz. It indicates that the response frequency of the BW motion increases slowly with the moment of inertia ratio, but the response frequency of the FW decreases sharply with the moment of inertia ratio.

Fig. 3.14(b) shows that the response frequency of the BW motion is about 18.1Hz and that of FW is about 107Hz when the moment of inertia ratio is 4 and the suspension span ratio is 1. As shown in Fig. 3.14(c), the response frequency of the FW decreases to 90.1Hz, and the response frequency of the BW increases to 18.1Hz when the moment of inertia ratio is 4 and the suspension span ratio increases to 1.5. In Fig. 3.14(d), when the moment of inertia ratio is 4 and the suspension span ratio is 1.5, the furcation of the whirling does not occur because the critical rotational frequency of the MSFW rotor is greater than the rotational frequency of the MSFW rotor. Thence, the response frequency of the FW increases slowly with the suspension span ratio, and the response frequency of the BW also increases with the suspension span ratio. Therefore, the frequency bandwidth between the response frequency of the FW and that of the BW decreases with the suspension span ratio.

TABLE. 3.IV. Frequency of whirling versus moment of inertial ratio when suspension span ratio is 0.5.

Moment of inertia ratio	1	2	3	4
Critical rotational frequency (Hz)	139.05	196.65	240.84	278.1
Frequency of BW motion (Hz)	9.86	10.1	10.3	10.6
Frequency of FW (Hz)	490	240	156	114
Frequency bandwidth (Hz)	480.14	229.9	145.7	103.4

TABLE. 3.V. Frequency of whirling versus moment of inertial ratio when suspension span ratio is 1.

Moment of inertia ratio	1	2	3	4
Critical rotational frequency (Hz)	175.89	248.74	304.65	351.77
Frequency of BW motion (Hz)	16	16.6	17.3	18.1
Frequency of FW (Hz)	484	233	149	107
Frequency bandwidth (Hz)	468	216.4	131.7	88.9

TABLE. 3.VI. Frequency of whirling versus moment of inertial ratio when suspension span ratio is 1.5.

Moment of inertia ratio	1	2	3	4
Critical rotational frequency (Hz)	224.1	317.09	388.35	448.43
Frequency of BW motion (Hz)	26.5	28.4	30.8	34.9
Frequency of FW (Hz)	473	222	136	90.1
Frequency bandwidth (Hz)	446.5	193.6	105.2	55.2

TABLE. 3.VII. Frequency of whirling versus moment of inertial ratio when suspension span ratio is 2.

Moment of inertia ratio	1	2	3	4
Critical rotational frequency (Hz)	278.1	351.77	430.83	556.21
Frequency of BW motion (Hz)	42.2	47.8	61	null
Frequency of FW (Hz)	458	202	106	null
Frequency bandwidth (Hz)	415.8	154.2	45	null

3.5.2 The Frequency Response of Rotation versus Suspension Span Ratio

Moreover, based on the whirling frequency data in TABLE. 3.IV, TABLE. 3.V, TABLE. 3.VI and TABLE. 3.VII, the relationship among the response frequency of the BW MOTION, the moment of inertia ratio and the suspension span ratio are plotted in Fig. 3.15. It shows that the response frequency of the BW motion increases with the suspension span ratio, and the response frequency of the BW motion also increases with the suspension span ratio. The relationship among the response frequency of the FW motion, the moment of inertia ratio and the suspension span ratio are shown in Fig. 3.16. The response frequency of the FW motion decreases slowly with the increase of the suspension span ratio, and the response frequency of the FW motion decreases quickly with the increase of the moment of inertia ratio. Finally, the frequency bandwidth between the response frequency of the BW MOTION and the FW motion is plotted in Fig. 3.17. This result indicates that the frequency bandwidth decreases with the suspension span ratio and the moment of inertia ratio, so the bifurcation of the BW motion and the FW motion would appear easily when the MSFW motion rotor has a small value of the suspension span ratio.

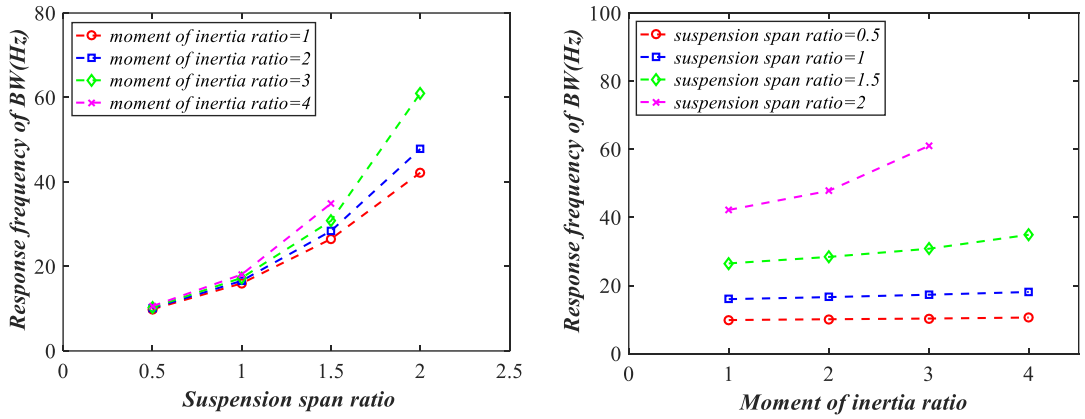

(a) (b)

Fig. 3.15. The response frequency of the BW motion, (a) the response frequency of the BW motion versus the suspension span ratio, (b) the response frequency of the BW motion versus the moment of inertia ratio.

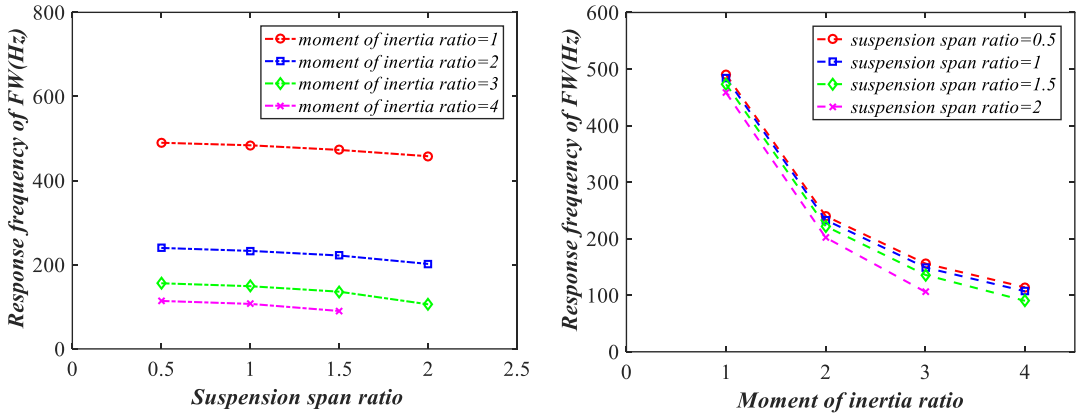

(a) (b)

Fig. 3.16. The response frequency of the FW motion, (a) the response frequency of the FW motion versus the suspension span ratio, (b) the response frequency of the FW motion versus the moment of inertia ratio.

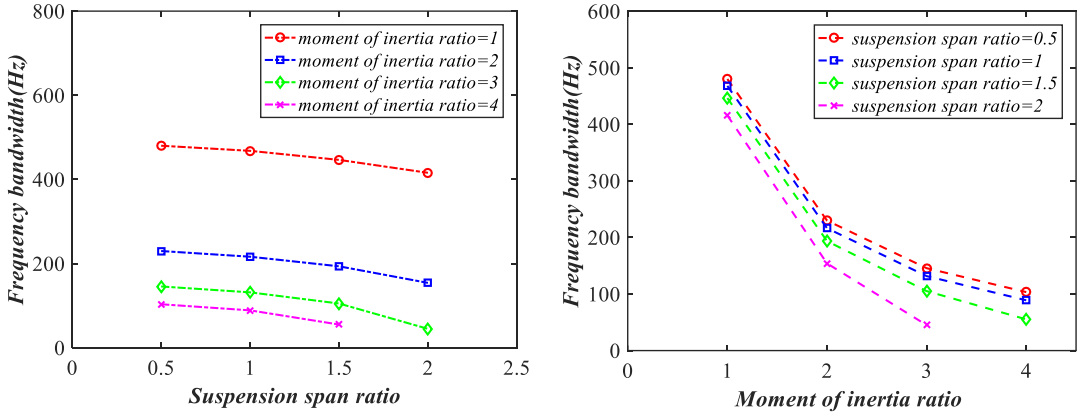

(a) (b)

Fig. 3.17. The frequency bandwidth between the BW motion and the FW motion, (a) the frequency bandwidth versus the suspension span ratio, (b) the frequency bandwidth versus the moment of inertia ratio.

3.6 The Stability Criterion of MSFW Rotor

3.6.1 The Stability of Rotation versus Moment of Inertia Ratio

This part is to testify the stability criterion of the whirling with influence of the moment of inertia ratio. When the rotational frequency of the MSFW rotor sets at 500Hz and the suspension span ratio of the radial AMB sets at 1, the frequency responses of the whirling with different moment of inertia ratios are illustrated in Fig. 3.18. For the response curves of the whirling of the MSFW rotor in Fig. 3.18 (a), the critical whirling frequency is 111Hz, there are

$$\begin{cases} Q = 0 \\ n = 0.5 + 1.5 - 1 - 0 = 1 \\ Z = Q - n \neq 0 \end{cases} \tag{3.20}$$

The whirling of the MSFW rotor is not stable.

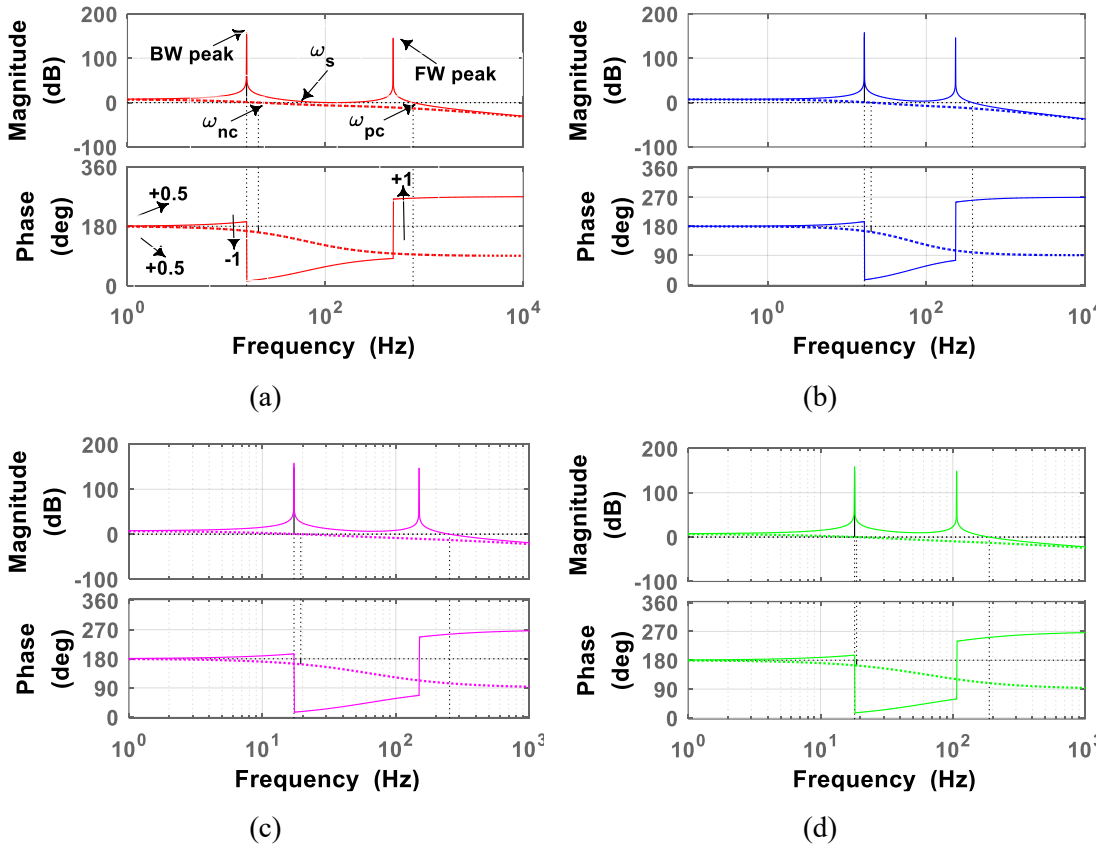

Fig. 3.18.The response curves of the whirling with the positive and negative frequency, (a) the suspension span ratio is 1 and the moment of inertia ratio is 1, (b) the suspension span ratio is 1 and the moment of inertia ratio is 2, (c) the suspension span ratio is 1 and the moment of inertia ratio is 3, (d) the suspension span ratio is 1 and the moment of inertia ratio is 4.

Furthermore, the separating frequency between the BW motion and the FW motion is 56Hz, the frequency range lower than the separating frequency is defined as the low-frequency range while the frequency range higher than the separating frequency is defined as the high-frequency range. The stability of the BW motion is judged within the frequency range lower than the separating frequency, and the stability of the FW motion is judged within the frequency range higher than the separating frequency. In detail, for the frequency range lower than the separating frequency, there are

$$\begin{cases} Q = 0 \\ n = 0.5 + 0.5 - 0 - 1 = 0 \\ Z = Q - n = 0 \end{cases} \tag{3.21}$$

The BW motion of the FW motion rotor is stable.

When the rotational frequency of the MSFW rotor is higher than the separating frequency of the BW motion and the FW motion, we have

$$\begin{cases} Q = 0 \\ n = 0 + 1 - 0 - 0 = 1 \\ Z = Q - n \neq 0 \end{cases} \tag{3.22}$$

So, the FW motion of the MSFW rotor is not stable.

When the suspension span ratio increases from 0.5 to 2, the stability status of the whirling is same as the case in Fig. 3.18(a). Consequently, the suspension span ratio of the radial AMBs at upper end and lower end does not cause serious influence on the stability of whirling of the MSFW rotor, but it affects the critical rotational frequency of the MSFW rotor.

3.6.2 The Stability of Rotation versus Suspension Span Ratio

This section is to test the stability criterion of the rotational motion of the MSFW rotor with the influence of the moment of inertia ratio. The frequency response curves of the radial motion with the suspension span ratio increases from 0.5 to 2 are calculated and plotted in Fig. 3.19. The rotational frequency of the MSFW rotor is assumed to be 500Hz and the moment of inertia ratio to be 1. In Fig. 3.19(a), the critical rotational frequency of the MSFW rotor is 236Hz, there are

$$\begin{cases} Q = 0 \\ n = 0.5 + 1.5 - 1 - 0 = 1 \\ Z = Q - n \neq 0 \end{cases} \tag{3.23}$$

The whirling of the MSFW rotor is not stable.

Moreover, the separating frequency of the BW motion and FW motion is 26Hz. The frequency range lower than the 26Hz is defined as the low-frequency range, the frequency range higher than the 26Hz is the high-frequency range. When the frequency of the MSFW rotor is lower than the separating frequency of the BW motion and the FW motion, we have

$$\begin{cases} Q = 0 \\ n = 0.5 + 0.5 - 0 - 1 = 0 \\ Z = Q - n = 0 \end{cases} \tag{3.24}$$

The BW motion of the MSFW rotor is stable.

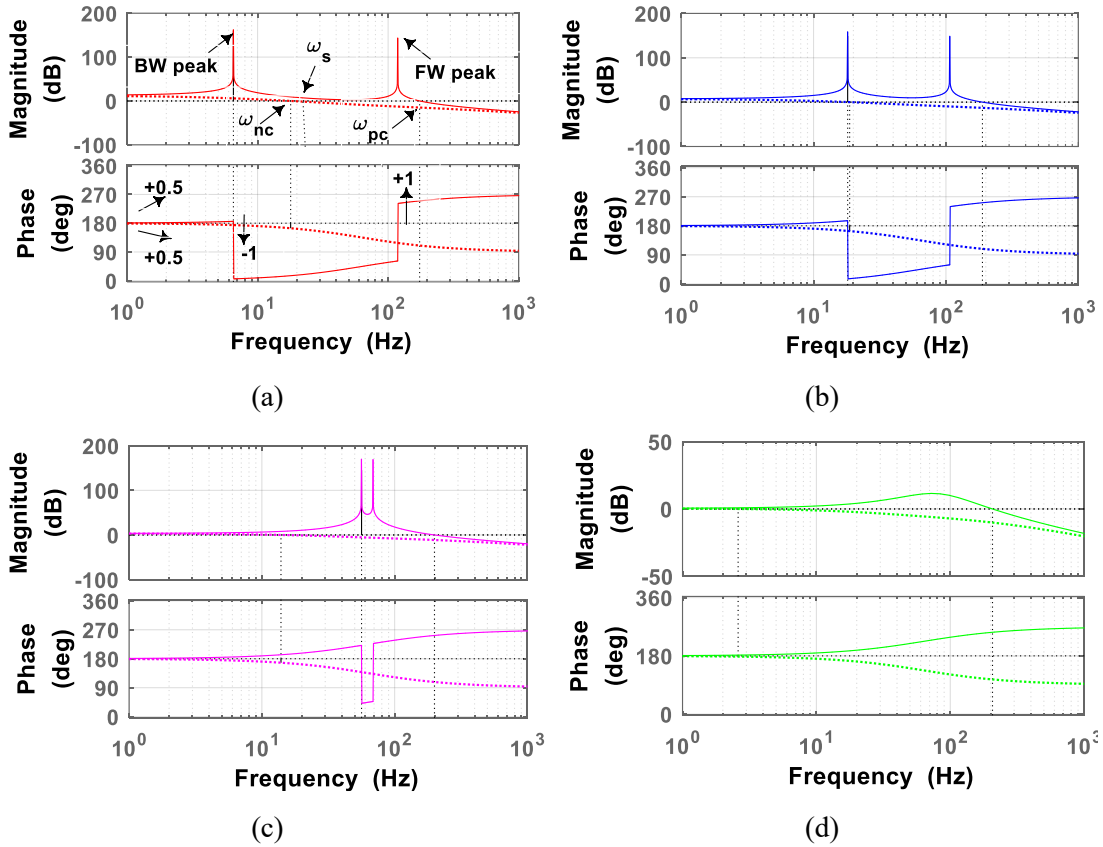

Fig. 3.19. The response curves of the whirling with the positive and negative frequency, (a) the suspension span ratio is 0.5 and the moment of inertia ratio is 4, (b) the suspension span ratio is 1 and the moment of inertia ratio is 4, (c) the suspension span ratio is 1.5 and the moment of inertia ratio is 4, (d) the suspension span ratio is 2 and the moment of inertia ratio is 4.

When the rotational frequency of the MSFW rotor is higher than the separating frequency of the BW motion and the FW motion, we have

$$\begin{cases} Q = 0 \\ n = 0 + 1 - 0 - 0 = 1 \\ Z = Q - n \neq 0 \end{cases} \tag{3.25}$$

The FW motion of the MSFW rotor is not stable.

As shown in Fig. 3.19(d), the critical rotational frequency of the MSFW rotor is 690Hz. The rotational frequency of the MSFW rotor is lower than the critical rotational frequency. We have

$$\begin{cases} Q = 1 \\ n = 0.5 + 0.5 - 0 - 0 = 1 \\ Z = Q - n = 0 \end{cases} \tag{3.26}$$

The FW motion and the BW motion of the MSFW rotor are both stable.

Therefore, for the MSFW rotor, the moment of inertia ratio could affect the stability of whirling motion, and the stability of whirling motion increases with the moment of inertia ratio. Moreover, the stability of whirling motion could be improved by increasing the suspension span ratio, and so the unstable vibration of the FW motion and the BW motion could be avoidable. In addition, the unstable high-frequency vibration of the FW motion easily occurs compared with the low-frequency vibration of the BW motion.

3.6.3 The Stability of Rotation versus Rotational Frequency

With the moment of inertia ratio set at 4 and the suspension span ratio set at 1, the frequency responses of the rotational motion at different rotating frequencies are calculated and plotted in Fig. 3.20. Because there are no gyroscopic coupling terms when the rotational frequency of the MSFW rotor is 0Hz, the response curve of the positive frequency is consistent with that of the negative frequency as shown in Fig. 3.20(a). When the rotational frequency of the MSFW rotor is not 0Hz, the response curves of the radial rotation for the positive frequency and the negative frequency are different as shown in Fig. 3.20(b) to (d).

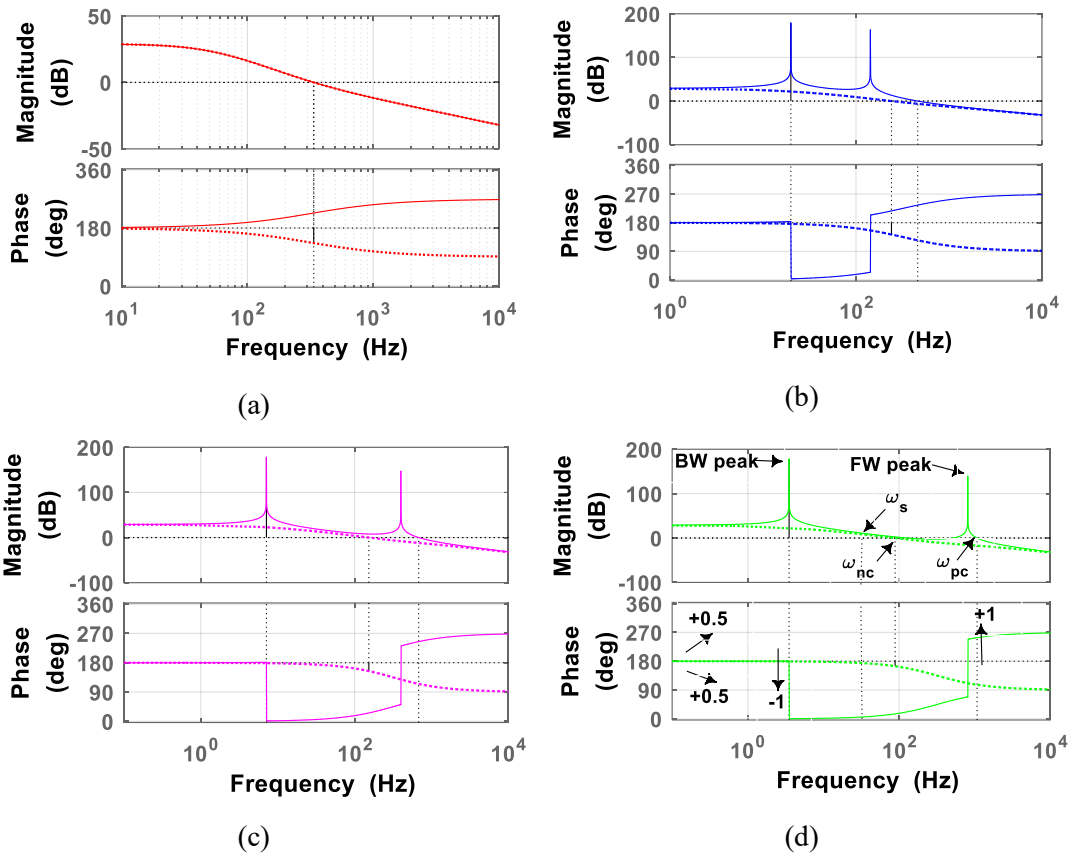

Fig. 3.20. The response curves for the positive and negative frequency, (a) the rotational frequency is 0, (b) the rotational frequency is 200Hz, (c) the rotational frequency is 500Hz, (d) the rotational frequency is 1000Hz.

Therefore, the stability criterion for the rotational motion could be described as following:

When the rotating frequency of MSFW rotor is 0Hz in Fig. 3.20(a), we have

$$\begin{cases} Q = 1 \\ n = 0.5 + 0.5 - 0 - 0 = 1 \\ Z = Q - n = 0 \end{cases} \tag{3.27}$$

The whirling of the MSFW rotor is stable.

When the rotational frequency of the MSFW rotor increases to 200Hz in Fig. 3.20(b), we have

$$\begin{cases} Q = 1 \\ n = 0.5 + 0.5 - 0 - 0 = 1 \\ Z = Q - n = 0 \end{cases} \tag{3.28}$$

The whirling of the MSFW rotor is still stable.

When the rotating frequency of MSFW rotor is 500Hz in Fig. 3.20(c), we have

$$\begin{cases} Q = 0 \\ n = 0.5 + 1.5 - 0 - 1 = 1 \\ Z = Q - n \neq 0 \end{cases} \tag{3.29}$$

The whirling of the MSFW rotor n is not stable.

The separating frequency of BW motion and FW motion is 43.97Hz. The frequency range lower than the 43.97Hz is defined as the low-frequency range, and the frequency range higher than the 43.97Hz is defined as the high-frequency range. When the frequency of the MSFW rotor is lower than the separating frequency of the BW motion and the FW motion, we have

$$\begin{cases} Q = 0 \\ n = 0.5 + 0.5 - 0 - 1 = 0 \\ Z = Q - n = 0 \end{cases} \tag{3.30}$$

The BW motion of the MSFW rotor is stable.

When the rotating frequency of MSFW rotor is higher than the separating frequency, we have

$$\begin{cases} Q = 0 \\ n = 0 + 1 - 0 - 0 = 1 \\ Z = Q - n \neq 0 \end{cases} \tag{3.31}$$

The FW motion of the MSFW rotor is not stable.

Fig. 3.20(d) shows that the rotational frequency of the MSFW rotor is 1000Hz, the stability status of whirling of the MSFW rotor is same as the stability status of the MSFW rotor at 500Hz. Therefore, the stability of whirling would be weakened by increasing the rotational speed of the MSFW rotor. Specially, the stability of the FW motion is easily affected by the rotational speed of the MSFW rotor.

3.7 The Experimental Verification

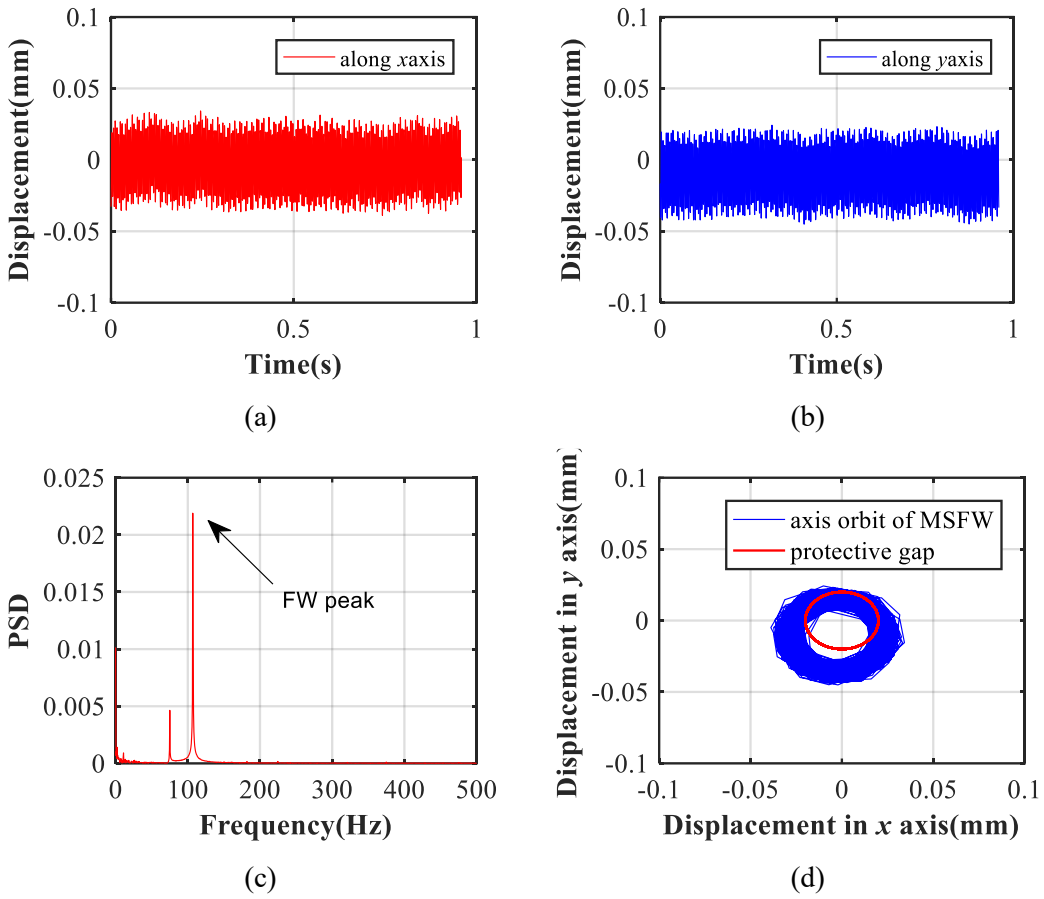

Fig. 3.21. The dynamic displacements of the MSFW rotor when suspension span ratio is 0.5, (a) dynamic displacements along *x* axis, (b) dynamic displacements along *y* axis, (c) the PSD of dynamic displacement, (d) the axis orbit of the MSFW rotor.

Based on the experimental setup in Fig. 2.18, when the suspension span ratio sets at 1 and the rotational frequency sets is 400Hz, the displacement deflections of the MSFW rotor along *x* and *y* axis are plotted in Fig. 3.21. The maximum displacement deflection of the MSFW rotor is about 0.027mm, which is greater than the protective gap, so the whirling of the MSFW rotor is not stable. Furthermore, the power spectrum density (PSD) of the dynamic displacements along *x* axis is shown in Fig. 3.21(c), the peak amplitude at 106Hz is the vibration amplitude of the FW motion, and this result is quietly close to the FW frequency (93.34Hz) in TABLE. 3.III. The axis orbit of the MSFW rotor is illustrated in Fig. 3.21(d), the red-line cycle presents the protective airgap (0.02mm) of the MSFW rotor, and the blue-line cycle is the real-time axis orbit of the MSFW rotor, it shows that the axis orbit of the MSFW rotor had exceeded the

protective gap. Therefore, the FW motion of the MSFW rotor is not stable, this result is consistent with analysis result in section 3.6.2.

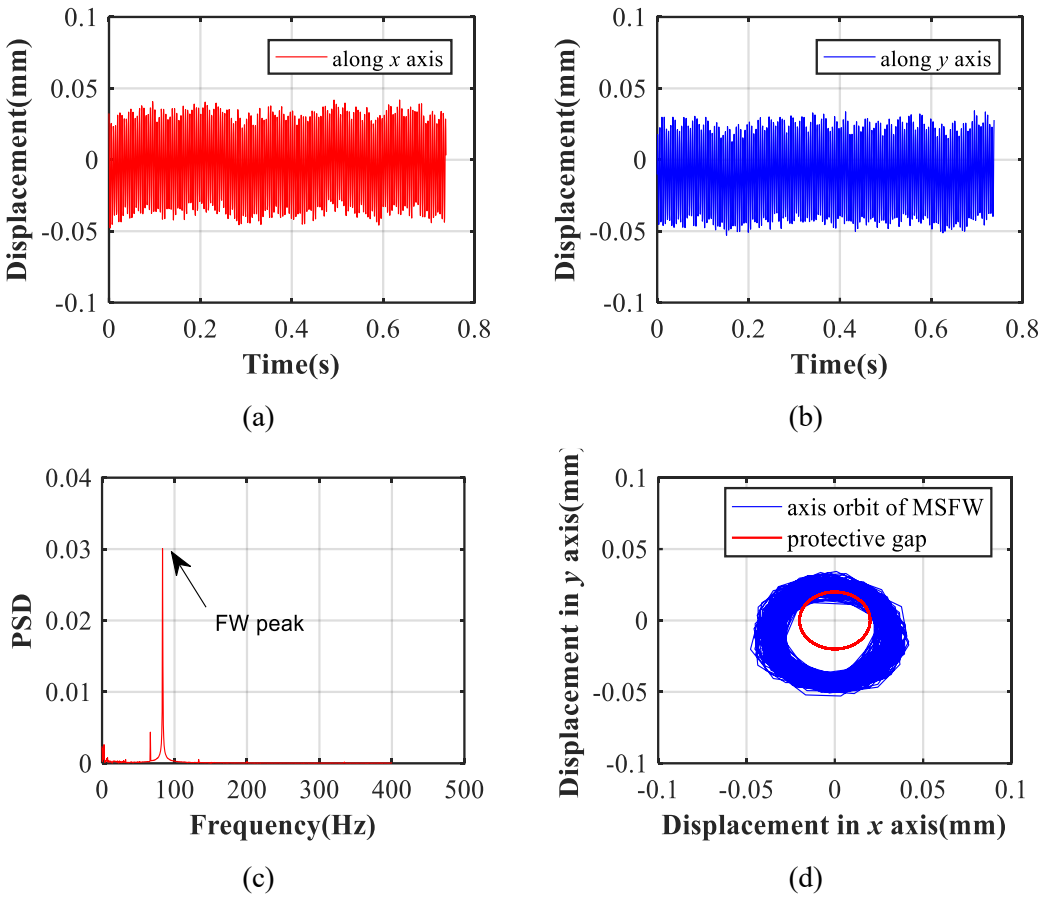

Fig. 3.22. The dynamic displacements of the MSFW rotor when suspension span ratio is 1, (a) dynamic displacements along *x* axis, (b) dynamic displacements along *y* axis, (c) the PSD of dynamic displacement, (d) the axis orbit of the MSFW rotor.

Furthermore, the suspension span ratio is tuned to 1, the displacement deflections of the MSFW rotor are illustrated in Fig. 3.22, and the maximum value of displacement deflection from the balanced position is 0.035mm, so the whirling motion of MSFW rotor is not stable. The peak frequency of the FW motion is 84Hz in Fig. 3.22(c), which approximately equal to the FW frequency (84.63Hz) in TABLE. 3.III. It indicates that the FW motion of the MSFW rotor is not stable. Finally, the axis orbit of the MSFW rotor in Fig. 3.22 (d) also verifies that the maximum displacement deflection of MSFW rotor had exceeded the protective airgap, so the FW motion is not stable.

Considering the variation of the suspension span ratio, the experiment validates that the whirling of the MSFW rotor will be unstable when the rotational frequency exceeds the critical

whirling frequency of the MSFW rotor. The unstable vibration of the FW more easily happens than the BW motion, and the frequency of the FW motion decreases with the suspension span ratio. Moreover, the whirling stability analysis based on the dual frequency bode diagram is useful to judge the whirling stability of the MSFW rotor based on experimental results.

3.8 Summary

The vibration characteristics of the MSFW rotor are analyzed based on frequency responses of the translational and rotational motions. The response magnitude of the translation is enlarged by increasing the proportional coefficient of control system, and the phase margin of translational motion decreases with the increase of proportional coefficient. The response magnitude of MSFW rotor's translational motion could be reduced with the increase of the derivative coefficient, and the phase margin of the translational motion increases with the increase of the derivative coefficient. Therefore, the vibration characteristics of the translation could be determined by the control parameters, and the vibration response of the translational motion could be suppressed by proper tuning of the proportional coefficient and the derivative coefficient.

For the rotational motion of the MSFW rotor, according to the distribution of the open-loop poles and the frequency response of the rotational control loop, the critical rotational frequency of the MSFW rotor increases with the moment of inertia ratio and the suspension span ratio. The BW motion and the FW motion will appear only when the rotating frequency of the MSFW rotor exceeds the critical rotational frequency. Therefore, the occurrences of the BW motion and the FW motion could be avoided if the moment of inertia ratio and the suspension span ratio are carefully chosen in the design of the MSFW rotor. Even if the BW motion and FW motion are not avoidable, the frequency bandwidth between the BW motion and the FW motion could be tuned by slightly adjusting the moment of inertia ratio. Moreover, vibration modes of the FW motion and the BW motion could be separated, and then the different control methods for different whirling modes could be designed and applied.

Moreover, the stability criterion of the whirling of the MSFW rotor are established based on the dual frequency bode diagram. The influences of the suspension span ratio and the moment of inertia ratio to the stability of the whirling are analyzed. The analysis result indicates that the moment of inertia ratio causes significant effect on the stability of the FW motion. A high value of the moment of inertia ratio could easily cause the FW motion of the MSFW rotor to become unstable. On the other hand, the suspension span ratio does not generate big influence on the stability of the FW motion and the BW motion, but it will affect the critical rotational frequency of the MSFW rotor and hence affect the stability of the FW motion and the BW motion as well.

Above all, a new analysis method about the vibration characteristics of the MSFW rotor is proposed, and this method provides some guidelines to the structural in the MSFW rotor. The stability criterion of the MSFW rotor based on the dual frequency bode diagram is an effective way to analyze the stability of the MSFW rotor's whirling vibration.

Chapter 4. The Vibration Absorbing Characteristics of MSFW Rotor

Based on the vibration analysis methods of the MSFW rotor in Chapter 2 and Chapter 3, the vibration behaviors of the MSFW rotor on the translation and the rotation had been studied. Furthermore, the active vibration control of MSFW rotor by adopting the additional DVA and control methods should be researched to effectively suppress the vibration response.

Therefore, the vibration absorbing characteristics of an axial AMB mounted at the suspension end of the MSFW rotor is analyzed. This axial AMB could be regarded as a kind of DVA. The stiffness characteristic and the damping characteristic of the axial AMB are modeled and analyzed. The axial AMB has the active controllability through properly changing the damping coefficient and the stiffness coefficient, and then the magnetic forces and the tilting torque are generated by the control system to control the radial tilting of MSFW rotor. Moreover, the dynamic equations of the MSFW rotor and the load rotor are derived, and their dynamic responses are analyzed, the vibration response of the MSFW rotor and the load rotor could be controlled through regulating the damping coefficient and the stiffness coefficient of axial AMB. Finally, by choosing different stiffness coefficients and damping coefficients, the experiments are designed to validate the theoretical analysis by analyzing dynamic displacements of the MSFW rotor at different rotating speeds. Consequently, the vibration control ability of the MSFW rotor is controllable by tuning the damping coefficient and the stiffness coefficient of control system, and the effective range of active vibration control is useful to the whole operational frequency of the MSFW rotor.

4.1 The Structure of MSFW Rotor and Load Rotor System

The two-mass rotational system of the MSFW rotor and the load rotor is shown in Fig. 4.1. The two pairs of radial AMBs could keep the stable suspension of MSFW at the radial equilibrium position by tuning the magnetic forces to, one pair of radial AMBs is mounted at the A-A end, and another pair of radial AMBs is mounted as the driving end (B-B end). The

axial AMB fixed at two ends of flywheel rotor is applied to control the dynamic responses of the MSFW rotor and the load rotor. Moreover, the eddy current displacement sensors at right end and left end of the MSFW rotor could timely detect the dynamic displacement of the MSFW rotor deflecting from the radial and axial equilibrium position. In the meanwhile, the load rotor is fixed at the right end of MSFW system, the MSFW rotor and the load rotor are driven by one PMSM.

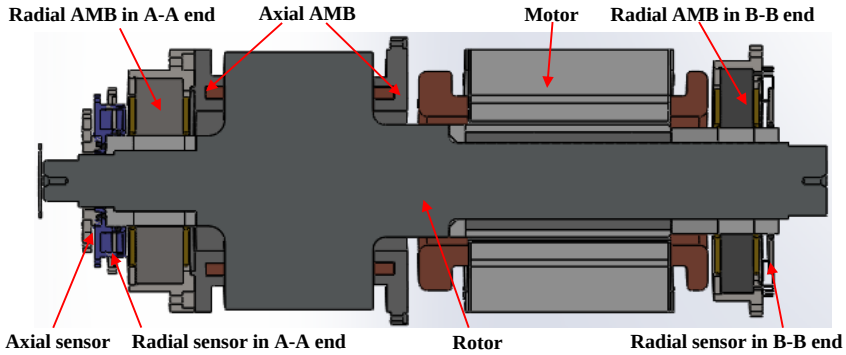

Fig. 4.1. The structure of the MSFW rotor and the load rotor system.

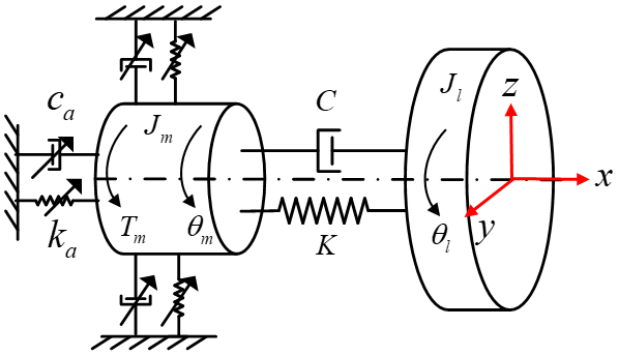

Fig. 4.2. The simplified model of the MSFW rotor and the load rotor system.

Based on the structure of the MSFW rotor and the load rotor system in Fig. 4.1. The coupling shaft connecting the MSFW rotor with the load rotor is modelled as a settled mass-spring connection, whose damping and stiffness are determined by the coupling shaft connecting the MSFW rotor with the load rotor. The AMB in axial and radial directions are modelled as three sets of tunable springs and dampers, their stiffness coefficients and damping coefficients could be regulated based on the negative displacement feedback of MSFW rotor. Comparing to normal two-mass resonant rotor system [111-113], the difference of the two-mass rotor system in Fig. 4.2 is that the effective frequency range of the normal two-mass rotor

system is a constant value, but the effective control frequency of the MSFW rotor and the load rotor system could be regulated by tuning the torques and forces of MSFW rotor.

Furthermore, the simplified model of the MSFW rotor and the load rotor system is shown in Fig. 4.2. The moment of inertia of the MSFW rotor is defined as J_m, J_l is defined as the moment of inertia of the load rotor. K is expressed as the constant stiffness of the coupling shaft connecting the MSFW rotor and the load rotor. T_m is expressed as the driving torque generated by the PMSM. C is expressed as the constant damping of the coupling shaft connecting the MSFW rotor and the load rotor. θ_m is expressed as the torsional angle of the MSFW rotor. θ_l is expressed as the torsional angle of the load rotor.

4.2 The Suspension Model of MSFW Rotor and Load Rotor

4.2.1 The Magnetic Force of Axial AMB

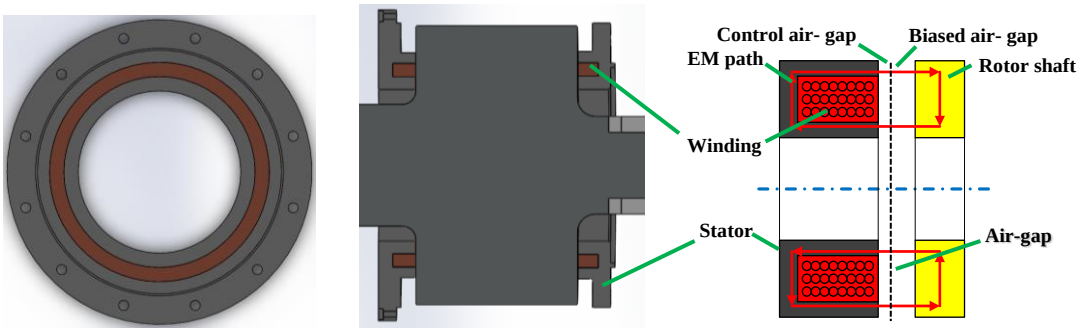

(a) (b)

Fig. 4.3. The structure of the axial AMB, (a) the prototype of the stator and the winding, (b) the simplified model of the axial AMB and the MSFW rotor.

The structure of the axial AMB and the MSFW rotor is illustrated in Fig. 4.3. An airgap exists between the stator of the axial AMB and the MSFW rotor. The airgap is separated into two parts including the control airgap and the bias airgap in the theoretical modelling and the control engineering of axial AMB. The bias airgap is designed to far greater than the controllable airgap. Based on the dynamic displacement feedback of MSFW rotor, the windings of axial AMB timely tune the magnetic flux to output the magnetic suspension force. The magnetic flux generated by the winding of axial AMB would pass through the stator, the airgap

between the rotor and stator, and the rotor, and it finally returns to the magnetic pole on the stator of axial AMB. The equivalent magnet path is illustrated in Fig. 4.3(b).

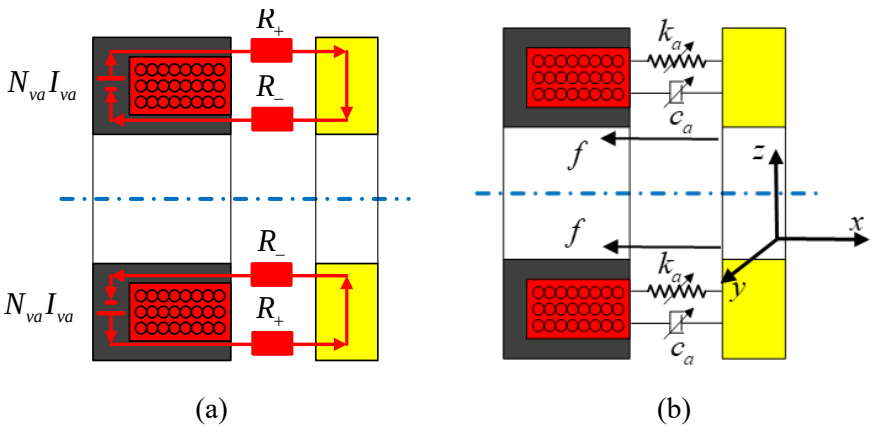

Fig. 4.4. The equivalent model of the axial AMB, (a) the equivalent magnet path of the axial AMB, (b) the equivalent force model of the axial AMB.

The magnet motive force generated by axial AMB could be written as

$$F=N_{va}\cdot\left(I_0+i\right) \tag{4.1}$$

where I_0 is defined as the bias current of axial AMB's winding. i is defined as the real-time control current of axial AMB's winding. N_{va} is defined as the turn number of axial AMB's winding.

In addition, the equivalent magnet reluctance in the positive airgap could be defined as R_+, the equivalent magnet reluctance in the negative airgap could be defined as R_-. So, the total equivalent reluctance of the airgap of axial AMB[114] is written as

$$R=R_++R_-=\frac{2\left(d_0+d\right)}{\mu_0 A} \tag{4.2}$$

where d_0 is defined as the bias airgap between the MSFW rotor and the stator. d is defined as the controllable airgap between the MSFW rotor and the stator. A is the cross-sectional area of the airgap between the MSFW rotor and the stator. μ_0 is the vacuum permeability.

Therefore, the magnet flux of the axial AMB is

$$\Phi=\frac{F}{R}=\frac{N_{va}\left(I_0+i\right)\cdot\mu_0 A}{2\left(d_0+d\right)} \tag{4.3}$$

The controllable magnetic force outputted by axial AMB could be regarded as the attractive force to actively control vibration response of rotor. Based on the Bio-savart law[115], the controllable magnetic force of axial AMB along axial direction is written as

$$f = \frac{\Phi^2}{\mu_0 A} = \frac{N_{va}^2 \mu_0 A}{4} \cdot \frac{\left(I_0 + i\right)^2}{\left(d_0 + d\right)^2} \tag{4.4}$$

The electromagnetic force coefficient of the axial AMB is defined as

$$k_{av} = \frac{N_{va}^2 \mu_0 A}{4} \tag{4.5}$$

Given that the rotor of axial AMB is suspended at equilibrium position with the conditions the control airgap d=0 and the control current i=0, the equations of displacement stiffness k_d and current stiffness k_i is expressed respectively as

$$\begin{cases} k_d = \dfrac{\partial f}{\partial d} = -2k_{av} \cdot \dfrac{\left(I_0 + i\right)^2}{\left(d_0 + d\right)^3} \approx -2k_{av} \cdot \dfrac{I_0^2}{d_0^3} \Big| \begin{matrix} i = 0 \\ d = 0 \end{matrix} \\ k_i = \dfrac{\partial f}{\partial i} = 2k_{av} \cdot \dfrac{I_0 + i}{\left(d_0 + d\right)^2} \approx 2k_{av} \cdot \dfrac{I_0}{d_0^2} \Big| \begin{matrix} i = 0 \\ d = 0 \end{matrix} \end{cases} \tag{4.6}$$

The resultant magnetic force of axial AMB could be expressed as

$$f = k_i i + k_d d \tag{4.7}$$

Therefore, the magnetic force of the axial AMB could be regulated by tuning the control current based on the displacement feedback.

4.2.2 The Feedback Control Model of Axial AMB

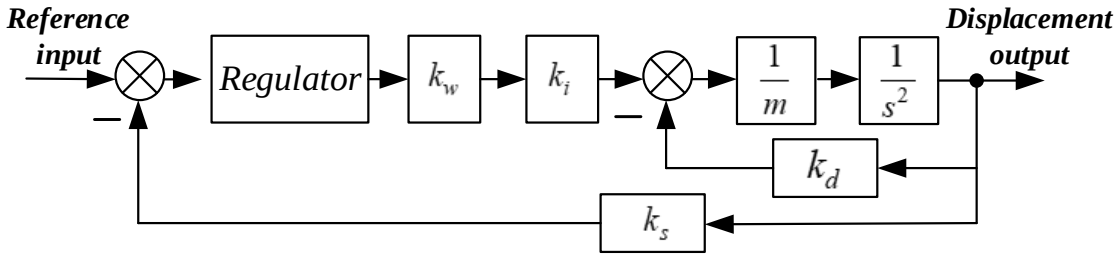

Fig. 4.5. The feedback control system of the axial AMB.

The closed loop feedback control scheme of the axial AMB in one DOF is shown in Fig. 4.5. The axial dynamic displacements deflecting the balanced state could be detected by the

eddy current displacement sensors, and then the displacement deflections could be used as the feedback terms. Furthermore, the differences between the measured displacements and the reference displacements are applied to regulate the damping coefficient and the stiffness coefficient of axial AMB. Finally, the closed loop transfer function of the axial AMB control system could be written into

$$G(s)=\frac{k_i k_w k_P + k_i k_w k_D s}{ms^2 + k_i k_w k_s k_D s + k_i k_w k_s k_P - k_d} \tag{4.8}$$

The comprehensive stiffness of the axial AMB is

$$k_{va} = k_i k_w k_s k_P - k_d = k_{iws} k_P - k_d \tag{4.9}$$

where k_s is the sensitivity of the eddy current displacement sensor, k_w is the amplification parameter, and k_P is defined as the tuning coefficient to regulate the comprehensive stiffness.

The comprehensive damping of the axial AMB could be written as

$$c_a = k_{iws} k_D \tag{4.10}$$

where k_D is defined as the tuning coefficient to regulate comprehensive damping.

As a result, the dynamic characteristics of the axial AMB could be equivalent to analyze the dynamic response of a controllable spring-damper system in Fig. 4.4(b). The comprehensive damping of the axial AMB could be regulated by the damping coefficient k_D, the comprehensive stiffness of the axial AMB could be tuned by the stiffness coefficient k_P.

4.2.3 The Torque Model of Axial AMB

As illustrated in Fig. 4.6(a), the MSFW rotor tilts about y axis with the tilting angle β_t, and then the axial AMBs would generate the magnetic forces f_{ty} to control the tilting of the MSFW rotor about y axis, and the corresponding titling torque is T_{ty} is also useful to control the tilting motion . Moreover, the tilting motion of the MSFW rotor about z axis with tilting angle α_t is shown in Fig. 4.6(b), and then the magnetic force f_{tz} outputted by the axial AMB would force the MSFW rotor back to the balanced state, and the equivalent torque T_{tz} could also control the tilting motion of MSFW rotor around z axis.

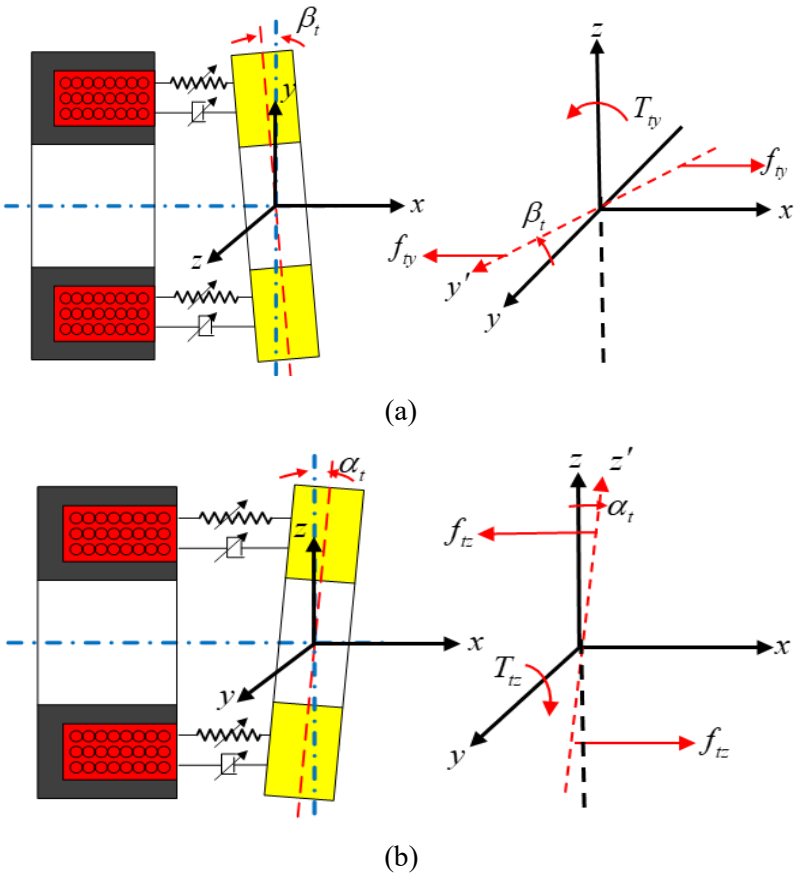

Fig. 4.6. The tilting status of the MSFW rotor, (a) the tilting status of the MSFW rotor about *y* axis, (b) the tilting status of the MSFW rotor about *z* axis.

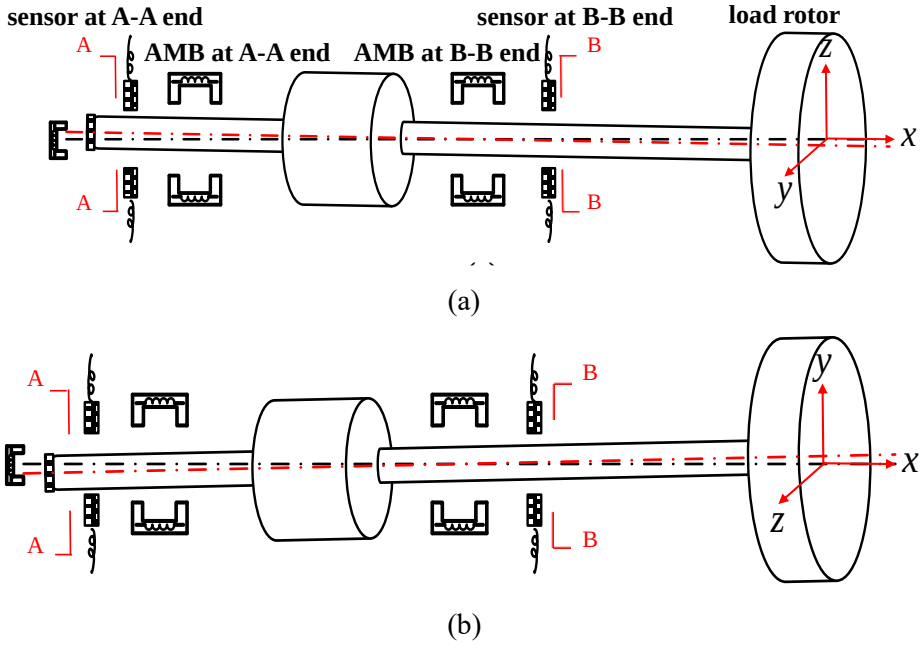

Fig. 4.7. The tilting status of the MSFW rotor, (a) the tilting status of the MSFW rotor about *y* axis, (b) the tilting status of the MSFW rotor about *z* axis.

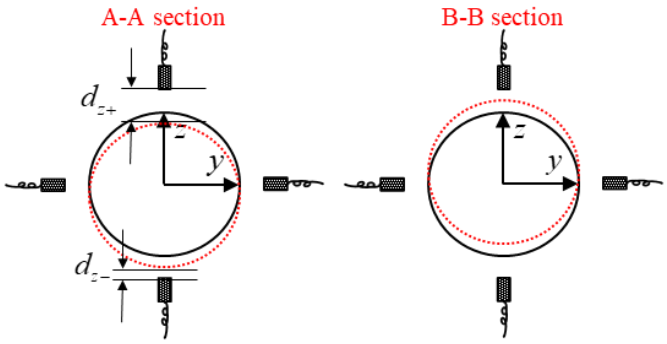

(a)

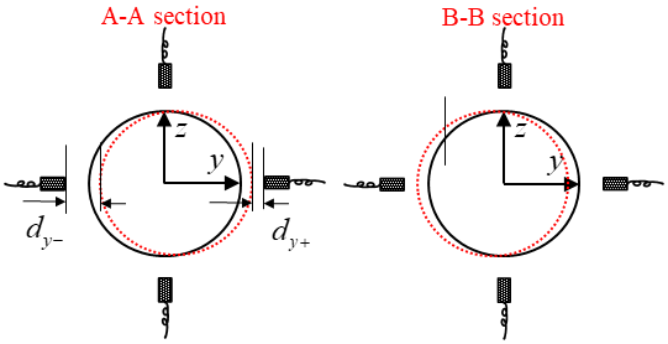

(b)

Fig. 4.8. The dynamic displacement variation of the MSFW rotor, (a) the titling status of the MSFW rotor about *y* axis, (b) the tilting status of the MSFW rotor about *z* axis.

Moreover, the titling torques generated by the axial AMB about *y* axis and *z* axis could be written into, respectively,

$$\begin{cases} T_{tz} = f_{tz} \cdot r = k_a \cdot \alpha_t + c_a \cdot \dot{\alpha}_t \\ T_{ty} = f_{ty} \cdot r = k_a \cdot \beta_t + c_a \cdot \dot{\beta}_t \end{cases} \tag{4.11}$$

where *r* is the radius of the axial AMB.

4.3 The Modeling of MSFW Rotor and Load Rotor System

4.3.1 The Modeling with Damping and Stiffness Coefficients of Axial AMB

According to the dynamics model of the MSFW rotor and the load rotor system in Fig. 4.2, the dynamic equations of the MSFW rotor and the load rotor could be written respectively as

$$\begin{cases} J_m \ddot{\theta}_m = T_m + k_a \theta_m + c_a \dot{\theta}_m - K\left(\theta_m - \theta_l\right) - C\left(\dot{\theta}_m - \dot{\theta}_l\right) \\ J_l \ddot{\theta}_l = K\left(\theta_m - \theta_l\right) + C\left(\dot{\theta}_m - \dot{\theta}_l\right) \end{cases} \tag{4.12}$$

Furthermore, the equivalent transfer functions about the MSFW rotor and the load rotor could be expressed separately into

$$\begin{cases} G_m(s)=\dfrac{\Theta_m(s)}{T_m(s)}=\dfrac{J_l s^2+Cs+K}{\left[J_m s^2+(C-c_a)s+(K-k_a)\right]\left(J_l s^2+Cs+K\right)-(Cs+K)^2} \\ G_l(s)=\dfrac{\Theta_l(s)}{T_m(s)}=\dfrac{Cs+K}{\left[J_m s^2+(C-c_a)s+(K-k_a)\right]\left(J_l s^2+Cs+K\right)-(Cs+K)^2} \end{cases} \tag{4.13}$$

Moreover, the dimensionless functions of the MSFW rotor and the load rotor in frequency domain could be written as

$$\begin{cases} G_m(s)=\dfrac{\lambda_l^2\left(1-\lambda_l^2+2j\xi_l\lambda_l\right)}{\lambda_l^2\left(1-\lambda_l^2+2j\xi_l\lambda_l\right)\left(1-\lambda_m^2+2j\xi_m\lambda_m\right)-\nu\lambda_m^2\left(1+2j\xi_l\lambda_l\right)^2} \\ G_l(s)=\dfrac{\lambda_l^2\left(1+2j\xi_l\lambda_l\right)}{\lambda_l^2\left(1-\lambda_l^2+2j\xi_l\lambda_l\right)\left(1-\lambda_m^2+2j\xi_m\lambda_m\right)-\nu\lambda_m^2\left(1+2j\xi_l\lambda_l\right)^2} \end{cases} \tag{4.14}$$

where $\omega_m=\sqrt{\dfrac{K-k_a}{J_m}}$ is defined as the natural frequency of the coupling shaft connecting the axial AMB and the MSFW rotor. $\omega_l=\sqrt{\dfrac{K}{J_l}}$ is defined as the natural frequency of the coupling shaft connecting the MSFW rotor and the load rotor. $\lambda_l=\dfrac{\omega}{\omega_l}$ is defined as the ratio between the rotational frequency ω and the natural frequency ω_l. $\lambda_m=\dfrac{\omega}{\omega_m}$ is defined as the ratio between the rotational frequency ω and the natural frequency ω_m. $\xi_m=\dfrac{C-c_a}{2J_m\omega_m}$ is defined as the damping coefficient of the coupling shaft connecting the axial AMB and the MSFW rotor. $\xi_l=\dfrac{C}{2J_l\omega_l}$ is defined as the damping coefficient of the coupling shaft connecting the MSFW rotor and the load rotor. $\nu=\dfrac{J_l}{J_m}$ is defined as the ratio between the moment of inertia of the load rotor and the MSFW rotor.

The simplified expression of the dimensionless frequency response functions in Eq.(4.14) could be rewritten into

$$\begin{cases} G_m(j\omega) = \dfrac{c + jd}{a + jb} \\ G_l(j\omega) = \dfrac{e + jf}{a + jb} \end{cases} \tag{4.15}$$

where

$$\begin{cases} a = \lambda_l^2\left(1-\lambda_l^2\right)\left(1-\lambda_m^2\right) - 4\xi_l\xi_m\lambda_l^3\lambda_m - v\lambda_m^2\left(1-4\xi_l^2\lambda_l^2\right) \\ b = 2\xi_l\lambda_l^3\left(1-\lambda_m^2\right) + 2\xi_m\lambda_m\lambda_l^2\left(1-\lambda_m^2\right) - 4v\xi_l\lambda_l\lambda_m^2 \\ c = \lambda_l\left(1-\lambda_l^2\right) \\ d = 2\xi_l\lambda_l^3 \\ e = \lambda_l^2 \\ f = 2\xi_l\lambda_l^3 \end{cases} \tag{4.16}$$

Based on the dimensionless frequency response functions in Eq.(4.15), the magnitude equations of the MSFW rotor and the load rotor could be derived and written as

$$\begin{cases} A_m = \left|G_m(j\omega)\right| = \dfrac{\sqrt{c^2 + d^2}}{\sqrt{a^2 + b^2}} \\ A_l = \left|G_l(j\omega)\right| = \dfrac{\sqrt{e^2 + f^2}}{\sqrt{a^2 + b^2}} \end{cases} \tag{4.17}$$

Therefore, the response magnitudes of the MSFW rotor and the load rotor could be used as the evaluation index for the stability of the MSFW rotor.

4.3.2 The Modeling with Stiffness Coefficients of Axial AMB

When the damping coefficient c_a of the coupling shaft connecting the axial AMB and the MSFW rotor is not considered and analyzed in the dynamic functions of the MSFW rotor and the load rotor system, and then the vibration control model of the axial AMB and the MSFW rotor could be equivalent to a mass block fixed at the right end and left end of flywheel rotor. So, the dimensionless frequency response functions of the MSFW rotor and the load rotor in Eq. (4.14) could be rewritten as

$$\begin{cases} G'_m(j\omega)=\dfrac{\lambda_l^2\left(1-\lambda_l^2+2j\xi_l\lambda_l\right)}{\lambda_l^2\left(1-\lambda_l^2+2j\xi_l\lambda_l\right)\left(1-\lambda_m^2+2j\xi'_m\lambda_m\right)-\nu\lambda_m^2\left(1+2j\xi_l\lambda_l\right)^2} \\ G'_l(j\omega)=\dfrac{\lambda_l^2\left(1+2j\xi_l\lambda_l\right)}{\lambda_l^2\left(1-\lambda_l^2+2j\xi_l\lambda_l\right)\left(1-\lambda_m^2+2j\xi'_m\lambda_m\right)-\nu\lambda_m^2\left(1+2j\xi_l\lambda_l\right)^2} \end{cases} \tag{4.18}$$

where $\xi'_m=\dfrac{C}{2J_m\omega_m}$ is defined as the damping coefficient of the coupling shaft connecting the axial AMB and the MSFW rotor.

The damping coefficient of the MSFW rotor increases, and the natural frequency of the MSFW rotor would not vary considering the vibration absorbing model of the axial AMB could be equivalent to a mass block. So, the simplified models of dimensionless frequency response functions are

$$\begin{cases} G'_m(j\omega)=\dfrac{c'+jd'}{a'+jb'} \\ G'_l(j\omega)=\dfrac{e'+jf'}{a'+jb'} \end{cases} \tag{4.19}$$

where

$$\begin{cases} a'=\lambda_l^2\left(1-\lambda_l^2\right)\left(1-\lambda_m^2\right)-4\xi_l\xi'_m\lambda_l^3\lambda_m-\nu\lambda_m^2\left(1-4\xi_l^2\lambda_l^2\right) \\ b'=2\xi_l\lambda_l^3\left(1-\lambda_m^2\right)+2\xi'_m\lambda_m\lambda_l^2\left(1-\lambda_m^2\right)-4\nu\xi_l\lambda_l\lambda_m^2 \\ c'=\lambda_l\left(1-\lambda_l^2\right) \\ d'=2\xi_l\lambda_l^3 \\ e'=\lambda_l^2 \\ f'=2\xi_l\lambda_l^3 \end{cases} \tag{4.20}$$

The magnitude equations of the MSFW rotor and the load rotor are respectively

$$\begin{cases} A'_m=\left|G'_m(j\omega)\right|=\dfrac{\sqrt{(c')^2+(d')^2}}{\sqrt{(a')^2+(b')^2}} \\ A'_l=\left|G'_l(j\omega)\right|=\dfrac{\sqrt{(e')^2+(f')^2}}{\sqrt{(a')^2+(b')^2}} \end{cases} \tag{4.21}$$

Therefore, the response magnitudes of the MSFW rotor and the load rotor could be controlled by regulating the stiffness coefficient of axial AMB.

4.3.3 The Modeling with Damping Coefficients of Axial AMB

When the stiffness coefficient k_a of the axial AMB is not analyzed and considered in the dynamic model of the MSFW rotor and the load rotor, the vibration absorbing method of the axial AMB could be simplified into a pure damper model, and then the dimensionless frequency response functions of the MSFW rotor and the load rotor in Eq. (4.14) could be rewritten as

$$\begin{cases} G_m''(j\omega) = \dfrac{\lambda_l^2\left(1-\lambda_l^2\right)}{\lambda_l^2\left(1-\lambda_l^2\right)\left(1-\left(\lambda_m''\right)^2+2j\xi_m''\lambda_m''\right)-\nu\left(\lambda_m''\right)^2\left(1+2j\xi_l\lambda_l\right)^2} \\ G_l''(j\omega) = \dfrac{\lambda_l^2}{\lambda_l^2\left(1-\lambda_l^2\right)\left(1-\left(\lambda_m''\right)^2+2j\xi_m''\lambda_m''\right)-\nu\left(\lambda_m''\right)^2\left(1+2j\xi_l\lambda_l\right)^2} \end{cases} \tag{4.22}$$

where $\omega_m'' = \sqrt{\dfrac{K}{J_m}}$ is defined as the natural frequency of the coupling shaft connecting the axial AMB and the MSFW rotor. $\xi_m'' = \dfrac{C-c_a}{2J_m\omega_m''}$ is defined as the damping coefficient of the coupling shaft connecting the axial AMB and the MSFW rotor, and $\lambda_m'' = \dfrac{\omega}{\omega_m''}$ is defined as the frequency ratio between the rotational frequency ω and the natural frequency ω_m''.

When the vibration absorbing model of the axial AMB is equivalent to the pure damper system, the natural frequency of the MSFW rotor would increase and the damping coefficient would decrease. The simplified models of dimensionless frequency response functions could be expressed as

$$\begin{cases} G_m''(j\omega) = \dfrac{c''+jd''}{a''+jb''} \\ G_l''(j\omega) = \dfrac{e''+jf''}{a''+jb''} \end{cases} \tag{4.23}$$

where

$$\begin{cases} a'' = \lambda_l^2\left(1-\lambda_l^2\right)\left(1-\left(\lambda_m''\right)^2\right)-\nu\left(\lambda_m''\right)^2\left(1-4\xi_l^2\lambda_l^2\right) \\ b'' = 2\lambda_l^2\left(1-\lambda_l^2\right)\xi_m''\lambda_m''-4\nu\left(\lambda_m''\right)^2\xi_l\lambda_l \\ c'' = \lambda_l\left(1-\lambda_l^2\right) \\ d'' = 0 \\ e'' = \lambda_l^2 \\ f'' = 0 \end{cases} \tag{4.24}$$

The magnitude equations of the MSFW rotor and the load rotor are

$$\begin{cases} A_m'' = \left|G_m''\left(j\omega\right)\right| = \dfrac{\sqrt{\left(c''\right)^2+\left(d''\right)^2}}{\sqrt{\left(a''\right)^2+\left(b''\right)^2}} \\ A_l'' = \left|G_l''\left(j\omega\right)\right| = \dfrac{\sqrt{\left(e''\right)^2+\left(f''\right)^2}}{\sqrt{\left(a''\right)^2+\left(b''\right)^2}} \end{cases} \tag{4.25}$$

So, the response magnitudes of the MSFW rotor and the load rotor could be controlled by tuning the damping coefficient of the axial AMB.

4.3.4 The Modelling without Considering Stiffness and Damping Coefficients of Axial AMB

When the damping coefficient c_a and the stiffness coefficient k_a of the axial AMB both are neglected, the dimensionless frequency response functions of the MSFW rotor and the load rotor in Eq.(4.14) could be simplified as

$$\begin{cases} G_m'''\left(j\omega\right) = \dfrac{\lambda_l^2\left(1-\lambda_l^2\right)}{\lambda_l^2\left(1-\lambda_l^2\right)\left(1-\left(\lambda_m'''\right)^2+2j\xi_m'''\lambda_m'''\right)-\nu\left(\lambda_m'''\right)^2\left(1+2j\xi_l\lambda_l\right)^2} \\ G_l'''\left(j\omega\right) = \dfrac{\lambda_l^2}{\lambda_l^2\left(1-\lambda_l^2\right)\left(1-\left(\lambda_m'''\right)^2+2j\xi_m'''\lambda_m'''\right)-\nu\left(\lambda_m'''\right)^2\left(1+2j\xi_l\lambda_l\right)^2} \end{cases} \tag{4.26}$$

where $\omega_m''' = \sqrt{\dfrac{K}{J_m}}$ is defined as the natural frequency of the coupling shaft connecting the MSFW rotor and the axial AMB. $\xi_m''' = \dfrac{C}{2J_m\omega_m'''}$ is defined as the damping coefficient of the

coupling shaft connecting the MSFW rotor and the axial AMB, and $\lambda_m''' = \dfrac{\omega}{\omega_m'''}$ is defined as the frequency ratio between the rotational frequency ω and the natural frequency ω_m'''.

The simplified models of dimensionless frequency response functions are

$$\begin{cases} G_m'''(j\omega) = \dfrac{c''' + jd'''}{a''' + jb'''} \\ G_l'''(j\omega) = \dfrac{e''' + jf'''}{a''' + jb'''} \end{cases} \tag{4.27}$$

where

$$\begin{cases} a''' = \lambda_l^2\left(1-\lambda_l^2\right)\left(1-\left(\lambda_m'''\right)^2\right) - v\left(\lambda_m''\right)^2\left(1-4\xi_l^2\lambda_l^2\right) \\ b''' = 2\lambda_l^2\left(1-\lambda_l^2\right)\xi_m'''\lambda_m''' - 4v\left(\lambda_m'''\right)^2\xi_l\lambda_l \\ c''' = \lambda_l\left(1-\lambda_l^2\right) \\ d''' = 0 \\ e''' = \lambda_l^2 \\ f''' = 0 \end{cases} \tag{4.28}$$

The magnitude equations of the MSFW rotor and the load rotor are

$$\begin{cases} A_m''' = \left|G_m'''(j\omega)\right| = \dfrac{\sqrt{\left(c'''\right)^2 + \left(d'''\right)^2}}{\sqrt{\left(a'''\right)^2 + \left(b'''\right)^2}} \\ A_l''' = \left|G_l'''(j\omega)\right| = \dfrac{\sqrt{\left(e'''\right)^2 + \left(f'''\right)^2}}{\sqrt{\left(a'''\right)^2 + \left(b'''\right)^2}} \end{cases} \tag{4.29}$$

Therefore, the response magnitudes of the MSFW rotor and the load rotor are determined by controlled by the damping coefficient of the coupling shaft connecting the MSFW rotor and the axial AMB.

4.4 The Dynamic Analysis of MSFW Rotor and Load Rotor

4.4.1 The Dynamic Characteristics of the Load Rotor with Stiffness Coefficient and Damping Coefficient of Axial AMB

According to the dynamic model of the MSFW rotor and load rotor in Eq. (4.14) and applying PD control model, the relationship between the dynamic characteristics of the load

rotor and the effect of the axial AMB are analyzed. The influence of the axial AMB's damping coefficient on the dynamic characteristics of the load rotor are illustrated in Fig. 4.9(a). When the damping coefficient of axial AMB is neglected, the magnitude peak of load rotor would occur. Evidently, the response magnitude of load rotor using the damping coefficient of axial AMB is smaller than the response magnitude neglecting the damping coefficient of axial AMB. Moreover, the relationship between the damping coefficient of axial AMB and the response characteristics of load rotor is illustrated in Fig. 4.9(b), the response magnitude of load rotor is reduced by controlling damping coefficient of the axial AMB.

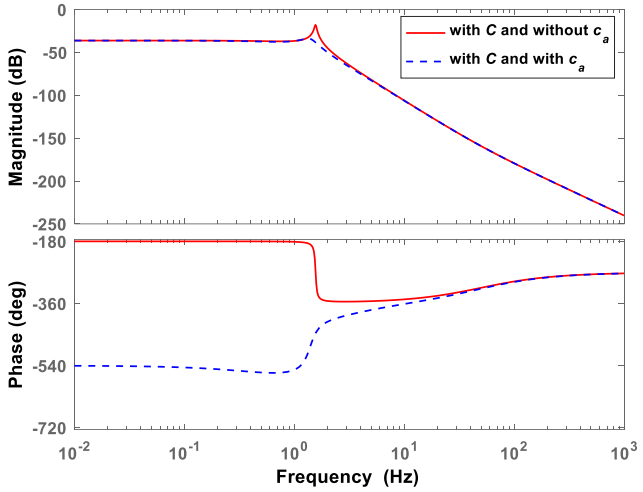

(a)

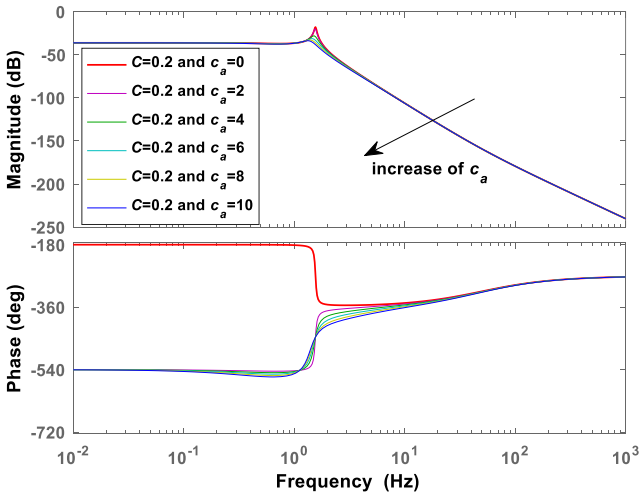

(b)

Fig. 4.9. The frequency characteristics of the load rotor using different damping coefficients of the axial AMB, (a) the response curves of frequency characteristics, (b) the frequency responses with different damping coefficients.

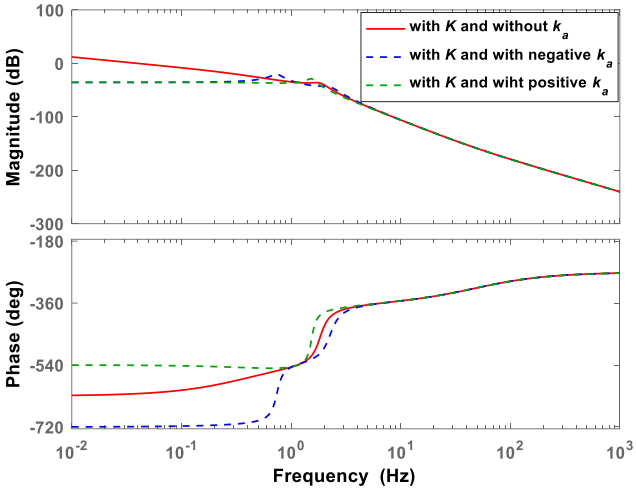

(a)

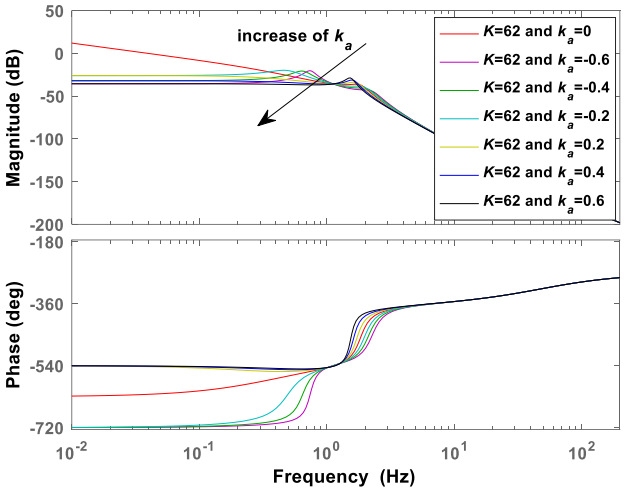

(b)

Fig. 4.10. The frequency characteristics of the load rotor using different stiffness coefficients of the axial AMB, (a) the response curves of frequency characteristics, (b) the frequency responses with different stiffness coefficients.

Furthermore, the influence of the axial AMB's comprehensive stiffness is investigated too. The frequency response curves of the load rotor with and without the comprehensive stiffness of the axial AMB are plotted in Fig. 4.10(a). The dynamic response of the load rotor is marked by the blue line in Fig. 4.10(a) when the comprehensive stiffness of the axial AMB is tuned to a negative value. There are two magnitude peaks with different frequencies, and the magnitude peak at low frequency is higher than the magnitude peak at high frequency. The dynamic response curve of the load rotor is marked by the green line in Fig. 4.10(a) when the comprehensive stiffness of the axial AMB is tuned to a positive value, and the results indicate that the positive comprehensive stiffness of axial AMB could eliminate the magnitude peak

occurring at the low frequency. In addition, the relationship between the comprehensive stiffness of axial AMB and the dynamic response of the load rotor is shown in Fig. 4.10(b), and the response magnitude of the load rotor is reduced by increasing the comprehensive stiffness of axial AMB. Consequent, the comprehensive stiffness of the axial AMB could affect the dynamic response of the load rotor too, and the response magnitude of the load rotor is mitigated by improving the stiffness coefficient of axial AMB.

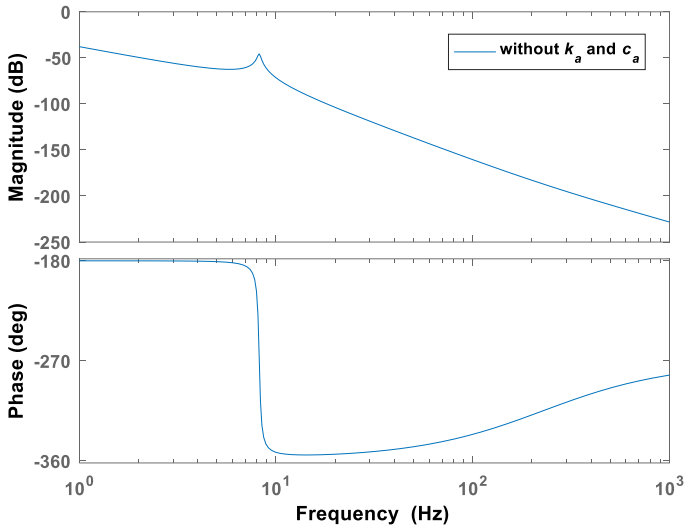

Fig. 4.11. The frequency response of the load rotor without the axial AMB.

Finally, the dynamic response of the load rotor without considering the axial AMB is shown in Fig. 4.11, and the response magnitude of the load is greater than the response magnitude of the load rotor in Fig. 4.10(a) with considering the comprehensive stiffness of axial AMB. So, the comparison results indicate that the damping coefficient and the comprehensive stiffness of the axial AMB are both effective to control dynamic characteristics of the load rotor.

4.4.2 The Dynamic Response Characteristics of the MSFW Rotor with Stiffness and Damping Coefficients of Axial AMB

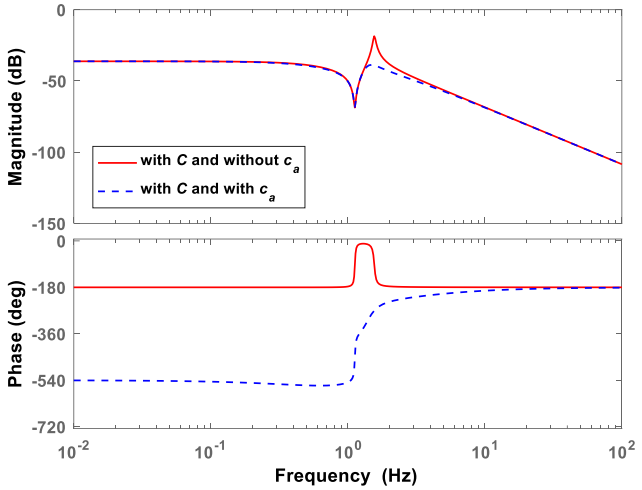

(a)

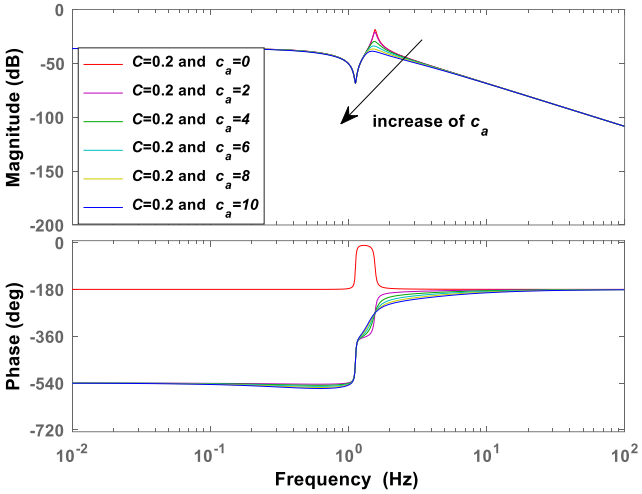

(b)

Fig. 4.12. The frequency responses of the MSFW rotor with different damping coefficients of the axial AMB, (a) the comparison of frequency responses, (b) the frequency responses of the MSFW rotor with different damping coefficients.

Moreover, the dynamic response curve of the MSFW rotor is plotted by the red line in Fig. 4.12(a) when the damping coefficient of the axial AMB is neglected, and the dynamic response curve of the MSFW rotor is marked by the blue line in Fig. 4.12(a) when the damping coefficient of the axial AMB is analyzed and considered. The response magnitude of the MSFW rotor considering the damping coefficient is smaller than that without considering the damping coefficient of the axial AMB. The damping coefficient of the axial AMB could cause influence on the dynamic characteristics of the MSFW rotor as well. The relationship between the

damping coefficient of the axial AMB and the dynamic response of the MSFW rotor is illustrated in Fig. 4.12(b). The damping coefficient of the axial AMB could suppress the response magnitudes of the MSFW rotor. Therefore, the damping coefficients of the axial AMB are also effective to control the dynamic characteristics of the MSFW rotor.

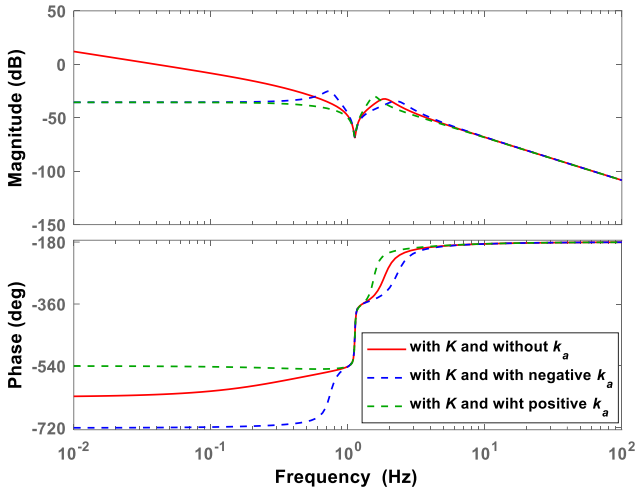

(a)

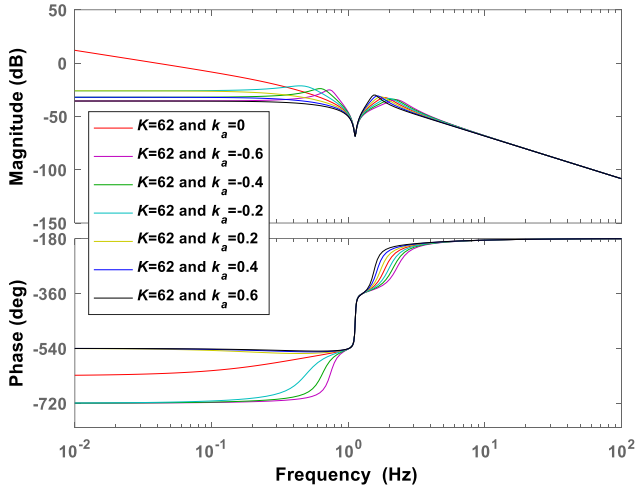

(b)

Fig. 4.13. The frequency responses of the MSFW rotor with different stiffness coefficients of the axial AMB, (a) the comparison of frequency responses, (b) the frequency responses of the MSFW rotor with different stiffness coefficients.

In Fig. 4.13(a), the dynamic response curve of the MSFW rotor is plotted by the blue line when the comprehensive stiffness of the axial AMB is regulated to the negative term. The dynamic response curve of the MSFW rotor using positive comprehensive stiffness is plotted by the green line. Based on the comparison result, the response magnitude of the MSFW rotor using the negative comprehensive stiffness coefficient is greater than the response magnitude

of the MSFW rotor using the positive comprehensive stiffness coefficient. The relationship between the comprehensive stiffness of the axial AMB and the dynamic response of the MSFW rotor is shown in Fig. 4.13(b). The response magnitude of the MSFW rotor is reduced by increasing the comprehensive stiffness of axial AMB. So, the positive comprehensive stiffness coefficient of the axial AMB could also tune the dynamic characteristics of the MSFW rotor.

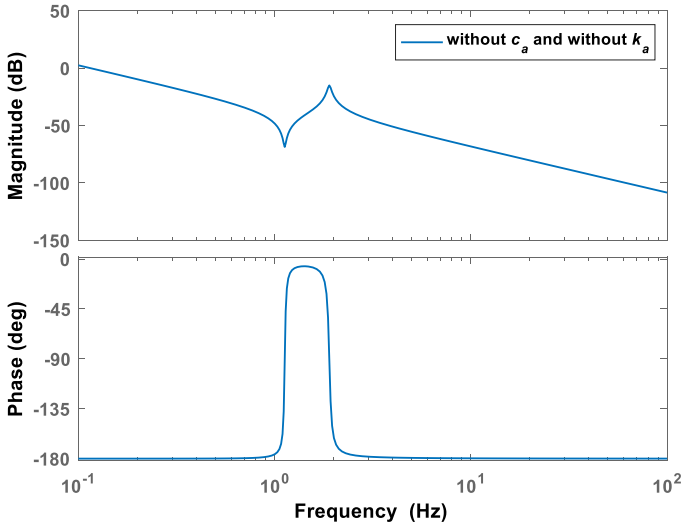

Fig. 4.14. The frequency response of the MSFW rotor without the axial AMB.

The dynamic response curve of the MSFW rotor is shown in Fig. 4.14 when the stiffness coefficient and damping coefficient of the axial AMB are both neglected. The response magnitude of the MSFW rotor without considering the stiffness coefficient and damping coefficient of the axial AMB is greater than that in Fig. 4.12 and Fig. 4.13. It shows that the positive stiffness and the damping coefficient of the axial AMB are effective to control the dynamic characteristics of the MSFW rotor.

4.5 The Experimental Verification of Axial AMB

4.5.1 The Magnetic Force and Torque

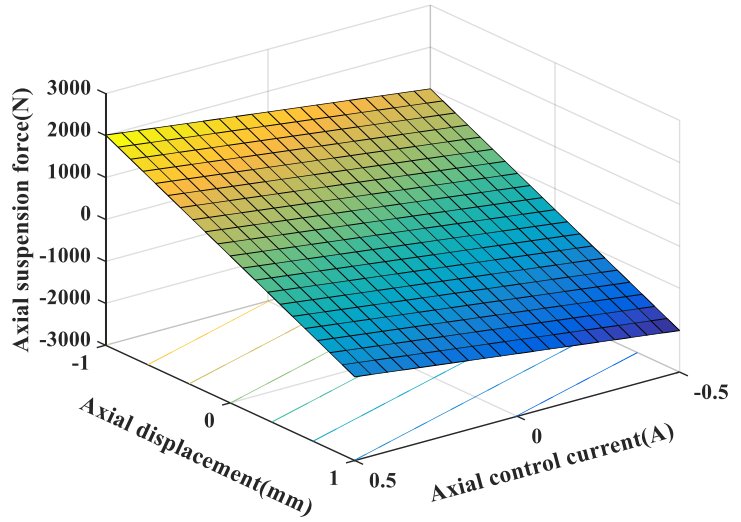

(a)

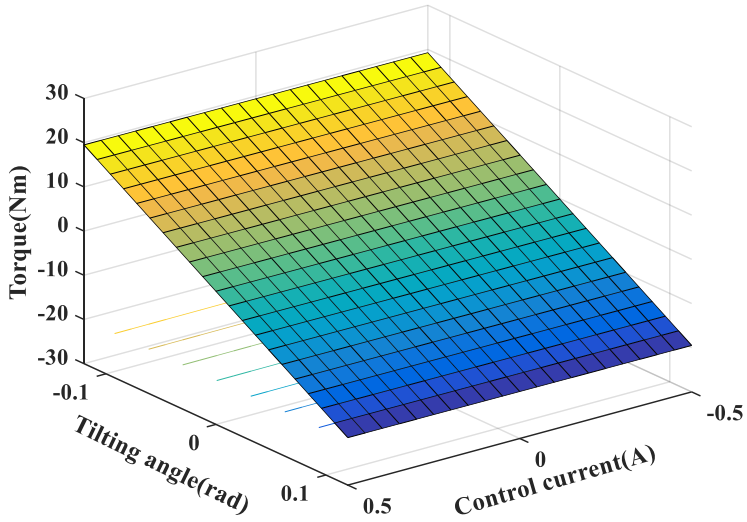

(b)

Fig. 4.15. The magnetic force and the torque of the axial AMB, (a) the magnetic force, (b) the torque.

The relationships amongst the control displacement of rotor, the control current of winding and the magnetic force of the axial AMB are shown in Fig. 4.15(a). The magnetic force of the axial AMB is inversely linear to the control displacement of rotor, but magnetic force of the axial AMB is positively linear to the control current. The current stiffness of the axial AMB is about 1750N/A, and the displacement stiffness of the axial AMB is about -550N/mm. The titling torques outputted by the axial AMB are plotted in Fig. 4.15(b). The titling torque is linear to

the control displacement and the control current within the small vicinity of the equilibrium position. The current stiffness of the axial AMB's tilting torque is about 2.3Nm/A, and the angle stiffness of the axial AMB's tilting torque is about -161.5Nm/rad. Therefore, tilting torques generated by the axial AMB are controllable by tuning the control current of the axial AMB based on the displacement feedback and the angle feedback of the MSFW rotor.

4.5.2 The Vibration of MSFW Rotor versus Damping of Axial AMB

The maximum displacement deflection of the MSFW rotor deviating from the balanced position in radial direction is index to evaluate the dynamic characteristics of MSFW rotor, and the great the maximum displacement deflection of MSFW rotor means that the MSFW rotor has serious vibration response. The dynamic displacements of the MSFW rotor are plotted and analyzed in Fig. 4.16 when the axial AMB has different stiffness coefficient and damping coefficients. First, the dynamic displacements of the MSFW rotor are analyzed when the axial AMB sets at different damping coefficients. The dynamic displacements of the MSFW rotor from the radial equilibrium position at different rotating speeds are shown in Fig. 4.17. The maximum displacement deflections deviating from the balanced position of MSFW rotor using different damping coefficients of axial AMB are shown in TABLE. 4.I. In detail, the maximum value of the MSFW rotor's displacement deflection is 0.0156mm when the damping coefficient of the axial AMB sets at 2 and the rotational speed of MSFW rotor is 2000rpm. The maximum value of the MSFW rotor's displacement deflection is reduced to 0.0078mm when the damping coefficient is 8 and the rotating speed of MSFW rotor is still 2000rpm. The maximum value of the MSFW rotor's displacement deflection is 0.0161mm when the rotational speed of MSFW rotor is increased to 8000rpm and the damping coefficient of axial AMB is 2. When the damping coefficient of axial AMB is increased to 8 at 8000rpm, the maximum value of the MSFW rotor's displacement deflection decreases to 0.0135mm.

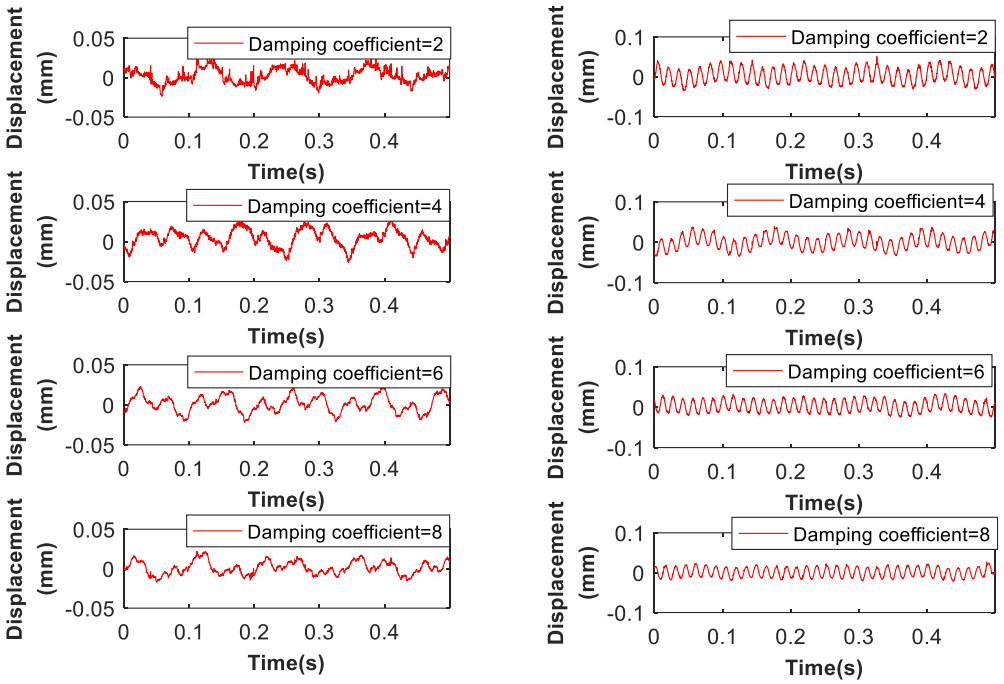

Fig. 4.16. The dynamic displacement variations of the MSFW rotor using different damping parameters, (a) the rotational speed is 2000rpm, (b) the rotational speed is 4000rpm, (c) the rotational speed is 6000rpm, (d) the rotational speed is 8000rpm.

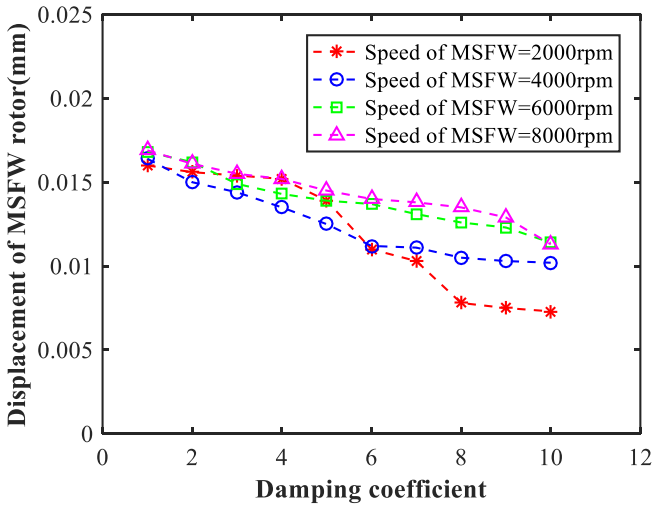

Fig. 4.17. The relationship between the maximum displacement deflection of the MSFW rotor and the damping coefficient of the axial AMB.

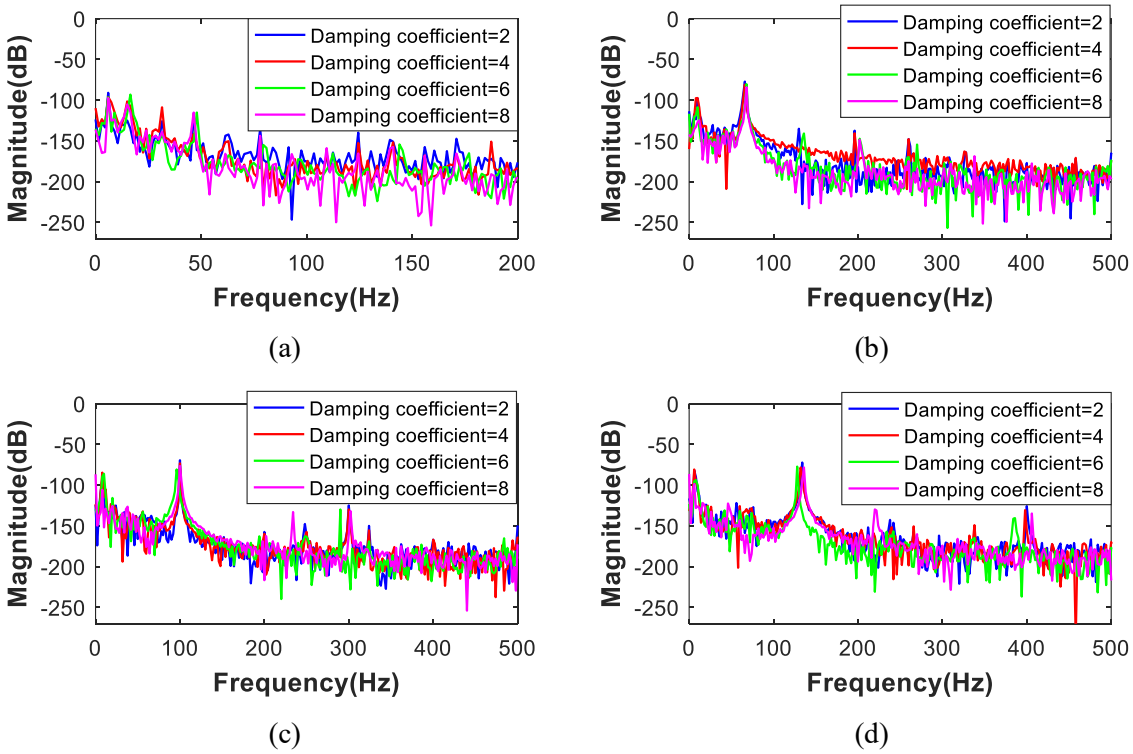

Fig. 4.18. The power spectrums of the MSFW rotor with different damping coefficients, (a) the rotational speed is 2000rpm, (b) the rotational speed is 4000rpm, (c) the rotational speed is 6000rpm, (d) the rotational speed is 8000rpm.

According to the dynamic displacement deflections of the MSFW rotor deviating from the balanced position in radial direction as shown in Fig. 4.16, the power spectrums of the MSFW rotor's dynamic displacement deflections with damping coefficients of the axial AMB and at different rotational speeds are plotted in Fig. 4.18. By analyzing the response magnitude of the

MSFW rotor at 2000rpm in Fig. 4.18(a), the response amplitude of the MSFW rotor is -108dB when the damping coefficient of the axial AMB is 2, and the response magnitude decreases to -141dB when the damping coefficient of the axial AMB is increased from 2 to 8. When the damping coefficient of the axial AMB sets at 2 and the rotational speed of MSFW rotor is accelerated to 8000rpm, the response magnitude of the MSFW rotor is about -73dB as shown in Fig. 4.18(d). It decreases to -79dB when the damping coefficient of axial AMB is improved to 8. Therefore, maximum value of the MSFW rotor's displacement deflection deviating from the balanced position would increase with the rotational speed of MSFW rotor, but it could be suppressed through increasing the axial AMB's damping coefficient.

TABLE. 4.I. The dynamic displacement of MSFW rotor using different damping coefficients of axial AMB.

	Maximum displacement deflection (mm)			
Damping	**2000(rpm)**	**4000(rpm)**	**6000(rpm)**	**8000(rpm)**
1	0.0160	0.0164	0.0168	0.0169
2	0.0156	0.0150	0.0162	0.0161
3	0.0154	0.0144	0.0149	0.0155
4	0.0152	0.0135	0.0143	0.0152
5	0.0139	0.0125	0.0139	0.0145
6	0.0110	0.0112	0.0137	0.0140
7	0.0103	0.0111	0.0131	0.0138
8	0.0078	0.0105	0.0126	0.0135
9	0.0075	0.0103	0.0123	0.0129
10	0.0073	0.0102	0.0114	0.0113

4.5.3 The Vibration of MSFW Rotor versus Stiffness of Axial AMB

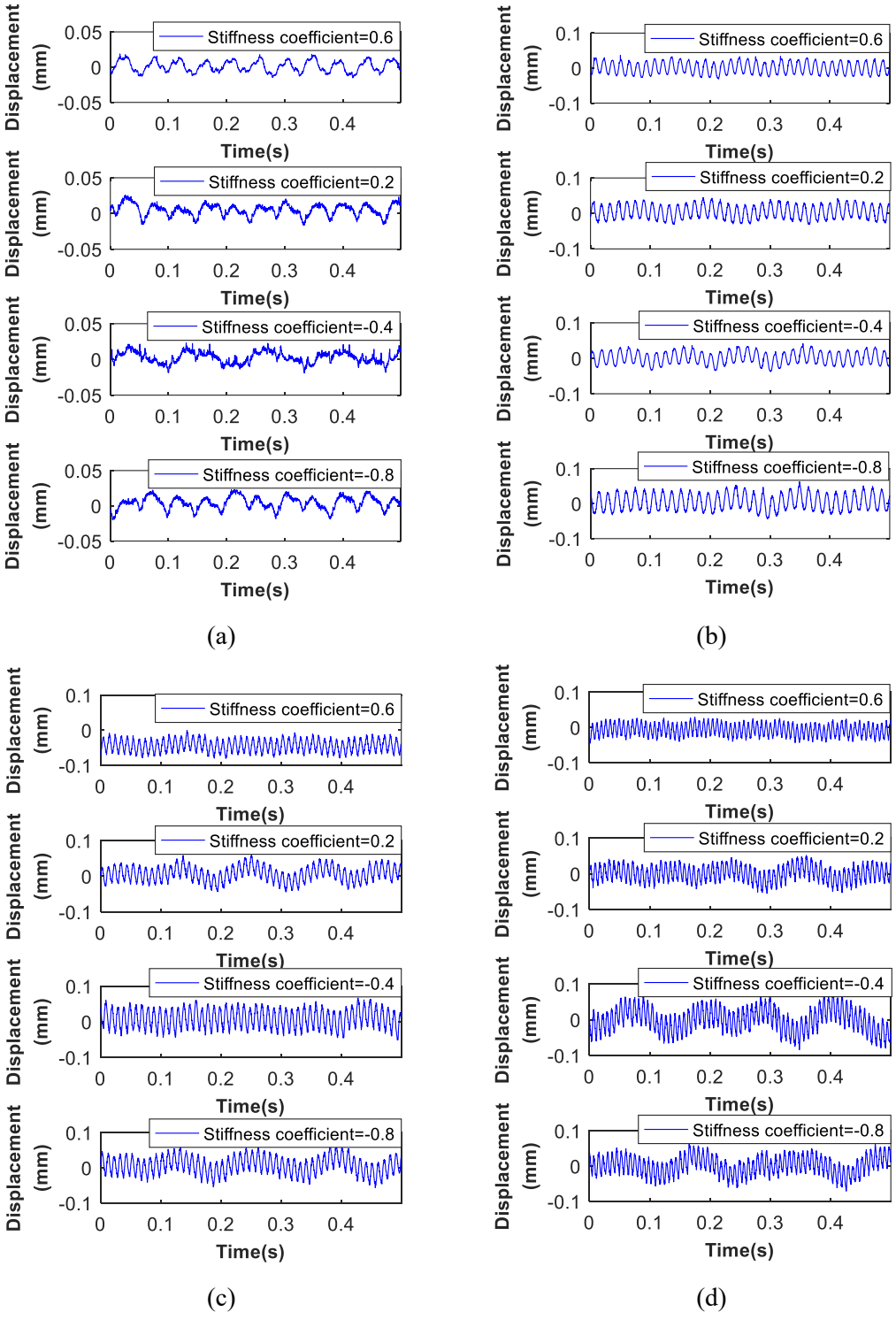

Fig. 4.19. The dynamic displacement variations of the MSFW rotor using different stiffness parameters, (a) the rotational speed is 2000rpm, (b) the rotational speed is 4000rpm, (c) the rotational speed is 6000rpm, (d) the rotational speed is 8000rpm.

The dynamic displacement variations of MSFW rotor with the axial AMB's different stiffness coefficients are recorded and illustrated in Fig. 4.19. The maximum values of MSFW

rotor's displacement deflection deviating from the balanced position are listed in TABLE. 4.II illustrated in Fig. 4.21. As illustrated in Fig. 4.19(a), the maximum value of MSFW rotor's displacement deflection is 0.0101mm when the stiffness coefficient of axial AMB is tuned to -8 and the rotating speed of MSFW rotor sets at 2000rpm. The maximum value of MSFW rotor's displacement deflection is reduced to 0.0049mm when the stiffness coefficient of axial AMB is 0.6. When the MSFW rotor works at 8000rpm and the stiffness coefficient of axial AMB is -0.8, the maximum value of MSFW rotor's displacement deflection deviating from the balanced position is 0.0139mm. The maximum value of MSFW rotor's displacement deflection is reduced to 0.0125mm when the axial AMB's stiffness coefficient is 0.6.

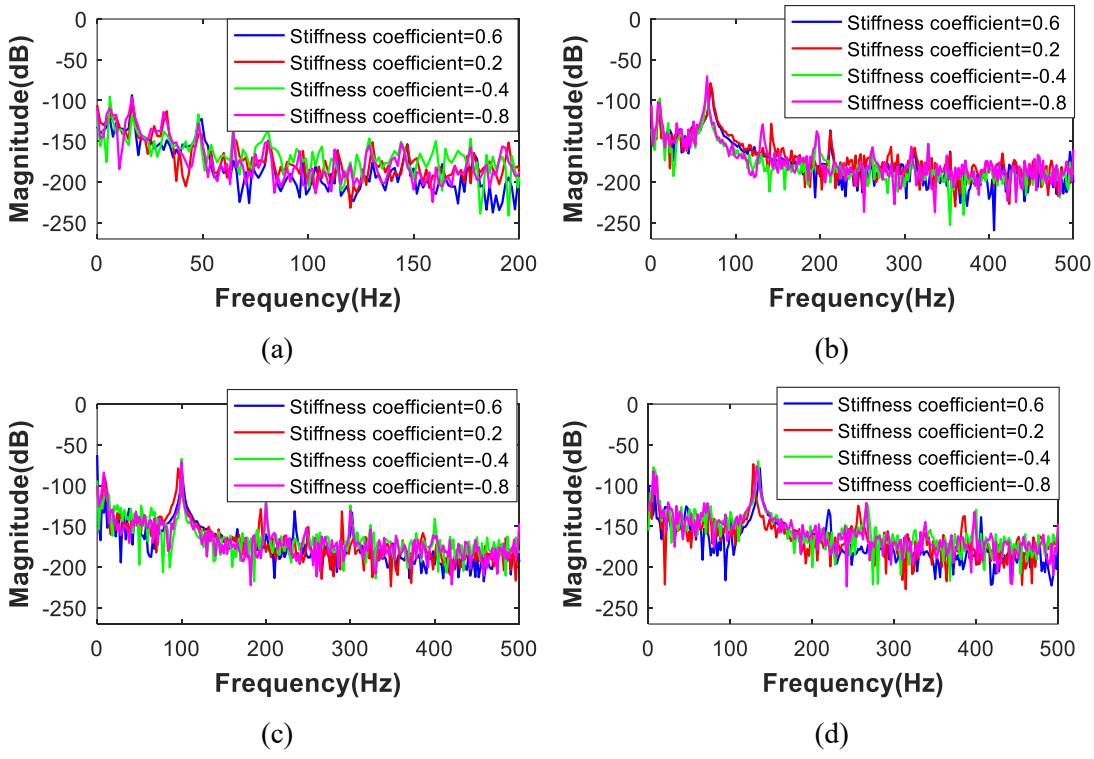

Fig. 4.20. The power spectrums of the MSFW rotor with different stiffness coefficients, (a) the rotational speed=2000rpm, (b) the rotational speed=4000rpm, (c) the rotational speed=6000rpm, (d) the rotational speed=8000rpm.

Moreover, the power spectrums of MSFW rotor's dynamic displacement deflections at 2000rpm are plotted in Fig. 4.20(a), and the response magnitude of MSFW rotor is about -113dB when the stiffness coefficient of axial AMB is -0.8, and then it is reduced to -148dB when the stiffness coefficient of axial AMB is increased to 0.6. The power spectrums of MSFW rotor at 8000rpm with different stiffness coefficients of the axial AMB are shown in Fig. 4.20(d),

and the response magnitude of MSFW rotor is about -70dB when the stiffness coefficient of axial AMB sets -0.8 and rotational speed is 8000rpm, and it would be reduced to -78dB with the stiffness coefficient of axial AMB increasing to 0.6.

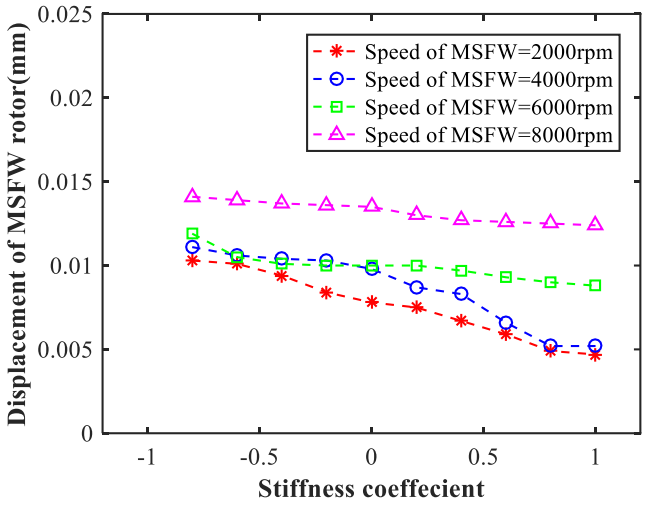

Fig. 4.21. The relationship between the maximum displacement deflection of the MSFW rotor and the stiffness coefficient of the axial AMB.

TABLE. 4.II. The dynamic displacement of the MSFW rotor using different stiffness coefficients of the axial AMB.

	Maximum displacement deflection (mm)			
Stiffness	**2000(rpm)**	**4000(rpm)**	**6000(rpm)**	**8000(rpm)**
8	0.0047	0.0052	0.0088	0.0124
0.6	0.0049	0.0052	0.0090	0.0125
0.4	0.0059	0.0066	0.0093	0.0126
0.2	0.0067	0.0083	0.0097	0.0127
0	0.0075	0.0087	0.0100	0.0130
-0.2	0.0078	0.0098	0.0100	0.0135
-0.4	0.0084	0.0103	0.0100	0.0136
-0.6	0.0094	0.0104	0.0101	0.0137
-0.8	0.0101	0.0106	0.0105	0.0139
-1	0.0103	0.0111	0.0119	0.0141

Based on above experimental results and analysis, the dynamic displacement variations of the MSFW rotor presents that the vibration amplitude would increase with its rotational speed. In the meanwhile, the vibration response of MSFW rotor could be mitigated by tuning the axial AMB's damping coefficient and stiffness coefficient. The effective control frequency of the vibration suppression could be covering all rotating speed of MSFW rotor.

4.5.4 The Vibration Response of MSFW Rotor in Acceleration Process

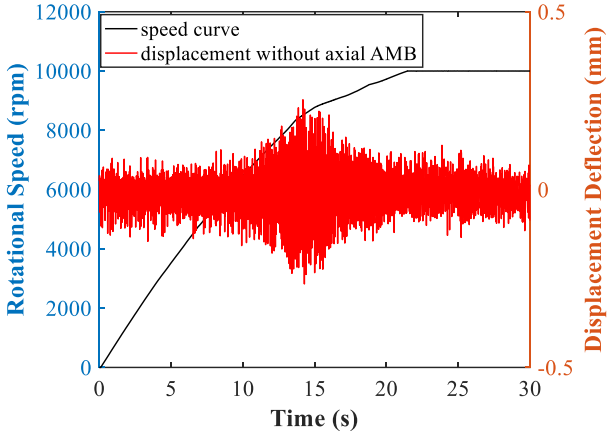

(a)

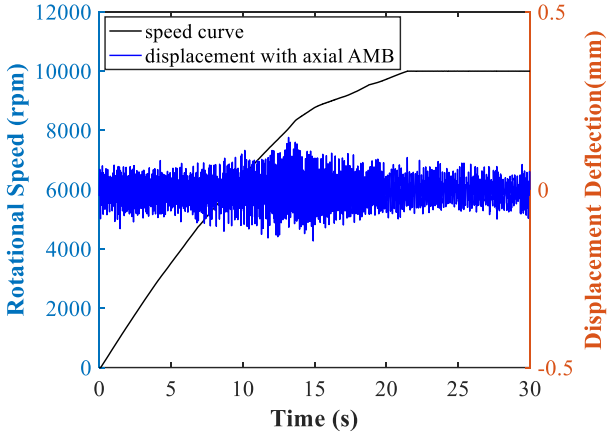

(b)

Fig. 4.22. The dynamic displacement deflections of MSFW rotor during the acceleration process, (a) without using the axial AMB, (b) with using the axial AMB.

The displacement deflections of MSFW rotor during the acceleration process form 0rpm to 10000rpm are illustrated in Fig. 4.22. The maximum displacement deflection (peak-peak value) is the physic term to assess the vibration response of MSFW rotor. When the tilting torque of axial AMB is not applied to compensate the disturbance torque of load rotor, the dynamic displacement variations deviating from the balanced position of MSFW rotor are plotted in Fig. 4.22(a), and the maximum value of dynamic displacement deviating from the balanced position is 0.5179mm during the acceleration process from 0rpm to 10000rpm. When the titling torque of axial AMB is used to mitigate the influence of disturbance torque acting on the load rotor during acceleration process, the maximum value of dynamic displacement deviating from the balanced position is reduced to 0.2912mm as shown in Fig. 4.22(b), and then

the relative reduction about the displacement deflection is about 43.8%. Therefore, the titling torque of axial AMB could be applied to suppress the vibration response of MSFW rotor during speed regulating process from the initial speed to the rated speed.

4.6 Summary

The axial AMB fixed on the right end and left end of the MSFW rotor is regarded as one kind of DVA to control the dynamic characteristics of the MSFW rotor. The active controllability of the axial AMB is analyzed using the theoretical models of the magnetic force and the tilting torque. The axial AMB's damping coefficient and comprehensive stiffness could be regulated by the closed loop displacement feedback control system of MSFW rotor. The damping coefficient and the stiffness coefficient of axial AMB could attenuate the vibration response of the MSFW rotor. In the meanwhile, the experimental results indicate that the maximum value of MSFW rotor's displacement variation deflecting from the balanced status increases with the rotating speed, also it is reduced with increasing of the damping coefficient and the stiffness coefficient of the axial AMB. Therefore, the AMB system could be applied to attenuate the vibration magnitudes of the motor with load rotor, so the applicable frequency width of vibration control could be enlarged.

Chapter 5. The Robust Control for MSFW Rotor

A DVA is applied to suppress the torsional vibration of MSFW rotor at rotation state. It is an additional device to improve the control precision of MSFW rotor. However, this DVA need enough space and control system to accomplish the stable control of MSFW rotor, so designing the suitable control method is very important to improve the control precision. Especially, the external disturbances could easily deflect MSFW rotor from its equilibrium status, and the current stiffness and the displacement stiffness of MSFW rotor will vary from their nominal values. Therefore, a robust control for MSFW rotor is needed to improve the disturbance attenuation and to reduce the influence caused by the uncertain displacement stiffness and current stiffness. In the following analysis, the motions of MSFW rotor are separated into translation and rotation. Different robust control schemes are designed and applied in the motion control of the MSFW rotor. On the one hand, for the translation of MSFW rotor, the H_∞ control function with a mixed sensitivity model would be proposed to attenuate uncertainties of current stiffness and displacement stiffness. For the rotation of MSFW rotor about radial directions, the μ-synthesis model is used to reject disturbances due to the variation of the rotational speed and the gyroscopic coupling. The numerical simulation is conducted to evaluate the anti-disturbance ability of the robust control model with an impulse disturbance, a sinusoidal disturbance, and a random disturbance. Finally, the experiment is conducted to validate the effectiveness of the proposed robust control model, and the conducted experiments show that the proposed robust control model has superior performance on suppressing the disturbance than the standard PID control model for the translational motion and the radial rotations of MSFW rotor.

5.1 The Uncertainty Analysis of Magnetic Force

Based on the magnetic force model of the axial and radial AMB developed in Chapter 2, the displacement stiffness k_d and the current stiffness k_i of the AMB system could be expressed as

$$\begin{cases} k_d = \dfrac{\mu_0 A N^2 I_0^2}{d_0^3} \\ k_i = \dfrac{\mu_0 A N^2 I_0}{d_0^2} \end{cases} \tag{5.1}$$

Therefore, the current stiffness and the displacement stiffness are affected by the bias airgap d_0 and the cross-sectional area A, so uncertain variations about the displacement stiffness and the current stiffness would be generated when the cross-sectional area and the bias airgap of the AMB vary from their nominal values. Especially, when there are mismatch and the assembly error between the MSFW rotor and the stator, the bias airgap will have an obvious deviation from the nominal value, and then the abrupt deflections of the current stiffness and the displacement stiffness from their respectively theoretical values would occur.

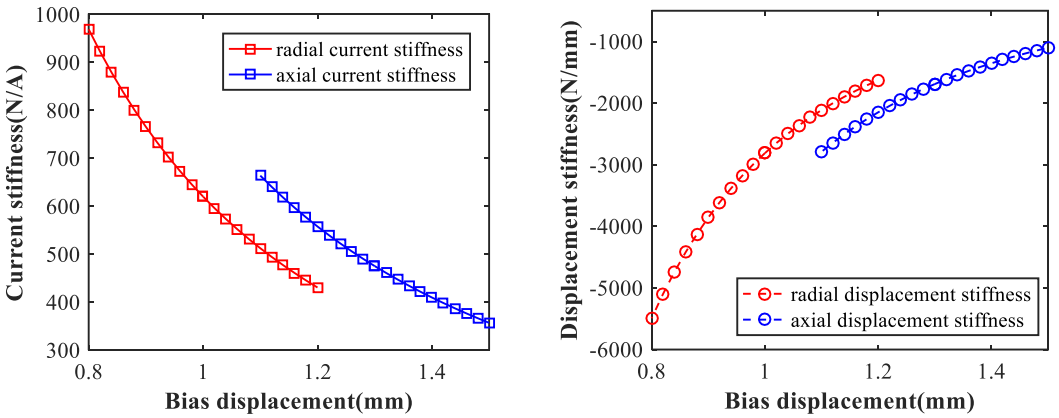

(a) (b)

Fig. 5.1. (a) The relationship between the deflection value of the current stiffness and the variation of the bias displacement, (b) The relationship between the deflection of the displacement stiffness and the variation the bias displacement.

The relationships among the variation of bias displacement, the variation of displacement stiffness, and the variation of current stiffness are shown in Fig. 5.1. For the magnetic suspension force generated by the radial AMB, when the nominal bias displacement is defined as 1mm and there is no deviation on bias displacement, the theoretical value of displacement stiffness in radial direction is -2800N/mm, and the theoretical value of current stiffness in radial direction is 620N/A. When the bias displacement of radial AMB varies 0.1mm from the balanced position in radial direction, the current stiffness in radial direction is reduced to 520N/A in Fig. 5.1(a), so the deflection value is 100N/A. The displacement stiffness in radial

direction is increased to -1800N/mm in Fig. 5.1(b), and then the deflection value is 1000N/mm. In addition, For the magnetic force of axial AMB, when the bias displacement in theory is defined as 1.3mm and there is no deviation on bias displacement, the theoretical value of axial current stiffness is 470N/A, and the theoretical value of axial displacement stiffness is -1700N/mm. When the axial bias displacement of axial AMB deflects 0.1mm from the balanced position in axial direction, the current stiffness in axial direction is reduced to 410N/A in Fig. 5.1(a), so the deflection value is 60N/A. The displacement stiffness in axial direction is increased to -1350N/mm in Fig. 5.1(b), and then the deflection value is 350N/mm.

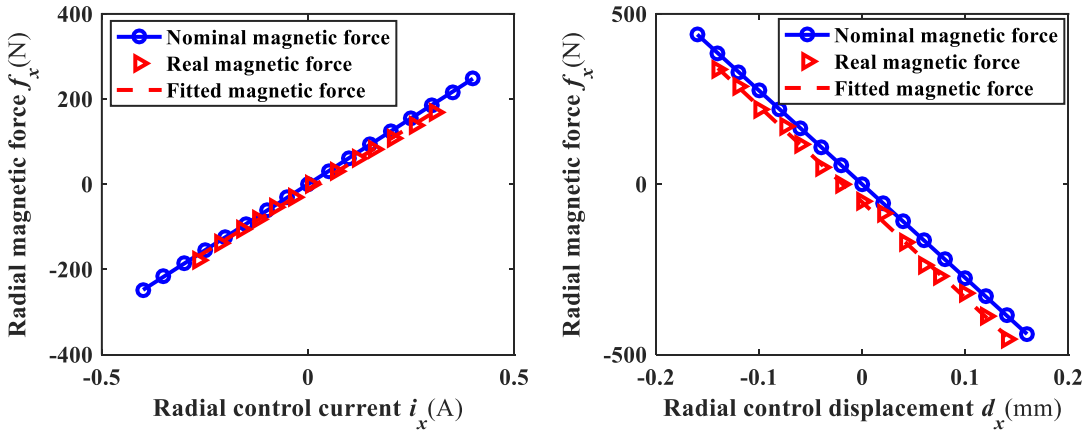

(a) (b)

Fig. 5.2. The radial magnetic force, (a) the relationship between radial control current and radial magnetic force, (b) (a) the relationship between radial control displacement and radial magnetic force.

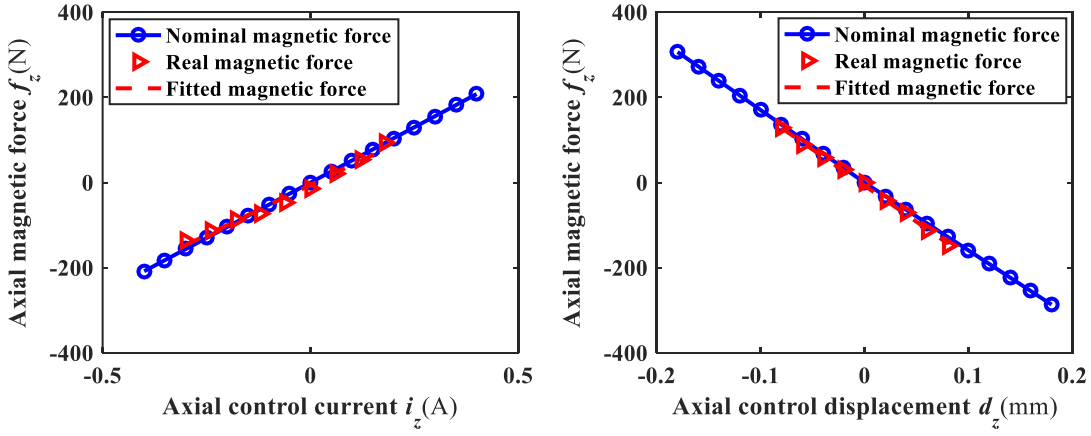

(a) (b)

Fig. 5.3. The axial magnetic force, (a) the relationship between axial control current and axial magnetic force, (b) the relationship between axial control displacement and axial magnetic force.

For the magnetic force in radial direction, the comparison curve between the nominal magnetic force and the real magnetic force is plotted in Fig. 5.2. The real magnetic force is presented by red triangle line, and the nominal magnetic force in radial direction is shown by blue circle line. The theoretical value of current stiffness is about 620N/A, and the theoretical value of displacement stiffness is about -2800N/mm. However, according to the linear fitting of the measured magnetic force in Fig. 5.2(b), the actual displacement stiffness is about -2810N/mm, and the actual current stiffness is about 608N/A. Similarly, the axial magnetic force is plotted in Fig. 5.3. The axial nominal current stiffness is 500N/A, and the axial nominal displacement stiffness is about -1700N/mm. Moreover, the actual displacement stiffness in axial direction is about -1702N/mm, and the actual current stiffness in axial direction is about 480N/A. Therefore, the actual displacement stiffness is quite close to the nominal displacement stiffness, but the current stiffness has obvious difference between the actual value and the nominal value.

5.2 The Control Model Design for MSFW Rotor

5.2.1 The Control Loop of MSFW Rotor's Translational Motion

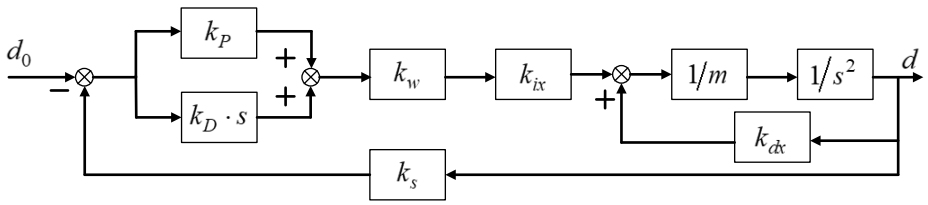

Fig. 5.4. The feedback control loop of translational motion in single DOF.

Based on the PD control model, the control scheme of the translational motion of the MSFW rotor is illustrated in Fig. 5.4. The control model of the translational motion includes the damping regulator k_D and the stiffness regulator k_P. The control voltage for the MAB system generated by the stiffness regulator and damping regulator is used to generate the control currents by the amplification coefficient k_w. The dynamic displacement vibrations of MSFW rotor deflecting from the equilibrium position are measured by the eddy current displacement sensor, and the sensitivity coefficient of the eddy current displacement sensor is k_s.

The magnetic force generated by the AMB could be expressed in terms of the displacement stiffness and the current stiffness as

$$f_x = k_{ix} i_x + k_{dx} d_x \tag{5.2}$$

Based on the displacement feedback of the MSFW rotor, the control current of the AMB could be written into

$$i_x = \left(k_P + k_D s\right) k_w k_s \cdot d_x \tag{5.3}$$

The magnetic force in radial direction could be rewritten as

$$f_x = \left(k_{ix} k_P k_w k_s + k_{dx}\right) \cdot d_x + k_{ix} k_D k_a k_s \cdot \dot{d}_x \tag{5.4}$$

And then, the closed loop transfer function of translational motion could be expressed as

$$G_t(s) = \frac{k_w k_s k_i k_D s + k_w k_s k_i k_P + k_d}{m s^2 + k_w k_s k_i k_D s + k_w k_s k_i k_P + k_d} \tag{5.5}$$

5.2.2 The Control Loop of MSFW Rotor's Rotational Motion

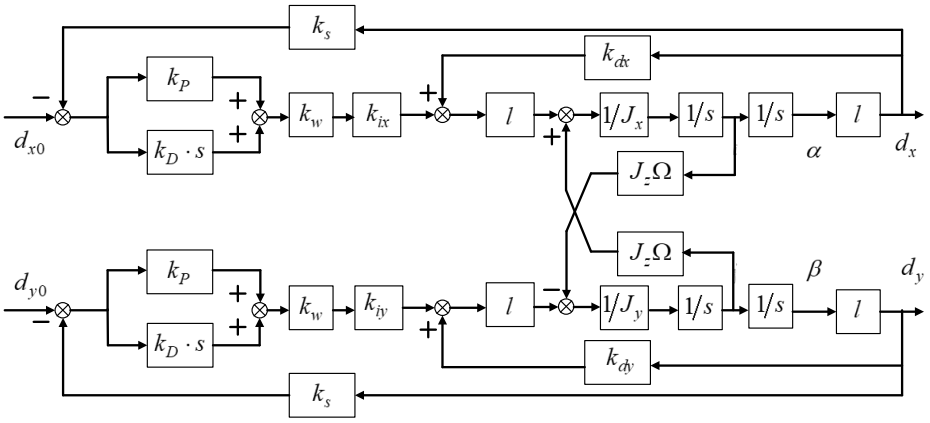

Fig. 5.5. The feedback control loop of MSFW rotor's rotational motion in two control DOFs.

The tilting torques outputted by the radial AMBs at the upper end and the lower end of MSFW rotor is used to control the rotational motion of the MSFW rotor. The rotational control scheme in two control DOFs of MSFW rotor is shown in Fig. 5.5. The gyroscopic coupling terms in two directions are introduced in the rotational motion, and they change with the rotating speed of MSFW rotor. Therefore, in the design procedure of the control system, the cross-feedback control including the rotating speed is utilized to control the gyroscopic coupling

terms in the rotational control of MSFW rotor. The nominal transfer function of rotational motion is expressed into

$$G_r(s) = \frac{2k_i k_w k_s (k_P + k_D s) l^2 + 2k_d l^2}{J_x s^2 - jJ_z \Omega s + 2k_i k_w k_s (k_P + k_D s) l^2 + 2k_d l^2} \tag{5.6}$$

5.3 The Robust Control Scheme of MSFW Rotor

5.3.1 The Controller Synthesis of Translational Motion

The controller synthesis for the translational motion of the MSFW rotor is illustrated in Fig. 5.6. $G_t(s)$ is the nominal transfer function of the translational motion. $K_t(s)$ is the controller function of the translational motion. $W_n(s)$ is defined as the transfer function of the input noise and the sensor noise. $W_d(s)$ is defined as the transfer function of the external disturbance. $W_p(s)$ is defined as the output weighting function, $W_e(s)$ is defined as the performance weighting function to evaluate the control performance of control model, and $W_u(s)$ is defined as defined as input weighting function.

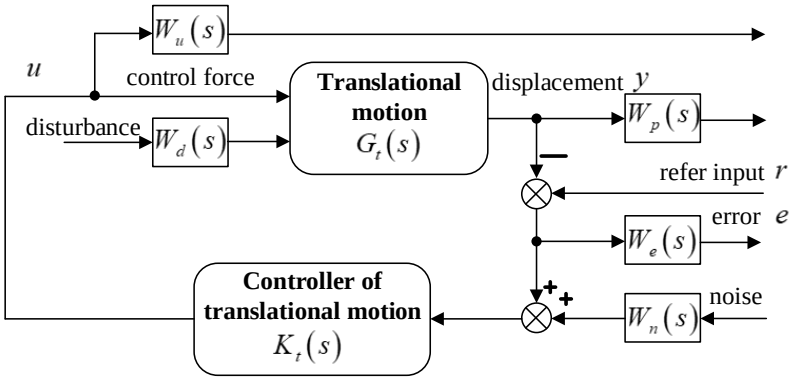

Fig. 5.6. The robust control scheme for the translational motion of the MSFW rotor.

Base on Eq.(5.5) and Eq. (5.6), the nominal transfer function $G_t(s)$ of the translational motion and the nominal transfer function $G_r(s)$ of the rotational motion satisfy the following conditions.

$$\begin{cases} \lim\limits_{s\to\infty} G_t(s) = 0 \\ \lim\limits_{s\to\infty} G_r(s) = 0 \end{cases} \tag{5.7}$$

So, the two closed-loop transfer functions of the translational motion and the rotational motion are both bounded input and bounded output response functions. For the control model synthesis of translational motion, the sensitivity function could be expressed into

$$S_t(s)=\frac{e_t(s)}{r_t(s)}=\frac{1}{1+G_t(s)K_t(s)} \tag{5.8}$$

The penalty sensitivity function is

$$R_t(s)=\frac{u_t(s)}{r_t(s)}=\frac{K_t(s)}{1+G_t(s)K_t(s)} \tag{5.9}$$

The complementary sensitivity function is

$$T_t(s)=\frac{y_t(s)}{r_t(s)}=\frac{G_t(s)K_t(s)}{1+G_t(s)K_t(s)} \tag{5.10}$$

Therefore, a stabilizing control function $K_t(s)$ should be used to guarantee the stability of the closed-loop transfer function of translational motion. The enhanced object model of the closed-loop transfer function is chosen as

$$\gamma_0=\min\left\|P_t\right\|_\infty=\min\left\|\begin{matrix}W_e(s)S_t(s)\\W_u(s)R_t(s)\\W_p(s)T_t(s)\end{matrix}\right\|_\infty \tag{5.11}$$

To keep the closed-loop stability of MSFW rotor's translational motion, the enhanced object model of the closed-loop transfer function must satisfy the followings

$$\gamma_0\le\gamma_t=\left\|P_t\right\|_\infty \tag{5.12}$$

where γ_t is chosen as the minimal optimization factor for the translational control system, so the robustness of the translational control system would be improved by increasing the value of γ_t.

The selections of the performance weighting function $W_e(s)$, the input weighting function $W_u(s)$ and the output weighting function $W_p(s)$ are decided by the minimal optimization factor. The performance weighting function $W_e(s)$ should designed as a low-pass filter to mitigate disturbance acting on the translational motion within low frequency range. The input weighting function $W_u(s)$ could reduce the order of the whole control system. The output weighting function $W_p(s)$ should be chosen as a high-pass filter with the high rising slope. Consequently,

the gain of complementary sensitivity function $T(s)$ could be weakened in high frequency range, and the gain of sensitivity function $S(s)$ would be weakened in low frequency range.

5.3.2 The Control Model Synthesis of Rotational Motion

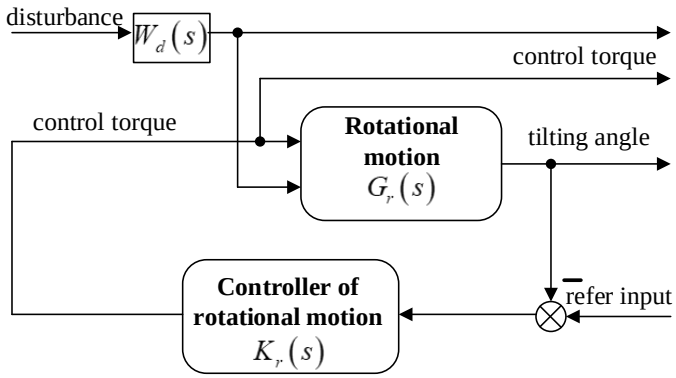

Fig. 5.7. The robust control scheme for the rotational motion of the MSFW rotor.

Based on the transfer function of the rotational motion in Eq.(5.6), the gyroscopic coupling terms existing in the rotational functions of MSFW rotor about radial axes would vary with rotating speed about the principal axial axis. Therefore, the gyroscopic coupling term is regarded as a variable disturbance besides other disturbance sources. For the rotational motion of the MSFW rotor, the gyroscopic coupling effect will be intensified with the increase of the rotational speed around the axial principal axis of the MSFW rotor. Moreover, the rotational motions of MSFW rotor about radial axes would cause the displacement stiffness and the current stiffness of radial AMB vary from their theoretical values. The uncertain current stiffness and the displacement stiffness could lead to disturbances on the rotational motions of MSFW rotor around radial axes. Therefore, a mixed μ-synthesis is chosen as the control method of rotational motion around radial axes, and the μ-synthesis control scheme is illustrated in Fig. 5.7, where $G_r(s)$ is the transfer function of the rotational motion and $K_r(s)$ is the synthesis controller of the rotational motion.

For the controller synthesis of the rotational motion, the sensitivity function could be expressed into

$$S_r(s)=\frac{e_r(s)}{r_r(s)}=\frac{1}{1+G_r(s)K_r(s)} \tag{5.13}$$

The penalty sensitivity function of rotational motion could be

$$R_r(s)=\frac{u_r(s)}{r_r(s)}=\frac{K_r(s)}{1+G_r(s)K_r(s)} \tag{5.14}$$

The complementary sensitivity function could be

$$T_r(s)=\frac{y_r(s)}{r_r(s)}=\frac{G_r(s)K_r(s)}{1+G_r(s)K_r(s)} \tag{5.15}$$

Therefore, a stabilizing control function $K_r(s)$ should be found to ensure the stability of closed-loop transfer function of the rotational motion around radial axes. The enhanced object model of the closed-loop transfer function is chosen as

$$\gamma_r=\min\|P_r\|_\infty=\min\left\|\begin{matrix}W_e(s)S_r(s)\\W_u(s)R_r(s)\\W_p(s)T_r(s)\end{matrix}\right\|_\infty \tag{5.16}$$

5.4 Numerical Simulation of Robust Control

5.4.1 The Uncertainty Analysis of Current Stiffness and Displacement Stiffness

5.4.1.1 The Uncertainty Response of Translational Motion

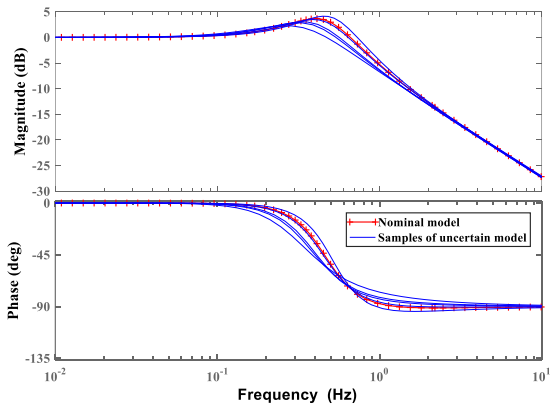

(a)

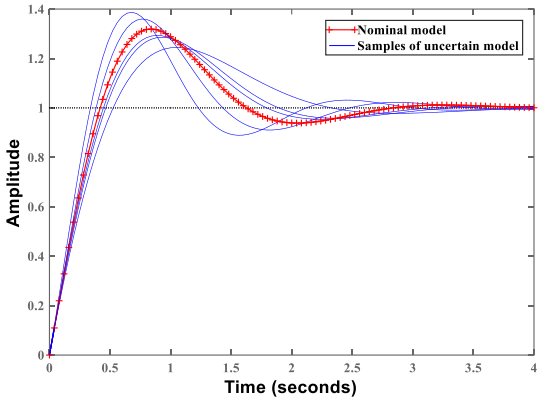

(b)

Fig. 5.8. The response curves of axial translation with uncertain current stiffnesses and displacement stiffnesses, (a) the frequency response curves of MSFW rotor's axial translation with uncertain current stiffnesses and displacement stiffnesses, (b) the step response curves of MSFW rotor's axial translation with uncertain current stiffnesses and displacement stiffnesses.

TABLE. 5.I. The simulation parameters of MSFW rotor system in robust control model.

Parameter	**Value**	**Unit**
Polar moment of inertia	J_m=0.67	kg·m^2
Equatorial moment of inertia	J_l=1.24	kg·m^2
Mass of MSFW rotor	m=150	kg
Current stiffness of radial AMB	k_{ix}=520	N/A
Displacement stiffness of radial AMB	k_{dx}=-2800	N/mm
Current stiffness of axial AMB	k_{iz}=500	N/A
Displacement stiffness of axial AMB	k_{dz}=-1700	N/mm
Distance from radial sensor to center of mass	l=476	mm
Amplification coefficient	k_w=0.2	A/V
Sensitivity of displacement sensor	k_s=3.3	V/mm
Proportional coefficient in axial translation loop	8.2	
Derivative coefficient in axial translation loop	20.5	

Based on the uncertainty analysis about the current stiffness and the displacement stiffness in section 5.1, and the system parameters used in simulation are listed in TABLE. 5.I, the deviation range of axial displacement stiffness as [-1800N/mm, -1600N/mm], and the changing range of axial current stiffness is chosen as [450N/A, 550N/A]. Moreover, comparing to translational motion of the MSFW rotor in radial direction, the axial translation is more complex because of the existence of self-weight, and the axial translation of MSFW rotor is selected as the analysis case in this chapter. With the uncertain current stiffness and displacement stiffness,

the frequency response and the step response of translational motion are illustrated in Fig. 5.8. The response curve of axial translation with the nominal model is plotted by red line, and the response curves of axial translation with uncertain models are plotted by blue line. For the step response of MSFW rotor in Fig. 5.8(b), there is distinct difference between the response magnitude of uncertain model and the response magnitude of theoretical model when the value of displacement stiffness and current stiffness departure from their theoretical values.

5.4.1.2 The Uncertainty Response of Rotational Motion

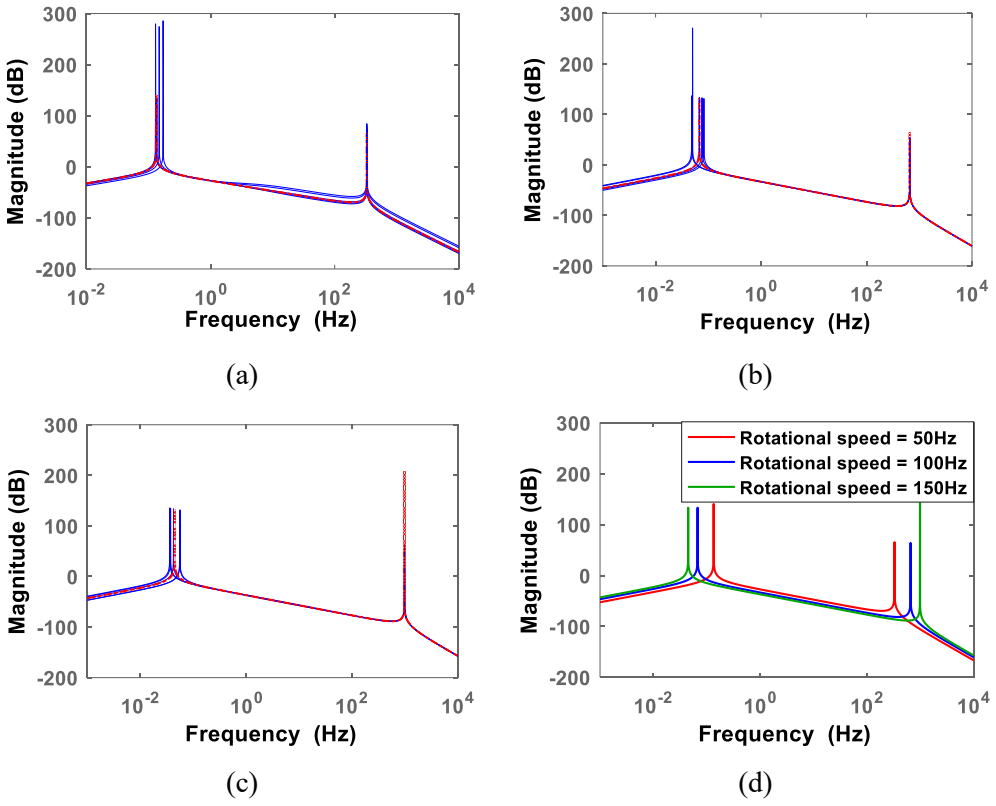

Fig. 5.9. The response curves of rotational motion at different rotating frequencies with uncertain current stiffnesses and displacement stiffnesses, (a) the rotating speed is 50Hz, (b) the rotating speed is 100Hz, (c) the rotating speed is 150Hz, (d) the response curves of the nominal rotational motion at different rotating speeds.

The uncertain range of displacement stiffness in radial direction is defined as [-2900N/mm, -2700N/mm], and varying range of current stiffness in radial direction is defined as [580N/A, 660N/A]. The frequency response curves of the MSFW rotor's rotational motions working at different rotating speeds are illustrated in Fig. 5.9. The frequency response curve of MSFW rotor's rotational motion with the nominal model is marked by red line, also the frequency response curves of MSFW rotor's rotational motion with the uncertain models are plotted by

blue line. The peak magnitude of BW motion occurs at low frequency, and the peak magnitude of FW motion happens at high frequency. When the displacement stiffness and the current stiffness deflect from the theoretical values, the response magnitude of the rotational motion has a distinct variation compared to the frequency response curve of the MSFW rotor with the nominal model. Moreover, the frequency response curves of MSFW rotor's rotational motion with theoretical model at different rotating speeds are shown in Fig. 5.9(d). The response magnitudes of the rotational motion change with the rotating speed of MSFW rotor. Consequent, the uncertainty about the current stiffness and the displacement stiffness also affects response curves of the rotational motion.

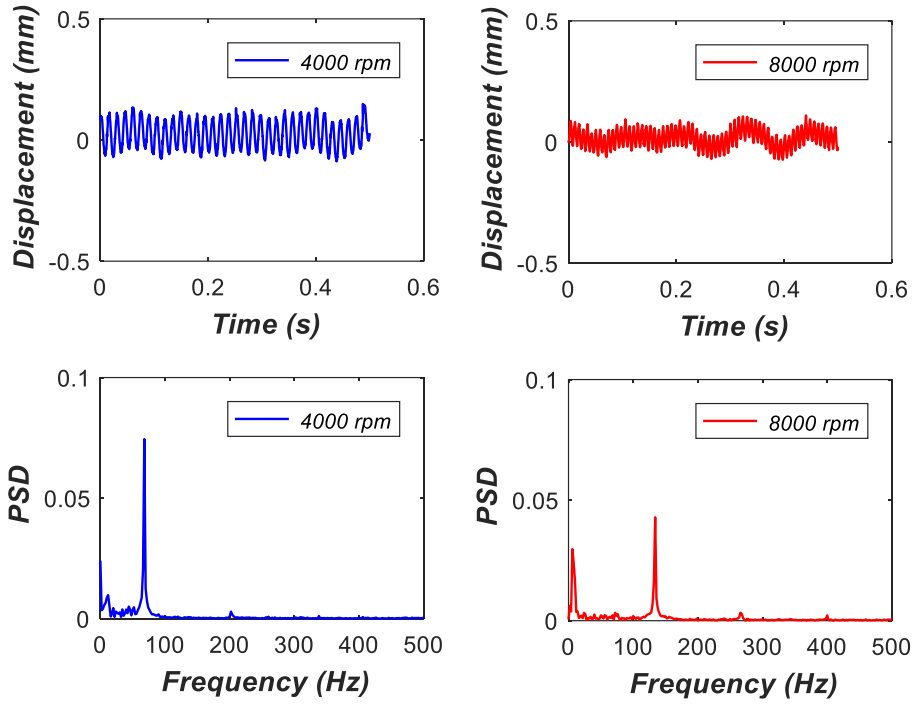

Fig. 5.10. The displacement deflection and PSD of the rotational motion, (a) the rotational speed is 4000rpm, (b) the rotational speed is 8000rpm.

The dynamic displacement deflection deviating from the balanced position of MSFW rotor will change with the variation of rotational speed. The maximum value of MSFW rotor's displacement deflections at 4000rpm is about 0.16mm as shown in Fig. 5.10, and the PSD of the dynamic displacement deflection at 67Hz (4000rpm) is 0.075. The maximum value of MSFW rotor's displacement deflections is 0.1mm when the rotating speed of MSFW rotor is

increased to 8000rpm, and the PSD of the dynamic displacement at 133Hz (8000rmp) is decreased to 0.04 while the PSD at the low frequency (6Hz) is increased to 0.03. So, when the MSFW rotor works at different rotational speeds, the dynamic displacement deflection, and the response magnitude of MSFW rotor would change, so the uncertainties of the current stiffness and the displacement stiffness will affect the control precision of the rotational motion.

5.4.2 The Robust Control Scheme for Translation

5.4.2.1 The Sensitivity and Performance Functions

According to the selection principles of the performance function and the sensitivity function introduced in section 5.3, the input weighting function of axial translation control is chosen as

$$W_{au}(s)=\frac{0.1s+10}{s+10} \tag{5.17}$$

The output weighting function of the axial translation control is

$$W_{ay}(s)=\frac{s+500}{0.01s+100000} \tag{5.18}$$

The performance weighting function of the axial translation control is

$$W_{ae}(s)=\frac{s+5000}{0.01s+10000} \tag{5.19}$$

The minimal value of the optimization factor is chosen as γ=0.5, so the H_∞ robust control function of the MSFW rotor's axial translation is expressed into

$$K_{at}(s)=\frac{0.2s^4+2.22\times10^6 s^3+2.01\times10^{12}s^2+4.3\times10^{13}s+4.29\times10^{13}}{s^5+1.01\times10^6 s^4+5.27\times10^9 s^3+1.37\times10^{12}s^2+1.38\times10^{13}s+6.34\times10^{12}} \tag{5.20}$$

The response curves of the output weighting function, the input weighting function and the performance weighting function for the axial translational motion of MSFW rotor are illustrated in Fig. 5.11. The response amplitude of the axial sensitivity function $S_a(s)$ is below the response amplitude of the input weighting function $1/W_{au}(s)$ in Fig. 5.11(a). The response amplitude of the axial control function $R_a(s)$ is below the response amplitude of the output weight function $1/W_{ay}(s)$ in Fig. 5.11(b). As illustrated in Fig. 5.11(c), the response amplitude

of the performance weighting function $1/W_{ae}(s)$ is greater than the response amplitude of the complementary sensitivity function $T_a(s)$.

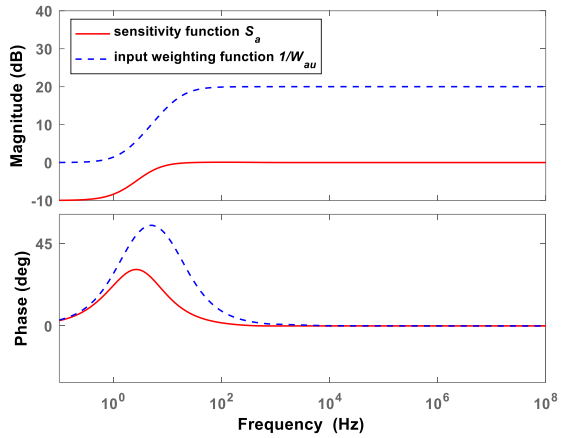

(a)

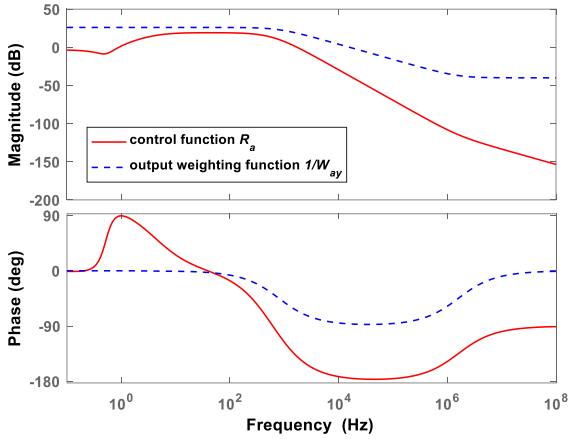

(b)

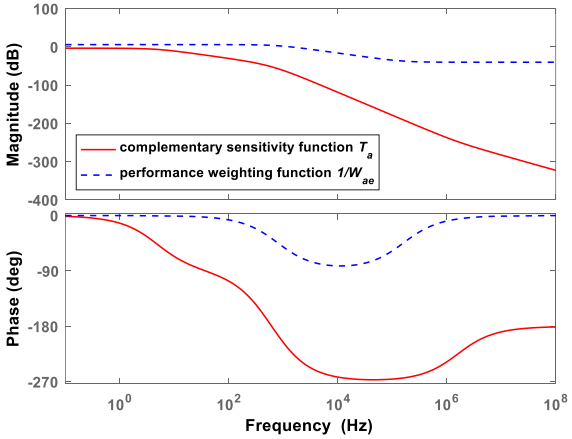

(c)

Fig. 5.11. The weighting functions of the MSFW rotor's axial translational control, (a) the response curves of the sensitivity function and the input weighting function, (b) the response curves of the control function and the output weighting function, (c) the response curves of the complementary sensitivity function and the performance weighting function.

For the translational control of MSFW rotor in radial direction, the input weighting function is

$$W_{ru}(s)=\frac{0.1s+50}{s+200} \tag{5.21}$$

The output weighting function of radial translational control is

$$W_{ry}(s)=\frac{s+5000}{0.01s+10000} \tag{5.22}$$

The performance weighting function of the radial translational control is

$$W_{re}(s)=\frac{s+5000}{0.01s+10000} \tag{5.23}$$

The frequency responses of the weighting functions and the performance function are illustrated in Fig. 5.12. The response amplitude of the radial translation's sensitivity function $S_r(s)$ is below the response amplitude of the input weighting function $1/W_{ru}(s)$ in Fig. 5.12(a). The response amplitude of the radial control function $R_r(s)$ is below that of the output weighting function $1/W_{ry}(s)$ in Fig. 5.12(b). As illustrated in Fig. 5.12(c), the response amplitude of performance weighting function $1/W_{re}(s)$ is greater than that of complementary sensitivity function $T_r(s)$.

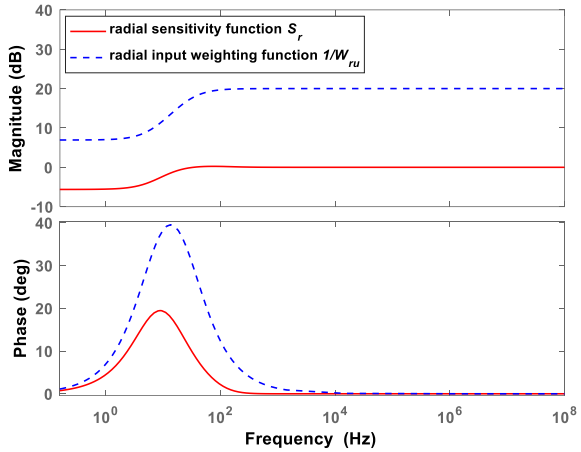

(a)

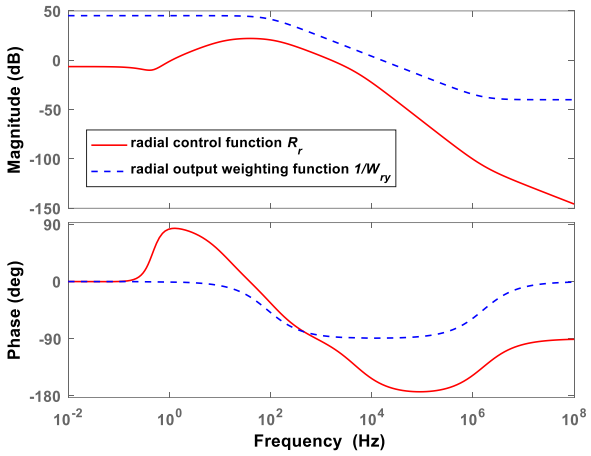

(b)

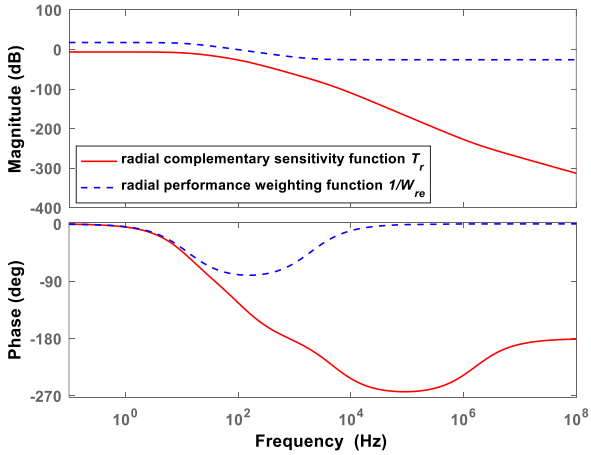

(c)

Fig. 5.12. The weighting functions of the radial translational control, (a) the response curves of the sensitivity function and the input weighting function, (b) the response curves of the control function and the output weighting function, (c) the response curves of the complementary sensitivity function and the performance weighting function.

The minimal value of the optimization factor γ=0.2. Therefore, the robust control function in the radial translational control is designed as

$$K_{rt}(s)=\frac{0.3s^4+6.07\times10^5 s^3+3.03\times10^{11}s^2+8.01\times10^{12}s+2.53\times10^{12}}{s^5+1.01\times10^6 s^4+5.36\times10^9 s^3+1.82\times10^{12}s^2+1.58\times10^{14}s+4.95\times10^{13}} \quad (5.24)$$

For the rotational control of the MSFW rotor with the gyroscopic coupling effect, the robust function could be designed as

$$K_r(s)=\frac{-85.18s^6-4\times10^4 s^5+8.3\times10^7 s^4+3.9\times10^{10}s^3+1.5\times10^{12}s^2+1.1\times10^{12}s+1.8\times10^{11}}{s^7+4.7\times10^2 s^6+2.2\times10^6 s^5+7.3\times10^8 s^4+6\times10^{10}s^3+5\times10^{11}s^2+2.9\times10^{11}s+4.7\times10^{10}} \quad (5.25)$$

The programming and coding about control functions of the translational and rotational motions in Eq.(5.20), (5.24) and (5.25) could be accomplished by the high-performance FPGA chip and the DSP chip in the MPU.

5.4.3 The Performance Comparison between Robust Control and PID Control

5.4.3.1 The Control Performances on Translational Motion

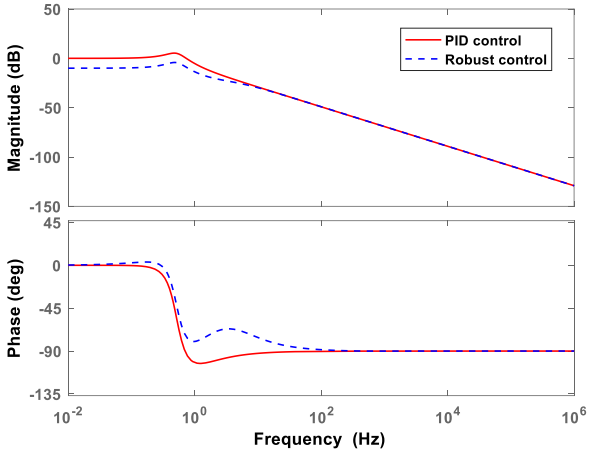

(a)

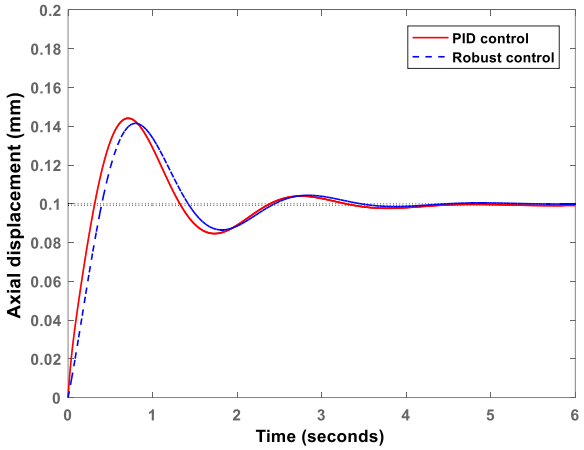

(b)

Fig. 5.13. The control performance of the axial translation, (a) the frequency response curves of the axial translation with PID control model and robust control model, (b) the step response curves of the axial translation with PID control model and robust control model.

In this part, numerical simulations are conducted to compare the control performances of the PID control model and the robust control functions applied in the axial translation and the radial rotation of MSFW rotor. Firstly, frequency response curves of translational control in

axial direction with the PID control model and the robust control function are compared. As shown in Fig. 5.13(a), the response magnitude of the robust control function is lower than response magnitude of the PID control model, so the robust control function owns better dynamic performance on translational control of MSFW rotor in axial direction than the PID control model. Moreover, the step response of the axial translational control is shown in Fig. 5.13(b). The step response curve of the robust control function is more precise than the PID control function, and then the robust control function owns higher control accuracy than the PID control in the axial suspension control of MSFW rotor.

When the MSFW rotor is stably suspended at the axial equilibrium point, an impulse disturbance is imposed on the MSFW rotor in axial direction. As shown in Fig. 5.14(a), the response curve of MSFW rotor with the PID control model is plotted by red line, and the response peak of axial displacement is 0.0268mm. Moreover, response curve of MSFW rotor with the robust control function is shown by blue line, and response peak of axial displacement is 0.0134mm. Therefore, the response amplitude of MSFW rotor with the robust control is quite lower than that of the PID control model in axial suspension control of MSFW rotor. In addition, the random disturbance is added on the axial suspension process of MSFW rotor as shown in Fig. 5.14(b). The RMS (root mean square) value of the dynamic displacement is used as the index for evaluating the control performance of MSFW rotor. The RMS value of the MSFW rotor with the PID control is about 0.0187mm, and the RMS of the MSFW rotor with the robust control is about 0.0067mm. The response curve of axial displacement is illustrated in Fig. 5.14(c) when a sinusoidal vibration source is imposed on the suspension process of MSFW rotor in axial direction, and the axial displacement of MSFW rotor oscillates with the sinusoidal vibration source. The response amplitude of the MSFW rotor with the PID control is about 0.0101mm, and the response magnitude of the MSFW rotor with the robust control function is about 0.0071mm.

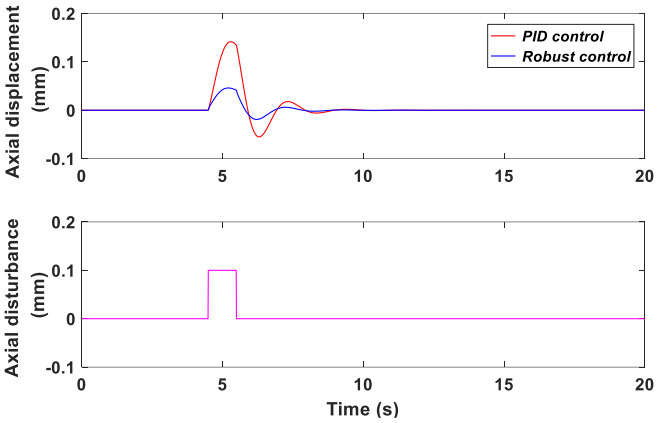

(a)

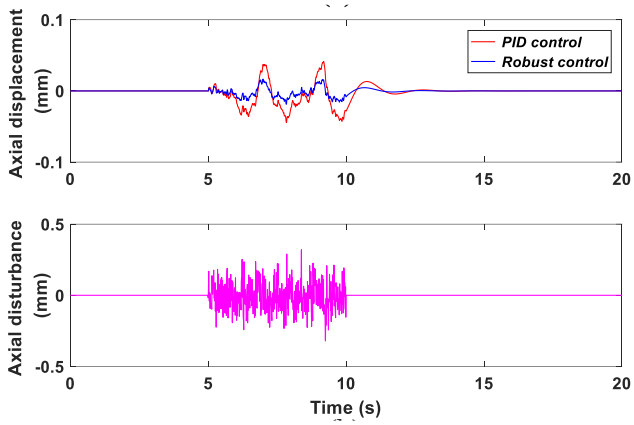

(b)

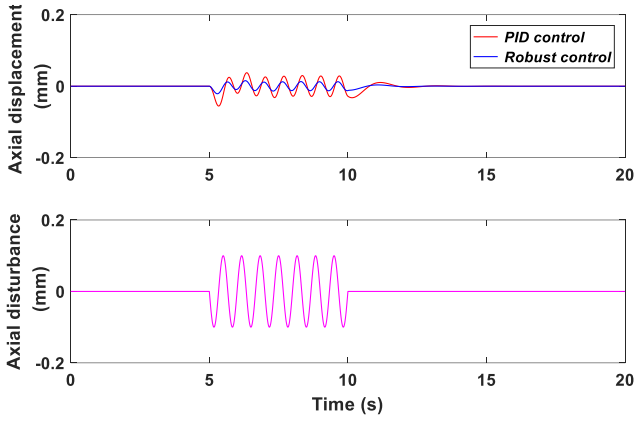

(c)

Fig. 5.14. The response curves of the MSFW rotor's axial suspension with the robust control function and PID control model when different disturbances are imposed on MSFW rotor, (a) the response curves of the MSFW rotor's axial suspension for the transient impulse disturbance, (b) The response curves of the axial suspension for the random disturbance, (c) The response curves of the axial suspension for the sinusoidal disturbance.

Above all, the simulations of the axial suspension of MSFW rotor with transient impulse disturbance, random disturbance, sinusoidal disturbances are developed, and simulation results indicate that the axial displacement of MSFW rotor would be affected by the disturbances

imposed on the axial suspension process. Moreover, as listed in TABLE. 5.II, comparing with the response magnitudes of the axial displacement of MSFW rotor, the robust control function has better ability on attenuating the disturbance force and torque than the PID control model for MSFW rotor with the uncertain current stiffness and displacement stiffness.

TABLE. 5.II. The control performance comparison of dynamic displacements in axial suspension with different disturbances.

	PID Control	Robust Control
Transient impulse disturbance (Peak)	0.0268mm	0.0134mm
Random disturbance (RMS)	0.0187mm	0.0067mm
Sinusoidal disturbance (Amplitude)	0.0101mm	0.0071mm

5.4.3.2 The Control Performances on Rotational Motion

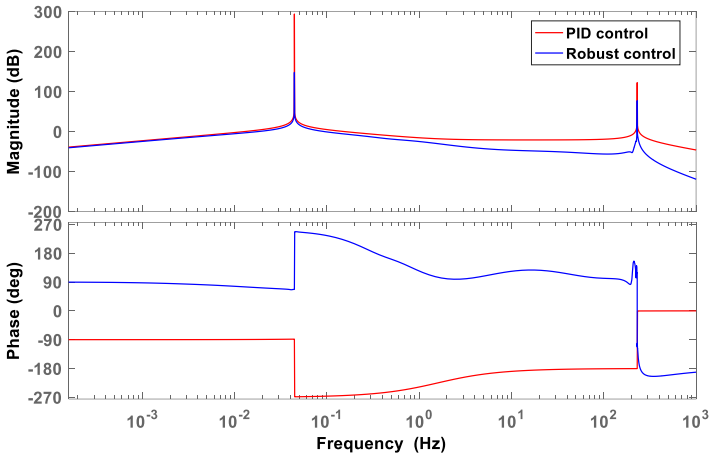

Fig. 5.15. The frequency response curves of the MSFW rotor's radial rotation function.

The simulation about the robust control function used in rotational control of MSFW rotor is conducted. The frequency responses of the rotational motion are illustrated in Fig. 5.15. The magnitude peak at low frequency is response peak of the BW motion, also the magnitude peak at high frequency is the response peak of the FW motion. The BW motion happens at 0.5Hz, and the FW motion occurs at 240Hz. For the robust control function, the response magnitude of the BW motion is about 148dB, and the response magnitude of the FW motion is about 76dB. For the PID control model, the response magnitude of the BW motion is about 294dB, and the response magnitude of the FW motion is about 122dB. Consequent, the robust control function

applied in the rotational motion of MSFW rotor can effectively suppress frequency responses of the BW and FW motions.

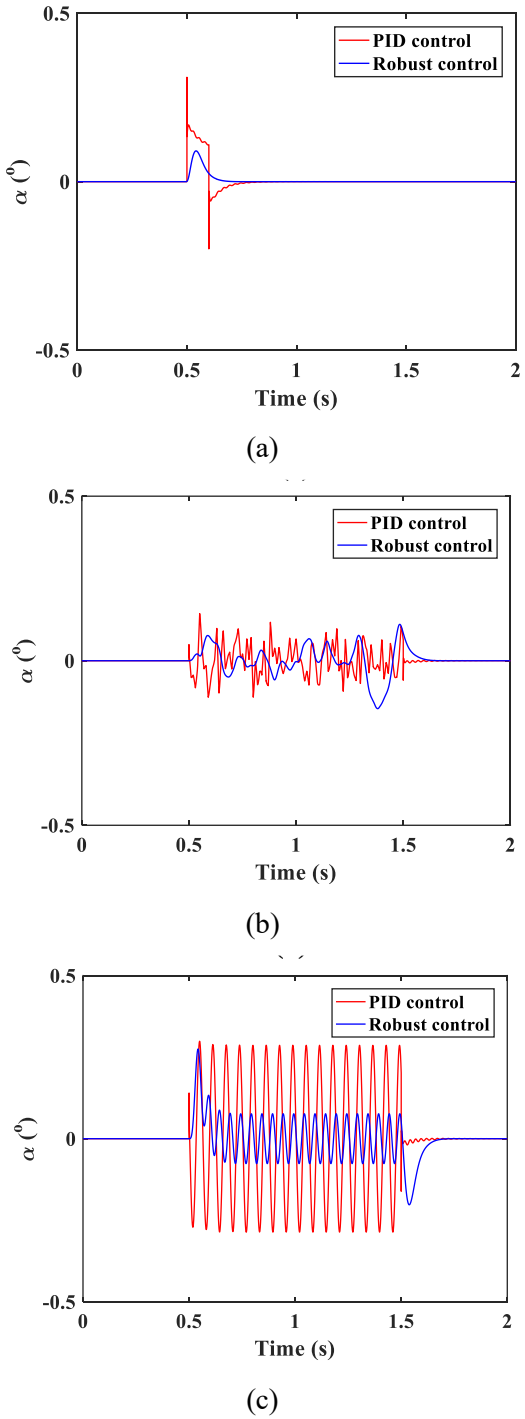

Fig. 5.16. The angle response of the MSFW rotor's rotation for different disturbances, (a) the impulse disturbance, (b) the random disturbance, (c) the sinusoidal disturbance.

An impulse disturbance, a random disturbance and a sinusoidal disturbance are imposed on the rotational motion of MSFW rotor, respectively, and the dynamic deflection of rotational angle α is chosen as the stability index of rotational motion. Firstly, an impulse disturbance is

imposed on rotational motion around radial axes of MSFW rotor, and the dynamic response magnitudes of rotational angles are shown in TABLE. 5.III and Fig. 5.16(a). For the PID control model used in the rotational motion of MSFW rotor, the peak-peak value of rotational angle around radial axis is 0.3099°. The peak-peak value of rotational angle with the robust control function is 0.09014°. Moreover, as shown in Fig. 5.16(b), when a random disturbance is acting on the rotational motion of MSFW rotor, the RMS value of MSFW rotor's rotational angle with the PID control model is 0.0433°, and the RMS value of MSFW rotor's rotational angle rotor with the robust control is reduced to 0.0089°. A sinusoidal disturbance is applied to the rotational motion of MSFW rotor as shown in Fig. 5.16(c). The response magnitude of MSFW rotor's rotational angle with the PID control model is 0.299°. The maximum response magnitude of MSFW rotor's rotational angle with the robust control function is 0.2749°, and the steady state value of MSFW rotor's rotational angle is about 0.1012°.

Above all, for the axial suspension and the rotational motion of MSFW rotor with uncertain displacement stiffness and current stiffness, the obtained simulation results show that the robust control function has better ability to reject the influences of disturbance forces and torque acting on the MSFW rotor than the PID control.

TABLE. 5.III. Comparison of control performance for the rotational motion.

	PID Control	**Robust Control**
Transient impulse disturbance (Peak)	0.3099°	0.0914°
Random disturbance (RMS)	0.0433°	0.0089°
Sinusoidal disturbance (Amplitude)	0.2749°	0.1012°

5.5 Experimental Verification of Stable Suspension

5.5.1 The Axial Stable Suspension of MSFW Rotor

The axial stable suspension is the most critical condition of MSFW rotor, and then the high-speed rotation could be realized. This section is about the experimental test for the stable suspension performance of the MSFW rotor in axial direction. The MSFW rotor is stably suspended at the axial equilibrium position, so the axial displacement deflection of MSFW rotor

would be zero. The load rotors with different masses are respectively imposed on coupling shaft of MSFW rotor along the axial direction. If the displacement deflection of the MSFW rotor occurs, the magnetic force generated by the axial AMB pushes MSFW rotor back to the equilibrium position based on the negative displacement feedback of MSFW rotor in axial direction. The displacement difference between the maximum value of displacement deflection and the minimum value of displacement deflection is used to analyze the dynamic characteristics of MSFW rotor with different loads.

As shown in Fig. 5.17, the response curve of MSFW rotor with the robust control function is shown by blue line, and the response curve of MSFW rotor with the PID control model is shown by red line. As shown in Fig. 5.17(a), when the load rotor with 20kg is imposed on MSFW rotor in axial direction, and the maximum value of the MSFW rotor's displacement deflection with the PID control model is about 0.55mm, and the maximum value of the MSFW rotor's displacement deflection using the robust control function is about 0.38mm. The maximum displacement deflection of the MSFW rotor with the PID control model is 0.63mm when the load with 40kg is imposed on coupling shaft of MSFW rotor in axial direction, the maximum value of the MSFW rotor's displacement deflection with the robust control function is reduced to 0.40mm. When load rotor is imposed on the MSFW rotor increases to 60kg in axial direction, the maximum displacement deflection of MSFW rotor with the PID control model is about 0.95mm, and that of the robust control function is about 0.53mm.

TABLE. 5.IV. The control performance comparison of dynamic displacements in axial suspension with different loads.

	PID Control	**Robust Control**	**Reduction**
Weight of load=20kg	0.556mm	0.38mm	30.9%
Weight of load=40kg	0.63mm	0.40mm	36.5%
Weight of load=60kg	0.95mm	0.53mm	44.2%

Therefore, as illustrated in TABLE. 5.IV, the comparison results between the maximum displacement deflection of MSFW rotor using the PID control model and maximum value of the MSFW rotor's displacement deflection using the robust control function show that the

robust control function are more effectively on reducing the effect of the disturbance imposing on the axial suspension process of MSFW rotor than PID control model.

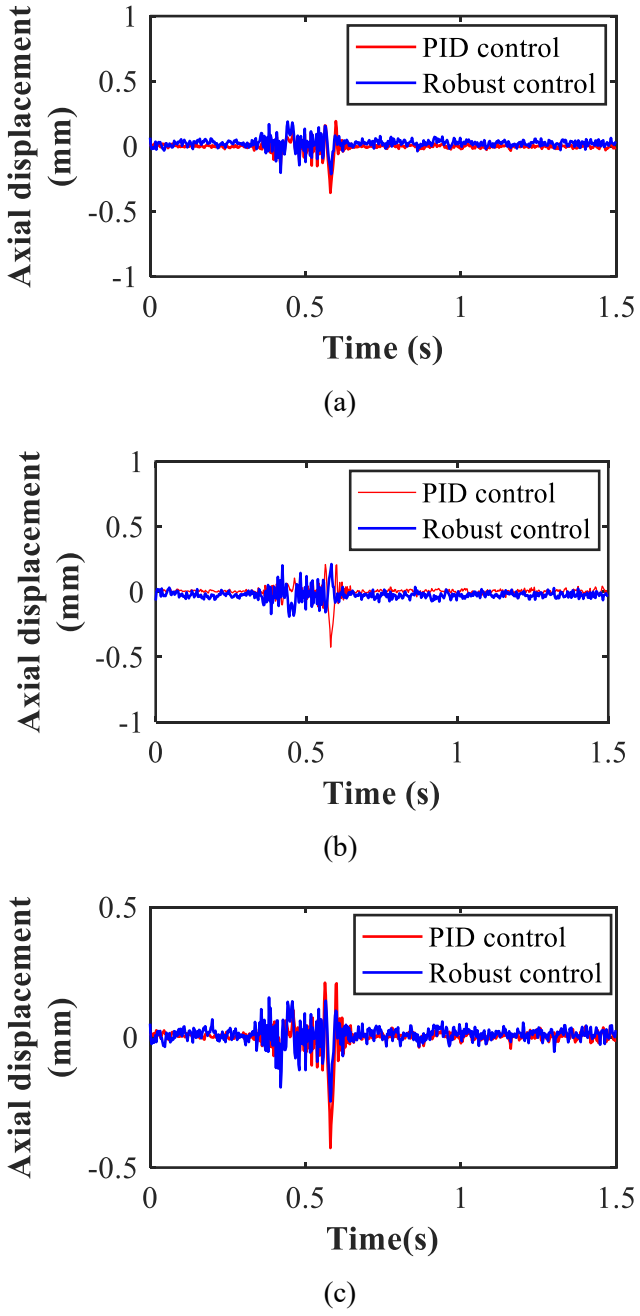

Fig. 5.17. The suspension curves of MSFW rotor with different loads in axial direction, (a) the suspension curve of MSFW rotor with 20kg load, (b) the suspension curve of MSFW rotor with 40kg load, (c) the suspension curve of MSFW rotor with 60kg load.

5.5.2 The Dynamic Suspension Process of MSFW Rotor

Moreover, the experiment tests of the dynamic suspension process of MSFW rotor with different loads are conducted to compare the control performances of the PID control and the

robust control. For the suspension curve of the MSFW rotor in axial direction, the suspension displacement of the MSFW rotor with the PID control and the robust control are compared, and the response peak and the settling time of the axial suspension process are used as the evaluation indices of the control performance for the MSFW rotor.

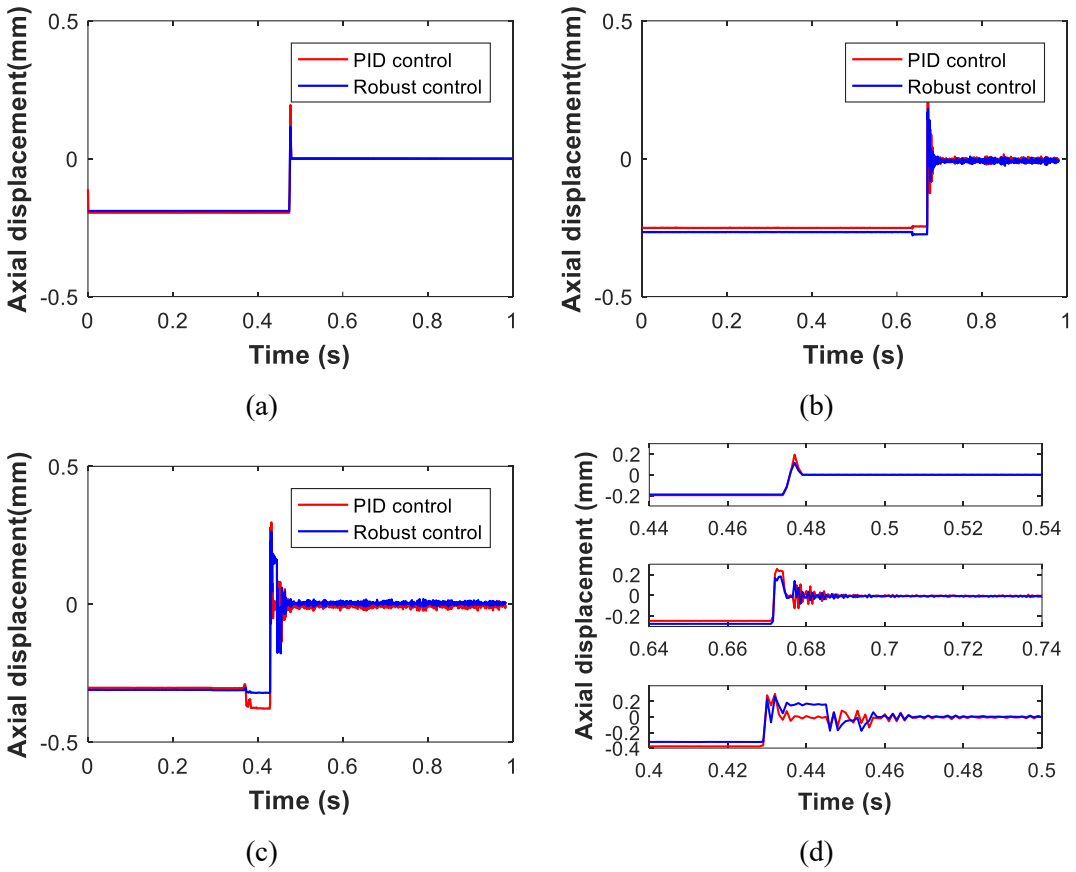

Fig. 5.18. Dynamic suspension processes of the MSFW rotor with different loads in axial direction, (a) the weight of load is 20kg, (b) the weight of load is 40kg, (c) the weight of load is 60kg, (d) the details of dynamic suspension process.

As shown in Fig. 5.18(a), when a 20kg load rotor is imposed on MSFW rotor in axial direction, the maximum transient response amplitude of MSFW rotor with the PID control model is about 0.19mm, and maximum transient response amplitude of MSFW rotor using the robust control function is 0.12mm. Moreover, the dynamic suspension process of MSFW rotor is shown in Fig. 5.18(b) when the load rotor is increased to 40kg. The transient response amplitude of the MSFW rotor with the PID control model is 0.26mm, but transient response amplitude of the MSFW rotor with the robust control function is reduced to 0.18mm. The dynamic suspension process of MSFW rotor is illustrated in Fig. 5.18(c) when the load rotor is

60kg. The transient response amplitude of the PID control model is 0.30mm, and that of the robust control function is about 0.26mm. Specifically, the partially details of the dynamic suspension process are illustrated in Fig. 5.18(d). The settling time of dynamic suspension in axial direction would be increased with the weight of load rotor added on MSFW rotor in axial direction. According to the comparison result (as listed in TABLE. 5.V) between the dynamic suspension processes of MSFW rotor with the PID control model and the robust control function in axial direction, the robust control function is more helpful on improving the suspension precision of MSFW rotor than the PID control model.

TABLE. 5.V. The control performance comparison of dynamic displacements in axial suspension using PID control model and robust control function with different loads.

	PID Control	Robust Control	Reduction
Weight of load=20kg	0.19mm	0.12mm	36.8%
Weight of load=40kg	0.26mm	0.18mm	30.8%
Weight of load=60kg	0.30mm	0.26mm	13.3%

5.5.3 The Disturbance Attenuation of Rotational Motion

Besides comparison result of control performances on translational suspension process of MSFW rotor in axial direction, the control performances of the PID control method and the robust control function on rotational motion are also analyzed. First, an impulse disturbance is adding on the rotational motion of MSFW rotor at different rotational speeds, and the maximum displacement deflection of MSFW rotor deviating from balanced position is utilized to evaluate the suspension precision of the applied control method.

As illustrated in Fig. 5.19(a), an impulse disturbance is imposed on the rotational motion of MSFW rotor when the rotating speed is 2000rpm. The displacement deflections in radial direction of MSFW rotor with the PID control model are plotted by red line, and the radial displacement deflections in radial direction of MSFW rotor with the robust control function are marked by blue line. The maximum displacement deflection of the MSFW rotor with the PID control in radial direction is 0.38mm, and that of the robust control is reduced to 0.24mm. The relative reduction is about 36.8%. Furthermore, the radial dynamic displacements of the MSFW

rotor adding an impulse disturbance are shown in Fig. 5.19(b) when the rotating speed of MSFW rotor is increased to 4000rpm. The maximum value of MSFW rotor's displacement deflection with the PID control model is about 0.97mm, and the maximum value of MSFW rotor's displacement deflection using the robust control function is declined to 0.70mm, so the relative decrease is about 27.8%.

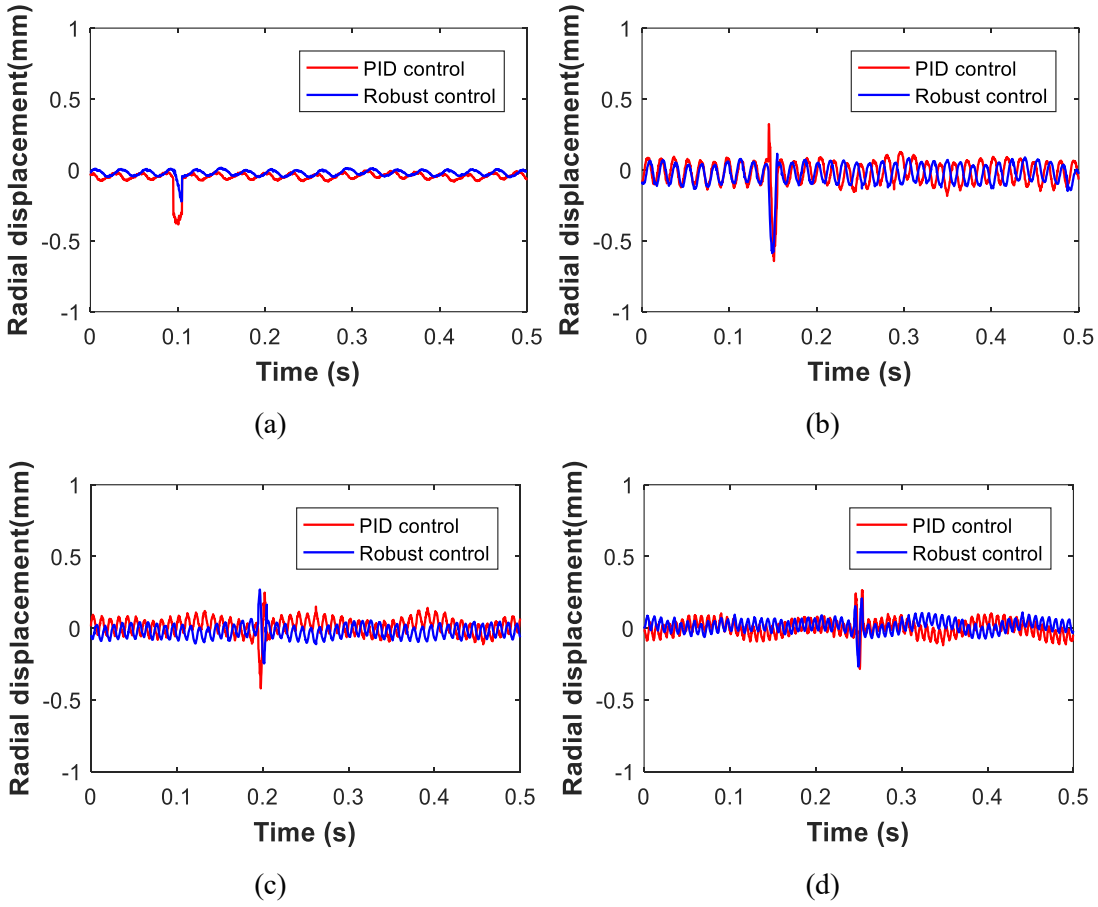

Fig. 5.19. The radial displacement of MSFW rotor with adding an impulse disturbance at different rotational speed, (a) the rotational speed is 2000rpm, (b) the rotational speed is 4000rpm, (c) the rotational speed is 6000rpm, (d) the rotational speed is 8000rpm.

An impulse disturbance is impacted on the rotational motion of MSFW rotor at 6000rpm. The dynamic response of MSFW rotor's radial displacement is shown in Fig. 5.19(c). The maximum displacement deflection of MSFW rotor with the PID control model is about 0.67mm, and that with the robust control function is reduced to 0.52mm, so the relative reduction on the maximum value of MSFW rotor's displacement deflection is 22.4%. The rotating speed of MSFW rotor is increased to the rated speed 8000rpm, the maximum value of MSFW rotor's displacement deflection using PID control model is 0.55mm in radial direction, and the

maximum value of MSFW rotor's displacement deflection using the robust control function is about 0.48mm, so the relative decline on the maximum value of MSFW rotor's displacement deflection is about 12.7%.

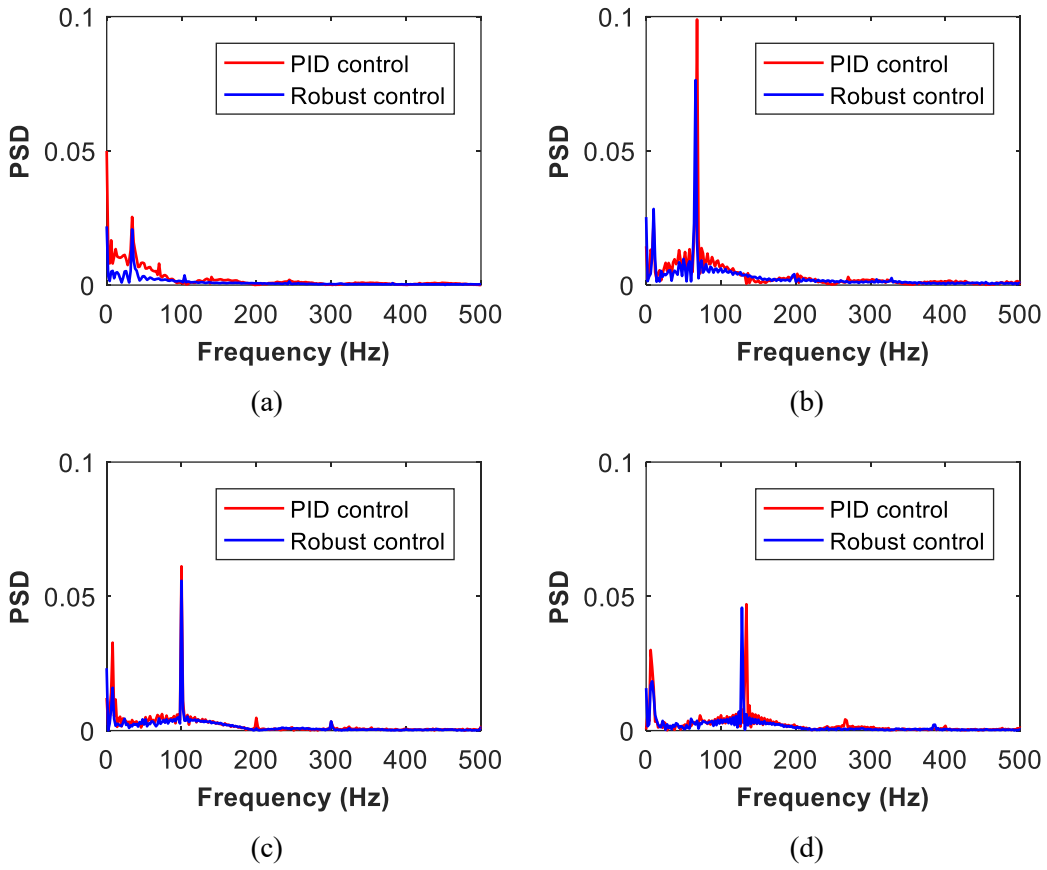

Fig. 5.20. The PSD of the radial displacement of MSFW rotor with adding an impulse-type disturbance, (a) the rotational speed is 2000rpm, (b) the rotational speed is 4000rpm, (c) the rotational speed is 6000rpm, (d) the rotational speed is 8000rpm.

TABLE. 5.VI. Comparison of the MSFW rotor's radial displacements with different control models.

	PID Control	Robust Control	Reduction
speed=2000rpm	0.38mm	0.24mm	36.8%
speed=4000rpm	0.97mm	0.70mm	27.8%
speed=6000rpm	0.67mm	0.52mm	22.4%
speed=8000rpm	0.55mm	0.48mm	12.7%
speed-up process	0.72mm	0.52mm	27.8%

The PSD of MSFW rotor's displacement in radial direction is shown in Fig. 5.20. As shown in Fig. 5.20(a), the PSD of the radial displacement with the PID control model is 0.025 when the rotating speed of MSFW rotor is 2000rpm, and the PSD of the radial dynamic

displacement with the robust control function is attenuated to 0.02. As shown in Fig. 5.20(d), the PSD of radial dynamic displacement with the PID control model at 134Hz is 0.047 when the rotating speed of MSFW rotor is accelerated to 8000rpm, and the PSD of radial dynamic displacement with the robust control function is 0.045.

According to TABLE. 5.VI, the comparison results between the maximum displacement deflection of MSFW rotor in radial direction using the PID control model and the robust control function validate that the robust control function is more effectively on attenuating the vibration responses caused by the disturbance forces and torque than PID control model for the rotational motion of MSFW rotor.

5.5.4 The Displacement Deflection of MSFW Rotor during Speed Regulation Process

The dynamic displacement variations of MSFW rotor during the speed regulation process are shown in Fig. 5.21. The rotating speed of MSFW rotor is accelerated from 0rpm to 7800rpm, and the dynamic displacement deflections of MSFW rotor in radial direction are measured. As shown in Fig. 5.21, the radial displacement deflection increases with the rotational speed of the MSFW rotor, and then it reaches to the constant term when the rotating speed reaches to rated rotating speed of MSFW rotor. The maximum value of MSFW rotor's displacement deflection in radial direction with the PID control model is shown in Fig. 5.21(a). The maximum displacement deflection of MSFW rotor in radial direction is 0.72mm. For the robust control, the maximum displacement deflection of MSFW rotor in radial direction is 0.52mm. As a result, the maximum dynamic displacements of MSFW rotor indicate that the robust control model could improve the stability of MSFW rotor during the speed-up process.

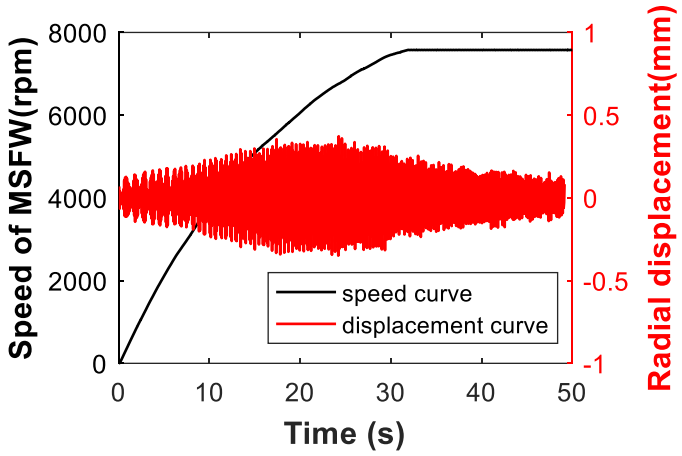

(a)

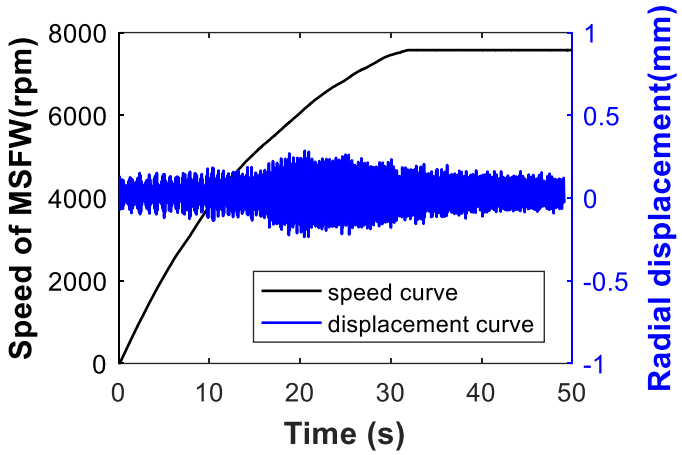

(b)

Fig. 5.21. The radial displacement of the MSFW rotor during the speed-up, (a) the radial displacement deflections of MSFW rotor using PID control model, (b) the radial displacement deflections of MSFW rotor using robust control function.

5.6 Summary

The uncertainties about the current stiffness and the displacement stiffness of the AMB system in the MSFW rotor are analyzed, and a robust control scheme for different motions of MSFW rotor is designed to attenuate disturbances imposing on MSFW rotor. The nominal values of the displacement stiffness and the current stiffness would be affected by the initial location of MSFW rotor, so the dynamic suspension process of the MSFW rotor could not be accurately controlled. Moreover, the external disturbances imposing on MSFW rotor affect the theoretical values of displacement stiffness and current stiffness too. Therefore, the robust control scheme is proposed to dwindle the disturbance responses of the translational motion

and the rotational motion. The simulation result indicated that the robust control function could improve the ability on diminishing the disturbance response of MSFW rotor than the PID control model when a transient impulse disturbance, a sinusoidal disturbance or a random disturbance is imposed on the MSFW rotor, respectively. Finally, the experimental results show that the maximum value of MSFW rotor's displacement deflection with the robust control function is smaller than that with the PID control model when the MSFW rotor works at different rotational speeds. Thence, the proposed robust control function of MSFW rotor could improve the control precision by reducing the effect of the disturbances acting on the MSFW rotor.

Chapter 6. The Internal Mode Control of MSFW Rotor

In Chapter 5, the robust control function is designed to improve the anti-disturbance ability of MSFW rotor with great weight, but gyroscopic coupling terms among four control channels in radial direction still exist which could also affect the control precision of the MSFW rotor. Therefore, the decoupling control could be designed to accomplish decoupling control of MSFW rotor without affecting the control precision.

For the MSFW rotor structure with great equatorial moment of inertia and the great self-weight, the system parameters such as the displacement stiffness and the current stiffness could often deflect from their nominal values, so the MSFW rotor with the great equatorial moment of inertia and the great self-weight is more sensitive to the parameter variations and the external disturbances. Moreover, the coupling terms varying with the rotating speed of MSFW rotor exist in the radial rotation of MSFW rotor. Therefore, the IMC and decoupling internal model control (DIMC) models are researched to accomplish the decoupling control among four DOFs in radial direction and improve the robustness of MSFW rotor with great equatorial moment of inertia and the great self-weight. Through applying the IMC model, the robust stability of the MSFW rotor with great equatorial moment of inertia and the great self-weigh could be improved when it turns at a high rotational speed. Furthermore, the DIMC model could accomplish the decoupling control in four radial control channels of the MSFW rotor, so the gyroscopic coupling effect in four radial control channels could be mitigated.

6.1 The Dynamic Model of MSFW Rotor for IMC

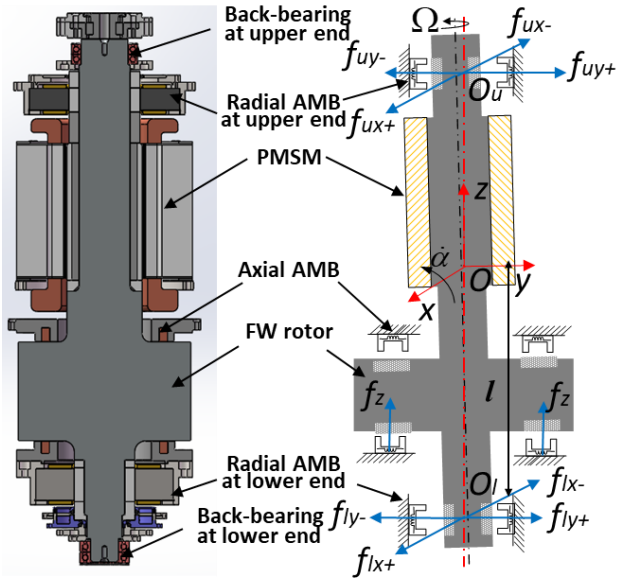

(a) (b)

Fig. 6.1. (a) the prototype of the MSFW rotor, (b) the force of the MSFW rotor.

The force analysis of the MSFW rotor is illustrated in Fig. 6.1, based on the dynamic model of the MSFW rotor in Eq.(2.22) and Eq.(2.23), the dynamic model of the MSFW rotor for the IMC model could be rewritten into

$$\begin{cases} m\ddot{d}_x = f_{ux+} - f_{ux-} + f_{lx+} - f_{lx-} = f_{ux} + f_{lx} \\ m\ddot{d}_y = f_{uy+} - f_{uy-} + f_{ly+} - f_{ly-} = f_{uy} + f_{ly} \\ J_x\ddot{\alpha} = f_{ux} \cdot l + f_{lx} \cdot l + J_z\Omega\dot{\beta} \\ J_y\ddot{\beta} = f_{uy} \cdot l + f_{ly} \cdot l - J_z\Omega\dot{\alpha} \end{cases} \tag{6.1}$$

The MSFW rotor is located at the balanced status when the resultant force and the tilting torque acting on the MSFW rotor are equal to zero. If the resultant force and the tilting torque acting on the MSFW rotor are not equal to zero, the MSFW rotor is located at a unbalanced state. Considering that the suspension span of the radial AMB at the upper end is same to that of the radial AMB at the lower end of MSFW rotor, the translational displacements in radial direction and the tilting angles around radial axes of MSFW rotor could be written as

$$\begin{cases} d_x = \dfrac{d_{ux} + d_{lx}}{2} \\ d_y = \dfrac{d_{uy} + d_{ly}}{2} \\ \alpha = \dfrac{d_{uy} - d_{ly}}{2l} \\ \beta = \dfrac{d_{ux} - d_{lx}}{2l} \end{cases} \tag{6.2}$$

Furthermore, the equations of motion of the MSFW rotor could be rewritten as

$$\begin{cases} m\left(\dfrac{\ddot{d}_{ux} + \ddot{d}_{lx}}{2}\right) = f_{ux} + f_{lx} \\ m\left(\dfrac{\ddot{d}_{uy} + \ddot{d}_{ly}}{2}\right) = f_{uy} + f_{ly} \\ J_x \dfrac{\left(\ddot{d}_{uy} - \ddot{d}_{ly}\right)}{2l} = f_{uy} \cdot l + f_{ly} \cdot l + J_z \Omega \dfrac{\left(\dot{d}_{ux} - \dot{d}_{lx}\right)}{2l} \\ J_y \dfrac{\left(\ddot{d}_{ux} - \ddot{d}_{lx}\right)}{2l} = f_{ux} \cdot l + f_{lx} \cdot l - J_z \Omega \dfrac{\left(\dot{d}_{uy} - \dot{d}_{ly}\right)}{2l} \end{cases} \tag{6.3}$$

The control forces of the MSFW rotor could be derived and written as

$$\begin{cases} f_{ux} = \dfrac{m}{4}\left(\ddot{d}_{ux} + \ddot{d}_{lx}\right) + \dfrac{J_x}{4l^2}\left(\ddot{d}_{ux} - \ddot{d}_{lx}\right) - \dfrac{J_z \Omega}{4l^2}\left(\dot{d}_{uy} - \dot{d}_{ly}\right) \\ f_{lx} = \dfrac{m}{4}\left(\ddot{d}_{ux} + \ddot{d}_{lx}\right) - \dfrac{J_x}{4l^2}\left(\ddot{d}_{ux} - \ddot{d}_{lx}\right) + \dfrac{J_z \Omega}{4l^2}\left(\dot{d}_{uy} - \dot{d}_{ly}\right) \\ f_{uy} = \dfrac{m}{4}\left(\ddot{d}_{uy} + \ddot{d}_{ly}\right) + \dfrac{J_y}{4l^2}\left(\ddot{d}_{uy} - \ddot{d}_{ly}\right) + \dfrac{J_z \Omega}{4l^2}\left(\dot{d}_{ux} - \dot{d}_{lx}\right) \\ f_{ly} = \dfrac{m}{4}\left(\ddot{d}_{uy} + \ddot{d}_{ly}\right) - \dfrac{J_y}{4l^2}\left(\ddot{d}_{uy} - \ddot{d}_{ly}\right) - \dfrac{J_z \Omega}{4l^2}\left(\dot{d}_{ux} - \dot{d}_{lx}\right) \end{cases} \tag{6.4}$$

And magnetic forces of the AMB system are

$$\begin{cases} f_{ux} = k_{ix} i_{ux} - k_{dx} d_{ux} \\ f_{lx} = k_{ix} i_{lx} - k_{dx} d_{lx} \\ f_{uy} = k_{iy} i_{uy} - k_{dy} d_{uy} \\ f_{ly} = k_{iy} i_{ly} - k_{dy} d_{ly} \end{cases} \tag{6.5}$$

Substituting Eq. (6.5) into Eq. (6.4), and the control currents in the AMB system along four control channels of radial direction could be written as

$$\begin{cases} i_{ux} = a_0\ddot{d}_{ux} + a_1 d_{ux} + a_2\ddot{d}_{lx} - a_3\left(\dot{d}_{uy} - \dot{d}_{ly}\right) \\ i_{lx} = a_0\ddot{d}_{lx} + a_1 d_{lx} + a_2\ddot{d}_{ux} + a_3\left(\dot{d}_{uy} - \dot{d}_{ly}\right) \\ i_{uy} = a_0\ddot{d}_{uy} + a_1 d_{uy} + a_2\ddot{d}_{ly} + a_3\left(\dot{d}_{ux} - \dot{d}_{lx}\right) \\ i_{ly} = a_0\ddot{d}_{ly} + a_1 d_{ly} + a_2\ddot{d}_{uy} - a_3\left(\dot{d}_{ux} - \dot{d}_{lx}\right) \end{cases} \tag{6.6}$$

where $a_0 = \dfrac{ml^2 + J_x}{4k_{ix}l^2}$, $a_1 = \dfrac{k_{dx}}{k_{ix}}$, $a_2 = \dfrac{ml^2 - J_x}{4k_{ix}l^2}$ and $a_3 = \dfrac{J_z\Omega}{4k_{ix}l^2}$.

There are displacement and force coupling terms existing in four control channels of MSFW rotor in radial direction. Along *x*-axis channel control loop of radial AMB at upper end, there are control displacements from other control channels such as d_{lx}, d_{uy} and d_{ly} except the main control displacement d_{ux}. Consequent, a decoupling control model is designed to accomplish the decoupling control of MSFW rotor in four control channels of radial direction. For the tilting motion of MSFW rotor around radial axes, the gyroscopic coupling terms relate to the rotating speed will cause an additional coupling to control channels in radial direction. Based on Eq. (6.6) and through the Laplace transform, the output displacement of the MSFW rotor in frequency-domain could be derived and written as

$$\begin{bmatrix} d_{ux}(s) \\ d_{lx}(s) \\ d_{uy}(s) \\ d_{lx}(s) \end{bmatrix} = G_p(s) \cdot \begin{bmatrix} I_{ux}(s) \\ I_{lx}(s) \\ I_{uy}(s) \\ I_{lx}(s) \end{bmatrix} \tag{6.7}$$

And the control matrix in four control channels could be expressed into

$$G_p^{-1}(s) = \begin{bmatrix} A(s) & B(s) \\ -B(s) & A(s) \end{bmatrix} \tag{6.8}$$

where $A(s) = \begin{bmatrix} a_0 s^2 + a_1 & a_2 s^2 \\ a_2 s^2 & a_0 s^2 + a_1 \end{bmatrix}$ and $B(s) = \begin{bmatrix} -a_3 s & a_3 s \\ a_3 s & -a_3 s \end{bmatrix}$.

Furthermore, the control matrix could be separated into a decoupling form as following

$$G_p^{-1}(s) = D(s) + W(s) \tag{6.9}$$

where the decoupling term of the control matrix is defined as

$$D(s)=\begin{bmatrix} A(s) & 0 \\ 0 & A(s) \end{bmatrix},$$

and the coupling term of the control matrix is defined as

$$W(s)=\begin{bmatrix} 0 & B(s) \\ -B(s) & 0 \end{bmatrix}.$$

Therefore, the coupling terms in the dynamic equation of the MSFW rotor could be suppressed by designing a compensation matrix to coupling term $W(s)$, and then the decoupling model of the MSFW rotor could be obtained.

6.2 The IMC and DIMC Models of MSFW Rotor

6.2.1 The IMC Model of MSFW Rotor

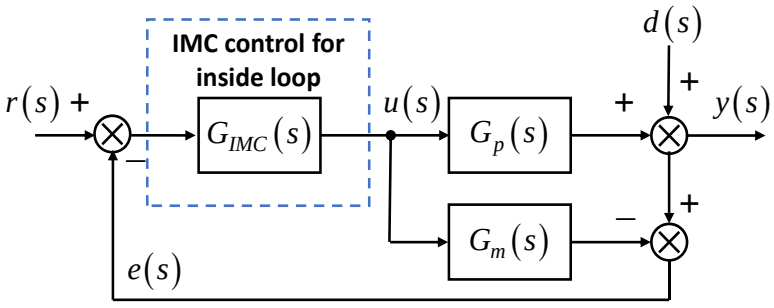

Fig. 6.2. The block diagram of the IMC model for the MSFW rotor.

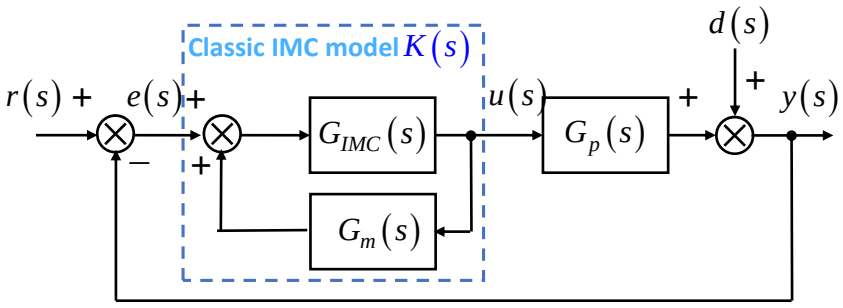

Fig. 6.3. The block diagram of equivalent IMC model for the MSFW rotor.

The control diagram of the IMC model used in displacement control model of MSFW rotor along four control channels in radial direction is shown in Fig. 6.2. $y(s)$ is defined as the output displacement of the IMC model. $r(s)$ is chosen as the reference input of the IMC model. $d(s)$ is defined as the disturbance input of the IMC model. $G_{IMC}(s)$ presents the IMC control model of

MSFW rotor, $G_p(s)$ is the real plant model of the MSFW rotor, and $G_m(s)$ equivalent control plant of MSFW rotor.

The control plant of MSFW rotor could be expressed as following

$$G_m(s) = G_{m+}(s) \cdot G_{m-}(s) \tag{6.10}$$

where $G_{m+}(s)$ is the irreversible model of the MSFW rotor, and $G_{m-}(s)$ is the reversible model of the MSFW rotor.

The low pass filter $G_f(s)$ is defined as

$$G_f(s) = \frac{1}{(\lambda s + 1)^2} \tag{6.11}$$

Therefore, the IMC model could be expressed as

$$G_{IMC}(s) = G_{m-}^{-1}(s) \cdot G_f(s) \tag{6.12}$$

Moreover, based on the control diagram of the IMC model as shown in Fig. 6.3, the equivalent control function could be expressed as

$$K(s) = \frac{G_{IMC}(s)}{1 - G_{IMC}(s) G_m(s)} \tag{6.13}$$

6.2.2 The DIMC Model of MSFW Rotor

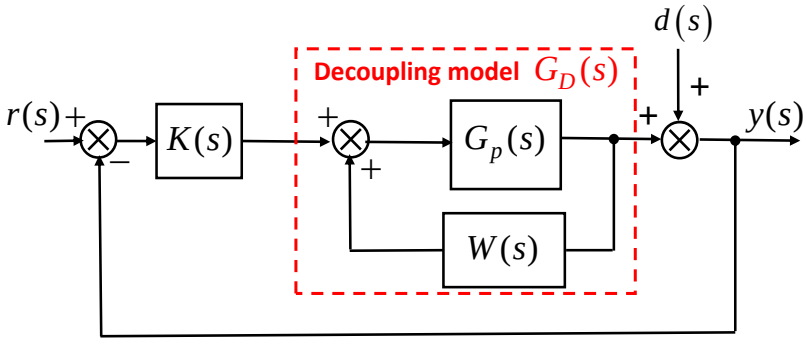

Fig. 6.4. The block diagram of the DIMC model for the MSFW rotor.

To control the coupling terms in Eq.(6.6), the control plant model of MSFW rotor could be decoupled by introducing an inner feedback matrix as shown in Fig. 6.4, and $K(s)$ is defined as the equivalent control model of MSFW rotor.

The closed loop transfer function of MSFW rotor could be written as

$$G_D(s) = \frac{G_p(s)}{1 - G_p(s)W(s)} \tag{6.14}$$

By using the decoupling matrix $G_p^{-1}(s)$ as Eq. (6.8), the dynamic equations of the MSFW rotor could be simplified into several decoupling model in different control loops. The decoupling control model of MSFW rotor yields

$$G_D(s) = D^{-1}(s) \tag{6.15}$$

For the decoupling model of MSFW rotor in radial control channels, the decoupling control model in four radial control channels is not necessary, so the inner feedback loop of MSFW rotor will be omitted, and the normal control model and standard control model could be applied. However, there are coupling terms among four control channels of the MSFW rotor, so the inner control loop could be useful to accomplish the decoupling control of MSFW rotor among different control channels in radial direction.

6.2.3 The Tracking Performance and Sensitivity Analysis of IMC Model

For four control channels of MSFW rotor in radial direction, the transfer function $G_{ry}(s)$ from the reference input displacement $r(s)$ to the output displacement $y(s)$ could be expressed into

$$G_{ry}(s) = \frac{y(s)}{r(s)} = \frac{K(s)G_p(s)}{1 + K(s)G_p(s)} \tag{6.16}$$

The error equation from the reference input displacement $r(s)$ to the output displacement $y(s)$ could be expressed into

$$e(s) = r(s) - y(s) = \frac{1}{1 + K(s)G_p(s)} r(s) \tag{6.17}$$

For the MSFW rotor, if the control plant $G_m(s)$ of MSFW rotor is enough exact to the real plant $G_p(s)$, the magnitude of error function could be obtained as following

$$|e(s)| = \left| \frac{1}{1+K(s)G_p(s)} r(s) \right|_{G_p(s)=G_m(s)} = 0 \tag{6.18}$$

The error function will approach to zero, it means that the reference input could be precisely tracked by the IMC model.

If there is a small deviation Δa_i of the ith system parameter a_i of MSFW rotor's control plant from the ideal value, and then the tracking performance of the control model with the parameter uncertainties could be expressed as

$$\frac{G_{ry}^{-1}(s)\Delta G_{ry}(s)}{a_i^{-1}\Delta a_i} \to a_i G_{ry}^{-1}(s) \frac{\partial G_{ry}(s)}{\partial a_i} \quad \text{as} \quad \Delta a_i \to 0 \tag{6.19}$$

The sensitivity function of IMC model could be defined as

$$S(s) = a_i G_i^{-1}(s) \frac{\partial G_{IMC}(s)}{\partial a_i}\bigg|_{G_p(s)=G_m(s)} \tag{6.20}$$

For the IMC model, there is

$$G_{IMC}(s) = G_{m-}^{-1}(s) \cdot G_f(s) \tag{6.21}$$

So, there is

$$\begin{aligned} S_{IMC}(s) &= a_i \left[G_{m-}^{-1}(s) G_f(s) \right]^{-1} \frac{\partial \left[G_{m-}^{-1}(s) G_f(s) \right]}{\partial a_i}\bigg|_{G_p(s)=G_m(s)} \\ &= a_i G_{m-}(s) \frac{\partial G_{m-}^{-1}(s)}{\partial a_i} \end{aligned} \tag{6.22}$$

For the DIMC model of the MSFW rotor, there is

$$G_{DIMC}(s) = G_D(s)D(s) = \frac{G_p(s)}{1 - G_p(s)W(s)} D(s) \tag{6.23}$$

The sensitivity function of the DIMC model is

$$S_{DIMC}(s) = a_i \left[\frac{\partial G_D(s)}{\partial a_i} D(s) + G_D(s) \frac{\partial D(s)}{\partial a_i} \right]\bigg|_{G_p(s)=G_m(s)} \tag{6.24}$$

If $G_p(s)$ is the precise control plant of the MSFW rotor, so we have

$$\frac{\partial G_p(s)}{\partial a_i}=0 \tag{6.25}$$

Differentiating Eq. (6.14) with respect to a_i, we have

$$\begin{aligned}\frac{\partial G_D(s)}{\partial a_i}&=G_D(s)\frac{\partial W(s)}{\partial a_i}G_D(s)\Big|_{G_p(s)=G_m(s)}\\&=D^{-1}(s)\frac{\partial W(s)}{\partial a_i}D^{-1}(s)\end{aligned} \tag{6.26}$$

Furthermore, the sensitivity function of the DIMC model could be rewritten as

$$S_{DIMC}(s)=a_iD^{-1}(s)\left[\frac{\partial W(s)}{\partial a_i}D^{-1}(s)D(s)+\frac{\partial D(s)}{\partial a_i}\right]=a_iD^{-1}(s)\frac{\partial G_m^{-1}(s)}{\partial a_i} \tag{6.27}$$

Therefore, the sensitivity functions of the IMC model and the DIMC model could be expressed into

$$\begin{cases}S_{IMC}(s)=a_iG_{m-}(s)\dfrac{\partial G_{m-}^{-1}(s)}{\partial a_i}\\S_{DIMC}(s)=a_iD^{-1}(s)\dfrac{\partial G_m^{-1}(s)}{\partial a_i}\end{cases} \tag{6.28}$$

6.2.4 The Anti-disturbance Performance and Robustness of IMC Model

For the IMC model used in four control channels of the MSFW rotor, the transfer function $G_{dy}(s)$ from the disturbance input term $d(s)$ to the output displacement term $y(s)$ could expressed as

$$G_{dy}^{IMC}(s)=\frac{y(s)}{d(s)}=\frac{1}{1+K(s)G_p(s)}=\frac{1-G_{m-}^{-1}(s)G_f(s)G_m(s)}{1+G_{m-}^{-1}(s)G_f(s)\left[G_p(s)-G_m(s)\right]} \tag{6.29}$$

When the equivalent control model of the MSFW rotor is exact to the real control plant, the magnitude equation of the disturbance transfer function could be written as

$$\left|G_{dy}^{IMC}(s)\right|=\left|\frac{1}{1+K(s)G_p(s)}\Big|_{G_p(s)=G_m(s)}\right|=\left|1-G_f(s)\right| \tag{6.30}$$

The robustness is determined by the parameters of the chosen filter. In detail, the response magnitude of the disturbance transfer function is amplified by increasing the low-pass filter λ,

and a small value of low-pass filter λ is beneficial to improving the robustness. Moreover, the robust performance of IMC model would be diminished with increasing the disturbance frequency.

As illustrated in Fig. 6.4, the disturbance transfer function of the DIMC model is

$$G_{dy}^{DIMC}(s)=\frac{y(s)}{d(s)}=\frac{1}{1+K(s)G_D(s)} \tag{6.31}$$

For the exact control plant model of MSFW rotor, the response magnitude of disturbance transfer function could be expressed as

$$\left|G_{dy}^{DIMC}(s)\right|=\left|1-G_f(s)\right| \tag{6.32}$$

Comparing Eq. (6.32)to Eq. (6.30), the DIMC model has same robust ability as the IMC model, the robust ability of MSFW rotor is determined by the parameters of chosen filter.

6.3 Simulation of IMC and DIMC Model

6.3.1 The Anti-disturbance Performance of IMC and DIMC Model

TABLE. 6.I. The simulation parameters of MSFW rotor system in IMC model.

Parameter	Value	Unit
Polar moment of inertia	J_x=0.67	kg·m^2
Equatorial moment of inertia	J_z=1.24	kg·m^2
Mass of MSFW rotor	m=150	kg
Current stiffness of radial AMB	k_{ix}=520	N/A
Displacement stiffness of radial AMB	k_{dx}=-2800	N/mm
Span from radial sensor to center of mass	l=476	mm
Amplification coefficient	k_w=0.2	A/V
Sensitivity of displacement sensor	k_s=3.3	V/mm

In a MIMO system of the MSFW rotor with parameters in TABLE. 6.I, the singular values of the frequency function matrix are the evaluation index for the frequency responses of the IMC model and the DIMC model. The singular values of the frequency function matrix could be written as

$$\sigma_i[G(j\omega)] = \sqrt{\delta_i[G^T(-j\omega)G(j\omega)]} \tag{6.33}$$

where δ_i is the ith eigenvalue of MSFW rotor's control plant in four radial control channels.

The relationship between the singular values and frequency responses of the IMC model and DIMC model at different rotating frequencies is shown in Fig. 6.5. When the MSFW rotor working at a high rotational frequency, the DIMC model has the same sensitivity performance as the IMC model in the low-frequency domain. The IMC model has a greater sensitivity peak than the DIMC model when the response frequency equals to the natural rotational frequency of MSFW rotor, so it indicates that an oscillation will occur at a high rotating frequency. Consequent, the DIMC model expresses better ability on mitigating the oscillatory behavior when MSFW rotor works at a high rotational frequency.

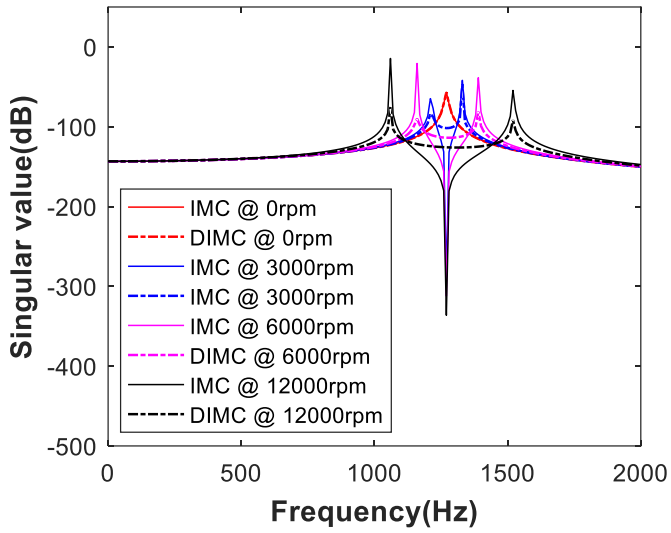

Fig. 6.5. The comparison about the singular values of the control plant with the IMC model and the DIMC model.

6.3.2 The Tracking Performance and Robustness of IMC and DIMC Model

To analyze the tracking performances of the IMC model and the DIMC model used in the MSFW rotor, a step displacement signal with 0.1mm amplitude is chosen as the reference input displacement. As shown in Fig. 6.6, the dynamic response curve of MSFW rotor with the DIMC model is shown by red line, the dynamic response curve of MSFW rotor with the IMC model is shown by blue line. For MSFW rotor using the IMC model, the maximum error between the

reference input and the response output is 0.03mm. For the MSFW rotor using DIMC model, the maximum error between the reference input and the response output is reduced to 0.02mm, but the rising time for the reference input using the DIMC model is higher than the IMC model. Moreover, an impulse disturbance is added on MSFW rotor after it is stably located at the radial balanced position. For the MSFW rotor using the IMC model and DIMC model, the displacement deflection from the balanced position is 0.02mm. Consequently, the excessive displacement overshoot in the step response curve could be mitigated using the DIMC model, and the settling time to reach the steady state and the rising time would be longer than the IMC model. When the low pass filter coefficients of the DIMC model and the IMC model are chosen as same values, the response magnitude of the MSFW rotor for the impulse disturbance would be the same.

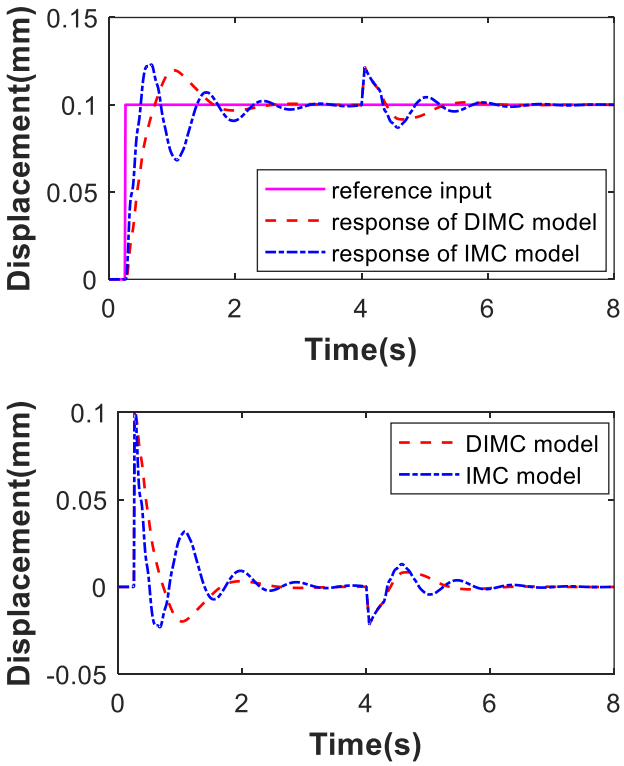

Fig. 6.6. The displacement response curves of the MSFW rotor using IMC model and DIMC model.

When the filter coefficient λ of the low pass filter is chosen as different values, an impulse disturbance is added on the MSFW rotor at the balanced position, and then displacement response curves of MSFW rotor are shown in Fig. 6.7, respectively. When the filter coefficient of the low pass filter λ=10, the displacement response curve of MSFW rotor is presented by

magenta line, the displacement error between the output displacement and the reference input displacement is 0.025mm, and the settling time approaching to the steady state is 0.86s. the filter coefficient of low pass filter λ=0.1, the displacement response curve of MSFW rotor for the impulse disturbance is plotted by the blue line, the displacement error between the output displacement and the reference input displacement is 0.016mm, and the settling time approaching to the steady state is 0.52s. Therefore, the anti-disturbance ability of MSFW rotor would be improved with a great filter coefficient of low pass filter λ, and the tracking lag for the reference input would be enlarged too.

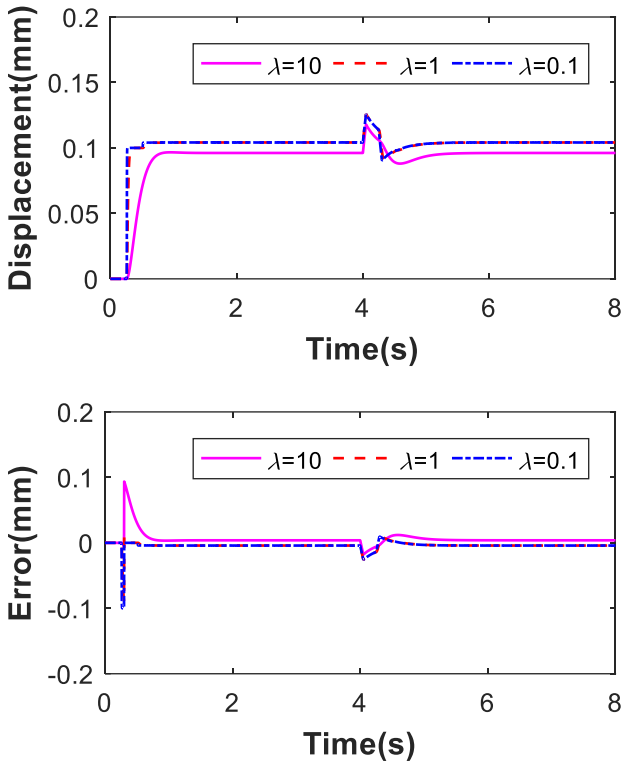

Fig. 6.7. The displacement response curves of MFW rotor using the IMC model when an impulse disturbance is added on it.

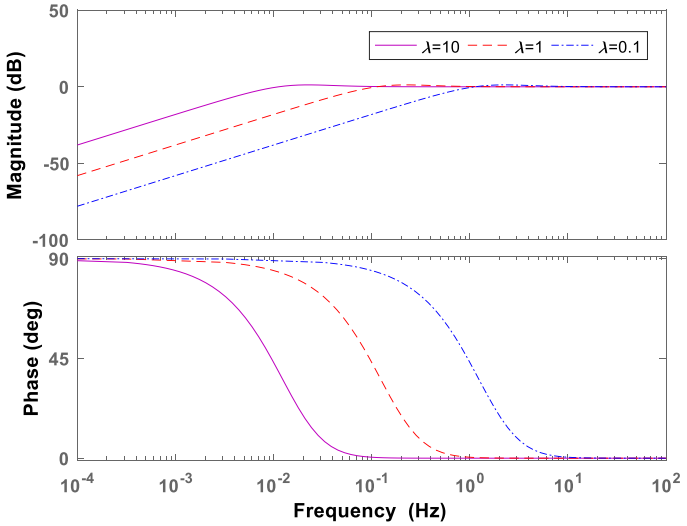

Fig. 6.8. The frequency response curves of disturbance transfer function choosing different values of the low-pass filter coefficient λ.

Moreover, choosing the different filter coefficients of the low pass filter, the frequency response curves of the disturbance transfer function are shown in Fig. 6.8. The response magnitude of the response curve when the low pass filter coefficient λ=0.1 is greater than the response magnitude choosing the low pass filter coefficient λ=1. It shows that the DIMC model and the IMC model are both sensitive to the disturbance acting on MSFW rotor although the low pass filter coefficient could be regulated, and the great value of low pass filter coefficient would reduce the cut-off frequency of disturbance transfer function. Therefore, a great value of low pass filter coefficient could diminish the frequency range of the imposed disturbance.

The simulation result indicates that the MSFW rotor using the DIMC model has good performance on mitigating the displacement overshoot and displacement oscillation. Moreover, the bigger value of low pass filter coefficient, the higher robustness of the MSFW rotor.

6.3.3 Comparison Between the IMC Model and the DIMC Model

The dynamic suspension displacements in four radial control channels of MSFW rotor using the IMC model are simulated and shown in Fig. 6.9. The magnetic suspension force of the radial AMB at upper end could make the MSFW rotor stably suspend at the equilibrium position at t=1s, there are obvious displacement deviations in other three radial control channels. Furthermore, an impulse disturbance force is added on stable suspension at upper end of MSFW

rotor along x axis at t=3s, the displacement term at the upper end in x axis d_{ux} has 0.07mm deviating from the equilibrium point, and a displacement deflection about 0.02mm occurs in other three control channels of the MSFW rotor. Using the DIMC model to the MSFW rotor, the dynamic suspension displacements of the MSFW rotor in four radial control channels are shown in Fig. 6.10. The displacement term at the upper end in x axis d_{ux} has a deflection of 0.08mm. At that instant, the displacement term d_{lx} at the lower end in x axis has a deflection about 0.03mm, but displacements d_{uy} and d_{ly} at the upper end and lower end in y axis are kept at the balanced status.

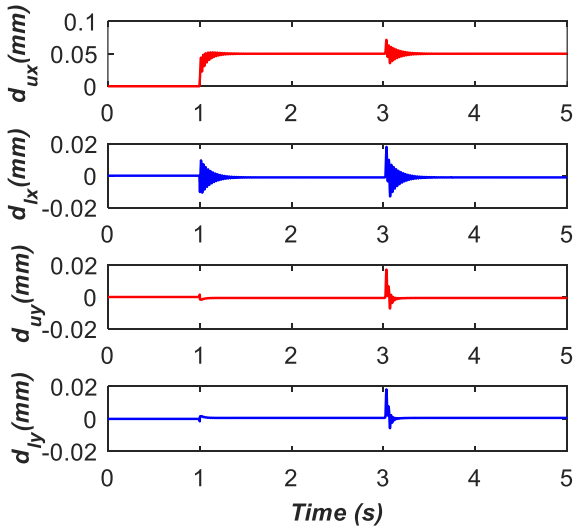

Fig. 6.9. The dynamic suspension displacements in four radial DOFs of MSFW rotor using the IMC model.

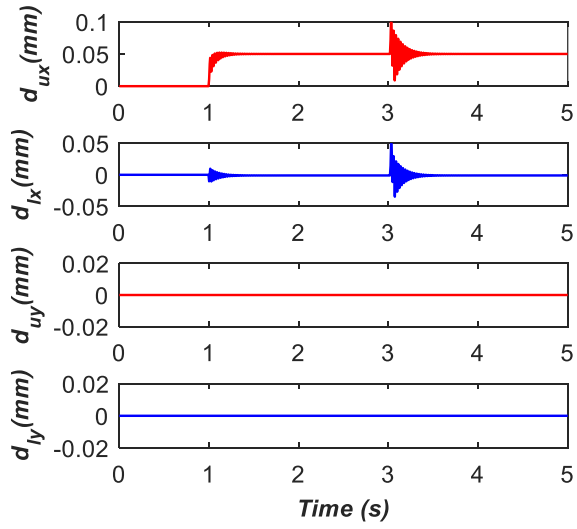

Fig. 6.10. The dynamic suspension displacements in four radial DOFs of MSFW rotor using the DIMC model.

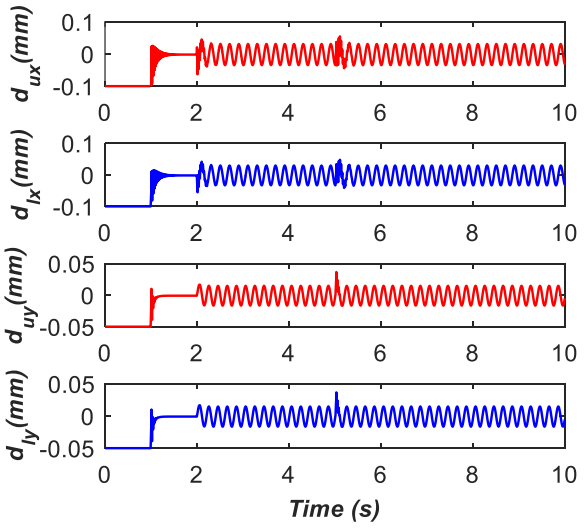

Fig. 6.11. The dynamic suspension displacements in four radial DOFs of MSFW rotor at 300rpm using the IMC model.

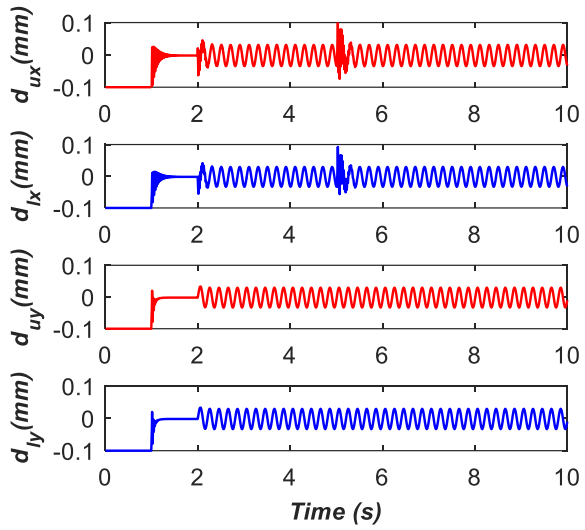

Fig. 6.12. The dynamic suspension displacements in four radial DOFs of MSFW rotor at 300rpm using the DIMC model.

When the IMC model is used to the MSFW rotor, the dynamic displacements of MSFW rotor are illustrated in Fig. 6.11 when the rotating speed is 300rpm. The displacement amplitude of the MSFW rotor is 0.015mm at the balanced state, and the deflection of the displacement terms d_{ux} and d_{lx} is 0.08mm when an impulse disturbance force is acting on control channel along lower end of x axis (displacement term d_{lx}), the deflection term of the displacement terms d_{uy} and d_{ly} is 0.048mm. When the DIMC model is used to the MSFW rotor, the dynamic displacements of MSFW rotor are plotted in Fig. 6.12. The displacement terms d_{uy} and d_{ly} could

keep stable when the disturbance is imposed on the control channel at the lower end of x axis, but the deflection value of displacement terms d_{ux} and d_{lx} increases to 0.08mm.

Furthermore, when the rotating speed of MSFW is increased to 6000rpm, the dynamic displacements in four radial control channels of MSFW rotor using the IMC model are illustrated in Fig. 6.13, the steady-state displacement value of MSFW rotor at the balanced state is 0.015mm. When an impulse disturbance is added on the control channel at upper end in x axis (the displacement term d_{ux}), the deflection amplitudes of displacement terms d_{ux} and d_{lx} are both 0.05mm, and the deflection amplitude of displacement terms d_{uy} and d_{ly} are both 0.04mm. The corresponding displacement defections of MSFW rotor using the DIMC model are illustrated in Fig. 6.14. The displacement terms d_{uy} and d_{ly} remain stable, but the deflection amplitude of the displacement terms d_{ux} and d_{lx} is 0.06mm.

Consequently, the DIMC model could reduce the coupling effect among four radial control channels when the MSFW rotor works at the dynamic suspension state and the static rotation state. Although the displacement deflections of controlled channels are intensified, the deflection is still in the range of safety. More importantly, dynamic displacement deflections in other uncontrolled channels of MSFW rotor are effectively mitigated.

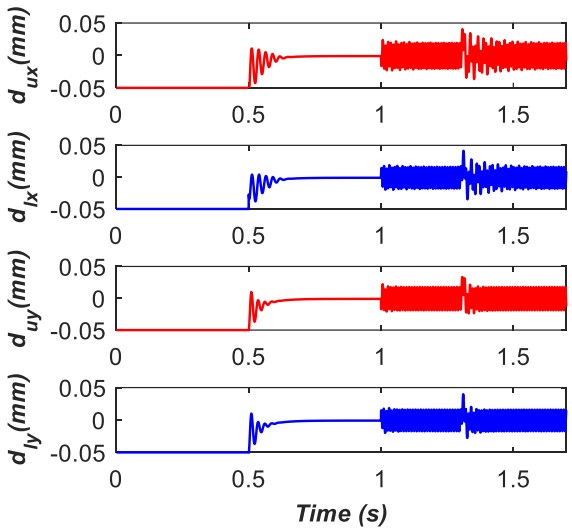

Fig. 6.13. The dynamic suspension displacements in four radial DOFs of MSFW rotor at 6000rpm using the IMC model.

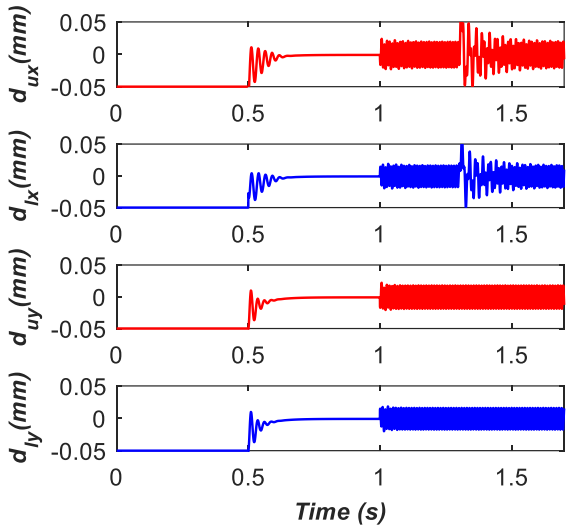

Fig. 6.14 The dynamic suspension displacements in four radial DOFs of MSFW rotor at 6000rpm using the DIMC model.

6.4 Experiment of IMC and DIMC Model

6.4.1 The Sensitivity Analysis of IMC and DIM Models

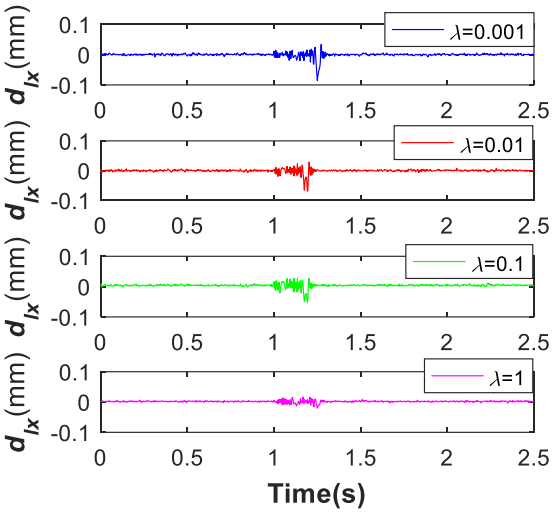

Fig. 6.15. The dynamic displacements in four radial DOFs of MSFW rotor applying different values of low-pass filter coefficient λ.

The relationships among the bias displacement variation, the current stiffness variation and the displacement stiffness variation are shown in Fig. 5.1. When the nominal bias displacement of MSFW rotor sets at 1mm in radial direction, the ideal value of the displacement stiffness is -2800N/mm in radial direction, and the ideal value of the radial current stiffness is 620N/A in radial direction. When the bias displacement variation of MSFW rotor is 0.1mm,

and the deflection term of displacement stiffness is 1000N/mm, and the deflection term of current stiffness is about 100N/A in radial direction. So, the current stiffness and the displacement stiffness of the MSFW rotor with great self-weight would be sensitive to the initial suspension location which is affected by the great self-weight.

When an impulse force disturbance with the 10% of MSFW rotor's self-weight amplitude is added on the control channel at the lower end of x axis by adding the disturbance signal of control windings, the dynamic displacements in four radial control channels of MSFW rotor are shown in Fig. 6.15. When the low pass filter coefficient is chosen as λ=1, the displacement deflection for the impulse disturbance is about 0.02mm as shown by the blue line. The displacement deflection for the impulse disturbance would be reduced to 0.085mm when low pass filter coefficient decreases to 0.001. Therefore, the great value of low pass filter coefficient could improve the disturbance rejection, and the sensitivity for disturbance could be suppressed by choosing a great value of low pass filter coefficient.

6.4.2 The Suspension Performance of IMC and DIMC Models

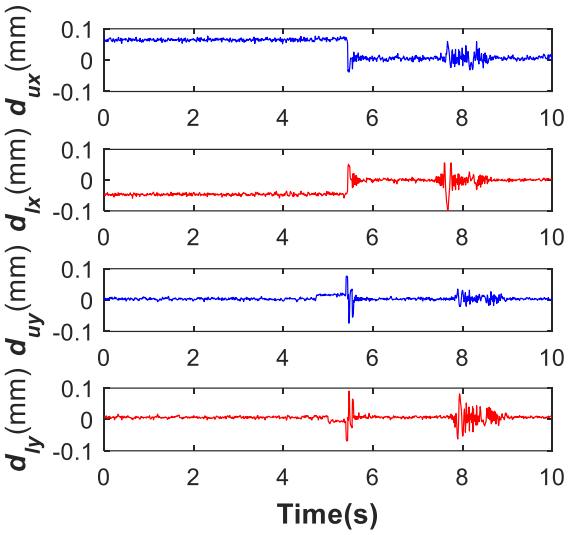

Fig. 6.16. The dynamic suspension traces in in four radial DOFs of MSFW rotor with the IMC model.

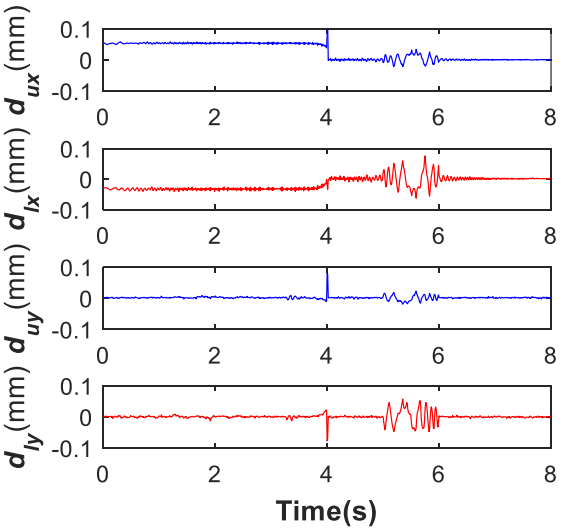

Fig. 6.17. The dynamic suspension traces in in four radial DOFs of MSFW rotor with the DIMC model.

When a step displacement signal is selected as the reference displacement input to make the MSFW rotor suspends at balanced position, and then an impulse disturbance force is imposed on the lower end of the MSFW rotor in x axis. The dynamic displacement variations in four radial control channels of MSFW rotor using the IMC model are illustrated in Fig. 6.16. The MSFW rotor is forced to be suspended at the equilibrium position in x axis at t=5s, and displacement terms d_{ux} and d_{lx} equal to zero. The displacement terms d_{uy} and d_{ly} have a deflection with amplitude 0.07mm because of the coupling terms existing in the four radial control channels of MSFW rotor. When the impulse disturbance is added on lower end of the MSFW rotor in x axis (displacement term d_{lx}) at t=5.5s, the displacement deflection is 0.08mm. The corresponding displacement variation of d_{ux} is 0.04mm. The displacement term d_{ly} at lower end of y axis is 0.07mm, and the displacement term d_{uy} at upper end of y axis is 0.03mm. The dynamic suspension displacements of MSFW rotor using the DIMC model are illustrated in Fig. 6.17, the displacement term d_{ly} at lower end of y axis is 0.06mm at t=4s, and the displacement term d_{uy} at upper end of y axis is 0.06mm too. The displacement deflection of displacement term d_{lx} at the lower end of x axis caused by the impulse disturbance force is 0.07mm while the deflection of displacement term d_{ly} is 0.05mm. So, the displacement deflection of d_{ly} is reduced by 28.6% by the DIMC model, also the displacement deflection of d_{uy} is reduced by 33.3%.

The dynamic suspension displacements of MSFW rotor using the IMC model when the rotating speed is 6000rpm are detected and illustrated in Fig. 6.18. The steady-state amplitude of MSFW rotor's displacement is about 0.025mm. The deflection value of displacement term d_{lx} at lower end of x axis is about 0.08mm when an impulse disturbance force is added on the lower end of x axis, and the deflection value of displacement term d_{ux} at upper end of x axis is 0.03mm. Moreover, the deflection value of displacement term d_{ly} at lower end of y axis is 0.04mm, and t the deflection value of displacement term d_{uy} at upper end of y axis is 0.03mm. The dynamic suspension displacements of MSFW rotor when the DIMC model is used are shown in Fig. 6.19. The steady-state suspension displacement of MSFW rotor is 0.015mm, the deflection value of the displacement term d_{lx} at lower end of x axis is 0.05mm, and the deflection value of the displacement term d_{ux} at upper end of x axis is 0.03mm. the deflection value of the displacement term d_{ly} at lower end of y axis is 0.035mm. Therefore, the DIMC model could reduce 12.5% displacement deflection of displacement term d_{ly} at lower end of y axis and 16.7% in displacement deflection of the displacement term d_{uy} compared with the IMC model.

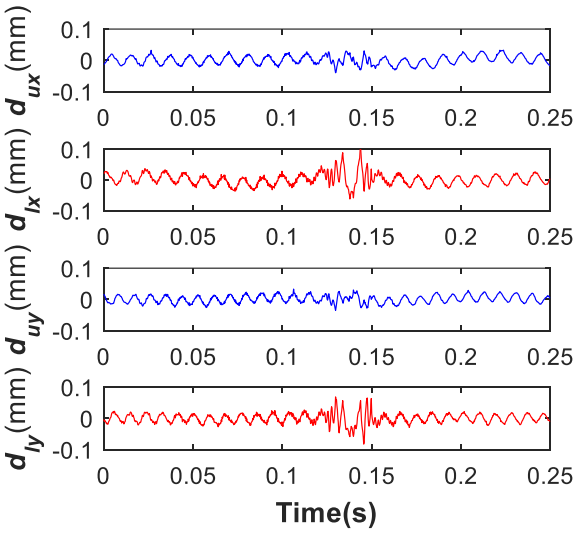

Fig. 6.18. The dynamic suspension displacements in four radial DOFs of MSFW rotor at 6000rpm using the IMC model.

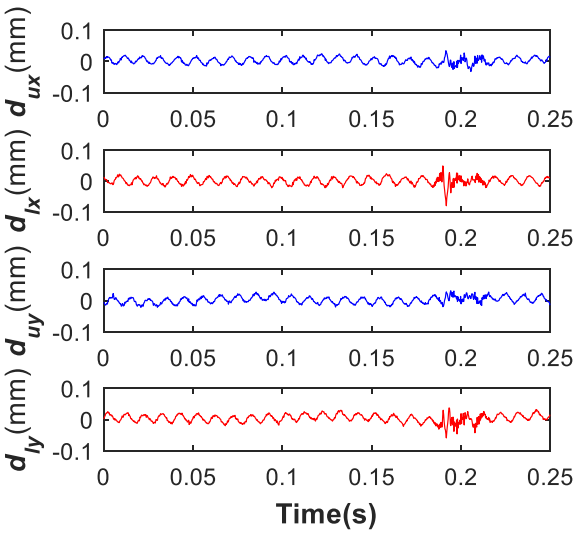

Fig. 6.19. The dynamic suspension displacements in four radial DOFs of MSFW rotor at 6000rpm using the DIMC model.

The dynamic displacement variations of MSFW rotor with the IMC model when the rotating speed is 10000rpm are illustrated in Fig. 6.20. The steady-state suspension displacement of MSFW rotor is about 0.015mm. The displacement deflection of displacement term d_{lx} at the lower end of x axis for impulse disturbance force is 0.09mm when the disturbance force is added on the lower end of x axis, and displacement deflection of displacement term d_{ux} at the upper end of x axis is 0.03mm. The displacement deflection of displacement term d_{ly} at the lower end of y axis is 0.08mm, and the displacement deflection of displacement term d_{uy} at the upper end of y axis is 0.03mm. The measured dynamic displacements of MSFW rotor utilizing the DIMC model are illustrated in Fig. 6.21, the steady-state amplitude of MSFW rotor is 0.01mm. The displacement deflection of displacement term d_{lx} at the lower end of x axis is 0.07mm when the disturbance force is added on the lower end of x axis, and the displacement deflection of displacement term d_{ux} at the upper end of x axis is 0.03mm. The displacement deflection of displacement term d_{ly} at the lower end of y axis is 0.07mm, and the displacement deflection of displacement term d_{uy} at the upper end of y axis is 0.02mm. So, the DIMC model has 12.5% reduction on displacement deflection of the displacement term d_{ly} and 33.3% reduction in the displacement term d_{uy}.

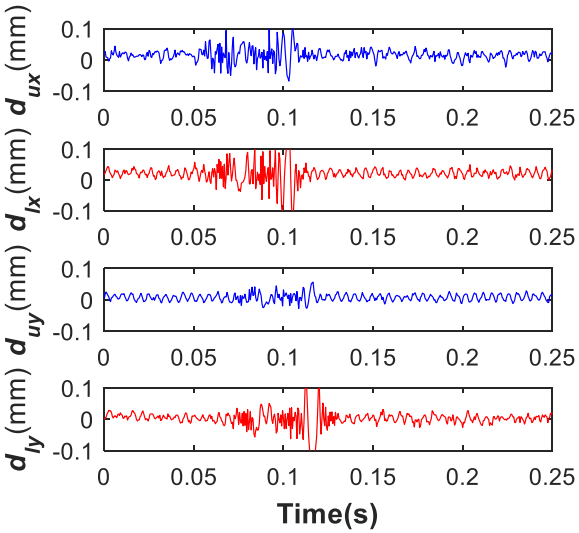

Fig. 6.20. The dynamic suspension displacements in four radial DOFs of MSFW rotor at 10000rpm using the IMC model.

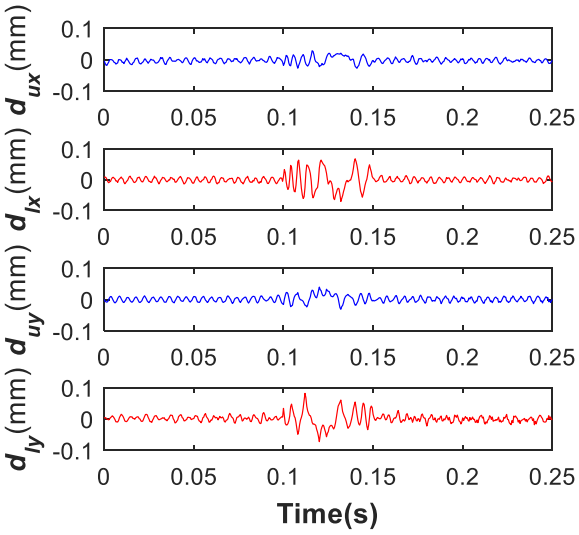

Fig. 6.21. The dynamic suspension displacements in four radial DOFs of MSFW rotor at 10000rpm using the DIMC model.

The dynamic suspension displacements of MSFW rotor using the DIMC model and the IMC model during speed regulation process are illuminated in Fig. 6.22 and Fig. 6.23, respectively. The speed curve of MSFW rotor during regulation process from 0rpm to 5000rpm is marked by green line. The dynamic displacements of MSFW rotor have obvious deflection at the beginning of the acceleration process and the deceleration process. As shown in Fig. 6.22, the maximum value of MSFW rotor's displacement deflection using the IMC model is 0.15mm during the speed regulation process, and the maximum value of MSFW rotor's displacement deflection during the deceleration process is 0.18mm. As illustrated in Fig. 6.23, the maximum

displacement deflection of MSFW rotor using the DIMC model is 0.08mm during the acceleration process, maximum displacement deflection of MSFW rotor is 0.09mm during the deceleration process. So, the maximum displacement deflection during the speed regulation process is reduced by 50% using the DMIC model of MSFW.

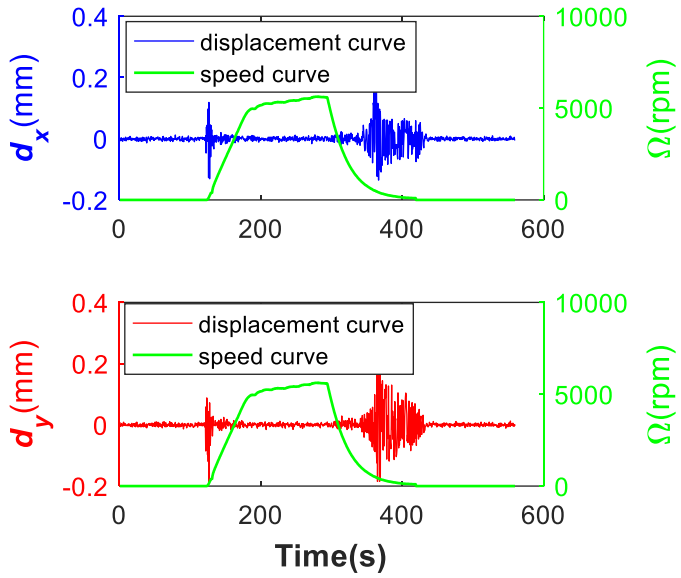

Fig. 6.22. The dynamic displacement deflections of MSFW rotor in radial direction with IMC model during speed regulation.

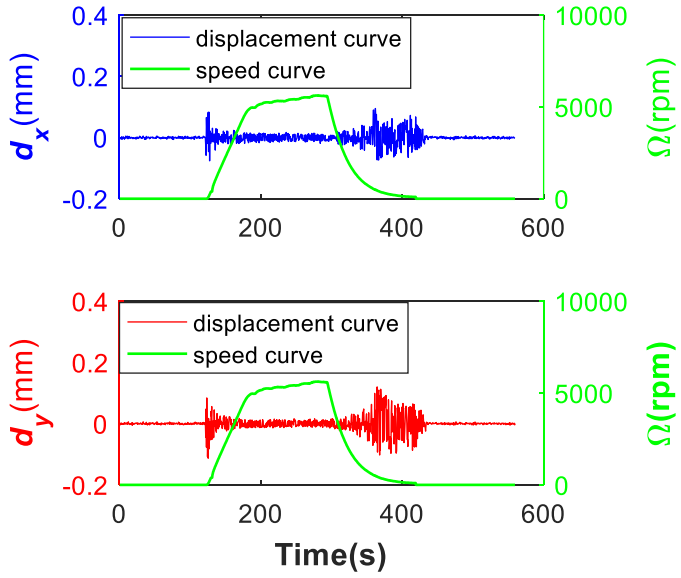

Fig. 6.23. The dynamic displacement deflections of MSFW rotor in radial direction with DIMC model during speed regulation.

Above all, based on the comparison results in TABLE. 6.II and TABLE. 6.III, although the simulation results display better control performances on the overshoot, the displacement

deflection, the coupling effect and the recovery time, the experimental results show similar trends like the simulation results.

TABLE. 6.II. Comparison of the displacement term d_{ly} of the IMC model and the DIMC model.

State of MSFW rotor	IMC model	DIMC model	Reduction
suspension process	0.07	0.06	14.3%
with static disturbance	0.07	0.05	28.6%
speed is 6000rpm	0.04	0.035	12.5%
speed is 10000rpm	0.08	0.07	12.5%

TABLE. 6.III. Comparison of the displacement term d_{uy} of the IMC model and the DIMC model.

State of MSFW rotor	IMC model	DIMC model	Reduction
suspension process	0.07	0.06	14.3%
with static disturbance	0.03	0.03	33.3%
speed is 6000rpm	0.03	0.025	16.7%
speed is 10000rpm	0.03	0.02	33.3%

6.5 Summary

The stability of the MSFW rotor is sensitive to the speed variation and the parameter uncertainty especially if the MSFW rotor has strong coupling effect. In the static suspension state of MSFW rotor, the robustness of the MSFW rotor is enhanced by regulating the low pass filter coefficient of IMC model so that the displacement deflection of the MSFW rotor can be reduced. In addition, the DIMC model is successfully applied for the MSFW rotor to accomplish the decoupling control in the four radial control channels of the MSFW rotor, and the displacement deflection of the MSFW rotor introduced by the coupling effect is attenuated by using the DIMC model. In the dynamical rotation state of the MSFW rotor, the dynamic displacement deflection of MSFW rotor is effectively controlled by both the DIMC model and the IMC model. Therefore, the displacement overshoot on dynamic response of MSFW rotor using the IMC model can be reduced. The IMC model is useful to improve the robust ability of MSFW rotor with great equatorial moment of inertia and great self-weight, and the coupling terms among four radial control channels of MSFW rotor could be suppressed by the DIMC model.

Chapter 7. Conclusions

This thesis is focused on the vibration analysis and the active vibration control of the MSFW rotor, the main contributions are divided in five parts as follows.

1. The vibration characteristics of MSFW rotor are clearly analyzed, it is the basic part of the research in the whole thesis.

The dynamic models of the MSFW rotor are established. The AMB system in radial and axial directions control motions of the MSFW rotor with five DOFs. The characteristics about the stiffness and the damping of the AMB system are analyzed, and they could be regulated based on the displacement feedback of the MSFW rotor. Moreover, the natural frequency of the MSFW rotor in translation is increased with the stiffness coefficient of control system, and the vibration transmissibility is reduced with the damping coefficient of control system. For tilting responses of the MSFW rotor when an impulse disturbance force is added on it, the titling angle of MSFW rotor would decrease with its rotating speed. For the harmonic disturbance imposed on the MSFW rotor, the MSFW rotor's titling angle around radial axis is increased with the increase of the rotational frequency. Finally, the response magnitude of MSFW rotor's translational displacement and tilting angle around radial axis could be attenuated by proper tuning of the damping coefficient and the stiffness coefficient of control system.

2. Based on frequency responses of the translation and the rotation, the dynamic characteristics of the MSFW rotor with the effects of structure parameters (suspension span ratio of radial AMBs and the moment of inertia ratio) are analyzed.

The critical rotational frequency of the MSFW rotor increases with the moment of inertia ratio and the suspension span ratio. The BW and the FW motions of the MSFW rotor happen when the rotational frequency exceeds the critical rotational frequency of the MSFW rotor. A proper value of the moment of inertia ratio and the suspension span ratio can avoid the

occurrences of the BW and the FW motions. Moreover, the frequency bandwidth between the BW and the FW motions can be regulated by slightly tuning the moment of inertia ratio. Therefore, the research about the structure parameters provides some guidelines to the structural design of the MSFW rotor system, especially to the suspension span of the radial AMBs in the MSFW rotor system.

3. The vibration absorbing ability of the AMB for the rotational machinery is analyzed. It is one kind of DVA for the rotational machinery by covering the whole working frequency.

Based on the frequency response of the MSFW rotor with the effect of the axial AMB, the dynamic displacement variations of MSFW rotor and load rotor decrease with increase of the damping coefficient and the stiffness coefficient. Therefore, the damping coefficient and the stiffness coefficient of the axial AMB could be used to attenuate the vibration responses of the MSFW rotor. Furthermore, the experimental results verify that the maximum value of MSFW rotor's displacement deflection from the balanced position increases with the increase of rotating frequency, and it could be attenuated by the damping coefficient and the stiffness coefficient of the axial AMB. Therefore, the AMB system could be regarded as a DVA to control vibration responses of the MSFW system with a load, and the applicable frequency width of vibration control could be enlarged in comparison to the passive DVA.

4. Robust control could enhance the stability of MSFW rotor with great mass and great equatorial moment of inertia when uncertainties of current stiffness and displacement stiffness of the AMB system exist.

For the MSFW rotor with heavy self-weight, the uncertain initial location of the MSFW rotor easily leads to the uncertainties of current stiffness and displacement stiffness, and therefore the suspension process of the MSFW rotor could not be accurately controlled. Moreover, the external disturbance also affects the nominal values of the current stiffness and the displacement stiffness. The gyroscopic coupling effect of the MSFW rotor with great

equatorial moment of inertia varies with the rotating speed, so it is regarded as an external disturbance acting on the MSFW rotor. Therefore, a robust control scheme is designed to mitigate the disturbance response of the translational motion and the radial rotation of MSFW rotor. Both simulation and experiment indicate that the maximum value of the MSFW rotor's displacement using the robust control function is smaller than that with the standard PID control model when the MSFW rotor turns at different rotating speeds.

5. The DIMC could realize the decoupling control in four radial control channels of MSFW rotor and improve the robustness when there are disturbances acting on the MSFW rotor.

The stability of the MSFW rotor is sensitive to the speed variation and the parameter uncertainty, especially if the MSFW rotor has strong coupling effect. In the static suspension state of the MSFW rotor, the displacement deflection of MSFW rotor is reduced, so the robust ability of MSFW rotor could be enhanced by regulating the low pass filter parameter of IMC model. The DIMC model using in MSFW rotor could be successfully applied to achieve a decoupling control in four radial control channels of MSFW rotor, and the displacement deflection of MSFW rotor introduced by the coupling effect is suppressed. In the dynamical rotation state of the MSFW rotor, the dynamic displacement of MSFW rotor is effectively controlled by both the DIMC model and the IMC model. The IMC model is useful to enhance the robust ability of MSFW rotor with great equatorial moment of inertia and great self-weight, and the DIMC model can mitigate the coupling terms in four radial control channels.

6. Comparison between the robust control and the DIMC used in the MSFW rotor.

Firstly, the control methods used in the MSFW rotor are tried to minimize the displacement deflection. Moreover, the different control methods are used for the MSFW rotor to solve the different problems. The robust control is used to MSFW rotor with great self-weight because the stiffness coefficients are easily affected by the disturbances acting on it. The robust control is designed to enhance the anti-disturbance performance. In addition, the DIMC is applied to

the MSFW rotor with coupling terms, so the coupling displacement is reduced by realizing the decoupling control in four radial channels.

Above all, the vibration analysis of the MSFW rotor establishes the foundation for future research about the active vibration control of the MSFW rotor. The vibration response of the MSFW for different disturbance sources are developed. The relationship amongst the vibration characteristics of the MSFW rotor, the suspension span ratio of the radial AMB and the moment of inertia ratio of the MSFW rotor are analyzed, so a design guideline for the MSFW rotor is derived based on this analysis result. In addition, the vibration absorbing ability of the axial AMB mounted on the MSFW rotor is tested. Both simulation results and experimental results show that the stiffness coefficient and the damping coefficient of the AMB could effectively attenuate the maximum displacement deflection of the MSFW rotor. A robust control scheme is applied to attenuate the influence on the vibration of the MSFW rotor introduced by the uncertainties of the current stiffness and the displacement stiffness. The test results prove that the maximum value of MSFW rotor's displacement deflection with external disturbance is minimized by the proposed robust control scheme. Finally, the DIMC can realize the decoupling control in the four radial control channels of MSFW rotor and improve the robustness when there are disturbances acting on the MSFW rotor.

Future work

Even though the successful vibration analysis method and active vibration control method of the MSFW rotor are reported in the present work. Many further researches about the vibration analysis methods and the active vibration control of MSFW rotor could be done in future.

Firstly, the structure optimization about the MFSW rotor could reduce the vibration response, so it is worthy of being studied in the future. The structural optimization of the rotor should be investigated to reduce the vibration response at high rotational speed caused by the asymmetrical span of the radial AMB system, and the optimization design about the AMB system could mitigate the mismatch and the assembly error.

Besides, the vibration analysis method of the MSFW rotor based on the rotational speed of the MSFW rotor should be developed, especially for the MSFW rotor working at a high rotational speed which exceeds its first natural rotational frequency. Since the MSFW rotor will have more vibration statuses such as the sup-harmonic vibration and the sub-harmonic vibration. Therefore, the vibration analysis of the MSFW rotor introducing the variable rotational speed will be a useful research topic to high speed MSFW rotor.

Moreover, different kinds of active vibration control methods of the MSFW rotor can be another research focus. When the MSFW rotor works at a high rotational frequency which exceeds its first natural rotational frequency, more complex and sensitive vibration statuses will occur, so the suitable active vibration control methods which focus on those vibration statuses are very important to improve the stability and control precision of the MSFW rotor. Specifically, to minimize the control current of MSFW rotor with great gravity, the optimization design of the control methods is worthy of being researched in order to reduce the control cost of MSFW rotor.

In addition, more applications of active vibration control using the electromagnetic vibration absorber can be considered in the future work. Considering the electromagnetic vibration absorber's advantages on the active controllability and the wide control frequency range, the electromagnetic vibration absorbers with different parameters and different structures

can be applied in other fields about active vibration control such as the active vibration control for elastic vibration and active vibration control for high-speed train.

Above all, there are many works about the vibration analysis and active vibration control of the MSFW rotor to improve the control performance of the MSFW rotor and to widen the application range of the electromagnetic vibration absorber.

Publications

B. Xiang and W. Wong, "Stable control of magnetically suspended motor with heavy self-weight and great moment of inertia," *ISA Transactions*, 2020/05/15/ 2020.(**IF**=4.304)

B. Xiang, Q. Guo, and W. Wong, "Active disturbance rejection control of test sample in electrostatic suspension system," *Mechanical Systems and Signal Processing*, vol. 148, p. 107187, 2021/02/01/ 2021. (**IF**=6.471)

B. Xiang and W. Wong, "Electromagnetic vibration absorber for torsional vibration in high speed rotational machine," *Mechanical Systems and Signal Processing,* vol. 140, 2020. (**IF**=6.471)

B. Xiang and W. Wong, "Vibration characteristics analysis of magnetically suspended rotor in flywheel energy storage system," *Journal of Sound and Vibration,* vol. 444, pp. 235-247, 2019. (**IF**=3.429)

B. Xiang and W. Wong, "Power compensation mechanism for AMB system in magnetically suspended flywheel energy storage system," *Measurement*, p. 108646, 2020/10/24/ 2020. (**IF**=3..364)

B. Xiang and W. Wong, "Decoupling Control of MSFW Rotor with Heavy Self-weight and Great Moment of Inertia Based on an Internal Model Control Model," *Journal of Vibration and Control* (in process) (**IF**=2.169)

W. Tong, **B. Xiang***, and W. Wong, "Gimbal torque and coupling torque of six degrees of freedom magnetically suspended yaw gimbal," *International Journal of Mechanical Sciences,* vol. 168, 2020. (**IF**=4.631)

B. Xiang and W. Wong, "Suspension Characteristics of Magnetically Suspended Frame in Inertially Stabilized Platform," in *2018 IEEE 18th International Power Electronics and Motion Control Conference (PEMC)*, 2018, pp. 776-783: IEEE.

Whirling Characteristics and Stability Analysis Method of Unsymmetrical Magnetically Suspended Motor. (submitted to *ISA Transactions*, under review after minor revision).

References

[1] F. G. Capponi, G. De Donato, and F. Caricchi, "Recent advances in axial-flux permanent-magnet machine technology," *IEEE Transactions on Industry Applications,* vol. 48, no. 6, pp. 2190-2205, 2012.

[2] J. Asama, R. Kawata, T. Tamura, T. Oiwa, and A. Chiba, "Reduction of force interference and performance improvement of a consequent-pole bearingless motor," *Precision Engineering,* vol. 36, no. 1, pp. 10-18, 2012.

[3] H. Bleuler *et al.*, *Magnetic bearings: theory, design, and application to rotating machinery*. Springer Science & Business Media, 2009.

[4] X. Xu, S. Chen, and Y. Zhang, "Automatic balancing of AMB systems using plural notch filter and adaptive synchronous compensation," *Journal of Sound and Vibration,* vol. 374, pp. 29-42, 2016.

[5] G. Schweitzer, "Safety and reliability aspects for active magnetic bearing applications-a survey," *Proceedings of the Institution of Mechanical Engineers, Part I: Journal of Systems and Control Engineering,* vol. 219, no. 6, pp. 383-392, 2005.

[6] M. Ahrens, L. Kucera, and R. Larsonneur, "Performance of a magnetically suspended flywheel energy storage device," *IEEE Transactions on control systems technology,* vol. 4, no. 5, pp. 494-502, 1996.

[7] B. Xiang and J. Tang, "Suspension and titling of vernier-gimballing magnetically suspended flywheel with conical magnetic bearing and Lorentz magnetic bearing," *Mechatronics,* vol. 28, pp. 46-54, 2015.

[8] J. Fang and Y. Ren, "High-precision control for a single-gimbal magnetically suspended control moment gyro based on inverse system method," *IEEE Transactions on Industrial Electronics,* vol. 58, no. 9, pp. 4331-4342, 2011.

[9] Y. Ren and J. Fang, "High-stability and fast-response twisting motion control for the magnetically suspended rotor system in a control moment gyro," *IEEE/ASME Transactions on Mechatronics,* vol. 18, no. 5, pp. 1625-1634, 2013.

[10] Y. Ren, D. Su, and J. Fang, "Whirling modes stability criterion for a magnetically suspended flywheel rotor with significant gyroscopic effects and bending modes," *IEEE Transactions on Power Electronics,* vol. 28, no. 12, pp. 5890-5901, 2013.

[11] J. Fang, S. Zheng, and B. Han, "AMB vibration control for structural resonance of double-gimbal control moment gyro with high-speed magnetically suspended rotor," *IEEE/ASME Transactions on Mechatronics,* vol. 18, no. 1, pp. 32-43, 2013.

[12] T. Schneeberger, T. Nussbaumer, and J. W. Kolar, "Magnetically levitated homopolar hollow-shaft motor," *IEEE/ASME transactions on mechatronics,* vol. 15, no. 1, pp. 97-107, 2010.

[13] X. Sun, L. Chen, and Z. Yang, "Overview of bearingless permanent-magnet synchronous motors," *IEEE Transactions on Industrial Electronics,* vol. 60, no. 12, pp. 5528-5538, 2013.

[14] J. Amemiya, A. Chiba, D. G. Dorrell, and T. Fukao, "Basic characteristics of a consequent-pole-type bearingless motor," *IEEE Transactions on Magnetics,* vol. 41, no. 1, pp. 82-89, 2005.

[15] S. Zheng and R. Feng, "Feedforward compensation control of rotor imbalance for high-speed magnetically suspended centrifugal compressors using a novel adaptive notch filter," *Journal of Sound and Vibration,* vol. 366, pp. 1-14, 2016.

[16] J. Asama, D. Kanehara, T. Oiwa, and A. Chiba, "Development of a compact centrifugal pump with a two-axis actively positioned consequent-pole bearingless motor," *IEEE Transactions on Industry Applications,* vol. 50, no. 1, pp. 288-295, 2014.

[17] S. Cheng, M. W. Olles, D. B. Olsen, L. D. Joyce, and S. W. Day, "Miniaturization of a magnetically levitated axial flow blood pump," *Artificial organs,* vol. 34, no. 10, pp. 807-815, 2010.

[18] B. Han, Q. Xu, and Q. Yuan, "Multiobjective optimization of a combined radial-axial magnetic bearing for magnetically suspended compressor," *IEEE Transactions on Industrial Electronics,* vol. 63, no. 4, pp. 2284-2293, 2016.

[19] T. Masuzawa, S. Ezoe, T. Kato, and Y. Okada, "Magnetically suspended centrifugal blood pump with an axially levitated motor," *Artificial organs,* vol. 27, no. 7, pp. 631-638, 2003.

[20] T. Masuzawa, T. Kita, K. i. Matsuda, and Y. Okada, "Magnetically Suspended Rotary Blood Pump with Radial Type Combined Motor-Bearing," *Artificial organs,* vol. 24, no. 6, pp. 468-474, 2000.

[21] J. Sun, C. Wang, and Y. Le, "Designing and Experimental Verification of the Axial Hybrid Magnetic Bearing to Stabilization of a Magnetically Suspended Inertially Stabilized Platform," *IEEE/ASME Transactions on Mechatronics,* vol. 21, no. 6, pp. 2881-2891, 2016.

[22] Q. Guo, G. Liu, B. Xiang, H. Liu, and T. Wen, "The disturbance rejection of magnetically suspended inertially stabilized platform," *Transactions of the Institute of Measurement and Control,* p. 0142331216661623, 2016.

[23] Q. Guo, G. Liu, B. Xiang, T. Wen, and H. Liu, "Robust control of magnetically suspended gimbals in inertial stabilized platform with wide load range," *Mechatronics,* vol. 39, pp. 127-135, 2016.

[24] X. Li, B. Anvari, A. Palazzolo, Z. Wang, and H. Toliyat, "A Utility Scale Flywheel Energy Storage System with a Shaft-less, Hub-less, High Strength Steel Rotor," *IEEE Transactions on Industrial Electronics,* 2017.

[25] A. Kailasan, T. Dimond, P. Allaire, and D. Sheffler, "Design and analysis of a unique energy storage flywheel system—An integrated flywheel, motor/generator, and magnetic bearing configuration," *Journal of Engineering for Gas Turbines and Power,* vol. 137, no. 4, p. 042505, 2015.

[26] W. Li, K. Chau, T. Ching, Y. Wang, and M. Chen, "Design of a high-speed superconducting bearingless machine for flywheel energy storage systems," *IEEE Transactions on Applied Superconductivity,* vol. 25, no. 3, pp. 1-4, 2015.

[27] J. Tang, K. Wang, and B. Xiang, "Stable control of high-speed rotor suspended by superconducting magnetic bearings and active magnetic bearings," *IEEE Transactions on Industrial Electronics,* vol. 64, no. 4, pp. 3319-3328, 2017.

[28] K. Wang, L. Zhang, B. Han, and S. Chen, "Analysis and Experiment of Self-Differential Eddy Current Displacement Sensor for AMBs Used in Molecular Pump," *IEEE Transactions on Instrumentation and Measurement,* 2018.

[29] K. Zhang, H. Wu, Q. Li, X. Zhang, and M. Zou, "Method of dynamic balancing for magnetic levitation molecular pump," ed: Google Patents, 2016.

[30] X. Ren, Y. Le, B. Han, and K. Wang, "Loss optimization and thermal analysis of a heteropolar magnetic bearing for a vacuum turbo-molecular pump," *International Journal of Applied Electromagnetics and Mechanics,* vol. 54, no. 4, pp. 673-690, 2017.

[31] Y. Zhang, S. Zheng, Q. Chen, and J. Fang, "Surge Detection Approach for Magnetically Suspended Centrifugal Compressors Using Adaptive Frequency Estimator," *IEEE Transactions on Industrial Electronics,* 2017.

[32] Y. Zhang, S. Zheng, Q. Chen, and K. Zhang, "A novel surge detection method based on magnetically suspended centrifugal compressor using adaptive notch filter," in *Control Conference (CCC), 2017 36th Chinese*, 2017, pp. 5578-5584: IEEE.

[33] Y. Le, J. Fang, and J. Sun, "Design of a Halbach array permanent magnet damping system for high speed compressor with large thrust load," *IEEE Transactions on Magnetics,* vol. 51, no. 1, pp. 1-9, 2015.

[34] P. Cui, Q. Wang, G. Zhang, and Q. Gao, "Hybrid Fractional Repetitive Control for Magnetically Suspended Rotor Systems," *IEEE Transactions on Industrial Electronics,* vol. 65, no. 4, pp. 3491-3498, 2018.

[35] E. Tang, B. Han, and Y. Zhang, "Optimum compensator design for the flexible rotor in magnetically suspended motor to pass the first bending critical speed," *IEEE Transactions on Industrial Electronics,* vol. 63, no. 1, pp. 343-354, 2016.

[36] X. Sun, Z. Xue, L. Chen, Z. Yang, and H. Zhu, "Radial position control of a magnetically suspended rotor system in a direct-driven spindle using inverse system scheme," *Transactions of the Institute of Measurement and Control,* vol. 38, no. 9, pp. 1073-1086, 2016.

[37] X. Xu, J. Liu, and S. Chen, "Synchronous Force Elimination in the Magnetically Suspended Rotor System With an Adaptation to Parameter Variations in the Amplifier Model," *IEEE Transactions on Industrial Electronics,* 2018.

[38] X. Ren, Y. Le, and B. Han, "System Electromagnetic Loss Analysis and Temperature Field Estimate of a Magnetically Suspended Motor," *Progress In Electromagnetics Research M,* vol. 55, pp. 51-61, 2017.

[39] Z. Huang, J. Fang, X. Liu, and B. Han, "Loss calculation and thermal analysis of rotors supported by active magnetic bearings for high-speed permanent-magnet electrical machines," *IEEE Transactions on Industrial Electronics,* vol. 63, no. 4, pp. 2027-2035, 2016.

[40] M. Cole, P. Keogh, and C. Burrows, "Vibration control of a flexible rotor/magnetic bearing system subject to direct forcing and base motion disturbances," *Proceedings of the Institution of Mechanical Engineers, Part C: Journal of Mechanical Engineering Science,* vol. 212, no. 7, pp. 535-546, 1998.

[41] Q. Chen, G. Liu, and S. Zheng, "Suppression of imbalance vibration for AMBs controlled driveline system using double-loop structure," *Journal of Sound and Vibration,* vol. 337, pp. 1-13, 2015.

[42] K. Jiang and C. Zhu, "Multi-frequency periodic vibration suppressing in active magnetic bearing-rotor systems via response matching in frequency domain," *Mechanical Systems and Signal Processing,* vol. 25, no. 4, pp. 1417-1429, 2011.

[43] J. Asama *et al.*, "Evaluation of a bearingless PM motor with wide magnetic gaps," *IEEE Transactions on Energy Conversion,* vol. 25, no. 4, pp. 957-964, 2010.

[44] J. Tang, B. Xiang, and Y. Zhang, "Dynamic characteristics of the rotor in a magnetically suspended control moment gyroscope with active magnetic bearing and passive magnetic bearing," *ISA transactions,* vol. 53, no. 4, pp. 1357-1365, 2014.

[45] J. Ji, L. Yu, and A. Leung, "Bifurcation behavior of a rotor supported by active magnetic bearings," *Journal of Sound and Vibration,* vol. 235, no. 1, pp. 133-151, 2000.

[46] J. Ji and C. Hansen, "Non-linear oscillations of a rotor in active magnetic bearings," *Journal of Sound and vibration,* vol. 240, no. 4, pp. 599-612, 2001.

[47] S.-M. Yang, "Electromagnetic actuator implementation and control for resonance vibration reduction in miniature magnetically levitated rotating machines," *IEEE Transactions on Industrial Electronics,* vol. 58, no. 2, pp. 611-617, 2011.

[48] J. Tang, K. Wang, Z. Peng, and S. Zhao, "Mechanical characteristics analysis of high-speed rotor in magnetically suspended control moment gyroscope," *Transactions of the Institute of Measurement and Control,* p. 0142331216678448, 2016.

[49] Y. Yan, D. Zhiquan, Z. Qianying, and W. Xiaolin, "Stator vibration analysis of bearingless switched reluctance motors," in *Electrical and Control Engineering (ICECE), 2010 International Conference on*, 2010, pp. 1993-1996: IEEE.

[50] J. Fang, Y. Ren, and Y. Fan, "Nutation and precession stability criterion of magnetically suspended rigid rotors with gyroscopic effects based on positive and negative frequency characteristics," *IEEE Transactions on Industrial Electronics,* vol. 61, no. 4, pp. 2003-2014, 2014.

[51] Y. Ren, X. Chen, Y. Cai, and W. Wang, "Rotation modes stability analysis and phase compensation for magnetically suspended flywheel systems with cross feedback controller and time delay," *Mathematical Problems in Engineering,* vol. 2016, 2016.

[52] S. Zheng, B. Han, Y. Wang, and J. Zhou, "Optimization of damping compensation for a flexible rotor system with active magnetic bearing considering gyroscopic effect," *IEEE/ASME Transactions on Mechatronics,* vol. 20, no. 3, pp. 1130-1137, 2015.

[53] C. Zhang, K. J. Tseng, T. D. Nguyen, and G. Zhao, "Stiffness analysis and levitation force control of active magnetic bearing for a partially-self-bearing flywheel system," *International Journal of Applied Electromagnetics and Mechanics,* vol. 36, no. 3, pp. 229-242, 2011.

[54] T. Dimond, P. Allaire, S. Mushi, Z. Lin, and S. Y. Yoon, "Modal tilt/translate control and stability of a rigid rotor with gyroscopics on active magnetic bearings," *International Journal of Rotating Machinery,* vol. 2012, 2012.

[55] T. Asami, O. Nishihara, and A. M. Baz, "Analytical solutions to H∞ and H2 optimization of dynamic vibration absorbers attached to damped linear systems," *Journal of vibration and acoustics,* vol. 124, no. 2, pp. 284-295, 2002.

[56] X. Chang, Y. Li, W. Zhang, N. Wang, and W. Xue, "Active disturbance rejection control for a flywheel energy storage system," *IEEE Transactions on Industrial Electronics,* vol. 62, no. 2, pp. 991-1001, 2015.

[57] S. Park, W. Kim, and S.-I. Kim, "A numerical prediction model for vibration and noise of axial flux motors," *IEEE Transactions on Industrial Electronics,* vol. 61, no. 10, pp. 5757-5762, 2014.

[58] W. Sun, Y. Li, J. Huang, and N. Zhang, "Vibration effect and control of In-Wheel Switched Reluctance Motor for electric vehicle," *Journal of Sound and Vibration,* vol. 338, pp. 105-120, 2015.

[59] H.-J. Shin, J.-Y. Choi, H.-I. Park, and S.-M. Jang, "Vibration analysis and measurements through prediction of electromagnetic vibration sources of permanent magnet synchronous motor based on analytical magnetic field calculations," *IEEE Transactions on Magnetics,* vol. 48, no. 11, pp. 4216-4219, 2012.

[60] S. M. Castano, B. Bilgin, E. Fairall, and A. Emadi, "Acoustic noise analysis of a high-speed high-power switched reluctance machine: Frame effects," *IEEE Transactions on Energy Conversion,* vol. 31, no. 1, pp. 69-77, 2016.

[61] J. Licari, C. E. Ugalde-Loo, J. B. Ekanayake, and N. Jenkins, "Damping of torsional vibrations in a variable-speed wind turbine," *IEEE transactions on energy conversion,* vol. 28, no. 1, pp. 172-180, 2013.

[62] H. Yao, Z. Chen, and B. Wen, "Dynamic vibration absorber with negative stiffness for rotor system," *Shock and Vibration,* vol. 2016, 2016.

[63] H. Ecker and T. Pumhössel, "Vibration suppression and energy transfer by parametric excitation in drive systems," *Proceedings of the Institution of Mechanical Engineers, Part C: Journal of Mechanical Engineering Science,* vol. 226, no. 8, pp. 2000-2014, 2012.

[64] H. Yao, T. Wang, B. Wen, and B. Qiu, "A tunable dynamic vibration absorber for unbalanced rotor system," *Journal of Mechanical Science and Technology,* vol. 32, no. 4, pp. 1519-1528, 2018.

[65] A. Abbasi, S. Khadem, S. Bab, and M. Friswell, "Vibration control of a rotor supported by journal bearings and an asymmetric high-static low-dynamic stiffness suspension," *Nonlinear Dynamics,* vol. 85, no. 1, pp. 525-545, 2016.

[66] A. Abbasi, S. Khadem, and S. Bab, "Vibration control of a continuous rotating shaft employing high-static low-dynamic stiffness isolators," *Journal of Vibration and Control,* vol. 24, no. 4, pp. 760-783, 2018.

[67] H. Navazi and M. Hojjati, "Nonlinear vibrations and stability analysis of a rotor on high-static-low-dynamic-stiffness supports using method of multiple scales," *Aerospace Science and Technology,* vol. 63, pp. 259-265, 2017.

[68] S. H. Kia, H. Henao, and G.-A. Capolino, "Torsional vibration effects on induction machine current and torque signatures in gearbox-based electromechanical system," *IEEE Transactions on Industrial Electronics,* vol. 56, no. 11, pp. 4689-4699, 2009.

[69] B. Al-Bedoor, K. Moustafa, and K. Al-Hussain, "Dual dynamic absorber for the torsional vibrations of synchronous motor-driven compressors," *Journal of sound and vibration,* vol. 220, no. 4, pp. 729-748, 1999.

[70] J. Zhou, D. Xu, and S. Bishop, "A torsion quasi-zero stiffness vibration isolator," *Journal of Sound and Vibration,* vol. 338, pp. 121-133, 2015.

[71] F. Doubrawa Filho, M. Luersen, and C. Bavastri, "Optimal design of viscoelastic vibration absorbers for rotating systems," *Journal of Vibration and Control,* vol. 17, no. 5, pp. 699-710, 2011.

[72] G. Liu, K. Lu, D. Zou, Z. Xie, Z. Rao, and N. Ta, "Development of a semi-active dynamic vibration absorber for longitudinal vibration of propulsion shaft system based on magnetorheological elastomer," *Smart Materials and Structures,* vol. 26, no. 7, p. 075009, 2017.

[73] A. Gonzalez-Buelga, L. Clare, S. Neild, S. Burrow, and D. Inman, "An electromagnetic vibration absorber with harvesting and tuning capabilities," *Structural Control and Health Monitoring,* vol. 22, no. 11, pp. 1359-1372, 2015.

[74] M. Sasaki and T. Sugiura, "Vibration reduction of rotor supported by superconducting magnetic bearing utilizing electromagnetic shunt damper," *IEEE Transactions on Applied Superconductivity,* vol. 26, no. 3, pp. 1-4, 2016.

[75] Y. Sun and M. Thomas, "Control of torsional rotor vibrations using an electrorheological fluid dynamic absorber," *Journal of Vibration and Control,* vol. 17, no. 8, pp. 1253-1264, 2011.

[76] R. S. Srinivas, R. Tiwari, and C. Kannababu, "Application of active magnetic bearings in flexible rotordynamic systems–A state-of-the-art review," *Mechanical Systems and Signal Processing,* vol. 106, pp. 537-572, 2018.

[77] A. A. Cavalini, T. V. Galavotti, T. S. Morais, E. H. Koroishi, and V. Steffen, "Vibration attenuation in rotating machines using smart spring mechanism," *Mathematical Problems in Engineering,* vol. 2011, 2011.

[78] C. Liu and G. Liu, "Equivalent damping control of radial twist motion for permanent magnetic bearings based on radial position variation," *IEEE Transactions on Industrial Electronics,* vol. 62, no. 10, pp. 6417-6427, 2015.

[79] G. Shahgholian and P. Shafaghi, "Simple analytical and robust controller design for two-mass resonant system," in *Computer and Electrical Engineering, 2009. ICCEE'09. Second International Conference on*, 2009, vol. 1, pp. 245-248: IEEE.

[80] G. Shahgholian, "Modeling and simulation of a two-mass resonant system with speed controller," *International Journal of Information and Electronics Engineering,* vol. 3, no. 5, p. 448, 2013.

[81] D.-H. Lee, J. Lee, and J.-W. Ahn, "Mechanical vibration reduction control of two-mass permanent magnet synchronous motor using adaptive notch filter with fast Fourier transform analysis," *IET electric power applications,* vol. 6, no. 7, pp. 455-461, 2012.

[82] T. Orlowska-Kowalska and K. Szabat, "Neural-network application for mechanical variables estimation of a two-mass drive system," *IEEE Transactions on Industrial Electronics,* vol. 54, no. 3, pp. 1352-1364, 2007.

[83] Y. Amer, A. El-Sayed, and F. El-Bahrawy, "Torsional vibration reduction for rolling mill's main drive system via negative velocity feedback under parametric excitation," *Journal of Mechanical Science and Technology,* vol. 29, no. 4, pp. 1581-1589, 2015.

[84] B. Xiang and W. on Wong, "Vibration characteristics analysis of magnetically suspended rotor in flywheel energy storage system," *Journal of Sound and Vibration,* vol. 444, pp. 235-247, 2019.

[85] M. Chen and C. R. Knospe, "Control approaches to the suppression of machining chatter using active magnetic bearings," *IEEE Transactions on control systems technology,* vol. 15, no. 2, pp. 220-232, 2007.

[86] B. Polajžer, J. Ritonja, G. Štumberger, D. Dolinar, and J.-P. Lecointe, "Decentralized PI/PD position control for active magnetic bearings," *Electrical Engineering,* vol. 89, no. 1, pp. 53-59, 2006.

[87] H. S. Zad, T. I. Khan, and I. Lazoglu, "Design and adaptive sliding-mode control of hybrid magnetic bearings," *IEEE Transactions on Industrial Electronics,* vol. 65, no. 3, pp. 2537-2547, 2018.

[88] S.-Y. Chen and F.-J. Lin, "Robust nonsingular terminal sliding-mode control for nonlinear magnetic bearing system," *IEEE Transactions on Control Systems Technology,* vol. 19, no. 3, pp. 636-643, 2011.

[89] S. Sivrioglu and K. Nonami, "Sliding mode control with time-varying hyperplane for AMB systems," *IEEE/ASME Transactions On Mechatronics,* vol. 3, no. 1, pp. 51-59, 1998.

[90] T. Schuhmann, W. Hofmann, and R. Werner, "Improving operational performance of active magnetic bearings using Kalman filter and state feedback control," *IEEE Transactions on Industrial Electronics,* vol. 59, no. 2, pp. 821-829, 2012.

[91] S. Sivrioglu, "Adaptive backstepping for switching control active magnetic bearing system with vibrating base," *IET Control Theory & Applications,* vol. 1, no. 4, pp. 1054-1059, 2007.

[92] F. Betschon and C. R. Knospe, "Reducing magnetic bearing currents via gain scheduled adaptive control," *IEEE/ASME transactions on mechatronics,* vol. 6, no. 4, pp. 437-443, 2001.

[93] Y. Park, "Design and implementation of an electromagnetic levitation system for active magnetic bearing wheels," *IET Control Theory & Applications,* vol. 8, no. 2, pp. 139-148, 2014.

[94] H. Du, N. Zhang, J. C. Ji, and W. Gao, "Robust fuzzy control of an active magnetic bearing subject to voltage saturation," *IEEE transactions on control systems technology,* vol. 18, no. 1, pp. 164-169, 2010.

[95] P.-Y. Couzon and J. Der Hagopian, "Neuro-fuzzy active control of rotor suspended on active magnetic bearing," *Journal of Vibration and Control,* vol. 13, no. 4, pp. 365-384, 2007.

[96] A. Noshadi, J. Shi, W. S. Lee, P. Shi, and A. Kalam, "Robust control of an active magnetic bearing system using H∞ and disturbance observer-based control," *Journal of Vibration and Control,* vol. 23, no. 11, pp. 1857-1870, 2017.

[97] A. Noshadi, J. Shi, W. S. Lee, P. Shi, and A. Kalam, "System identification and robust control of multi-input multi-output active magnetic bearing systems," *IEEE Transactions on control Systems technology,* vol. 24, no. 4, pp. 1227-1239, 2016.

[98] A. H. Pesch, A. Smirnov, O. Pyrhönen, and J. T. Sawicki, "Magnetic Bearing Spindle Tool Tracking Through ${\mu} $-Synthesis Robust Control," *IEEE/ASME Transactions on Mechatronics,* vol. 20, no. 3, pp. 1448-1457, 2015.

[99] S.-L. Chen and C.-C. Weng, "Robust control of a voltage-controlled three-pole active magnetic bearing system," *IEEE/ASME Transactions on Mechatronics,* vol. 15, no. 3, pp. 381-388, 2010.

[100] Z. Gosiewski and A. Mystkowski, "Robust control of active magnetic suspension: analytical and experimental results," *Mechanical Systems and Signal Processing,* vol. 22, no. 6, pp. 1297-1303, 2008.

[101] D. H. Lee, J. B. Park, Y. H. Joo, K. C. Lin, and C. H. Ham, "Robust H∞ control for uncertain nonlinear active magnetic bearing systems via Takagi-Sugeno fuzzy models," *International Journal of Control, Automation and Systems,* vol. 8, no. 3, pp. 636-646, 2010.

[102] H. Balini, C. W. Scherer, and J. Witte, "Performance Enhancement for AMB Systems Using Unstable $ H_ {\infty} $ Controllers," *IEEE Transactions on Control Systems Technology,* vol. 19, no. 6, pp. 1479-1492, 2011.

[103] İ. S. Kuseyri, "Robust control and unbalance compensation of rotor/active magnetic bearing systems," *Journal of Vibration and Control,* vol. 18, no. 6, pp. 817-832, 2012.

[104] C. E. Garcia and M. Morari, "Internal model control. A unifying review and some new results," *Industrial & Engineering Chemistry Process Design and Development,* vol. 21, no. 2, pp. 308-323, 1982.

[105] B. A. Francis and W. M. Wonham, "The internal model principle of control theory," *Automatica,* vol. 12, no. 5, pp. 457-465, 1976.

[106] D. Rivera, M. Morarl, and S. Skogestad, "Internal Model Control: Pid Controller Design," *Industrial and Engineering Chemistry Process Design and Development,* vol. 25, no. 1, pp. 252-265, 1986.

[107] S. Li and H. Gu, "Fuzzy adaptive internal model control schemes for PMSM speed-regulation system," *IEEE Transactions on Industrial Informatics,* vol. 8, no. 4, pp. 767-779, 2012.

[108] J. Fang and Y. Ren, "High-precision control for a single-gimbal magnetically suspended control moment gyro based on inverse system method," *IEEE Transactions on Industrial Electronics,* vol. 58, no. 9, pp. 4331-4342, 2010.

[109] X. Sun, B. Su, L. Chen, Z. Yang, X. Xu, and Z. Shi, "Precise control of a four degree-of-freedom permanent magnet biased active magnetic bearing system in a magnetically suspended direct-driven spindle using neural network inverse scheme," *Mechanical Systems and Signal Processing,* vol. 88, pp. 36-48, 2017.

[110] D. J. Griffith and G. Ruppeiner, "Introduction to electrodynamics," *American Journal of Physics,* vol. 49, no. 12, pp. 1188-1189, 1981.

[111] G. Shahgholian and P. Shafaghi, "Simple analytical and robust controller design for two-mass resonant system," in *2009 Second International Conference on Computer and Electrical Engineering*, 2009, vol. 1, pp. 245-248: IEEE.

[112] A. Ghaemmaghami, R. Kianoush, and X. X. Yuan, "Numerical modeling of dynamic behavior of annular tuned liquid dampers for applications in wind towers," *Computer-Aided Civil and Infrastructure Engineering,* vol. 28, no. 1, pp. 38-51, 2013.

[113] K. Szabat and T. Orlowska-Kowalska, "Vibration suppression in a two-mass drive system using PI speed controller and additional feedbacks—Comparative study," *IEEE Transactions on Industrial Electronics,* vol. 54, no. 2, pp. 1193-1206, 2007.

[114] J. Fang, C. Wang, and T. Wen, "Design and optimization of a radial hybrid magnetic bearing with separate poles for magnetically suspended inertially stabilized platform," *IEEE Transactions on Magnetics,* vol. 50, no. 5, pp. 1-11, 2014.

[115] Griffiths and DavidJ, *Introduction to electrodynamics /-3rd ed*. Introduction to electrodynamics /-3rd ed, 2006.